

MEMBRANE TRAFFICKING DEFECTS CONTRIBUTE TO NEURODEGENERATIVE DISEASES

by

Jennifer L. Peotter

A dissertation submitted in partial fulfillment of
the requirements for the degree of

Doctor of Philosophy
(Biochemistry)

at the

UNIVERSITY OF WISCONSIN–MADISON

2022

Date of final examination: 06/23/2022

This dissertation is approved by the following members of the Final Oral Committee:

Anjon Audhya, Biomolecular Chemistry
Edwin Chapman, Neuroscience
Erik Dent, Neuroscience
Michael Sheets, Biomolecular Chemistry
Amy Weeks, Biochemistry

© Copyright by Jennifer L. Peotter 2022

All Rights Reserved

Acknowledgements

I would like to thank my advisor, Professor Jon Audhya, for his guidance and support throughout my graduate career at the University of Wisconsin–Madison. I have learned a great deal over the past few years through working with Jon and in his lab. He provided an environment that fosters independence and personal growth, through which I learned to be both an independent scientist and a strong collaborator. Additionally, I am thankful for Jon’s support in pursuing an untraditional career path and for allowing me time to gain skills outside of the lab.

A truly unique aspect about the Audhya Lab was the amazing people I have had the pleasure to meet and work with over the past few years. I would like to thank Dr. Molly Lettman for her encouragement and words of advice over the years. I have truly enjoyed working with her and collaborating closely. I would also like to thank Dr. Raakhee Shankar and Peter Luong for their valuable friendship. They have been and continue to be a great place for scientific discussion and camaraderie. I would also like to thank the rest of the Audhya Lab: Aryel Clarke, William Kasberg, Iryna Pustova, Kevin Swift, and Ziheng Zhang. I am exceedingly grateful for our strong working relationship and respect for one another. Graduate school can be very stressful but going to work with all of these amazing people made a huge difference.

I would also like to thank my thesis committee, Dr. Ed Chapman, Dr. Erik Dent, Dr. Mike Sheets, and Dr. Amy Weeks. As well as my previous committee members Dr. Dave Pagliarini and Dr. Jill Wildonger. I greatly appreciate all of your time, feedback, and encouragement throughout my PhD. Being able to have such a diversity of expertise across my committee was very valuable and something I greatly appreciated. I would also specifically like to thank Dr. Chapman and his lab members Dr. Mazdak Bradberry and Dr. Jason Vevea for their collaborative efforts and support in all things neuroscience related.

I would also like to thank the Senes Lab and the Peters Lab at the University of Wisconsin–Madison, which I worked in during my undergraduate and postgraduate times, respectively. Both Dr. Alessandro Senes, Dr. Donna Peters, and all of their lab personal were instrumental in shaping my passion for research as well as my pursuit of a PhD.

Outside of my research there are many people who have been instrumental in my graduate school experience and career path. Specifically, I would like to thank all of those I have had the pleasure of working with at WiSolve Consulting Group. Dr. Chris Konop and Dr. Inca Dieterich were integral to me becoming a part of the organization and pushed me to find the confidence to try new things. I would also like to thank Dr. Shaswath Sekar Chandrasekar for our great partnership in leading the organization together. Being a part of this organization, and all of the people I was able to work with and meet, was a very transformative experience and something that I am very thankful for.

I would like to thank my parents, Cheryl and Ben Peotter, for supporting me throughout my life and for raising me with the confidence to take on any challenge. You have always encouraged me to try new things and fostered independence which has allowed me to take on many new opportunities. Additionally, I would also like to thank my sisters, Dr. Ashley Peotter and Wendy Peotter, for their support and friendship throughout my life.

Finally, I would like to thank my fiancé, Dr. Nick Kwiecien, for his encouragement and support over the previous years. As a previous graduate student, he knew better than most the challenges and setbacks that can accompany a PhD tenure. Nick took it all in stride and was a constant sounding board throughout this journey. I am also thankful for Nick's encouragement and ambition that pushed me to look outside my comfort zone and pursue my career path. I am truly thankful to have you in my life.

Table of contents

Acknowledgements	i
Table of contents	iii
Abstract	vii
List of abbreviations	viii
Chapter 1. COPII-mediated trafficking at the ER/ERGIC interface	1
Introduction	3
The COPII coat	3
Regulation of the COPII coat assembly	8
Regulation of COPII coat disassembly at the ER/ERGIC interface	15
Regulation of COPII carrier formation and transport mediated by posttranslational modifications.	18
Conclusions and perspectives	23
Figures.	25
References	28
Chapter 2. Neurological disorders linked to mutations in TFG.	42
Introduction.	44
TFG p.R106C mutation disrupts protein transport through the early secretory pathway and endosomal pathway.	44

HMSN-P is related to a p.P285L TFG mutation linked to inclusion bodies and UPS dysfunction	48
TFG mutations related to CMT2, ALS, and PD.	50
Conclusion	52
References	54
Chapter 3. TFG regulates secretory and endosomal sorting pathways in neurons to promote their activity and maintenance	58
Introduction	60
Results	62
The TFG p.R106C mutation causes progressive gait dysfunction	62
The TFG p.R106C mutation causes alterations in hind limb electrophysiology and central nervous system pathology	64
The TFG p.R106C mutation impairs neuronal protein trafficking from the ER	66
TFG regulates the trafficking of Rab4-positive endosomes in axons and dendrites	68
The TFG p.R106C mutation perturbs gephyrin trafficking to alter inhibitory postsynaptic currents	69
Discussion	70
Materials and methods	74
Figures	80

References	93
Chapter 4. Acetyl-CoA flux from the cytosol to the ER regulates engagement and quality of the secretory pathway	102
Introduction	104
Results	105
Aberrant AT-1 activity affects secretory pathway-related processes	105
Altered AT-1 activity results in morphological reorganization of the ER, ERGIC, and Golgi apparatus	106
Altered AT-1 activity disrupts normal protein trafficking	107
Aberrant AT-1 models display defects in Golgi-dependent N-glycan modification and a shift in the quality of the secretome	109
Aberrant AT-1 models display expansion of the lysosomal network	113
Discussion	114
Methods	116
Figures	129
References	155
Chapter 5. Discussion and future directions	160
Appendix A. Pathogenic TFG mutations underlying Hereditary Spastic Paraplegia impair secretory proteins trafficking and axon fasciculation	166

Introduction	168
Results	170
A clinically relevant mutation in TFG disrupts its ability to form compact ring complexes	170
The TFG (p.R106C) mutation impairs secretory protein trafficking and elevates ER stress	174
The distribution of TFG in cortical neurons is disrupted by the p.R106C mutation	178
TFG functions to promote axon bundling	179
Discussion	181
Experimental procedures	183
Figures	187
References	214

Abstract

Proper membrane trafficking is critical for neurons to maintain health and biological functions and many neurological disorders have been linked to defects in membrane trafficking. Current research has begun to shed light on the underlying pathomechanisms, but questions still remain as to why neurons are acutely susceptible to defects in membrane trafficking. Here, we have utilized a mutation in Trk-fused gene (TFG) that was previously discovered in patients with Hereditary Spastic Paraplegia (HSP) to evaluate the affect this point mutation has on Coat Protein complex II (COPII) mediated trafficking, where TFG is canonically known to function, and to investigate a neuronal specific function for TFG. For this work, we used an animal model that harbors the same homozygous mutation found in patients with HSP and strongly recapitulates the gait deficits observed in patients. Primary cortical neurons collected from this model revealed a kinetic delay in cargo transport from the endoplasmic reticulum (ER) to the Golgi. Interestingly, this work also revealed a function for TFG in neurites that was associated with Rab4-positive endosomes. Further, in the presence of the HSP-related mutation, Rab4 endosome function was affected, and the clustering of some inhibitory synaptic proteins was decreased. Taken together, this work revealed a dual role for TFG in neurons, both the canonical function in COPII-mediated transport and a novel role in Rab4-mediated endosome sorting, both of which are altered in the presence of the HSP associated mutation. This dual function for TFG in neurons may begin to explain the sensitivity neuronal cells have to defects in membrane trafficking.

List of abbreviations

ACE1	Ancestral coatomer element 1
ALS	Amyotrophic lateral sclerosis
B4GALT2	Beta-1,4-Galactosyltransferase 2
B4GALT4	Beta-1,4-Galactosyltransferase 4
BFA	Brefeldin A
CAD	Conditional aggregation domain
CCD	Central conserved domain
CCD	Charge-coupled device
CD	Cation-dependent
CD	Circular dichroism
CI	Cation-independent
CKII	Casein kinase II
CMT2	Charcot-Marie-Tooth disease type 2
CNS	Central nervous system
COPI	Coat Protein complex I
COPII	Coat Protein complex II
CRISPR	Clustered regularly interspaced short palindromic repeats
CST	Corticospinal tract
CTD	Carboxyl-terminal domain
CUL3	Cullin-3
DDA	Data-dependent acquisition
DDS	Dimer-dimer solubilizer
DIA	Data-independent acquisition

DiLeu	Dimethylated leucine
D_{max}	Maximal inter-atomic distance
DTT	Dithiothreitol
ELD	ER localization determinant
EMG	Electromyography
ER	Endoplasmic reticulum
ERES	ER exit sites
ERGIC	ER-Golgi intermediate compartment
EThcD	Electron-transfer higher-energy collision dissociation
FA	Formic acid
FUT8	Fucosyltransferase 8
GAP	Guanine nucleotide activating protein
GEF	Guanine nucleotide exchange factor
H&E	Hematoxylin and eosin
HILIC	Hydrophilic interaction liquid chromatography
HMSN-P	Hereditary motor and sensory neuropathy with proximal dominant involvement
HSP	Hereditary spastic paraplegia
IAA	Iodoacetamide
INAD	Infantile neuroaxonal dystrophy
iPSCs	Induced pluripotent stem cells
L1CAM	L1 cell adhesion molecule
LFB	Luxol fast blue
M6P	Mannose-6-phosphate

M6PRs	M6P receptors
ManII	Mannosidase II
MEFs	Mouse embryonic fibroblasts
MRI	Magnetic resonance imaging
NA	Numerical aperture
NSD	Normalized spatial discrepancy
NSD	Normalized spatial discrepancy
OGA	O-GlcNAcase
O-GlcNAc	O-Linked β -N-acetylglucosamine
OGT	O-GlcNAc transferase
OST	Oligosaccharyl transferase
PD	Parkinson's disease
PI3P	Phosphatidylinositol 3-phosphate
PTM	Posttranslational modifications
QC	Quality control
R_g	Radius of gyration
SAXS	Small-angle X-ray scattering
SCX LC	Strong cation exchange liquid chromatography
SIM	Structure-illumination microscopy
siRNAs	Small interfering RNAs
SLC35A1	Solute Carrier Family 35 Member A1
SLC35A2	Solute Carrier Family 35 Member A2
SLC35C1	Solute Carrier Family 35 Member C1
ST3GAL3	ST3 beta-Galactoside alpha-2,3-sialyltransferase 3

ST6GAL1	ST6 Beta-Galactoside Alpha-2,6-Sialyltransferase 1
ST6GAL2	ST6 Beta-Galactoside Alpha-2,6-Sialyltransferase 2
TDP-43	TAR DNA-binding protein 43
TEER	Tether of ERGIC at ER
TFA	Trifluoroacetic acid
TFG	Trk-fused gene
ULK1	Unc-51 like kinase
UPR	Unfolded protein response
UPS	Ubiquitin-proteasome system
VSVG	Vesicular stomatitis virus G protein
WT	Wild type

Chapter 1. COPII-mediated trafficking at the ER/ERGIC interface

The work presented in this chapter has been published:

Peotter, J., Kasberg, W., Pustova, I., and Audhya, A. (2019) COPII-mediated trafficking at the ER/ERGIC interface. *Traffic*.

Abstract

Coat proteins play multiple roles in the life cycle of a membrane-bound transport intermediate, functioning in lipid bilayer remodeling, cargo selection and targeting to an acceptor compartment. The Coat Protein complex II (COPII) coat is known to act in each of these capacities, but recent work highlights the necessity for numerous accessory factors at all stages of transport carrier existence. Here, we review recent findings that highlight the roles of COPII and its regulators in the biogenesis of tubular COPII-coated carriers in mammalian cells that enable cargo transport between the endoplasmic reticulum and ER-Golgi intermediate compartments, the first step in a series of trafficking events that ultimately allows for the distribution of biosynthetic secretory cargoes throughout the entire endomembrane system.

1. Introduction

The first membrane fission and fusion steps in the mammalian secretory pathway are mediated by Coat Protein complex II (COPII), which promotes the formation of transport carriers at unique, ribosome-free subdomains of the endoplasmic reticulum (ER) to facilitate the delivery of cargoes, including an array of membrane proteins and lipids, to juxtaposed ER-Golgi intermediate compartment (ERGIC).¹⁻⁵ A combination of in vitro biochemical assays, proteomic studies, single particle electron microscopy-based techniques and X-ray crystallography approaches have been used to provide mechanistic insights into COPII coat assembly and disassembly. Collectively, this work has led to a much improved understanding of how COPII, together with a variety of regulatory factors, support transport carrier fission and fusion at the ER/ERGIC interface.

The initial description of COPII was based on studies using yeast as a model system and highlighted the assembly of a 10-nm-thick electron dense coat on ~60 to 65 nm vesicles that were able to fuse with Golgi membranes following GTP hydrolysis-mediated disassembly.⁶ In contrast, contemporaneous studies demonstrated that ER to Golgi transport in mammalian cells requires the sequential actions of COPII and another coat complex (COPI), with COPII acting specifically at the ER to enable cargo transport to pre-Golgi intermediates composed of vesicular-tubular clusters, now commonly referred to as ERGIC membranes.^{7,8} Thus, unlike yeast, the activity of COPII in the mammalian secretory pathway is largely restricted to a ~300 to 500 nm space between the ER and ERGIC and is unlikely to play a direct role in ERGIC to Golgi trafficking.¹

2. The COPII coat

The COPII coat complex consists of two proteinaceous layers that are capable of deforming highly curved ER membranes to generate cargo-laden transport intermediates. The inner layer is composed of a flexible Sar1-Sec23-Sec24 lattice, while the outer cage is made up of Sec13-Sec31

heterotetramers.⁹⁻¹² Assembly of COPII complexes is initiated by activation of Sar1, a small Ras-like GTPase, which is mediated by the integral membrane guanine nucleotide exchange factor (GEF) Sec12/PREB.¹³⁻¹⁵ In mammals, two Sar1 isoforms are expressed in most tissues, and although *in vitro* studies have defined only modest differences in their activities, Sar1A and Sar1B (~90% sequence identity) have been suggested to play distinct roles *in vivo*, particularly in the ER export of chylomicrons within enterocytes of the small intestine.¹⁶⁻²⁰ Patients lacking Sar1B (or expressing mutant forms predicted to impair nucleotide or membrane binding) exhibit fat malabsorption disorders due to impaired chylomicron (often >200 μm in size) secretion into the bloodstream, even though Sar1A is present and expressed normally.^{16,21} These data suggest that Sar1B is uniquely suited to drive the formation of large COPII-coated transport carriers (some more than 1 μm in diameter) *in vivo*. In contrast, most cultured cells grown *in vitro* can tolerate individual inhibition of either Sar1A or Sar1B, while their co-depletion leads to potent cargo trafficking defects.^{22,23}

The crystal structure of mammalian Sar1A is characteristic of other Ras superfamily GTPases with two mobile switch regions and a core of six central beta-strands positioned between three flanking alpha helices^{24,25} (Figure 1). The guanine-nucleotide-binding pocket contains a highly conserved GxxxxGKT Walker A motif (P-loop; residues 32-39) and serves as a docking site for Sec12 to catalyze GTP loading.^{15,27} Mutation of threonine 39 to asparagine generates a dominant negative isoform, which is constitutively bound to GDP and blocks COPII carrier formation.^{7,28,29} Conversely, mutation of histidine 79 to glycine within switch II dramatically reduces GTP hydrolysis and enables constitutive association of Sar1 with Sec23-Sec24 heterodimers, its major effector.^{7,28} Importantly, Sar1H79G strongly potentiates membrane tubulation, but potently blocks COPII-mediated transport in cells, suggesting a key role for GTP hydrolysis during carrier scission.^{18,30-36}

Unlike other members of the Ras superfamily that use myristoyl or prenyl modifications for membrane association, Sar1 isoforms employ a unique amino-terminal amphipathic helix to sample

membranes.³³ However, only when activated by Sec12 is Sar1GTP able to stably penetrate the bilayer to initiate membrane remodeling and COPII coat assembly.^{30,37} Importantly, active Sar1 exhibits curvature sensitivity, showing enhanced affinity for bent membranes.³⁰ Thus, as the membrane becomes more highly deformed, Sar1 is able to bind more tightly, thereby promoting the formation of a tubular transport intermediate. Consistent with this idea, electron and fluorescence microscopy-based *in vitro* studies have demonstrated that Sar1 is capable of forming organized lattices on artificial liposomes, converting them into tubules and even detached vesicles at high concentrations.³¹ The intrinsic GTPase activity of Sar1 is also stimulated by the presence of highly curved membranes.³⁰ Ultimately, Sar1 likely concentrates in regions of elevated curvature, such as the necks of budding transport carriers, where it can facilitate rapid fission upon GTP hydrolysis.³⁸ Although speculative, Sar1B may uniquely drive the generation of large, unconventional COPII carriers by exhibiting slower GTPase activity in cells as compared to Sar1A and providing additional time to enclose sizable substrates including chylomicrons within a carrier ahead of neck scission.

Sculpting of COPII carriers is further governed by Sar1GTP-mediated recruitment of a Sec23-Sec24 lattice composed of repeating ~15 nm bowtie-shaped units that form a helical array.^{9,10,37,39} Crystallographic and electron microscopy-based analysis of the membrane proximal region of yeast Sec23-Sec24 shows it to be concave, with a positively charged surface that is conserved in their mammalian paralogs and may stabilize curvature of the underlying phospholipid bilayer.¹⁰ Even though the proteins exhibit limited sequence similarity, the overall folds of Sec23 and Sec24 are closely related, and they are linked via intimate hydrogen bonding and van der Waals interactions, which join their trunk domains to generate an intersubunit beta-sheet (Figure 1). The trunk domain of Sec23 further contacts the switch II region of Sar1, but the neighboring helical domain is most critical for recognizing switch I and the active GTP-bound state.¹⁰ Additionally, the gelsolin-like domain of Sec23 plays a key role in promoting GTP hydrolysis on Sar1 by providing a catalytic arginine finger *in trans* to the active

site, thereby serving as a guanine nucleotide activating protein (GAP).^{10,40} Thus, somewhat paradoxically, completion of the inner layer of the COPII coat drives GTP hydrolysis on Sar1, promoting disassembly from the membrane surface. However, the integrity of Sar1GTP-Sec23-Sec24 complexes must be sufficiently long-lived to enable completion of COPII carrier biogenesis. Based on *in vitro* studies, the lifetime of such complexes is ~30 seconds, suggesting that COPII carriers at ER subdomains form at a similar rate as compared to other vesicle biogenesis events, including clathrin-mediated budding from the cell surface.⁴¹⁻⁴³

Like Sar1, mammals express two isoforms of Sec23 that are ~85% identical to one another. Although mutations in Sec23B have been implicated in anemia and various forms of cancer, and the Sec23-AF382L mutation causes cranioleptoculofacial dysplasia, the paralogs appear to be largely redundant for function and only vary by distinct tissue expression profiles.⁴⁴⁻⁴⁷ Both isoforms stably interact with any of the four Sec24 isoforms (A-D), which serve as adaptors for numerous integral membrane secretory proteins, including receptors for luminal cargoes that must be guided out of the ER.⁴⁸ Degenerate motifs enable a wide range of clients to be sorted into COPII carriers, with structural studies highlighting binding pockets on Sec24A and Sec24B that can associate with LxxLE and DxE sorting signals, while Sec24C and Sec24D harbor surface grooves for the IxM packaging motif.⁴⁹⁻⁵² Additionally, other cargo binding domains may exist on each Sec24 paralog, further expanding their ability to capture a multitude of cargoes.^{50,53} Although Sec24A and Sec24B exhibit significant overlap in cargo selectivity, mutational analysis in mice has uncovered a potentially unique role for Sec24A in PCSK9 secretion, a key regulator of plasma cholesterol levels, which is mediated by the PCSK9 receptor Surf4.^{54,55} However, this selectivity may only be the result of differences in the expression profiles of Sec24A and Sec24B. Consistent with this idea, Sec24A exhibits 5- to 10-fold higher expression as compared to Sec24B in the mouse liver.⁵⁵ Similarly, conditional deletion of Sec24C in

murine neural progenitors results in extensive neuronal cell death, but the phenotype can be rescued by ectopic expression of Sec24D.^{56,57}

Inner COPII coat assembly enables Sec13-Sec31 recruitment and outer cage formation in cells. Specifically, based on the analysis of yeast protein fragments, the extended proline-rich domain of Sec31 binds directly to a surface on Sec23 that includes the gelsolin, trunk and β -barrel domains, and extends over switch II of GTP-bound Sar1⁵⁸ (Figure 1). These data explain the ordered process by which Sar1GTP-Sec23-Sec24 complexes must first associate with membranes, followed by outer cage assembly. However, the outer cage also drives organization of the inner coat to form a coherent lattice, with homotypic Sec23 interactions largely governing lateral associations.⁵⁹ Based on indirect measurements of GTP hydrolysis on Sar1, which leverage changes in tryptophan fluorescence believed to accompany the transition of Sar1 from the GTP- to the GDP-bound state, binding of Sec31 has been suggested to accelerate Sar1 GTPase activity.⁴¹ The crystal structure of the yeast Sar1-Sec23-Sec31 ternary complex suggests a mechanism by which this occurs, involving optimization of the geometry of the histidine within switch II of Sar1 and a nucleophilic water molecule that bridges the imidazole side chain and the gamma phosphate of a GTP analog.⁵⁸ However, in the absence of an analogous structure for a metazoan COPII complex, the extent to which Sec31 activates GTP hydrolysis in animal cells remains ill-defined.

Sec31 isoforms are comprised of multiple domains, including a series of seven amino-terminal WD40 repeats that form a 7-bladed beta-propeller, another WD40 repeat (beta-blade) that co-assembles with Sec13, a series of alpha-helices that create an alpha-solenoid, an ancestral coatomer element (ACE1) domain, a proline-rich domain that contacts Sar1GTP-Sec23-Sec24, and another carboxyl-terminal alpha-helical domain.^{9,12} The much smaller Sec13 also contains a series of WD40 repeats (six) and forms a 7-bladed beta-propeller after incorporating the beta-blade of Sec31. Sec13-Sec31 dimers assemble into heterotetramers via a domain swap between two ACE1 domains to create an overall rod-

like structure that is approximately 28 nm in length.¹² Further co-assembly of four Sec31 beta-propellers at the termini of four distinct rods form one of many vertices within a cage.^{11,60} Additionally, the angle between the terminal beta-propeller domains and alpha-helical central rod is flexible, creating a hinge that allows the cage to vary in dimension, depending on the size of the transport carrier it must encase.^{12,60,61} A second potential hinge was identified more recently, which allows the beta-propeller domains of Sec13 and Sec31 to move relative to one another.⁶² Based on cryoEM studies, the underlying inner coat is positioned such that Sec23 protomers appear below each vertex and in the middle of triangular faces of the outer cage, and Sec24 subunits are located in the middle of square faces of cuboctahedrons or pentagons of icosidodecahedrons, providing sufficient space to accommodate the cytosolic domains of integral membrane cargoes.⁵⁹ Direct association between the inner and outer coat was recently confirmed using yeast proteins, although the cryoEM density failed to overlap completely with the crystal structure of the Sar1GTP-Sec23-Sec31 interface, potentially due to the inherent flexibility of proline-rich domains.³⁷ Unlike components of the inner coat, only a single Sec13 locus is found in mammals. However, two Sec31 paralogs have been identified, which are only ~47% identical. Based on subcellular localization studies, Sec31A and Sec31B distributions do not overlap precisely, raising the question of whether the two subunits are able to co-assemble into a single cage.⁶³ Regardless, the diversity of COPII components expressed in mammals enables numerous types of carriers to be generated that can vary not only in size and subunit composition, but also cargo content.

3. Regulation of COPII coat assembly

Although COPII-mediated carrier formation has been reconstituted using minimal or chemically defined systems *in vitro*,^{32,39} several regulators of this process have been identified in mammalian cells that either facilitate localized COPII subunit assembly at specialized ER subdomains or promote coat disassembly, which is necessary after carrier scission to enable fusion with neighboring

ERGIC membranes. One major driver of ER subdomain selection is the large scaffolding protein Sec16A, which interacts directly with several components of the COPII machinery.⁶⁴⁻⁶⁶ Its depletion reduces the number of COPII budding sites on the ER and attenuates the rate at which secretory cargoes leave the ER. At a biochemical level, only half of Sec16A has been well characterized, with little known about its first 1000 amino acids, beyond their dispensability for localization in overexpression studies.⁶⁷ The remaining protein is comprised of three domains with varying roles in regulating COPII dynamics. The carboxyl-terminal domain (CTD) exhibits a conserved function for binding to Sec12, which helps to enrich the integral membrane GEF for Sar1 at ER sub- domains to make them competent for COPII carrier formation.⁶⁸ The CTD additionally harbors a proline-rich region, which likely facilitates Sec23 recruitment via its gelsolin-like domain (Figure 1). This interaction may also obstruct outer COPII coat assembly, as the Sec31 proline-rich domain must also associate with the same surface on Sec23 to direct overall COPII coat architecture.^{58,59} This potential role for Sec16A in delaying Sec31 action may also extend to non-metazoan systems. Specifically, the carboxyl-terminal half of yeast Sec16 has been suggested to impede the stimulatory effect of Sec31 on Sar1 GTP hydrolysis.⁶⁹ Surprisingly, the effect appears to be mediated by an association between Sec16 and the COPII cargo adaptor Sec24. This interaction could offer a unique sensing mechanism to delay outer coat assembly until transport carriers are first loaded with cargo. A mutation in Sec24 that disrupts its association with Sec16 leads to the formation of smaller transport carriers, suggesting that accelerated GTP hydrolysis results in premature scission.⁶⁹ By extension, slowing GTP hydrolysis should promote the formation of larger COPII carriers. Further studies are necessary to demonstrate whether mammalian Sec16A directly or indirectly regulates the Sar1 GTPase cycle.

Upstream of the CTD is the central conserved domain (CCD) of Sec16A, which is found in all Sec16 paralogs across evolution. The CCD is comprised of a beta-blade followed by a helical ACE1 domain, highly similar to the organization of Sec31 isoforms.⁷⁰ Analogously, Sec16 binds to Sec13 as

a heterotetramer, in which Sec13 associates with the beta-blade of Sec16, and the ACE1 domains dimerize to form an extended ~16.5 nm rod.⁷⁰ Unlike Sec31, however, Sec16 lacks an amino-terminal beta-propeller, preventing its assembly into cage-like structures. Thus, Sec16 recruits Sec13 to ER subdomains, but again may act to impede outer coat assembly by sequestering Sec13 until the appropriate time in the COPII coat assembly pathway.

Upstream of the Sec16A CCD is an ER localization determinant (ELD), which was recently shown to bind to the proline-rich domains of two members of the Tango1/cTAGE5 family (Tango1L and Tango1S) that govern the ER export of several collagen isoforms in large COPII transport carriers.⁷¹⁻⁷³ Surprisingly, while both Tango1 isoforms are required for efficient collagen secretion, only Tango1L harbors a SH3-like domain that can engage HSP47, a collagen-specific molecular chaperone, suggesting that Tango1 family members may possess additional roles in regulating COPII-mediated transport beyond acting merely as a cargo receptor.⁷⁴ Consistent with this idea, loss of both Tango1L and Tango1S was shown to cause Sec16A to be partially redistributed from ER subdomains and reduce overall COPII coat assembly.⁷¹ Conversely, depletion of Sec16A causes Tango1 isoforms to disperse throughout the ER network. Thus, Tango1 and Sec16A play complementary roles in directing the distribution of COPII budding sites on the ER, although it continues to remain unclear how these subdomains are initially formed or maintained. Tango1 additionally plays an important role in localizing a related family member cTAGE5, which also functions in ER collagen export without directly associating with cargo.⁷⁵ The interaction between Tango1 and cTAGE5 is mediated by coiled coil domains found in the cytosolic sides of each protein. A second flanking coiled coil domain in cTAGE5 also contacts Sec12, facilitating its specific accumulation at COPII budding sites on the ER, but without affecting GEF activity.^{76,77} In contrast, neither of the Tango1 coiled coil domains exhibit an ability to associate with Sec12. Structural analysis of these coiled coil motifs should provide mechanistic insight into the specificity of their associations.

All members of the Tango1/cTAGE5 family also bind to the inner COPII coat protein Sec23 via its gelsolin-like domain⁷² (Figure 1). Based on X-ray crystallography studies, the interaction is mediated by tripeptide PPP motifs within the proline-rich domain of Tango1, of which there are seven that associate with a series of surface aromatic residues on Sec23.⁷⁸ Thus, individual Tango1/cTAGE5 proteins can recruit multiple Sec23 protomers, likely in complex with Sec24 subunits, as a transport carrier begins to assemble. It remains unclear whether these associations occur in synergy with Sec16A-mediated Sec23 binding or in competition, as they likely share a common interface. However, given the interdependent roles for Sec16A and Tango1/cTAGE5 in establishing subdomains on the ER capable of COPII budding, it appears more probably that they function together to drive inner coat assembly. In contrast, regions on the ER devoid of these factors are unlikely to support COPII carrier biogenesis, even though Sar1 may continually sample the membrane via its flexible amphipathic helix.³⁰ Taken together, current evidence suggests a model in which Sec16A and members of the Tango1/cTAGE5 family concentrate Sec12 to enable local GTP loading onto Sar1, which deforms and tubulates ER microdomains, while simultaneously recruiting Sec23-Sec24 complexes to further transform membrane tubules into cargo-laden transport carriers. Based on several electron microscopy-based studies, the ER/ERGIC interface in mammalian cells is largely populated by clustered, dumbbell-shaped transport intermediates, as well as more spherical, detached vesicles.⁷⁹⁻⁸¹ The presence of these dumbbell-shaped structures is most consistent with the initial formation of COPII-coated tubules, with GTPase activity on Sar1 generating intermittent constrictions at areas of elevated concentration. Ultimately, a fraction of these more highly bent regions undergo scission, perhaps stochastically due to a locally elevated GTP hydrolysis, enabling cargoes to be separated from the ER and begin their movement in an anterograde manner. In the case of highly elongated cargoes, such as fibrillar collagens that can reach ~300 nm in length and ~1.5 nm in diameter,⁸² steric hindrance may be sufficient to prevent scission reactions that would otherwise cause cargoes to become inappropriately severed.

Alternatively, members of the Tango1/cTAGE5 family may play more active roles in driving the formation of large COPII-coated transport intermediates. Tango1L possesses a Tether of ERGIC at ER (TEER) domain, a coiled coil motif that is capable of binding to ERGIC membranes in trans.⁸³ Although the mechanism by which this occurs remains unclear, direct recruitment of ERGIC to sites of COPII carrier formation on the ER could provide an additional reservoir of membrane to generate transport intermediates. Given the enormous surface area of the ER, it is questionable whether membrane ever becomes limiting during collagen export, but local deposition from an alternative source could augment the kinetics of carrier biogenesis. Based on super resolution imaging studies, Tango1L has been suggested to assemble into ring structures that encircle COPII carriers at their base on ER membranes, potentially providing a scaffold onto which ERGIC membranes could be recruited.^{84,85} However, other non-diffraction-limited approaches have failed to resolve such rings.^{86,87} Instead, these structures may only form in response to non-physiological accumulation of collagen within the ER, which was necessary to initially observe Tango1 ring assembly.⁸⁴ In contrast, more recent studies suggest that Tango1, together with Hsp47, cTAGE5 and Sec12, actually enter the large COPII carriers that enable collagen export from the ER.⁸⁷ These factors are subsequently retrieved from ERGIC and Golgi membranes via the action of retrograde COPI transport, while collagen continues on its journey through the secretory pathway toward the cell surface. Importantly, by trafficking on large COPII carriers, Tango1/cTAGE5 family members would promote continual Sec12 GEF activity and maintain Sar1 in a GTP bound state. These actions may limit membrane constriction associated with GTP hydrolysis on Sar1 along the length of transport carriers, thereby ensuring fibrillar collagens can be properly packaged in large COPII carriers. Potentially in a similar manner, the fatty acid binding protein FABP5 was shown recently to bind Sec12 and enhance GTP loading onto Sar1, thereby promoting the formation of large COPII transport carriers capable of packaging collagens as well as large lipoproteins.⁸⁸

Unlike conventional COPII-coated transport carriers that generally range in size from 50 to 200 nm and have been repeatedly resolved at the ER/ERGIC interface using electron microscopy-based approaches, larger COPII carriers have been more challenging to visualize in a native setting. This is at least in part due to the cell lines that have been chosen for analysis, most of which do not produce high levels of fibrillar collagens or other large cargoes. Although recent studies highlight the existence of large carriers that contain collagen and stain positively for COPII subunits, in most cases, their destinations are unclear.⁸⁹ Instead, these carriers may participate in a noncanonical form of autophagy, which targets misfolded procollagens to the lysosome for degradation.⁹⁰ In the absence of a large number of transport intermediates to analyze, some have even argued that collagens in the early secretory pathway may not even use a transport intermediate.⁹¹ Instead, direct connections between ER and ERGIC membranes could enable collagens to be exported from the ER in the absence of a vesicular carrier. Formation of these tubular connections would still require the COPII machinery to drive membrane remodeling and members of the Tango1/cTAGE5 family to recruit collagen and ERGIC membranes and maintain the activity of Sar1, but mechanisms to maintain the unique identities of the ER and ERGIC in such a model still require elucidation.⁹² Additionally, examination of native collagen trafficking by leveraging CRISPR/Cas9 technology to tag their endogenous isoforms would dramatically improve on current approaches that use over-expression, which likely activate ER stress responses and the unfolded protein response (UPR) and may lead to artifacts.⁹³

Assembly of the outer COPII cage, mediated largely by contacts between Sec31 and Sec23, likely displaces several of the regulatory factors that initially stimulate formation of the inner adaptor layer of the COPII coat. Based on direct competition assays, the proline-rich domain of Sec31 exhibits higher affinity for the Sec23 gelsolin-like domain as compared to members of the Tango1/cTAGE5 family.⁷⁸ By displacing these factors, Sec31 acts to downregulate further GTP loading onto Sar1 and may shift the equilibrium toward Sar1 GTP hydrolysis, which is predicted to promote detachment of

COPII carriers from the ER. Recruitment of Sec13-Sec31 heterotetramers to the ER has been suggested to be regulated by several factors. Based on immunoprecipitation studies, soluble Sec13-Sec31 complexes interact with the large phospholipase A1-like factor p125A.⁹⁴⁻⁹⁷ The carboxyl-terminal region of p125A binds to acidic phospholipids, facilitating its targeting to COPII budding sites that are enriched for phosphatidic acid and phosphatidylinositol 4-phosphate, while its central domain (residues ~260-600) is sufficient for interaction with Sec31.^{94,98} Although a mechanistic understanding of this association is lacking, biochemical studies further suggest that p125A binds to Sec23 via its adjacent, amino-terminal proline-rich domain, potentially serving as a bridge to bring Sec31 into close proximity of the inner coat⁹⁸ (Figure 1). Overexpression studies also suggest that p125A displaces Sec16A from COPII complexes, further promoting outer COPII cage assembly as carriers emerge from the ER and leave Sec16A behind.⁹⁴ The Sec31 binding partner ALG-2 (also known as PDCD6) has also been proposed to facilitate an interaction between the outer COPII cage and the inner coat. Specifically, ALG-2 associates with the proline-rich domain of Sec31 and alters its conformation to increase its affinity for Sec23.⁹⁹ Again, the structural basis for this phenomenon has yet to be defined, but in vitro studies suggest that the presence of ALG-2 slows the rate at which COPII carriers bud from the ER. Thus, ALG-2 appears to facilitate interaction between the two layers of the COPII coat, while negatively regulating carrier scission, potentially via negative regulation of GTP hydrolysis on Sar1 until COPII assembly can be completed. Notably, ALG-2 harbors a calcium binding EF-hand, and the localization of ALG-2 to COPII budding sites requires the presence of calcium.¹⁰⁰ Additionally, the calcium binding protein Annexin A11 further promotes stable association of Sec31 with COPII budding sites, using ALG-2 as an adaptor.¹⁰¹ Together, these data suggest that cytosolic calcium levels regulate COPII carrier formation, linking early secretory pathway function to various signaling cascades that are dependent on calcium influx, including the ER stress response and the UPR.¹⁰² Nonetheless, Sec23 remains the most prominent recruiting factor for the outer COPII components, best illustrated by the

effect of a relatively subtle missense mutation (F382L) in Sec23A that underlies Cranio-lenticulo-sutural dysplasia, which results in impaired Sec13-Sec31 assembly at ER sub- domains.^{17,47} Strikingly, patients harboring this mutation accumulate coated tubules that are readily observed in skin fibroblasts, further indicating that outer coat assembly plays a major role in regulating carrier scission, as opposed to initial carrier formation.⁴⁷

4. Regulation of COPII coat disassembly at the ER/ERGIC interface

To enable efficient secretory cargo transport from the ER to the ERGIC, COPII coat assembly must be balanced by rapid disassembly following transport carrier scission. Based on the distribution and dynamics of COPII complexes in cells, the lifetime of the coat is brief and largely relegated to small ~500 nm areas scattered over the entire ER network, which extends throughout cells, but is most highly concentrated in the peri-nuclear region. Super resolution imaging has demonstrated that essentially all ER subdomains that produce COPII carriers are juxtaposed to ERGIC membranes, even in areas densely packed by Golgi cisternae, suggesting that COPII coat disassembly is coupled to fusion with ERGIC, as opposed to direct fusion with the Golgi.⁷⁹ Many have questioned the origin of ERGIC membranes, with a consensus view suggesting that homotypic fusion of COPII carriers initially produces tubular-vesicular clusters that become enriched with ERGIC markers, and subsequent homotypic and/or heterotypic fusion events maintain the identity of the organelle.^{8,103} A major requirement for such an organization is a mechanism to locally tether COPII carriers for a sufficient period of time to allow coat complexes to disassemble and expose SNAREs necessary to drive fusion events. Recent work suggests that COPII carrier tethering is mediated by small ring-like homo-oligomers composed of Trk-fused gene (TFG) subunits.^{79,86,104}

TFG was originally described as a fusion partner for the TrkA receptor tyrosine kinase, generated following a chromosomal translocation and functioning as a potent driver of cell

transformation.¹⁰⁵ Subsequently, several additional oncogenic TFG fusion proteins have been identified, each carrying the amino-terminal portion of TFG, including its PB1 domain and adjacent coiled coil motif.¹⁰⁶ Structural analysis using single particle electron microscopy has demonstrated that this region of TFG is sufficient to form ~11 nm octameric rings, with a central ~4 nm pore.⁷⁹ These data highlight the ability of the TFG amino-terminus to multimerize fusion partners, many of which are kinase domains that require co-assembly to elicit activity. However, oligomerization alone was shown to be insufficient to enable the TrkA kinase domain to transform cells. Instead, localization to the ER/ERGIC interface plays a critical role in oncogenesis, although the precise downstream targets that cause cells to become transformed remain undefined.¹⁰⁴

Based on the analysis by circular dichroism, the carboxyl-terminal portion of TFG (residues 125-400) is largely unstructured, with a propensity to self-associate, thereby linking TFG octamers into a higher order meshwork.⁷⁹ These characteristics are highly reminiscent of synapsin, another disordered protein, which was shown recently to undergo phase separation to generate liquid droplets.¹⁰⁷ However, unlike other liquid droplet-like, membraneless organelles such as P granules or PML nuclear bodies, phase separated synapsin is able to capture small liposomes *in vitro* and play a key role in clustering synaptic vesicles in neuronal synapses. Analogously, phase separated TFG may tether COPII-coated transport carriers at the ER/ERGIC interface.⁸⁶ Consistent with this idea, overexpression of TFG leads to the formation of large spherical structures in cells that sequester COPII carriers.⁷⁹ Moreover, depletion of TFG leads to the accumulation of COPII carriers throughout the cytoplasm, no longer restricted to the ER/ERGIC interface.^{79,86} Biochemical studies have demonstrated that the last ~20 amino acids of TFG binds directly to Sec23 with high affinity, and its disordered domain is enriched with proline residues (>16%) that likely facilitate binding to the Sec23 gelsolin-like domain⁸⁶ (Figure 1). These findings provide a potential molecular basis for hypothetical TFG liquid droplets to tether COPII-coated transport intermediates at the ER/ERGIC interface with specificity, although additional

studies are required to validate this idea. Strikingly, in the absence of COPII carrier formation, TFG fails to accumulate near ER subdomains, suggesting that the presence of COPII-coated transport carriers is a prerequisite for concentrated assembly of TFG in cells.⁸⁶ Beyond binding to Sec23 and tethering COPII carriers, TFG has also been shown to interact with ALG-2 in a calcium-dependent manner.¹⁰⁸ *in vitro* studies suggest that this association may enhance co-assembly of TFG octamers into larger complexes. However, depletion of ALG-2 has minimal impact on the levels of TFG at the ER/ERGIC interface.¹⁰⁸ Further work is necessary to define the mechanistic basis for TFG assembly in the early secretory pathway and how this process is regulated.

Surprisingly, as opposed to binding COPII carriers via the outer cage, TFG directly associates with the inner adaptor layer and utilizes the same interface on Sec23 as Sec31 uses for binding (Figure 1). Based on biochemical competition assays, TFG exhibits an ability to disrupt the association between the two COPII subunits, suggesting that it promotes outer coat disassembly at the ER/ERGIC interface, while simultaneously restricting the distribution of partially coated carriers.⁸⁶ Exposure of the inner coat may also facilitate its association with the downstream TRAPP tethering complex, which functions on ERGIC membranes to promote COPII carrier fusion and cargo delivery. In particular, the TRAPPC3 subunit of the TRAPP complex, which exhibits a flattened alpha-beta fold, has been proposed to bind to Sec23.^{109,110} The interaction does not affect GAP activity, but little else is known regarding the mechanism of association or whether it would affect the ability of inner COPII-coated carriers to remain partitioned with putative TFG liquid droplets or be released for ERGIC fusion. Alternatively, dissociation of the inner COPII coat may be facilitated by GTP hydrolysis on Sar1 that remains associated with the transport carrier after scission from the ER.⁴¹ Although some biochemical data suggest that Sar1 is released from transport carriers rapidly after the budding process, localization studies have yet to define its distribution at the ER/ERGIC interface.⁶ Thus, it remains very possible

that GTP-bound Sar1 persists on COPII carriers following scission, and local tethering mediated by TFG provides sufficient time for GTP hydrolysis to enable inner coat disassembly.

Although deletion of TFG results in early embryo lethality, point mutations have been identified in several patients suffering from various forms of neurological disease.^{86,111,112} Analysis of these mutant alleles has underscored the importance of the TFG ring-like architecture in regulating COPII-mediated cargo transport. Specifically, mutations in the PB1 domain or the coiled coil domain underlie early onset forms of complicated hereditary spastic paraplegia (HSP) and result in defective ring assembly without impairing the ability of TFG to homo-oligomerize.¹¹¹ Although mutations in other factors that form liquid droplets in neurons have been suggested to promote their aggregation leading to neuronal toxicity, localization studies indicate that amino-terminal mutations in TFG cause it to become more diffusely distributed.^{111,113,114} These data suggest an alternative mechanism for neurodegeneration in HSP patients harboring TFG mutations. Consistent with this idea, stem-cell-derived neurons harboring the TFG (p.R106C) mutation exhibit a defect in axon pathfinding, likely caused by impaired trafficking of high molecular weight adhesion molecules that normally mediate axon bundling and their maintenance.¹¹¹ Other mutations that affect the disordered domain of TFG have been implicated in late onset sensory neuropathies.¹¹² However, the impact of these mutations to TFG structure and function remain to be defined.

5. Regulation of COPII carrier formation and transport mediated by posttranslational modifications

Posttranslational modifications (PTMs) play important regulatory roles in cell signaling, protein-protein interactions and membrane remodeling processes. Although numerous PTMs have been mapped on components of the early secretory pathway, we still have only an elementary understanding of their contributions to membrane trafficking. β -linked N-acetylglucosamine (O-GlcNAc)

modifications are found frequently at serine and threonine residues on both nuclear and cytoplasmic proteins.^{115,116} These modifications are highly reversible and cycle on and off rapidly throughout the lifetime of the protein. In animals, O-GlcNAc transferase (OGT) is responsible for the addition of this modification, while O-GlcNAcase (OGA) mediates its removal.¹¹⁷ Based on mass spectrometry-based analysis, O-GlcNAc modified sites have been identified on Sec23A, Sec24C, Sec31A and TFG¹¹⁸ (Figure 2). In general, O-GlcNAcylation of COPII subunits is high during interphase and low during mitosis, when early secretory pathway trafficking is suspended.¹¹⁹ The roles of O-GlcNAc modification vary, with those found on Sec31A clustered within its hinge region, suggesting a potential function in regulating the flexibility of the outer COPII cage and thereby impacting cargo selection, while O-GlcNAc modified sites on Sec23A and Sec24C appear to regulate protein- protein interactions.¹¹⁸ Although the specific binding partners of the inner COPII coat proteins that require OGT activity have yet to be identified, mutation of one modified site in Sec23A (S184A) within its trunk domain results in defective collagen export from the ER, suggesting that the regulators may play a role in controlling Sar1 GTPase activity.¹¹⁸ TFG also undergoes O-GlcNAc modification, which may promote co-assembly of octamers to enhance the kinetics of liquid droplet formation. Alternatively, modification of TFG could enable the recruitment of a binding partner, similar to that brought in by Sec23A or Sec24C, to further support large carrier transport. Consistent with this idea, depletion studies suggest that TFG plays a particularly critical role in the anterograde movement of large COPII cargoes.^{111,120}

PTM by the E3 ubiquitin ligase Cullin-3 (CUL3) has also been proposed to facilitate the formation of unconventionally large COPII carriers. Specifically, the addition of mono-ubiquitin to Sec31A has been suggested to augment the size of the COPII coat, although a mechanistic basis for this effect remains unresolved.^{121,122} A major hurdle has been identifying a specific ubiquitin-modified site on Sec31A that mediates enlargement of the outer COPII cage, and mutational analysis has failed to specify any individual lysine residues in Sec31A that are required for collagen secretion from the ER.

Several adaptors are necessary for Sec31A ubiquitinylation by CUL3, including KLHL12, which harbors a series of Kelch-like repeats that form a β -propeller tertiary structure, and the calcium binding factors ALG-2 and Pef1 that can associate to form heterodimers.¹²¹⁻¹²³ Based on co-immunoprecipitation studies, all five proteins form a complex, with KLHL12 present as a dimer.¹²² Additionally, Pef1 must itself be ubiquitin-modified by CUL3 to enable Sec31A ubiquitinylation, ensuring that only active CUL3 complexes are recruited to budding sites to drive large COPII carrier formation.¹²² The requirement for Pef1 and ALG-2 further suggests that the formation of large COPII carriers may rely on transient increases in cytosolic calcium. However, direct evidence to support this idea is lacking. Moreover, recent data now argue against a direct role for CUL3-KLHL12 in collagen secretion, implicating them instead in regulation of UPR signaling and collagen biosynthesis.¹²⁴ An alternative explanation for the role of ubiquitin-modification in the early secretory pathway has also been suggested by studies showing that misfolded forms of procollagen are targeted to the lysosome via noncanonical autophagic transport carriers that originate at or near the ER. Instead of mediating large COPII carrier formation, it is possible that ubiquitin-modification of Sec31A facilitates recognition of sites harboring cargoes destined for lysosomal degradation, as opposed to secretion.⁹⁰ With clear evidence accumulating that COPII functions in the generation of membranes necessary for autophagosome formation, the role of ubiquitin-modification in generating large secretory carriers may require substantial revision.

Beyond ubiquitin and O-GlcNAc modifications, COPII components are also subject to phosphorylation, although most sites have yet to be unambiguously mapped and only a selected few have been assigned a functional or regulatory role. Casein Kinase II (CKII) has been implicated in Sec31A phosphorylation, which may impede its association with the inner COPII coat¹²⁵ (Figure 2). Specifically, two regions of Sec31A are phosphorylated by CKII, the alpha-solenoid (S527 and S799) and its carboxyl-terminal alpha-helical domain (S1163 and T1165). Although none of the

phosphorylated residues are positioned within known Sec31A binding interfaces, mutations within the alpha-solenoid that block phosphorylation stabilize association with Sec23.¹²⁵ Thus phosphorylation of Sec31A may either delay outer coat assembly to facilitate cargo loading and prevent premature carrier scission, or potentially help drive disassembly of the outer cage after carrier scission is complete. Structural analysis is necessary to provide further insights into the role of Sec31A phosphorylation during COPII-mediated membrane transport, and localization studies are required to determine CKII distribution at the ER/ERGIC interface, which will shed light on the timing of its action in the early secretory pathway.

Further regulation of COPII coat assembly is mediated by phosphorylation of Sec23 isoforms by the Unc-51 like kinase (ULK1), an enzyme most often associated with regulating the autophagy pathway in response to nutrient availability (Figure 2). When modified on sites within the trunk and β -barrel domains of Sec23A (S207, S312 and T405), its interaction with Sec31A is dramatically reduced, suggesting that ULK1 activation impedes full COPII coat assembly required for secretory protein export from the ER, and shifts its function toward the biogenesis of donor membranes needed for autophagosome formation.¹²⁶ ULK1 has also been shown to phosphorylate Sec23B within the trunk domain (S186) (Figure 2), but in this case, phosphorylation disrupts an interaction with the F-box protein FBXW5, which normally targets Sec23B for proteasome-mediated degradation.¹²⁷ In addition to stabilizing Sec23B, phosphorylation of Sec23B by ULK1 inhibits its binding to Sec24C and Sec24D, but not Sec24A or Sec24B, and allows for redistribution of Sec23B to ERGIC membranes to fuel autophagosome biogenesis.¹²⁷ At a mechanistic level, it remains unclear how phosphorylation of Sec23B would influence Sec24 binding in an isoform-specific manner, but impaired association with Sec24C and Sec24D would likely reduce overall secretory protein efflux from the ER. Together, these findings highlight multiple pathways by which ULK1 activation retunes the role of the COPII machinery to meet cellular demands in response to changing environmental conditions. However, the

major question of how COPII components relocate from ER subdomains to ERGIC membranes in response to starvation remains unanswered.

One possibility is that ULK1 targets additional components in the early secretory pathway to enable transport of COPII machinery across the ER/ERGIC interface. In particular, Sec16A has been shown to be phosphorylated by ULK1 and its paralog ULK2 (Figure 2). Both kinases associate with the CCD domain of Sec16A and promote phosphorylation upstream of their binding site (S846).¹²⁸ A mutant isoform of Sec16A, which cannot be phosphorylated, exhibits reduced accumulation at ER subdomains and also impairs recruitment of the Sec24C cargo adaptor.¹²⁸ Although one interpretation of these data argues that ULK1 activity plays a constitutive role in supporting anterograde trafficking of biosynthetic cargoes, an alternative view predicts that active ULK kinases selectively stimulate the secretion of only certain cargo to ERGIC membranes in response to starvation, one of which may be Sec12, which would enable Sar1GTP accumulation to drive the formation of LC3 lipidation-active vesicles for autophagosome biogenesis.¹²⁹⁻¹³¹ However, Sec16A has also been identified as an ERK7 kinase substrate during serum or amino acid starvation, with phosphorylation within its carboxyl-terminus leading to dispersal from ER subdomains.¹³² Further work is needed to better understand how various signaling pathways converge on the early secretory pathway during nutrient deprivation.

Lastly, Sec16A has also been shown to be a target of ERK2/MAPK1 in actively proliferating cells, downstream of growth factor stimulation. Phosphorylation by ERK2 within the amino-terminal half of Sec16A (T415) increases the number of Sec16A-marked ER subdomains, potentially augmenting the capacity of COPII-mediated membrane trafficking¹³³ (Figure 2). Based on high throughput, mass spectrometry-based analysis, several other components of the early secretory pathway are also subject to PTM, both under steady state conditions and following various forms of exogenous stimulation. We are now only beginning to understand the complex regulatory systems in place to modulate secretory efflux, which likely occurs in a cell type specific manner. In the future, it will be

critical to decipher these pathways to fully appreciate how membrane transport at the ER/ERGIC interface influences overall tissue homeostasis.

6. Conclusions and perspectives

Over the last 25 years, the field has witnessed a dramatic expansion in the defined roles for COPII in membrane transport, with numerous implications for normal human development and disease. The impacts of pathological point mutations that affect early secretory pathway components are now becoming understood not only at the cellular level but also at a structural level, which should enable the development of therapeutic approaches to combat disease. Nevertheless, some very fundamental questions remain unresolved. How are COPII budding sites on the ER defined? What is the structure of a native, intact COPII coat? How are transport intermediates organized at the ER/ERGIC interface? What imparts vectorial transport between ER and ERGIC membranes in the absence of cytoskeletal elements? What drives full COPII coat disassembly? For several of these problems, improvements in focused ion beam technology and cryoEM-based techniques should provide conclusive answers. With high resolution views of COPI and clathrin coats now defined, solution of the COPII coat structure is likely forthcoming.¹³⁴⁻¹³⁷ However, it will be critical to examine coat architecture and underlying membrane morphology in several mammalian cell types, which express a variety of cargoes, including fibrillar collagens or chylomicrons. In this regard, use of genome-edited human stem cells that express native levels of functionally tagged COPII subunits (to enable correlative light and electron microscopy) and differentiated to distinct cell fates is necessary to obtain physiologically relevant structures that are likely to be present in developing tissues. For now, we propose a working model for COPII-mediated transport that includes a series of steps that act in a coordinated fashion at the ER/ERGIC interface (Figure 3). The next 25 years will undoubtedly yield an array of new and exciting findings that detail

additional regulatory aspects governing function of the early secretory pathway, with the prospect of a full mechanistic understanding of COPII-mediated trafficking just over the horizon.

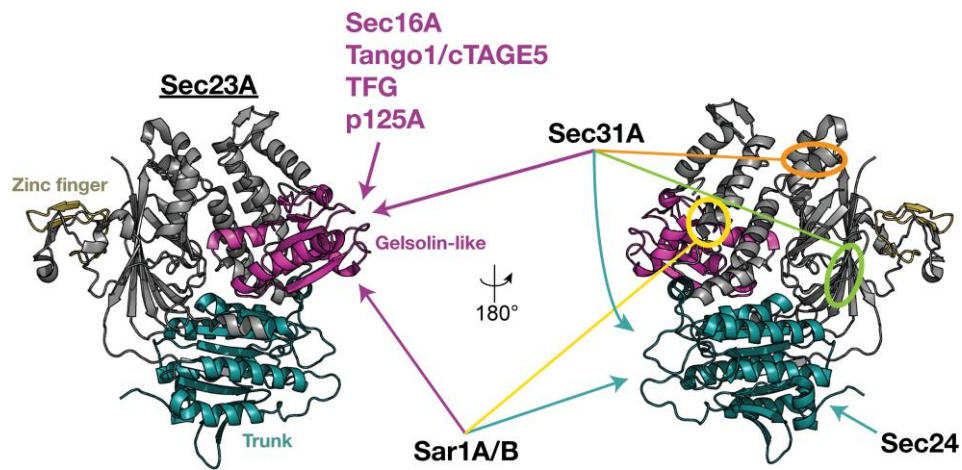


Figure 1. Sec23 acts as an interaction hub for control over COPII carrier assembly and disassembly. An illustration highlighting the various interaction partners that have been identified for Sec23A/B. Numerous regulators are believed to compete for binding with the Sec23 gelsolin-like domain, enabling a stepwise assembly and disassembly pathway for COPII carrier biogenesis. The structure of Sec23A depicted is adapted from PDB 5VNO²⁶

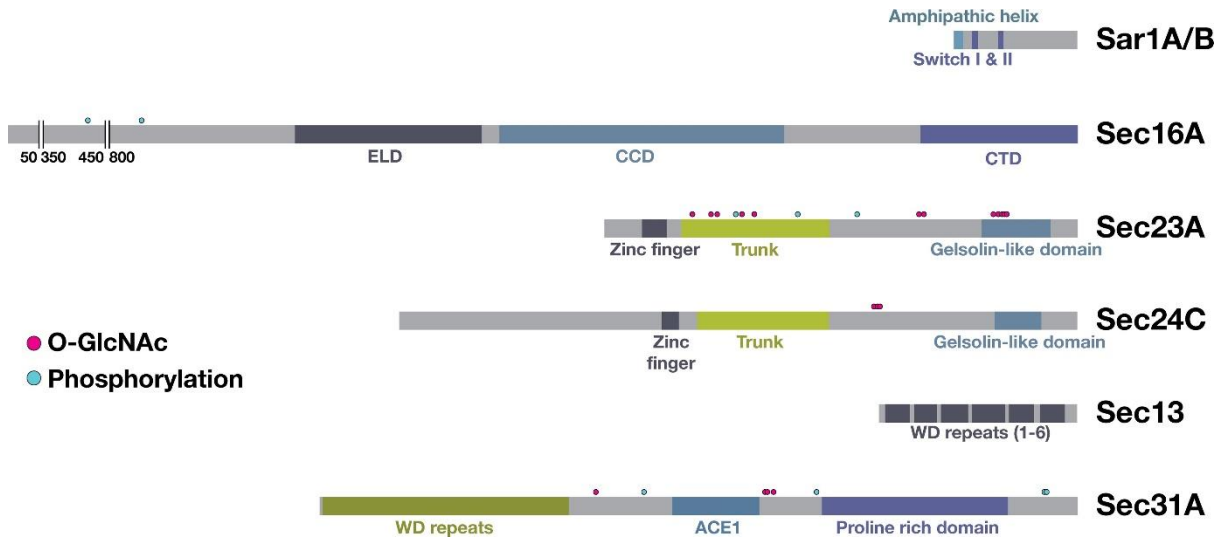


Figure 2. Components of the COPII transport system are subject to posttranslational modifications that regulate their functions. An illustration showing the distribution of posttranslationally modified residues on COPII components and several regulators of COPII carrier transport

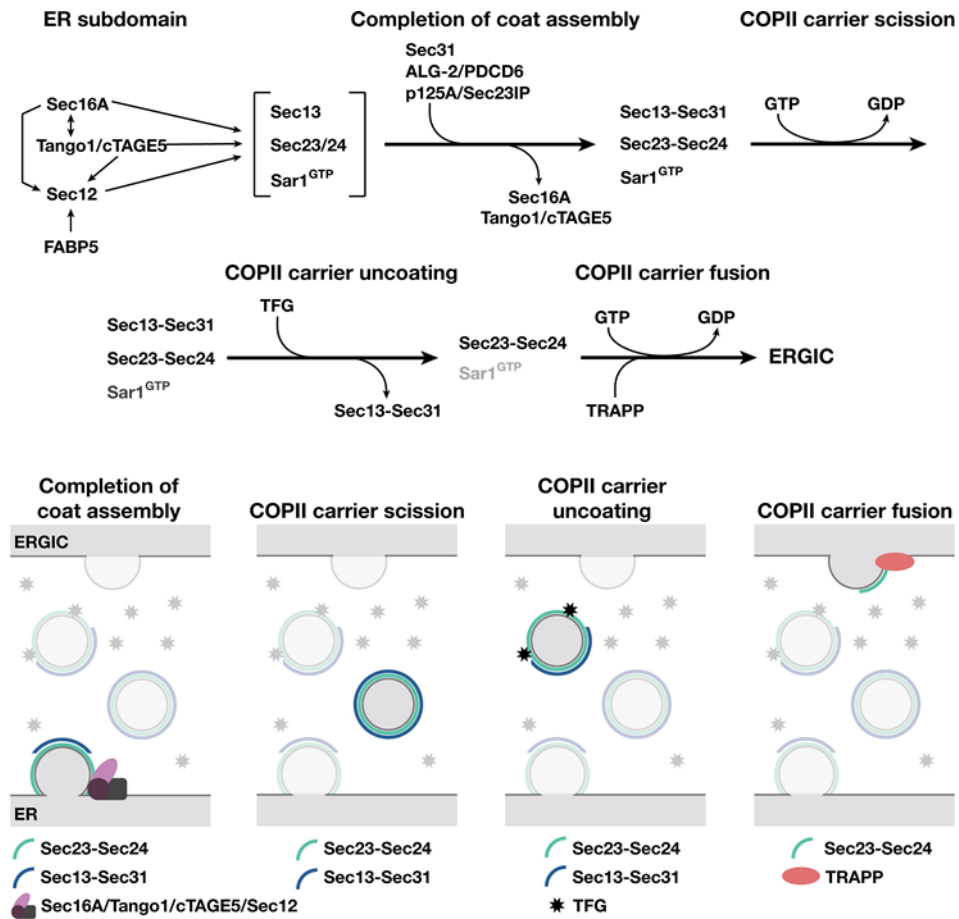


Figure 3. Working model for COPII-mediated transport at the ER/ERGIC interface. Based on current findings, we proposed a speculative model highlighting a set of sequential regulatory steps that ensure COPII coat assembly and disassembly during cargo transport from the ER to ERGIC membranes

References

1. Hanna MG, Peotter JL, Frankel EB, Audhya A. Membrane transport at an organelle interface in the early secretory pathway: take your coat off and stay a while: evolution of the metazoan early secretory pathway. *Bioessays*. 2018;40:e1800004.
2. Zanetti G, Pahuja KB, Studer S, Shim S, Schekman R. COPII and the regulation of protein sorting in mammals. *Nat Cell Biol*. 2011;14: 20-28.
3. Budnik A, Stephens DJ. ER exit sites—localization and control of COPII vesicle formation. *FEBS Lett*. 2009;583:3796-3803.
4. Barlowe C, Helenius A. Cargo capture and bulk flow in the early secretory pathway. *Annu Rev Cell Dev Biol*. 2016;32:197-222.
5. Aridor M. COPII gets in shape: lessons derived from morphological aspects of early secretion. *Traffic*. 2018;19:823-839.
6. Barlowe C, Orci L, Yeung T, et al. COPII: a membrane coat formed by Sec proteins that drive vesicle budding from the endoplasmic reticulum. *Cell*. 1994;77:895-907.
7. Aridor M, Bannykh SI, Rowe T, Balch WE. Sequential coupling between COPII and COPI vesicle coats in endoplasmic reticulum to Golgi transport. *J Cell Biol*. 1995;131:875-893.
8. Appenzeller-Herzog C, Hauri HP. The ER-Golgi intermediate compartment (ERGIC): in search of its identity and function. *J Cell Sci*. 2006;119:2173-2183.
9. Stagg SM, LaPointe P, Razvi A, et al. Structural basis for cargo regulation of COPII coat assembly. *Cell*. 2008;134:474-484.
10. Bi X, Corpina RA, Goldberg J. Structure of the Sec23/24-Sar1 prebudding complex of the COPII vesicle coat. *Nature*. 2002;419: 271-277.
11. Stagg SM, Gürkan C, Fowler DM, et al. Structure of the Sec13/31 COPII coat cage. *Nature*. 2006;439:234-238.

12. Fath S, Mancias JD, Bi X, Goldberg J. Structure and organization of coat proteins in the COPII cage. *Cell*. 2007;129:1325-1336.
13. Nakan,o A, Muramatsu M. A novel GTP-binding protein, Sar1p, is involved in transport from the endoplasmic reticulum to the Golgi apparatus. *J Cell Biol*. 1989;109:2677-2691.
14. Barlowe C, Schekman R. SEC12 encodes a guanine-nucleotide-exchange factor essential for transport vesicle budding from the ER. *Nature*. 1993;365:347-349.
15. Weissman JT, Plutner H, Balch WE. The mammalian guanine nucleotide exchange factor mSec12 is essential for activation of the Sar1 GTPase directing endoplasmic reticulum export. *Traffic*. 2001;2: 465-475.
16. Jones B, Jones EL, Bonney SA, et al. Mutations in a Sar1 GTPase of COPII vesicles are associated with lipid absorption disorders. *Nat Genet*. 2003;34:29-31.
17. Fromme JC, Ravazzola M, Hamamoto S, et al. The genetic basis of a craniofacial disease provides insight into COPII coat assembly. *Dev Cell*. 2007;13:623-634.
18. Long KR, Yamamoto Y, Baker AL, et al. Sar1 assembly regulates membrane constriction and ER export. *J Cell Biol*. 2010;190: 115-128.
19. Fryer LG, Jones B, Duncan EJ, et al. The endoplasmic reticulum coat protein II transport machinery coordinates cellular lipid secretion and cholesterol biosynthesis. *J Biol Chem*. 2014;289:4244-4261.
20. Loftus AF, Hsieh VL, Parthasarathy R. Modulation of membrane rigidity by the human vesicle trafficking proteins Sar1A and Sar1B. *Biochem Biophys Res Commun*. 2012;426:585-589.
21. Levy E, Poinot P, Spahis S. Chylomicron retention disease: genetics, biochemistry, and clinical spectrum. *Curr Opin Lipidol*. 2019;30(2): 134-139.
<https://doi.org/10.1097/MOL.0000000000000578>.

22. Cutrona MB, Beznoussenko GV, Fusella A, Martella O, Moral P, Mironov AA. Silencing of mammalian Sar1 isoforms reveals COPII- independent protein sorting and transport. *Traffic*. 2013;14: 691-708.
23. Sané AT, Seidman E, Peretti N, et al. Understanding chylomicron retention disease through Sar1b Gtpase gene disruption: insight from cell culture. *Arterioscler Thromb Vasc Biol*. 2017;37:2243-2251.
24. Huang M, Weissman JT, Beraud-Dufour S, et al. Crystal structure of Sar1-GDP at 1.7 Å resolution and the role of the NH₂ terminus in ER export. *J Cell Biol*. 2001;155:937-948.
25. Rao Y, Bian C, Yuan C, et al. An open conformation of switch I revealed by Sar1-GDP crystal structure at low Mg²⁺. *Biochem Biophys Res Commun*. 2006;348:908-915.
26. Ma W, Goldberg E, Goldberg J. ER retention is imposed by COPII protein sorting and attenuated by 4-phenylbutyrate. *Elife*. 2017;8:6.
27. McMahon C, Studer SM, Clendinen C, Dann GP, Jeffrey PD, Hughson FM. The structure of Sec12 implicates potassium ion coordination in Sar1 activation. *J Biol Chem*. 2012;287:43599-43606.
28. Rowe T, Aridor M, McCaffery JM, Plutner H, Balch WE. COPII vesicles derived from mammalian endoplasmic reticulum (ER) microsomes recruit COPI. *J Cell Biol*. 1996;135:895-911.
29. Aridor M, Fish KN, Bannykh S, et al. The Sar1 GTPase coordinates biosynthetic cargo selection with endoplasmic reticulum export site assembly. *J Cell Biol*. 2001;152:213-229.
30. Hanna MG 4th, Mela I, Wang L, et al. Sar1 GTPase activity is regulated by membrane curvature. *J Biol Chem*. 2016;291:1014-1027.

31. Hariri H, Bhattacharya N, Johnson K, Noble AJ, Stagg SM. Insights into the mechanisms of membrane curvature and vesicle scission by the small GTPase Sar1 in the early secretory pathway. *J Mol Biol.* 2014;426:3811-3826.
32. Schindler AJ, Schekman R. In vitro reconstitution of ER-stress induced ATF6 transport in COPII vesicles. *Proc Natl Acad Sci USA.* 2009;106:17775-17780.
33. Lee MC, Orci L, Hamamoto S, Futai E, Ravazzola M, Schekman R. Sar1p N-terminal helix initiates membrane curvature and completes the fission of a COPII vesicle. *Cell.* 2005;122:605-617.
34. Bacia K, Futai E, Prinz S, et al. Multibudded tubules formed by COPII on artificial liposomes. *Sci Rep.* 2011;1:17.
35. Schenk NA, Dahl PJ, Hanna MG 4th, et al. A simple supported tubulated bilayer system for evaluating protein-mediated membrane remodeling. *Chem Phys Lipids.* 2018;215:18-28.
36. Bielli A, Haney CJ, Gabreski G, Watkins SC, Bannykh SI, Aridor M. Regulation of Sar1 NH₂ terminus by GTP binding and hydrolysis promotes membrane deformation to control COPII vesicle fission. *J Cell Biol.* 2005;171:919-924.
37. Hutchings J, Stancheva V, Miller EA, Zanetti G. Subtomogram averaging of COPII assemblies reveals how coat organization dictates membrane shape. *Nat Commun.* 2018;9:4154.
38. Kurokawa K, Suda T, Nakano A. Sar1 localizes at the rims of COPII-coated membranes in vivo. *J Cell Sci.* 2016;129:3231-3237.
39. Matsuoka K, Orci L, Amherdt M, et al. COPII-coated vesicle formation reconstituted with purified coat proteins and chemically defined liposomes. *Cell.* 1998;93:263-275.
40. Yoshihisa T, Barlowe C, Schekman R. Requirement for a GTPase-activating protein in vesicle budding from the endoplasmic reticulum. *Cell.* 2004;118:591-605.

41. Antonny B, Madden D, Hamamoto S, Orci L, Schekman R. Dynamics of the COPII coat with GTP and stable analogues. *Nat Cell Biol.* 2001;3:531-537.
42. Ehrlich M, Boll W, Van Oijen A, et al. Endocytosis by random initiation and stabilization of clathrin-coated pits. *Cell.* 2004;118: 591-605.
43. Li D, Shao L, Chen BC, et al. ADVANCED IMAGING. Extended-resolution structured illumination imaging of endocytic and cytoskeletal dynamics. *Science.* 2015;349:aab3500.
44. Khoriaty R, Hesketh GG, Bernard A, et al. Functions of the COPII gene paralogs SEC23A and SEC23B are interchangeable in vivo. *Proc Natl Acad Sci USA.* 2018;115:E7748-E7757.
45. Schwarz K, Iolascon A, Verissimo F, et al. Mutations affecting the secretory COPII coat component SEC23B cause congenital dyserythropoietic anemia type II. *Nat Genet.* 2009;41:936-940.
46. Yehia L, Niazi F, Ni Y, et al. Germline heterozygous variants in SEC23B are associated with Cowden syndrome and enriched in apparently sporadic thyroid cancer. *Am J Hum Genet.* 2015;97: 661-676.
47. Boyadjiev SA, Fromme JC, Ben J, et al. Cranio-lenticulo-sutural dysplasia is caused by a SEC23A mutation leading to abnormal endoplasmic-reticulum-to-Golgi trafficking. *Nat Genet.* 2006;38: 1192-1197.
48. Wendeler MW, Paccaud JP, Hauri HP. Role of Sec24 isoforms in selective export of membrane proteins from the endoplasmic reticulum. *EMBO Rep.* 2007;8:258-264.
49. Mancias JD, Goldberg J. Structural basis of cargo membrane protein discrimination by the human COPII coat machinery. *EMBO J.* 2008; 27:2918-2928.
50. Mossesso E, Bickford LC, Goldberg J. SNARE selectivity of the COPII coat. *Cell.* 2003;114:483-495.

51. Miller EA, Beilharz TH, Malkus PN, et al. Multiple cargo binding sites on the COPII subunit Sec24p ensure capture of diverse membrane proteins into transport vesicles. *Cell*. 2003;114:497-509.
52. Nishimura N, Balch WE. A di-acidic signal required for selective export from the endoplasmic reticulum. *Science*. 1997;277:556-558.
53. Barlowe C. Molecular recognition of cargo by the COPII complex: a most accommodating coat. *Cell*. 2003;114:395-397.
54. Chen XW, Wang H, Bajaj K, et al. SEC24A deficiency lowers plasma cholesterol through reduced PCSK9 secretion. *Elife*. 2013; 2:e00444.
55. Emmer BT, Hesketh GG, Kotnik E, et al. The cargo receptor SURF4 promotes the efficient cellular secretion of PCSK9. *Elife*. 2018;7.
56. Wang B, Joo JH, Mount R, et al. The COPII cargo adapter SEC24C is essential for neuronal homeostasis. *J Clin Invest*. 2018;128:3319- 3332.
57. Adams EJ, Chen XW, O'Shea KS, Ginsburg D. Mammalian COPII coat component SEC24C is required for embryonic development in mice. *J Biol Chem*. 2014;289:20858-20870.
58. Bi X, Mancias JD, Goldberg J. Insights into COPII coat nucleation from the structure of Sec23.Sar1 complexed with the active fragment of Sec31. *Dev Cell*. 2007;13:635-645.
59. Bhattacharya N, O'Donnell J, Stagg SM. The structure of the Sec13/31 COPII cage bound to Sec23. *J Mol Biol*. 2012;420: 324-334.
60. Noble AJ, Zhang Q, O'Donnell J, et al. A pseudoatomic model of the COPII cage obtained from cryo-electron microscopy and mass spectrometry. *Nat Struct Mol Biol*. 2013;20:167-173.
61. Copic A, Latham CF, Horlbeck MA, D'Arcangelo JG, Miller EA. ER cargo properties specify a requirement for COPII coat rigidity mediated by Sec13p. *Science*. 2012;335:1359-1362.

62. Paraan M, Bhattacharya N, Uversky VN, Stagg SM. Flexibility of the Sec13/31 cage is influenced by the Sec31 C-terminal disordered domain. *J Struct Biol.* 2018;204:250-260.
63. Stankewich MC, Stabach PR, Morrow JS. Human Sec31B: a family of new mammalian orthologues of yeast Sec31p that associate with the COPII coat. *J Cell Sci.* 2006;119:958-969.
64. Watson P, Townley AK, Koka P, Palmer KJ, Stephens DJ. Sec16 defines endoplasmic reticulum exit sites and is required for secretory cargo export in mammalian cells. *Traffic.* 2006;7:1678-1687.
65. Bhattacharyya D, Glick BS. Two mammalian Sec16 homologues have nonredundant functions in endoplasmic reticulum (ER) export and transitional ER organization. *Mol Biol Cell.* 2007;18:839-849.
66. Inuma T, Shiga A, Nakamoto K, et al. Mammalian Sec16/p250 plays a role in membrane traffic from the endoplasmic reticulum. *J Biol Chem.* 2007;282:17632-17639.
67. Hughes H, Budnik A, Schmidt K, et al. Organisation of human ER- exit sites: requirements for the localisation of Sec16 to transitional ER. *J Cell Sci.* 2009;122:2924-2934.
68. Montegna EA, Bhave M, Liu Y, Bhattacharyya D, Glick BS. Sec12 binds to Sec16 at transitional ER sites. *PLoS One.* 2012;7:e31156.
69. Kung LF, Pagant S, Futai E, et al. Sec24p and Sec16p cooperate to regulate the GTP cycle of the COPII coat. *EMBO J.* 2012;31:1014- 1027.
70. Whittle JR, Schwartz TU. Structure of the Sec13-Sec16 edge element, a template for assembly of the COPII vesicle coat. *J Cell Biol.* 2010;190:347-361.
71. Maeda M, Katada T, Saito K. TANGO1 recruits Sec16 to coordinately organize ER exit sites for efficient secretion. *J Cell Biol.* 2017; 216:1731-1743.
72. Saito K, Chen M, Bard F, et al. TANGO1 facilitates cargo loading at endoplasmic reticulum exit sites. *Cell.* 2009;136:891-902.

73. Maeda M, Saito K, Katada T. Distinct isoform-specific complexes of TANGO1 cooperatively facilitate collagen secretion from the endoplasmic reticulum. *Mol Biol Cell*. 2016;27:2688-2696.
74. Ishikawa Y, Ito S, Nagata K, Sakai LY, Bächinger HP. Intracellular mechanisms of molecular recognition and sorting for transport of large extracellular matrix molecules. *Proc Natl Acad Sci USA*. 2016; 113:E6036-E6044.
75. Saito K, Yamashiro K, Ichikawa Y, et al. cTAGE5 mediates collagen secretion through interaction with TANGO1 at endoplasmic reticulum exit sites. *Mol Biol Cell*. 2011;22:2301-2308.
76. Saito K, Yamashiro K, Shimazu N, Tanabe T, Kontani K, Katada T. Concentration of Sec12 at ER exit sites via interaction with cTAGE5 is required for collagen export. *J Cell Biol*. 2014;206:751-762.
77. Tanabe T, Maeda M, Saito K, Katada T. Dual function of cTAGE5 in collagen export from the endoplasmic reticulum. *Mol Biol Cell*. 2016; 27:2008-2013.
78. Ma W, Goldberg J. TANGO1/cTAGE5 receptor as a polyvalent template for assembly of large COPII coats. *Proc Natl Acad Sci USA*. 2016;113:10061-10066.
79. Johnson A, Bhattacharya N, Hanna M, et al. TFG clusters COPII-coated transport carriers and promotes early secretory pathway organization. *EMBO J*. 2015;34:811-827.
80. Mironov AA, Mironov AA Jr, Beznoussenko GV, et al. ER-to-Golgi carriers arise through direct en bloc protrusion and multistage maturation of specialized ER exit domains. *Dev Cell*. 2003;5:583-594.
81. Zeuschner D, Geerts WJ, van Donselaar E, et al. Immuno-electron tomography of ER exit sites reveals the existence of free COPII-coated transport carriers. *Nat Cell Biol*. 2006;8:377-383.

82. Buehler MJ. Nanomechanics of collagen fibrils under varying cross-link densities: atomistic and continuum studies. *J Mech Behav Biomed Mater.* 2008;1:59-67.
83. Santos AJ, Raote I, Scarpa M, Brouwers N, Malhotra V. TANGO1 recruits ERGIC membranes to the endoplasmic reticulum for procollagen export. *Elife.* 2015;4.
84. Raote I, Ortega Bellido M, Pirozzi M, et al. TANGO1 assembles intorings around COPII coats at ER exit sites. *J Cell Biol.* 2017;216: 901-909.
85. Raote I, Ortega-Bellido M, Santos AJ, et al. TANGO1 builds a machine for collagen export by recruiting and spatially organizing COPII, tethers and membranes. *Elife.* 2018;7.
86. Hanna MG 4th, Block S, Frankel EB, et al. TFG facilitates outer coat disassembly on COPII transport carriers to promote tethering and fusion with ER-Golgi intermediate compartments. *Proc Natl Acad Sci USA.* 2017;114:E7707-E7716.
87. Yuan L, Kenny SJ, Hemmati J, Xu K, Schekman R. TANGO1 and SEC12 are copackaged with procollagen I to facilitate the generation of large COPII carriers. *Proc Natl Acad Sci USA.* 2018;115:E12255- E12264.
88. Melville D, Gorur A, Schekman R. Fatty-acid binding protein 5 modulates the SAR1 GTPase cycle and enhances budding of large COPII cargoes. *Mol Biol Cell.* 2019;30:387-399.
89. Gorur A, Yuan L, Kenny SJ, Baba S, Xu K, Schekman R. COPII-coated membranes function as transport carriers of intracellular procollagen I. *J Cell Biol.* 2017;216:1745-1759.
90. Omari S, Makareeva E, Roberts-Pilgrim A, et al. Noncanonical autophagy at ER exit sites regulates procollagen turnover. *Proc Natl Acad Sci USA.* 2018;115:E10099-E10108.
91. McCaughey J, Stevenson NL, Cross S, Stephens DJ. ER-to-Golgi trafficking of procollagen in the absence of large carriers. *J Cell Biol.* 2019;218(3):929-948.
92. Raote I, Malhotra V. Protein transport by vesicles and tunnels. *J Cell Biol.* 2019;218(3):737-739.

93. Karagöz GE, Acosta-Alvear D, Walter P. The unfolded protein response: detecting and responding to fluctuations in the protein- folding capacity of the endoplasmic reticulum. *Cold Spring Harb Perspect Biol.* 2019. <http://doi.org/10.1101/cshperspect.a033886>.
94. Klinkenberg D, Long KR, Shome K, Watkins SC, Aridor M. A cascade of ER exit site assembly that is regulated by p125A and lipid signals. *J Cell Sci.* 2014;127:1765-1778.
95. Tani K, Mizoguchi T, Iwamatsu A, Hatsuzawa K, Tagaya M. p125 is a novel mammalian Sec23p-interacting protein with structural similar-ity to phospholipid-modifying proteins. *J Biol Chem.* 1999;274: 20505-20512.
96. Mizoguchi T, Nakajima K, Hatsuzawa K, et al. Determination of func-tional regions of p125, a novel mammalian Sec23p-interacting pro- tein. *Biochem Biophys Res Commun.* 2000;279:144-149.
97. Shimoi W, Ezawa I, Nakamoto K, et al. p125 is localized in endoplas- mic reticulum exit sites and involved in their organization. *J Biol Chem.* 2005;280:10141-10148.
98. Ong YS, Tang BL, Loo LS, Hong W. p125A exists as part of the mam- malian Sec13/Sec31 COPII subcomplex to facilitate ER-Golgi trans- port. *J Cell Biol.* 2010;190:331-345.
99. la Cour JM, Schindler AJ, Berchtold MW, Schekman R. ALG-2 atten- uates COPII budding in vitro and stabilizes the Sec23/Sec31A com- plex. *PLoS One.* 2013;8:e75309.
100. Yamasaki A, Tani K, Yamamoto A, Kitamura N, Komada M. The Ca²⁺-binding protein ALG-2 is recruited to endoplasmic reticulum exit sites by Sec31A and stabilizes the localization of Sec31A. *Mol Biol Cell.* 2006;17:4876-4887.
101. Shibata H, Kanadome T, Sugiura H, et al. A new role for annexin A11 in the early secretory pathway via stabilizing Sec31A protein atthe endoplasmic reticulum exit sites (ERES). *J Biol Chem.* 2015;290: 4981-4993.

102. Bahar E, Kim H, Yoon H. ER stress-mediated signaling: action potential and Ca(2+) as key players. *Int J Mol Sci.* 2016;17:1558.
103. Xu D, Hay JC. Reconstitution of COPII vesicle fusion to generate a pre-Golgi intermediate compartment. *J Cell Biol.* 2004;167:997- 1003.
104. Witte K, Schuh AL, Hegermann J, et al. TFG-1 function in protein secretion and oncogenesis. *Nat Cell Biol.* 2011;13:550-558.
105. Greco A, Mariani C, Miranda C, et al. The DNA rearrangement that generates the TRK-T3 oncogene involves a novel gene on chromosome 3 whose product has a potential coiled-coil domain. *Mol Cell Biol.* 1995;15:6118-6127.
106. Chen Y, Tseng SH. Targeting tropomyosin-receptor kinase fused gene in cancer. *Anticancer Res.* 2014;34:1595-1600.
107. Milovanovic D, Wu Y, Bian X, De Camilli P. A liquid phase of synapsin and lipid vesicles. *Science.* 2018;361:604-607.
108. Kanadome T, Shibata H, Kuwata K, Takahara T, Maki M. The calcium-binding protein ALG-2 promotes endoplasmic reticulum exit site localization and polymerization of Trk-fused gene (TFG) protein. *FEBS J.* 2017;284:56-76.
109. Kim YG, Sohn EJ, Seo J, et al. Crystal structure of bet3 reveals a novel mechanism for Golgi localization of tethering factor TRAPP. *Nat Struct Mol Biol.* 2005;12:38-45.
110. Cai H, Yu S, Menon S, et al. TRAPPI tethers COPII vesicles by binding the coat subunit Sec23. *Nature.* 2007;445:941-944.
111. Slosarek EL, Schuh AL, Pustova I, et al. Pathogenic TFG mutations underlying hereditary spastic paraplegia impair secretory protein trafficking and axon fasciculation. *Cell Rep.* 2018;24:2248-2260.

112. Yagi T, Ito D, Suzuki N. TFG-related neurologic disorders: new insights into relationships between endoplasmic reticulum and neurodegeneration. *J Neuropathol Exp Neurol.* 2016;75:299-305.
113. Patel A, Lee HO, Jawerth L, et al. A liquid-to-solid phase transition of the ALS protein FUS accelerated by disease mutation. *Cell.* 2015;162:1066-1077.
114. Wegmann S, Eftekharzadeh B, Tepper K, et al. Tau protein liquid-liquid phase separation can initiate tau aggregation. *EMBO J.* 2018; 37:e98049.
115. Tarbet HJ, Toleman CA, Boyce M. A sweet embrace: control of protein-protein interactions by O-linked β -N-acetylglucosamine. *Biochemistry.* 2018;57:13-21.
116. Hart GW, Slawson C, Ramirez-Correa G, Lagerlof O. Cross talk between O-GlcNAcylation and phosphorylation: roles in signaling, transcription, and chronic disease. *Annu Rev Biochem.* 2011;80: 825-858.
117. Hanover JA, Krause MW, Love DC. The hexosamine signaling pathway: O-GlcNAc cycling in feast or famine. *Biochim Biophys Acta.* 1800;2010:80-95.
118. Cox NJ, Unlu G, Bisnett BJ, et al. Dynamic glycosylation governs the vertebrate COPII protein trafficking pathway. *Biochemistry.* 2018; 57:91-107.
119. Dudognon P, Maeder-Garavaglia C, Carpentier JL, Paccaud JP. Regulation of a COPII component by cytosolic O-glycosylation during mitosis. *FEBS Lett.* 2004;561:44-50.
120. McCaughey J, Miller VJ, Stevenson NL, et al. TFG promotes organization of transitional ER and efficient collagen secretion. *Cell Rep.* 2016;15:1648-1659.
121. Jin L, Pahuja KB, Wickliffe KE, et al. Ubiquitin-dependent regulation of COPII coat size and function. *Nature.* 2012;482:495-500.
122. McGourty CA, Akopian D, Walsh C, et al. Regulation of the CUL3 ubiquitin ligase by a calcium-dependent co-adaptor. *Cell.* 2016;167:525-538.e14.

123. Canning P, Cooper CD, Krojer T, et al. Structural basis for Cul3 protein assembly with the BTB-Kelch family of E3 ubiquitin ligases. *J Biol Chem*. 2013;288:7803-7814.
124. Kim K, Park S, Kim J. Cullin3-RING ubiquitin ligases are intimately linked to the unfolded protein response of the endoplasmic reticulum. bioRxiv 428136. doi: <https://doi.org/10.1101/428136>
125. Koreishi M, Yu S, Oda M, Honjo Y, Satoh A. CK2 phosphorylates Sec31 and regulates ER-to-Golgi trafficking. *PLoS One*. 2013;8: e54382.
126. Gan W, Zhang C, Siu KY, Satoh A, Tanner JA, Yu S. ULK1 phosphorylates Sec23A and mediates autophagy-induced inhibition of ER-to-Golgi traffic. *BMC Cell Biol*. 2017;18:22.
127. Jeong YT, Simoneschi D, Keegan S, et al. The ULK1-FBXW5-SEC23B nexus controls autophagy. *Elife*. 2018;7.
128. Joo JH, Wang B, Frankel E, et al. The noncanonical role of ULK/- ATG1 in ER-to-Golgi trafficking is essential for cellular homeostasis. *Mol Cell*. 2016;62:491-506.
129. Ge L, Melville D, Zhang M, Schekman R. The ER-Golgi intermediate compartment is a key membrane source for the LC3 lipidation step of autophagosome biogenesis. *Elife*. 2013;2:e00947.
130. Ge L, Zhang M, Schekman R. Phosphatidylinositol 3-kinase and COPII generate LC3 lipidation vesicles from the ER-Golgi intermediate compartment. *Elife*. 2014;3:e04135.
131. Ge L, Wilz L, Schekman R. Biogenesis of autophagosomal precursors for LC3 lipidation from the ER-Golgi intermediate compartment. *Autophagy*. 2015;11:2372-2374.
132. Zacharogianni M, Kondylis V, Tang Y, et al. ERK7 is a negative regulator of protein secretion in response to amino-acid starvation by modulating Sec16 membrane association. *EMBO J*. 2011;30:3684-3700.

133. Farhan H, Wendeler MW, Mitrovic S, et al. MAPK signaling to the early secretory pathway revealed by kinase/phosphatase functional screening. *J Cell Biol.* 2010;189:997-1011.
134. Dodonova SO, Diestelkoetter-Bachert P, von Appen A, et al. VESIC-ULAR TRANSPORT. A structure of the COPI coat and the role of coat proteins in membrane vesicle assembly. *Science.* 2015;349: 195-198.
135. Avinoam O, Schorb M, Beese CJ, Briggs JA, Kaksonen M. ENDOCY- TOSIS. Endocytic sites mature by continuous bending and remo- deling of the clathrin coat. *Science.* 2015;348:1369-1372.
136. Dodonova SO, Aderhold P, Kopp J, et al. 9 Å structure of the COPI coat reveals that the Arf1 GTPase occupies two contrasting molecu- lar environments. *Elife.* 2017;6.
137. Fotin A, Cheng Y, Sliz P, et al. Molecular model for a complete clathrin lattice from electron cryomicroscopy. *Nature.* 2004;432:573-579.

Chapter 2: Neurological disorders linked to mutations in TFG

Abstract

The dysregulation of protein trafficking is a common feature in many neurological disorders and affect several important pathways that are responsible for maintaining proper cellular health and function. One of these impacted pathways is the early secretory pathway, responsible for protein transport from the endoplasmic reticulum to the Golgi. Integral to this pathway is TFG, known to cluster the Coat Protein complex II (COPII) proteins, which has recently been implicated in multiple neurological disorders. Here, we review a number of mutations in TFG that have been linked to Hereditary Spastic Paraplegia (HSP), sensory neuropathy with proximal dominant involvement (HMSN-P), Charcot-Marie-Tooth disease type 2 (CMT2), Parkinson's disease (PD), and Amyotrophic Lateral Sclerosis (ALS). Although much research remains to understand the associated pathomechanisms, links to defects in the early secretory pathway, cytoplasmic aggregations, and ER stress response have been identified.

1. Introduction

Over the past decade, *tropomyosin-receptor kinase fused gene* (TFG) has been linked to multiple neurological disorders, including Hereditary Spastic Paraplegia (HSP), sensory neuropathy with proximal dominant involvement (HMSN-P), Charcot-Marie-Tooth disease type 2 (CMT2), Parkinson's disease (PD), and Amyotrophic Lateral Sclerosis (ALS).^{1,2,3,4,5} While these neurological disorders all have unique clinical manifestations, the upper and lower motor neurons and peripheral axons are all variably affected. Point mutations in TFG have been identified in patients with HSP, HMSN-P, CMT2, PD, and ALS suggesting that TFG may have a specialized role in supporting neuronal health or proper neurological function.

Originally described as DNA arrangement that results in an oncogenic product, TFG is known to play an important role in the early secretory pathway, responsible for trafficking from the endoplasmic reticulum (ER) to the ER-Golgi intermediate compartment (ERGIC) via Coat Protein complex II (COPII).⁶ Previous work has demonstrated that TFG clusters the required COPII components at the ER-ERGIC interface and may also facilitate the uncoating of COPII carriers prior to fusion with the ERGIC membrane.^{7,8} Although TFG is expressed ubiquitously across all tissues, it has been found to be highly expressed in the brain and the question still remains how mutations in TFG lead to the described neurological disorders.¹ Recent work investigating a number of these specific mutations has suggested that TFG may have a specialized function in neurons and that mutations causing changes to TFG structure and/or function are linked to defects in protein oligomerization, clustering, and cytoplasmic aggregation.

2. TFG p.R106C mutation disrupts protein transport through the early secretory pathway and endosomal pathway

One of the most widely studied TFG mutations in patients with Hereditary Spastic Paraplegia (HSP) was first identified in two siblings who presented with a set of neurological symptoms that were consistent with a complicated form of HSP and included a combination of early-onset spastic paraplegia, neuropathy, and optical atrophy.¹ The causative mutation was determined to be a homozygous variant, c.316C>T, identified in *TFG* via Sanger sequencing which resulted in a p.R106C mutation in TFG.¹ The p.R106C TFG mutation has additionally been identified in a number of other patients presenting with early-onset infantile neuroaxonal dystrophy (INAD) and complicated HSP.^{9,10} Investigation into the underlying mechanism revealed a defect in TFG clustering and localization in neurons which leads to a decrease in the kinetics of transport from the ER to the Golgi.¹¹ Additionally, TFG has recently been identified to impact endosomal trafficking in neurites, both axons and dendrites, which is linked to defects in clustering of important synaptic proteins.¹¹ Altogether, this recent work has begun to identify how the p.R106C mutation in TFG leads to neurodegenerative diseases such as HSP.

TFG is known to play an important role in the early secretory pathway and is commonly clustered at the ER/ERGIC interface.^{8,12} However, neurons homozygous for the R106C mutation demonstrate a change in this localization that causes a much more diffuse distribution of TFG. Interestingly, it has also been demonstrated that TFG is localized to neurites, but the majority is not associated with any COPII machinery, suggesting a neuronal specific role for TFG in addition to its canonical role in the early secretory pathway.¹¹ Previous work has highlighted the importance of proper TFG localization in order to sequester COPII components at ERES and aid in the uncoating of COPII carriers prior to fusion with the ER-Golgi intermediate compartment (ERGIC).⁸ Primary cortical neurons collected from a rodent model homozygous for the p.R106C TFG mutation showed a significant proportion of TFG diffused away from traditional TFG ‘clusters’ which were observed in controls. iPSC derived cortical neurons homozygous for R106C showed a similar diffusion of TFG

away from ER exit sites compared to controls.¹¹ Of note, this impact on TFG distribution appears to be cell type dependent with iPSC derived fibroblasts homozygous for the p.R106C mutation exhibiting no diffusion of TFG away from ERES or COPII machinery.¹³ Recent work has also found TFG in the neurites, both axons and dendrites, of cortical neurons which are surprisingly not positive for COPII machinery but instead colocalized with Rab4-positive endosomes.¹¹ Taken together, this work demonstrates that the p.R106C TFG mutation affects the distribution of TFG in neurons, causing a diffusion away from its traditional localization at ERES and likely impacts the dynamics of the early secretory pathway. Additionally, TFG may have a neuronal specific role in relation to Rab4-positive endosomes in neurites. These findings may demonstrate, in part, why the homozygous p.R106C TFG mutation specifically affects the central nervous system and presents as a neurological disease, even though TFG is ubiquitously expressed.

TFG is known to oligomerize into tight, octameric, ring-like structures that cluster at the ER/ERGIC interface and facilitate proper transport through the early secretory pathway and biochemistry experiments have revealed the R106C mutation affects the ability of TFG to tightly oligomerize but does not inhibit self-association.^{14,13} Previous *in vivo* work has shown that TFG forms octamers and that the presence of the R106C mutation causes a reduced Stokes radius and sedimentation value, demonstrating a significant proportion of TFG p.R106C fails to assemble into an octamer.^{1,14} Additional hydrodynamic studies using the coiled-coil domain of TFG, found that the R106C mutation did not disrupt the ability of TFG to homo-oligomerize compared to the unmutated control which demonstrates that the R106C mutation does not fully disrupt or unfold the cc domain.¹³ Illustrating a potential mechanism by which the p.R106C mutation in TFG leads to a decrease in oligomerization and clustering at the ER/ERGIC interface, resulting in the early secretory transport delays.

The p.R106C mutation in TFG has also been shown to decrease the trafficking kinetics of cargo being moved through the early secretory pathway as well as impacting Rab4-positive endosome

transport in distal neurites.¹¹ The recent identification of these underlying defects in protein transport in neurons harboring the R106C mutation have begun to establish a cause for the neurodegenerative phenotype observed in patients. Trafficking studies using an inducible release system, demonstrated that the transport of L1 cell adhesion molecular, L1CAM, was significantly delayed in its transport from the ER to the Golgi in primary cortical neurons harboring the p.R106C neurons compared to controls.¹⁵ Importantly, it was noted that L1CAM transport was not inhibited but just kinetically slowed. This work also supported earlier findings that demonstrated a decrease in L1CAM on the cell surface at DIV10 iPSC derived cortical neurons homozygous for the R106C mutation compared to controls.^{11,13} Interestingly, trafficking studies using iPSC derived melanocytes homozygous for the R106C mutation did not show a delay in trafficking from the ER to the Golgi.¹³ Taken together, these findings highlight that the p.R106C TFG mutations leads to a delay in the transport of proteins out of the ER but in a neuronal specific manner.

In addition to the canonical role of TFG in the early secretory pathway, recent work has also determined that TFG puncta are present in both the axons and dendrites of cortical neurons and that its association with Rab4-positive endosomes likely impacts the transport of synaptic cargo in neurites.¹¹ In neurites of iPSC derived cortical neurons and primary cortical neurons homozygous for the R106C mutation, Rab4-positive endosome numbers are decreased as well a decrease in the average velocity of these endosomes. An important GABA receptor scaffold protein, Gephyrin, has been shown to be transported along Rab4- and P13P- positive endosomes.^{11,16} In the presence of p.R106C TFG mutation in primary cortical neurons, there is a small but significant decrease in the clustering of Gephyrin at post-synaptic inhibitory sites. A significant decrease in GABA clustering was also observed at these sites compared to controls.¹¹ Although the role for TFG in Rab4-positive endosome transport is still not fully understood, the R106C mutation clearly impacts the transport and clustering of important synaptic proteins that likely contribute to the neurodegenerative phenotype observed in HSP.

Although much remains unknown, a recent rodent model that strongly recapitulates patient phenotypes has begun to shed light on the underlying pathomechanisms associated with the TFG p.R106C HSP.¹¹ This work, in conjunction with the previous research, suggests that the p.R106C mutation in TFG affects proper TFG oligomerization and cluster in neurons, negatively impacting both trafficking in the early secretory pathway as well as endosomal transport in neurites. Overtime, this negatively impacts neuronal health and may lead to neurodegeneration. A rodent model, homozygous for the R106C mutation has been shown via electromyography to have aberrant axonal firing in the hind limbs, a strong proxy for spasticity observed in HSP patients. Additionally, primary neurons collected from this model demonstrate a decrease in the amplitude of mini inhibitory postsynaptic currents which may be related to the decreased clustering of inhibitory synaptic proteins gephyrin and GABA_AR.¹¹ Additional work will be needed to understand the mechanism by which the p.R106C TFG mutation leads to neurodegeneration but current work does demonstrate a defect in protein transport that likely affects neuronal health. Specifically, this has been shown to alter proper clustering of important inhibitory postsynaptic proteins which may begin to explain the increase in aberrant axonal firing and eventually be connected to the spasticity observed in HSP patients with the p.R106C TFG mutation.

3. HMSN-P is related to a p.P285L TFG mutation linked to inclusion bodies and UPS dysfunction

Mutations in TFG can cause varying neurodegenerative diseases, including the p.P285L mutation in TFG that was first identified, a result of a c.854C>T substitution in *TFG*, in individuals from an affected family that were clinically diagnosed with a hereditary motor and sensory neuropathy with proximal dominant involvement (HMSN-P).⁴ Although the underlying mechanism remains unknown, research has suggested that this mutation may affect the ubiquitin-proteasome system (UPS) and cause ER stress, leading to the existence of observed TFG-positive inclusion bodies.^{4,17,18} Additionally,

neuropathological findings of patients showed neuronal loss, spinal cord atrophy, and gliosis.^{19,20} A number of individuals, clustered in families, have been identified in recent years that harbor this autosomal dominant mutation, this in addition to developing models will hopefully lead to advancements in understanding the underlying pathomechanisms.

The p.P285L mutation in TFG and the associated HMSN-P have been identified in a number of individuals of families in Korea, Iran, Brazil, and two distinct regions of Japan and shares some disease phenotypes with familial amyotrophic lateral sclerosis (ALS).^{4,21,22,23,24,5} Clinically, HMSN-P is characterized as slowly progressive muscle weakness and atrophy (usually with a late onset around a patient's 40s), earlier painful cramps (patient's 20s), distal sensory involvement, and respiratory failure in some patients at the end stage.²⁵ It is important to note that clinical variability has been observed.⁵ Interestingly, the widely observed predominant proximal weakness with prevalent fasciculation is very similar to that of patients diagnosed with familial ALS.²⁵ Furthermore, TAR DNA-binding protein 43 (TDP-43) cytoplasmic inclusions were observed via immunohistochemistry in motor neurons of HMSN-P patients positive for the P285L mutation and in neuro-2a cells overexpressing TFG p.P285L.⁴ The presence of these TDP-43 inclusions is a pathological hallmark of ALS and frontotemporal dementia.^{26,27,28} While the exact link between these TDP-43 inclusions and disease it not yet fully established, some research has suggested that the mislocalization of TDP-43 to the cytoplasm from the nucleus may be the actual driver of disease, possibly through causing neuronal toxicity with inclusions forming as a downstream affect.^{26,29,30,31} Further, the loss of the nuclear pool of TDP-43 which is important in RNA regulation and stabilization may be contributing to disease onset and progression in both HMSN-P and ALS.²⁶

In addition to TDP-43 inclusions, the p.P285L TFG mutation has also been linked to aggregations of TFG, impaired UPS activity, and ER stress. Immunohistochemical observations from a patient after death revealed TFG-positive aggregations in the motor and spinal cord neurons that were

also positive for ubiquitin.⁴ Initial studies have found TFG-positive aggregates to also be positive for TDP-43, but this appears to be cell-type dependent.^{4,20} To better understand the drivers that may be causing these aggregations to form, researchers used HMSN-P, positive for the P285L mutation, patient iPSC-derived motor neurons.¹⁷ Utilizing this model, it was observed that there was an increase in overall TFG protein levels and that induction of cellular stress caused TFG-positive aggregates to form.¹⁷ Additionally, a decrease in proteasome activity and an increase in ubiquitinated proteins was observed, clearly highlighting a dysfunction of the UPS.¹⁷ A CRISPR correction of the p.P285L TFG mutation alleviated these observed impacts on the UPS.¹⁷ Further studies have suggested that the TFG p.P285L mutation acts as a ‘gain of function’ mutation that enhances ER stress through inhibiting the effect of the UPS.¹⁸

While much more work is needed to understand the mechanistic drivers behind the HMSN-P linked p.P285L mutation in TFG, there are clear dysfunctions in the UPS and protein aggregation phenotypes observed. A dysregulation of the UPS could likely lead to the observed aberrant accumulation of ubiquitinated proteins. Over time, this lack of proper cellular clearance and accumulation of toxic proteins, in addition to the impaired ER stress response, could result in the neurodegeneration that is observed in HMSN-P patients. Further research and a strong animal model that recapitulates this unique mutation would likely provide key insights into disease progression and mechanisms.

4. TFG mutations related to CMT2, ALS, and PD

In addition to the R106C and P285L mutations in TFG that have been identified in patients with HSP and HMSN-P, respectively, widespread sequencing has revealed a number of other mutations in TFG that are associated with neuropathies. These include a p.R22W, p.G269V, and p.R383H mutation in TFG that have been found in patients with HSP, Charcot-Marie-Tooth disease type 2 (CMT2), and

both ALS and Parkinson's disease, respectively. Although, little is known about the underlying mechanism that drives disease in these cases, it is evident that dysregulation in TFG structure or function has a negative impact on neuronal health.

Similar to the R106C mutation, a p.R22W TFG mutation was identified in a Sudanese family that was diagnosed with a complex form of HSP.² This autosomal recessive HSP, which arose from a missense change c.64C>T, presented with similar clinical symptoms such as early onset, motor neuronal demyelination, and motor axonal degradation. However, no visual impairment was observed like that in the patients harboring the p.R106C mutation in TFG.^{2,1} The PB1 domain, in which the p.R22W mutation occurs, and the adjacent coiled-coil domain has been shown to be sufficient for forming octameric ring structures in solution.¹² The p.R22W mutation in TFG has been shown, through biochemical studies, to disrupt octamer formation, only forming dimers in solution.² Analogously, negative stain EM using full-length TFG have observed a defect in proper octameric ring assembly in the presence of the R22W mutation that is very similar to that observed in the presence of the R106C mutation.¹³ While much more work is needed to define the impact this mutation has on TFG structure and function, a lack of proper TFG clustering, similar to that found in studies using the p.R106C TFG mutation, is likely a contributing factor.

Two recently described mutations in the disordered C-terminal of TFG have exhibited aggregation phenotypes reminiscent to those observed in the presence of the P285L mutation. A p.G269V mutation in TFG was identified in a Taiwanese family diagnosed with Charcot-Marie-Tooth disease type 2 (CMT2). The affected individuals exhibited a late onset (age 28-40) and had slowly progressive symmetrical muscle atrophy and mild sensory loss.³ Biochemistry experiments revealed that TFG G269V likely had a propensity to form aggregates as it was found in the insoluble fraction, compared to TFG WT which was predominantly found in the soluble fraction. Additionally, overexpression experiments in HEK293 cells revealed TFG G269V formed cytoplasmic aggregates that

were also positive for TFG WT, suggesting this autosomal dominant mutation may act in a loss of function manner by sequestering TFG WT in these aggregations.³ Another mutation in this disorder region of TFG, p.R383H, was identified in a Korean family with individuals diagnosed with both ALS and Parkinson's disease, presenting some clinical variation that included bradykinesia, progressive limb weakness, and muscle atrophy.³² Overexpression experiments in HeLa cells found TFG R383H caused the formation of cytoplasmic aggregates, positive for TFG and TDP-43.³² These TFG-positive cytoplasmic aggregations observed using the G269V and R383H variant of TFG are very similar to observations found with the P285L variant and suggests this disordered region may be important in regulating proper clustering, possibly through phase separation.^{20,6}

5. Conclusion

With the advances in genetic sequencing related technology, a number of previously unknown genes and mutations have been linked to various diseases, including the neurological disorders discussed here. While the mutations in TFG related to HSP, HMSN-P, CMT2, PD, ALS vary in their clinical presentation and location within the protein, the current research underscores the importance of proper TFG structure and function in maintaining neuronal health. Why these mutations in TFG, which is ubiquitously expressed, lead specifically to neurological disorders still remains unanswered. It is likely that TFG has a specialized role in highly polarized neurons. Recent work using the p.R106C TFG mutation demonstrated a novel function for TFG in the trafficking of Rab4-positive endosomes, which is altered in the presence of the mutation.¹¹ Additionally, models for ALS and PD have highlighted that the corresponding mutations in TFG can lead to an increase in propensity for cytoplasmic aggregations to occur, in which neurons may be highly susceptible to such protein aggregations.^{4,17} A neuronal specific role for TFG and a susceptibility for toxic protein aggregations in neurons may begin to explain how the discussed mutations in TFG lead to neurological disorders. An important, and likely necessary step,

for further research would be the development and use of research models that more closely recapitulate the neuronal environment.

References

1. Beetz, C. *et al.* Inhibition of TFG function causes hereditary axon degeneration by impairing endoplasmic reticulum structure. *Proc. Natl. Acad. Sci.* 110, 5091–5096 (2013).
2. Elsayed, L. E. O. *et al.* Hereditary spastic paraplegias: identification of a novel SPG57 variant affecting TFG oligomerization and description of HSP subtypes in Sudan. *Eur. J. Hum. Genet.* 25, 100–110 (2016).
3. Tsai, P. C. *et al.* A novel TFG mutation causes Charcot-Marie-Tooth disease type 2 and impairs TFG function. *Neurology* 83, 903–912 (2014).
4. Ishiura, H. *et al.* The TRK-fused gene is mutated in hereditary motor and sensory neuropathy with proximal dominant involvement. *Am. J. Hum. Genet.* 91, 320–329 (2012).
5. Alavi, A. *et al.* HMSN-P caused by p.Pro285Leu mutation in TFG is not confined to patients with Far East ancestry. *Neurobiol. Aging* 36, 1606.e1-1606.e7 (2015).
6. Peotter, J., Kasberg, W., Pustova, I. & Audhya, A. COPII-mediated trafficking at the ER/ERGIC interface. *Traffic* 1–13 (2019). doi:10.1111/tra.12654
7. Johnson, A. *et al.* TFG clusters COPII-coated transport carriers and promotes early secretory pathway organization. *EMBO* 34, 811–827 (2015).
8. Hanna, M. G. *et al.* TFG facilitates outer coat disassembly on COPII transport carriers to promote tethering and fusion with ER–Golgi intermediate compartments. *Proc. Natl. Acad. Sci.* 114, E7707–E7716 (2017).
9. Harlalka, G. V *et al.* Novel Genetic , Clinical , and Pathomechanistic Insights into TFG-Associated Hereditary Spastic Paraplegia. *Hum. Mutat.* 37, 1157–1161 (2016).
10. Catania, A. *et al.* R106C TFG variant causes infantile neuroaxonal dystrophy “plus” syndrome. *Neurogenetics* 19, 179–187 (2018).
11. Peotter, J. L. *et al.* TFG regulates multiple trafficking pathways in cortical neurons to promote

- their long-term maintenance. *Manuscript in Preparation*.
12. Johnson, A. *et al.* TFG clusters COPII-coated transport carriers and promotes early secretory pathway organization. *Embo J* 34, 811–827 (2015).
 13. Slosarek, E. L. *et al.* Pathogenic TFG Mutations Underlying Hereditary Spastic Paraplegia Impair Secretory Protein Trafficking and Axon Fasciculation. *Cell Rep.* 24, 2248–2260 (2018).
 14. Witte, K. *et al.* TFG-1 function in protein secretion and oncogenesis. *Nat. Cell Biol.* 13, 550–558 (2011).
 15. Bowen, A. B., Bourke, A. M., Hiester, B. G., Hanus, C. & Kennedy, M. J. Golgi-independent secretory trafficking through recycling endosomes in neuronal dendrites and spines. *Elife* 1–27 (2017).
 16. Papadopoulos, T. *et al.* Endosomal phosphatidylinositol 3-phosphate promotes gephyrin clustering and GABAergic neurotransmission at inhibitory postsynapses. *J. Biol. Chem.* 292, 1160–1177 (2017).
 17. Murakami, N. *et al.* Proteasome impairment in neural cells derived from HMSN-P patient iPSCs. *Mol. Brain* 1–10 (2017). doi:10.1186/s13041-017-0286-y
 18. Yagi, T., Ito, D. & Suzuki, N. Evidence of TRK-Fused Gene (TFG1) function in the ubiquitin-proteasome system. *Neurobiol. Dis.* 66, 83–91 (2014).
 19. Fujita, K. *et al.* Brainstem and spinal cord motor neuron involvement with optineurin inclusions in proximal dominant hereditary motor and sensory neuropathy. *J. Neurol. Neurosurg. Psychiatry* 82, 1402–1403 (2011).
 20. Maeda, K., Idehara, R. & Mukaisho, K. I. Presence of colocalised phosphorylated TDP-43 and TFG proteins in the frontotemporal lobes of HMSN-P. *J. Neurol. Neurosurg. Psychiatry* 91, 1231–1232 (2020).
 21. Takashima, H. *et al.* A new type of hereditary motor and sensory neuropathy linked to

- chromosome 3. *Ann. Neurol.* 41, 771–780 (1997).
22. Miura, S. *et al.* Hereditary motor and sensory neuropathy with proximal dominancy in the lower extremities, urinary disturbance, and paroxysmal dry cough. *J. Neurol. Sci.* 273, 88–92 (2008).
 23. Lee, S. S. *et al.* Proximal dominant hereditary motor and sensory neuropathy with proximal dominance association with mutation in the TRK-fused gene. *JAMA Neurol.* 70, 607–615 (2013).
 24. Maeda, K. *et al.* Hereditary motor and sensory neuropathy (proximal dominant form, HMSN-P) among Brazilians of Japanese ancestry. *Clin. Neurol. Neurosurg.* 109, 830–832 (2007).
 25. Yagi, T., Ito, D. & Suzuki, N. TFG-related neurologic disorders: New insights into relationships between endoplasmic reticulum and neurodegeneration. *J. Neuropathol. Exp. Neurol.* 75, 299–305 (2016).
 26. Tziortzouda, P., Van Den Bosch, L. & Hirth, F. Triad of TDP43 control in neurodegeneration: autoregulation, localization and aggregation. *Nat. Rev. Neurosci.* 22, 197–208 (2021).
 27. Hasegawa, M. *et al.* Phosphorylated TDP-43 in frontotemporal lobar degeneration and amyotrophic lateral sclerosis. *Science (80-.)*. 314, (2006).
 28. Arai, T. *et al.* TDP-43 is a component of ubiquitin-positive tau-negative inclusions in frontotemporal lobar degeneration and amyotrophic lateral sclerosis. *Biochem. Biophys. Res. Commun.* 351, 602–611 (2006).
 29. Guerrero, E. N. *et al.* Amyotrophic lateral sclerosis-associated TDP-43 mutation Q331K prevents nuclear translocation of XRCC4-DNA ligase 4 complex and is linked to genome damage-mediated neuronal apoptosis. *Hum. Mol. Genet.* 28, 2459–2476 (2019).
 30. Barmada, S. J. *et al.* Cytoplasmic mislocalization of TDP-43 is toxic to neurons and enhanced by a mutation associated with familial amyotrophic lateral sclerosis. *J. Neurosci.* 30, 639–649 (2010).

31. Suk, T. R. & Rousseaux, M. W. C. The role of TDP-43 mislocalization in amyotrophic lateral sclerosis. *Mol. Neurodegener.* 15, 1–16 (2020).
32. Yoo, D., Lee, W., Lee, S., Sung, J. & Jeon, G. S. A Novel TFG Mutation in a Korean Family with α -Synucleinopathy and Amyotrophic Lateral Sclerosis. *Mov. Disord.* 37, 384–391 (2022).

Chapter 3. TFG regulates secretory and endosomal sorting pathways in neurons to promote their activity and maintenance

The work presented in this chapter is currently under review:

Peotter, J. L., Pustova, I., Lettman, M. M., Shatadal, S., Bradberry, M. M., Winter-Reed, A. D., Charan, M., Sharkey, E. E., Bren, A. M., Ole, A. K., Chapman, E. R., Salamat, S., and Audhya, A. TFG regulates secretory and endosomal sorting pathways in neurons to promote their activity and maintenance.

Manuscript under review.

Summary

Molecular pathways that intrinsically regulate neuronal maintenance are poorly understood, but rare pathogenic mutations that underlie neurodegenerative disease can offer important insights into the mechanisms that facilitate life-long neuronal function. Here, we leverage a rat model to demonstrate directly that the TFG p.R106C variant implicated previously in complicated forms of hereditary spastic paraplegia (HSP) underlies progressive spastic paraparesis with accompanying ventriculomegaly and thinning of the corpus callosum, consistent with disease phenotypes identified in adolescent patients. Analyses of primary cortical neurons obtained from CRISPR/Cas9-edited animals reveal a kinetic delay in biosynthetic secretory protein transport from the endoplasmic reticulum (ER), in agreement with prior induced pluripotent stem cell-based studies. Moreover, we identify an unexpected role for TFG in the trafficking of Rab4A-positive recycling endosomes specifically within axons and dendrites. Impaired TFG function compromises the transport of at least a subset of endosomal cargoes, which we show results in downregulated inhibitory receptor signaling that may contribute to excitation-inhibition imbalances. In contrast, the morphology and trafficking of other organelles, including mitochondria and lysosomes, are unaffected by the TFG p.R106C mutation. Our findings demonstrate a multifaceted role for TFG in secretory and endosomal protein sorting that is unique to cells of the central nervous system and highlight the importance of these pathways to maintenance of corticospinal tract motor neurons.

1. Introduction

The corticospinal tract (CST; also known as the pyramidal tract) is one of the major pathways involved in relaying information from the cerebral cortex of the brain to the spinal cord to enable coordinated walking as well as other movements (1, 2). Injury to the upper motor neurons that form the CST, which can result from genetically inherited pathogenic mutations or traumatic injury, impairs motor function and may lead to lifelong disability (3, 4). The mechanisms that underlie neurodegeneration following an insult remain largely unknown, at least in part due to an insufficient understanding of the fundamental systems that act normally to maintain neuronal function. However, key insights into these homeostatic pathways have been gleaned from the identification and characterization of rare genetic variants implicated in neurodegenerative disease. In the case of hereditary spastic paraplegias (HSPs), which are characterized by progressive weakness and spasticity of the limbs, mutations in more than 80 distinct genes have been linked to neurodegeneration within the CST, with a majority encoding factors that regulate subcellular organelle dynamics and function (5, 6). In particular, multiple recessive point mutations in Trk-fused gene (TFG; also called SPG57), which regulates early secretory pathway organization, have been suggested to cause early onset forms of HSP, although direct impacts on neuronal physiology and behavior have yet to be defined (7-11).

TFG was originally identified as part of an oncogenic fusion with the TrkA receptor tyrosine kinase (12). Subsequently, its native role during the earliest stages of biosynthetic membrane protein transport was revealed. Specifically, TFG functions to cluster and/or uncoat COPII transport carriers following their budding from subdomains on the endoplasmic reticulum (ER) (13-16). Consistent with this activity, inhibition of TFG kinetically delays the movement of cargoes from the ER to ER-Golgi intermediate compartments (ERGIC), elevating ER stress, reducing cell proliferation, and promoting apoptosis when depletion is highly penetrant (14-19). Germline deletion in metazoan systems, including *C. elegans* and rodents, results in early embryonic lethality (13, 15), but numerous point mutations have

been identified in patients suffering from various neurological disorders, including HSP, amyotrophic lateral sclerosis (ALS), hereditary motor and sensory neuropathy with proximal dominant involvement (HMSN-P), Charcot-Marie-Tooth disease (CMT) type 2, and Parkinson's disease (7-11, 20-24). Based on in situ hybridization studies and immunohistochemistry, TFG expression has been observed throughout the brain and spinal cord, but it is also seen in many other tissues (7, 25, 26). Thus, it is unknown why pathological TFG variants primarily impact the nervous system, especially considering the gene is expressed ubiquitously.

The inheritance patterns of TFG mutations that have been identified in the population vary, as do the disease phenotypes associated with each. Mutations found within the carboxyl-terminal disordered region appear to act dominantly, encode proteins that exhibit a propensity to form amyloid fibrils, and have been implicated in late-onset neuropathies (20, 22, 24, 27-31). In contrast, those in the structured amino-terminal PB1 and coiled coil domains are autosomal recessive, impair the ability of TFG to assemble into octameric ring structures, and have been associated with early onset, complicated forms of HSP (7-11, 14, 32). Likely due to its repetitive identification in several independent families, multiple studies have specifically attempted to define the phenotypic impacts resulting from the TFG p.R106C mutation found within the coiled coil domain (7, 11, 14, 32-34). Using patient-derived fibroblasts homozygous for the variant, roles for TFG in autophagy and mitochondrial function have been suggested (33, 34). Additionally, ectopic overexpression of TFG p.R106C in primary mouse hippocampal neurons leads to mitochondrial fragmentation (11), while induced pluripotent stem cell (iPSC)-derived cortical neurons natively expressing TFG p.R106C in a homozygous manner exhibit defects in axon fasciculation (32). Other studies have further implicated TFG in innate immunity and regulation of the ubiquitin-proteasome system (29, 35). Despite these many efforts however, it continues to remain unclear whether a mutation in TFG is sufficient to cause the motor dysfunction and

spasticity phenotypes associated with HSP, nor it is evident how neuronal function is negatively affected by pathological variants.

To address these issues, we used CRISPR/Cas9-mediated genome editing to introduce the TFG p.R106C mutation into Sprague Dawley rats. Our use of rats as opposed to mice was intentional, since rats have consistently been found to be more comparable to primates, both anatomically and physiologically (36, 37). We demonstrate that rats homozygous for the TFG p.R106C variant develop progressive motor deficits, thinning of the corpus callosum, ventriculomegaly, and hind limb spasticity, each independent of sex, recapitulating the major phenotypes displayed by HSP patients (38). Additionally, we show that trafficking of an integral membrane protein through the early secretory pathway is slowed in primary dissociated cortical neurons expressing the TFG p.R106C mutation, consistent with our previous studies using human iPSC-derived neurons (32). Moreover, we find that TFG is also targeted to another subcellular compartment in neurons beyond the ER/ERGIC interface. Specifically, in axons and dendrites, TFG localizes with Rab4A-positive endosomes and regulates their transport, thereby impacting the trafficking of an additional set of cargoes, some of which function in neuronal excitability. In contrast, we fail to identify lysosomal defects resulting from the TFG p.R106C mutation, distinguishing it from several other variants implicated in HSP (39, 40). Together, our findings highlight multiple roles for TFG function in neurons, uniquely sensitizing them to pathological TFG point mutations that otherwise have more limited impacts on other cell types.

2. Results

The TFG p.R106C mutation causes progressive gait dysfunction

Exome sequencing studies have linked numerous missense mutations in TFG to rare forms of neurodegenerative disease (7-11, 20-24, 30, 31, 33, 41, 42). However, none have been directly shown to be causative of phenotypes that are associated with neurodegeneration. To address this problem, we

used CRISPR/Cas9-mediated genome editing in embryos from Sprague Dawley rats to introduce the TFG p.R106C mutation, which has been associated with complicated forms of HSP in multiple independent families (7, 9, 11, 33). Two additional silent mutations were incorporated in parallel to enhance editing efficiency (Fig. 1A). In total, three founders were identified (two males and one female), all of which were heterozygous for the point mutation desired (c.316C>T) based on next generation sequencing. The founders were backcrossed independently to control animals, and their progeny were subjected to sequencing. Three animals bred from distinct founders that expressed the TFG p.R106C variant were selected based on the absence of mutations around the 10 most highly ranked potential off-target sites. Each was independently backcrossed an additional four times to reduce the potential existence of off-target effects that may have occurred during the initial editing experiments. Since no differences in fecundity or viability were observed between the three resulting colonies, a single one was selected for continued maintenance. To reduce the likelihood of suppressor mutations arising in the population, only heterozygous TFG p.R106C animals were used in all subsequent breeding.

Diagnostic criteria for HSPs typically include slowly progressing spastic weakness of the legs that results in ambulatory dysfunction (43). To determine whether animals expressing the TFG p.R106C mutation exhibit progressive difficulty walking, we conducted a series of quantitative kinematic gait analyses by recording animals from three different vantage points as they traversed a clear platform (Fig. 1B). Animals of both sexes were marked with small black spots on multiple body parts and examined at 6, 13, and 25 weeks of age. The markings were used to train a neural network model based on feature detectors from previously generated pose estimation networks (44). The positional coordinates of each point over time were then used to calculate various kinematic parameters. Consistent with progressive motor dysfunction that predominantly impacts the lower body of HSP patients, rats homozygous for the TFG p.R106C mutation displayed significant gait deficits compared

to control animals, which worsened with age (Fig. 1 C-F and SI Appendix, Fig. S1). In particular, the stereotypic oscillating pattern of side-to-side hind body movement during walking was significantly disrupted in homozygous mutant animals as they grew older. Although initially normal, by 13 weeks of age, both male and female rats homozygous for the TFG p.R106C mutation exhibited exaggerated side-to-side hind body movements, which became even more pronounced in 25-week-old animals (Fig. 1 C-E). Additionally, homozygous mutant animals exhibited a progressively diminished ability to maintain normal tail height during walking (Fig. 1F), a phenotype observed in rodent models of ALS and indicative of a reduced ability to control muscles important for hind body motion (45). Cross-body movement coordination, as defined by forelimb movement on one side of the body being in concert with the hind limb of the opposite side, was similarly impaired by TFG dysfunction (SI Appendix, Movies S1-S3).

We also analyzed the stride of animals, demonstrating that rats homozygous for the TFG p.R106C mutation exhibit a progressively extended period of time when each limb makes contact with the platform (stance phase) (SI Appendix, Fig. S1 A-C). The duration of the swing phase however, when no limb contact is made with the platform, was unaffected by the TFG mutation. Average walking velocity was also normal in homozygous TFG p.R106C animals (SI Appendix, Fig. S1 D), and as we expected due to its recessive nature, heterozygous TFG p.R106C animals did not exhibit any gait defects compared to control animals (Fig. 1 C-F and SI Appendix, Fig. S1). Taken together, our data indicate that the TFG p.R106C mutation is responsible for gait abnormalities and hind limb motor defects in mammals, which progressively reduce hind body stability, consistent with progressive lower limb dysfunction observed in HSP patients (38).

The TFG p.R106C mutation causes alterations in hind limb electrophysiology and central nervous system pathology

Lower limb spasticity is a hallmark of HSP that is typically diagnosed on physical exam (46). In patients suffering from complicated forms of the disease, including those harboring the TFG p.R106C mutation, electromyography (EMG) targeting a resting leg muscle has been used to highlight lower motor neuron dysfunction (7, 33). To determine whether this mutation in TFG is specifically responsible for altered skeletal muscle electrical activity, we used EMG to examine the hind limb gastrocnemius muscles of our CRISPR/Cas9-modified animals, anesthetized using ketamine. At 6 weeks of age, control and TFG mutant animals showed no significant differences in spontaneous electrical activity in these muscles (Fig. 2 A and B). However, 13-week-old homozygous TFG p.R106C animals exhibited an increasing frequency of EMG spikes, reaching statistical significance at 25 weeks of age (Fig. 2 A and B). The irregular firing pattern identified in the homozygous mutant animals suggested muscle fasciculation consistent with decreased inhibition of motor neurons, as opposed to muscle denervation. In contrast, neither control nor heterozygous TFG p.R106C mutant animals showed similar signs of muscle spasticity, consistent with the point mutation acting recessively (Fig. 2 A and B).

Magnetic resonance imaging (MRI) is widely used in clinical settings to help differentiate distinct groups of HSP patients (47). Using this approach, specific brain MRI patterns have been identified that appear to be characteristic of several complicated forms of HSP (48, 49). To determine the impact of the TFG p.R106C mutation on brain morphology, we harvested tissue from control and mutant animals at various timepoints (6, 13, and 25 weeks of age, identical to those used in gait analysis studies) during development and conducted H&E (hematoxylin and eosin) and LFB (Luxol fast blue) staining of paraffin-embedded sections. Consistent with neuroimaging of adolescent patients with the TFG p.R106C mutation, rats homozygous for the variant exhibited thinning of the corpus callosum, while no such defect was seen in control or heterozygous animals (Fig. 3 A and B). Additionally, we found that the ventricles of homozygous TFG p.R106C animals became progressively dilated (Fig. 3 A and C), a phenotype associated previously with the TFG p.R106C mutation in patients (33), as well as

a complicated, X-linked form of HSP known as MASA syndrome (Mental retardation, Aphasia, Shuffling gait, and Adducted thumbs) that results from mutations in SPG1, which encodes the axonal cell adhesion molecule L1CAM (50, 51).

In addition to brain morphology, we also examined the axons of upper motor neurons within the CST, which are among the longest in animals and have been shown to degenerate in HSP (5). Specifically, we used electron microscopy to measure the thickness of myelin sheaths in the lumbar segments of the spinal cord. These studies demonstrated reduced CST axon myelination in homozygous TFG p.R106C animals relative to controls, consistent with motor deficits being largely restricted to the hind limbs (Fig. 3 D). Finally, based on previous work showing an elevated inflammatory response in many forms of neurodegenerative disease (52, 53), we examined the distribution of Iba1-positive microglia and S100beta-positive astrocytes throughout the motor cortex of control and mutant animals using immunohistochemistry. These studies demonstrated increased density of both cell types in 25-week-old homozygous TFG p.R106C animals as compared to controls, suggesting that central nervous system (CNS) inflammation and astrogliosis accompany progressive neuronal dysfunction in HSP (Fig. 3 E and F).

The TFG p.R106C mutation impairs neuronal protein trafficking from the ER

Our previous work using human stem cell-derived cortical neurons indicated that the accumulation of a cell surface axonal membrane protein (L1CAM) was diminished when TFG function was perturbed, potentially due to reduced secretory protein transport (32). To independently confirm and extend this finding, we used primary rat cortical neurons harvested from control and TFG p.R106C mutant embryos and quantitatively imaged surface L1CAM at different timepoints after plating. Following 10 days in culture, homozygous TFG p.R106C mutant neurons exhibited significantly less L1CAM labeling on the plasma membrane as compared to controls, despite similar levels of the protein

being expressed irrespective of genotype (Fig. 4 A and B). In contrast, TFG p.R106C mutant neurons cultured for 14 days *in vitro* exhibited no significant differences in surface L1CAM accumulation as compared to controls, suggesting only a kinetic delay in secretory cargo transport when TFG is mutated (SI Appendix, Fig. S2A). To directly test this idea, we leveraged an inducible release system in which L1CAM fused to HaloTag is initially trapped in the ER lumen, but remains capable of entering the secretory pathway following its disaggregation, which is mediated by an inert rapamycin analog referred to as DDS (dimer-dimer solubilizer) (54, 55). In control primary rat cortical neurons, released L1CAM concentrated quickly within the peri-nuclear Golgi after DDS addition (Fig. 4C). In contrast, neurons homozygous for the TFG p.R106C mutation exhibited a significant delay in L1CAM transport through the early secretory pathway (Fig. 4C).

We previously used single particle electron microscopy to demonstrate that TFG assembles into small octameric ring structures, which can further self-associate to form liquid-like condensates at the interface between ER and ERGIC membranes (14-16, 28). Additionally, we found that the p.R106C mutation within the TFG coiled coil domain disrupts its ability to form rings *in vitro*, potentially impacting its capacity to phase separate in cells (32). To examine this possibility, we conducted a series of immunofluorescence studies using primary rat cortical neurons harvested from our animal models. In control neurons, TFG was found in high-, medium-, and low-intensity structures in both cell bodies and neuronal processes (Fig. 4 D and E and SI Appendix, Fig. S2B). However, in homozygous TFG p.R106C neurons, the number of TFG-positive structures, particularly those of high intensity, was significantly decreased as compared to controls, suggesting a defect in the ability of TFG to concentrate and form condensates (Fig. 4 D and E). Importantly, the loss of TFG-positive structures was not due to diminished stability of the protein based on immunoblotting studies of control and TFG p.R106C mutant brain extracts (SI Appendix, Fig. S2C). Based on the critical role for TFG in the early secretory pathway,

these findings offer a potential explanation for the reduced kinetics of L1CAM trafficking and axon plasma membrane accumulation in neurons expressing the TFG p.R106C mutation.

TFG regulates the trafficking of Rab4A-positive endosomes in axons and dendrites

Localization studies in multiple cell types across a variety of species indicate that TFG functions in the early secretory pathway (13-17, 34, 57, 58). In neurons, the majority of protein synthesis is believed to occur within cell bodies, which are enriched with rough ER and Golgi membranes (59-61). However, we found that TFG additionally localizes to structures within axons and dendrites, with similar densities in each (Fig. 4F). To determine whether all TFG-positive structures correspond to sites of COPII transport carrier formation, we co-stained neurons with antibodies directed against TFG and Sec31A, a component of the outer COPII coat complex. For these studies, we used human stem cell-derived cortical neurons, which enables better resolution of individual neuronal processes as compared to primary cortical neuron cultures. Within cell bodies, TFG co-localized tightly with Sec31A (Fig. 5A), similar to our findings in epithelial cells (14, 15). However, within neurites, only a minority of TFG-positive structures localized together with Sec31A (Fig. 5A). These data indicate that specifically in axons and dendrites, TFG is distributed beyond the ER/ERGIC interface.

To define the localization of TFG in neurites, we first engineered human iPSCs to express a GFP fusion to the endogenous protein using CRISPR/Cas9-mediated editing. Following neuronal differentiation, we examined the relative distribution of a number of different organelle markers and found that TFG co-localized specifically with Rab4A-positive endosomes in neurites, with increasing frequency farther away from the cell body (Fig. 5 B and C). In contrast, TFG and Rab4A exhibited minimal co-localization in processes that were proximal (less than 70 μm) to cell bodies (Fig. 5 B and C).

To assess a functional role for TFG at Rab4A-positive endosomes, we first examined their distribution in control and homozygous TFG p.R106C mutant neurons derived from human iPSCs. These studies demonstrated that the number of Rab4A-positive endosomes was significantly reduced in neurites when TFG function was impaired as compared to controls (Fig. 5 D and E). Additionally, the average velocity of Rab4A-positive endosomes was decreased in homozygous TFG p.R106C primary rat cortical neurons relative to controls (Fig. 5F). Together, these data indicate that TFG localizes with Rab4A-positive endosomes to regulate their trafficking in axons and dendrites. In contrast, we failed to identify impacts to Golgi volume, mitochondrial morphology, or lysosome diameter in neurons homozygous for the TFG p.R106C mutation, arguing against the idea that the variant causes pleiotropic defects on organelle structure/function (SI Appendix, Fig. S2 D-F).

The TFG p.R106C mutation perturbs gephyrin trafficking to alter inhibitory postsynaptic currents

To gain further insights into the role of TFG in neuronal membrane trafficking, we immunoprecipitated it from rat brain extracts and used mass spectrometry to define potential interacting proteins. To our surprise, we identified gephyrin, a scaffolding protein important for clustering inhibitory postsynaptic receptors (62-64), at high sequence coverage in TFG immunoprecipitates (Fig. 6A). To confirm this association, TFG and gephyrin were expressed recombinantly in bacteria and shown to interact in pull-down studies (Fig. 6B).

Previous studies have shown that dendritic trafficking of gephyrin is mediated by endosomes containing phosphatidylinositol 3-phosphate (PI3P), a lipid that can be detected on membranes using a GFP fusion to the FYVE domain from Hrs (65, 66). Based on our work demonstrating that TFG regulates endosomal trafficking, we aimed to determine whether gephyrin uses a Rab4A-dependent pathway to accumulate at synapses. For these studies, a GFP-tagged probe for gephyrin (67) was

transiently transfected into primary rat cortical neurons that had been transduced with a mScarlet fusion to Rab4A. Imaging of their relative movements in neurites using spinning disk confocal microscopy demonstrated that gephyrin moves on Rab4A-positive endosomes prior to accumulating at synapses (Fig. 6 C and D), and consistent with previous work, we found that the majority of Rab4A-positive endosomes also harbor PI3P (SI Appendix, Fig. S3A).

To determine whether TFG dysfunction impairs gephyrin transport, we measured the concentration of gephyrin at inhibitory synapses marked by the GABA transporter VGAT (68) in control and mutant neurons using quantitative fluorescence microscopy. These studies revealed that gephyrin accumulation at these sites was significantly reduced in neurons homozygous for the TFG p.R106C variant as compared to controls (Fig. 6E). Similarly, we found significantly reduced levels of the GABAA receptor at synapses in mutant neurons as compared to control neurons (Fig. 6F).

A prediction of decreased inhibitory receptor concentration at synapses is altered neuronal electrophysiology. To explore this possibility, primary rat cortical neurons from control animals and animals homozygous for the TFG p.R106C mutation were grown in vitro and subjected to patch clamp studies (Fig. 6G). Although we failed to show detectable changes in the frequency or kinetics of spontaneous neurotransmitter release (SI Appendix, Fig. S3 B and C), we identified a significant decrease in the amplitude of spontaneous inhibitory postsynaptic currents in neurons homozygous for the TFG p.R106C mutation as compared to controls (Fig. 6 H and I). These data are consistent with TFG dysfunction resulting in diminished inhibitory receptor signaling in neurons.

3. Discussion

To define the impacts of HSP-associated variants, previous studies have typically relied upon ectopic overexpression of mutant transgenes or approaches that aim to eliminate gene products (69). While these efforts have provided glimpses into the effects of various missense mutations implicated in

disease, there are several concerns regarding their use. In particular, overexpression typically perturbs the dynamics and/or activity of proteins, leading to results that lack physiological relevance. Additionally, most mutations that cause HSP alter protein function, as opposed to abolish it (5, 69). Over the past two decades, more than 20 different mouse models harboring mutations related to those found in HSP patients have been generated, but few exhibit motor deficits analogous to phenotypes exhibited by humans (6, 70). On the occasions that ambulatory dysfunction is observed, onset typically occurs late during development, often more than a year after birth, creating challenges in defining the etiology of disease (71-73). In other cases, immortalized cell lines or patient-derived fibroblasts have been employed, but these are limited as accurate models given their derivation from diseased tissue or a lineage that has no relevance to central nervous system function (74). The most frequently used cells are also aneuploid, leading to gene misexpression and genomic instability, which is a source of variation between different isolates of the same cell line and even between cells within a clonal population. Overall, these issues have impeded progress in the field to delineate the molecular basis of phenotypes associated with HSPs.

As an alternative approach, we have leveraged the precision of CRISPR/Cas9-mediated gene editing technology to study the specific impacts of a recessive missense mutation associated with a complicated form of HSP using Sprague Dawley rats as a model system. At a fundamental level, the rat motor cortex exhibits a similar architecture to that observed in humans, subdivided into distinct regions that perform unique functions, while still exhibiting a high degree of connectivity (36). Based on our findings, the rat TFG p.R106C model recapitulates many of the pathological phenotypes associated with complicated HSPs, including progressive motor dysfunction with early onset, hind limb spasticity, thinning of the corpus callosum, and signs of axon degeneration within the corticospinal tract. This contrasts numerous mouse models, including deletion of SPG15, the second most common cause of autosomal recessive HSP with thin corpus callosum (75, 76). Specifically, SPG15 knock out mice do

not exhibit significant motor abnormalities until a year of age, nearly half the normal lifespan of C57BL/6 animals, and thinning of the corpus callosum is not observed even after 16 months (76). Similarly, mouse models harboring pathological mutations in SPG4, the most common cause of HSP, exhibit only mild gait phenotypes with late onset (77-82). Taken together, our data indicate that the TFG p.R106C rat model represents an ideal setting to explore the molecular basis of neuronal dysfunction that underlies HSP.

Previous studies in our lab have leveraged human iPSCs that were edited to express the TFG p.R106C mutation and subsequently differentiated into glutamatergic cortical neurons (32). Analysis of these neurons revealed a defect in axon fasciculation that was caused at least in part by impaired accumulation of the cell adhesion molecule L1CAM at the axonal plasma membrane. Similar to TFG, mutations in L1CAM also underlie complicated forms of HSP with early onset, and patients often present with a thin or absent corpus callosum (50, 51, 83). Using primary cortical neurons obtained from our rat TFG p.R106C model, we have now independently confirmed a defect in the normal targeting of L1CAM to the surface of axons. Furthermore, our data suggest that this likely results from a kinetic delay in L1CAM trafficking through the early secretory pathway, consistent with a role for TFG at the ER/ERGIC interface (15, 16). Based on recent work, such a defect would impair the innervation of CST pyramidal neurons by inhibitory chandelier cells, resulting in an imbalance between excitatory and inhibitory synaptic inputs and potentially contributing to motor dysfunction (84).

In addition, our studies have separately uncovered a role for TFG within neuronal processes that further regulates the balance between neuronal excitation and inhibition. Specifically, the TFG p.R106C mutation disrupts normal endosomal trafficking of gephyrin to synapses, thereby impairing inhibitory GABAergic signaling (64). However, gephyrin and L1CAM are unlikely to be the sole cargoes impacted by mutations in TFG. Instead, our data suggest that TFG regulates at least two unique and essential cargo trafficking pathways in neurons, both COPII-mediated secretory protein transport

and Rab4A-dependent endosomal sorting, which likely elevates the susceptibility of neuronal cells to mutations in TFG (Fig. 7). Consistent with this idea, patients expressing TFG variants invariably present with nervous system dysfunction, while non-neuronal phenotypes are rare, despite data demonstrating that TFG regulates secretory protein trafficking in other tissues (18, 26).

Although previous studies have raised the possibility that lysosomal dysfunction, defined by increased lysosome size and abnormal morphology, represents a unifying pathway for the pathogenesis of genetically diverse HSPs (39, 40), we failed to demonstrate consequences of the TFG p.R106C mutation on lysosome volume or distribution in primary cortical neurons obtained from homozygous mutant animals. However, further studies will be necessary to determine whether mutations in TFG affect lysosomal activity in other ways. Given the intimate relationship between endosomes and lysosomes (85), it would not be surprising if disruptions to Rab4A-mediated endosomal trafficking caused by the TFG p.R106C mutation ultimately culminates in diminished lysosome function in long-lived neurons. Alternatively, TFG may possess additional roles in endolysosomal protein trafficking that contribute to lysosome activity. Indeed, recent studies using immortalized cell lines suggest that TFG accumulates transiently with a subset of early endosomes that harbor the ESCRT-0 subunit Hrs following exposure to Wnt3a or epidermal growth factor (EGF) to regulate downstream signal transduction pathways (86, 87). The mechanisms by which TFG contributes to Wnt and EGF signaling remain unclear, and further studies will be necessary to determine whether TFG functions analogously in neuronal cells. However, based on its proposed role in the early secretory pathway, we speculate that TFG facilitates the clustering of endosomes, similar to its role in COPII carrier clustering at the ER/ERGIC interface (16). In the case of COPII-mediated transport, TFG binds directly to the inner coat component Sec23, thereby enabling carriers to be tethered to one another (15). Future work aimed at defining TFG binding partners on Hrs-positive early endosomes and Rab4A-positive recycling

endosomes will be necessary to validate this idea, which will lead to a better understanding of how TFG contributes to neuronal maintenance.

4. Materials and Methods

Generation and analysis of CRISPR/Cas9-edited Sprague Dawley rats

Studies using Sprague Dawley rats were conducted in compliance with all relevant ethical regulations for animal testing and research and were approved by the Institutional Animal Care and Use Committee of the University of Wisconsin-Madison. For CRISPR/Cas9-mediated genome editing, Sprague Dawley embryos were microinjected with a cocktail consisting of a guide RNA directed at exon 4 of TFG (5'-GTCGAGAACTGATAGAACTT-3'), a single stranded DNA repair template encoding the p.R106C mutation, and purified Cas9. Appropriately edited animals were outbred with wild-type Sprague Dawley rats (Envigo) as heterozygotes. For all studies, three males and three females of each genotype were minimally analyzed unless otherwise noted. Littermate controls were used, and data analysis was performed in a blinded manner.

For quantitative gait measurements, animals were evaluated using a MotoRater apparatus (TSE systems) equipped with a flat platform (88). Multiple anatomical points were marked prior to recording animals as they traversed the walkway (at least three times per imaging session; at least two imaging sessions were conducted for each rat). DeepLabCut was used to extract representative frames from each video, and at least 350 frames were manually annotated and used to train a convolution neural network that was capable of pose estimation tracking (44). Separate neural networks were trained for each age group analyzed. After the initial training, each network was evaluated and validated based on visual assessment, and DeepLabCut assigned pixel error. Each model was further refined until sufficient accuracy was achieved by using algorithmic identification of frames with outlier points that were corrected manually and used to re-train the model. Calculation of kinematic parameters was performed

using custom MATLAB scripts, and assessment of step cycle duration and stance/swing phases was performed using SimiMotion (Simi Reality Motion Systems GmbH, Germany).

For electromyography studies, animals were anesthetized using intraperitoneal injection of ketamine (100 mg/kg) and xylazine (10 mg/kg). A surface ground electrode was placed on the tail, a reference pin electrode was placed in the thigh, and the active recording electrode was inserted into the gastrocnemius muscle. Electrophysiological recordings (five per limb) were collected using a VikingQuest system (Natus), and spikes (following cessation of insertional activity with a peak-to-peak amplitude greater than 20 μ V) were counted.

For immunofluorescence and histological staining of tissues, animals were anesthetized using isoflurane and transcardially perfused with PBS, followed by 4% PFA prior to paraffin embedding. Five-micron coronal sections were prepared using a microtome, captured onto glass slides, deparaffinized with xylene, and rehydrated ahead of staining. For electron microscopy studies, animals were perfused with 5% glutaraldehyde, 4% paraformaldehyde, 9 mM CaCl₂, and 0.08 M sodium cacodylate (pH 7.4), followed by post-fixation, embedding, and sectioning. Ultrathin sections were post-stained to enhance contrast and imaged using a Tecnai T12 transmission electron microscope (Thermo Fisher).

Isolation and growth of primary rat cortical neurons

Embryos (embryonic day 18) were decapitated and cortices were dissected into ice cold Hibernate A that was supplemented with B27. Cortices were digested using 0.25% trypsin for 25 minutes and triturated using a pipette following inactivation by DMEM growth media containing 10% fetal bovine serum. Cells were plated onto poly-D-lysine coated coverslips or chamber slides and grown in Neurobasal-A media supplemented with B27, penicillin, streptomycin, and GlutaMax at 37°C and 5% CO₂. A fraction of the media (one-third) was changed every seven days. To introduce transgenes,

primary neurons were grown in culture for 2-9 days and either transduced with purified lentiviral particles or transfected using Lipofectamine LTX with Plus reagent.

Induced pluripotent stem cell (iPSC) cultures and differentiation

Human iPSCs (IMR90-4 obtained from WiCell) were cultured on Matrigel-coated substrates in E8 media, as described previously (89). For CRISPR/Cas9-mediated editing to generate HaloTag fusion proteins expressed from their endogenous locus, iPSCs were electroporated using a Gene Pulser Xcell System (Bio-rad) in Opti-MEM with purified Cas9, a targeted guide RNA, and a plasmid-based repair template. Single cells were isolated using fluorescence activated cell sorting (FACS), and clonal populations were subsequently screened by immunoblotting, Sanger sequencing, and fluorescence microscopy. Edited iPSCs were differentiated into cortical forebrain neurons as described previously. In brief, iPSCs were first treated with Y-27632 (10 nM) and grown in neuronal differentiation media (NDM; composed of DMEM/F12 and Neurobasal-A media (1:1), supplemented with N2, B27, and Glutamax), followed by dual SMAD inhibition. Neurospheres generated were plated onto Matrigel-coated plates to form rosettes, which were grown in NDM in the presence of SMAD inhibitors, and after 14 days, rosettes were transferred into NDM supplemented with FGF-2 (10 ng/mL) and heparin (2 μ g/mL) and grown in suspension for an additional seven days. Neuronal rosettes were then dissociated and seeded onto plates or coverslips coated with poly-L-ornithine and Matrigel in neuronal maturation media (NMM; Neurobasal-A media containing B27, Glutamax, BDNF (10 ng/mL), GDNF (10 ng/mL), 1 μ M cAMP, and 0.1 μ M compound E) to generate cortical neurons.

Fluorescence microscopy studies

For H&E- and LFB-stained tissue sections, images were acquired using a uScope HXII slide scanner. Fluorescence imaging was conducted either on a Nikon Eclipse Ti2-E spinning disk confocal microscope equipped with a Yokogawa CSU-W1 scanhead, a 60x oil immersion objective and an ORCA-Fusion BT sCMOS camera, or an ImageXpress Micro 4 High-Content Imaging System (Molecular Devices). To measure the size of anatomic brain features, structures were traced in ImageJ for analysis. For cell counting, a region of interest was drawn, and cell number was quantified using Imaris software (Oxford Instruments).

Immunofluorescence studies of dissociated primary rat cortical neurons and iPSC-derived neurons were conducted similarly. Neuronal cells were fixed using paraformaldehyde (4%) and sucrose (4%) and blocked using 10% BSA. Permeabilization was conducted using 0.2% TritonX-100 when necessary, followed by incubation with primary antibodies overnight at 4°C. Following extensive washing, neurons were incubated with dye-labeled secondary antibodies for one hour at room temperature, followed by additional washing and mounting onto glass slides using VectaShield Antifade media prior to confocal imaging.

Live-cell imaging was conducted within a Tokai Hit Stage Top Incubation System set to 37°C and 5% CO₂. All image analysis was conducted using Imaris or ImageJ software. For HaloTag-L1CAM trafficking assays, primary cortical neurons were transfected after being grown in culture for 5-7 days (DIV5-DIV7). Following 14 days in culture, cells were dye-labeled with JFX650-HaloTag ligand and treated with DDS prior to fixation at various timepoints after cargo release.

Whole-cell voltage-clamp recordings

After dissection, cortices were treated with trypsin for 30 minutes at 37 °C, triturated in DMEM containing 10% FBS, and plated onto 18 mm poly-D-lysine-coated coverslips (1/3 cortex per 12-well plate). The media was changed to Neurobasal-A supplemented with B27 and Glutamax, and no further

media changes were performed after the day of plating. Recordings were performed at room temperature on neurons grown for 14-19 days in a bath containing 128 mM NaCl, 2.5 mM KCl, 2 mM CaCl₂, 1 mM MgCl₂, 25 mM HEPES, 30 mM glucose (~310 mOsm/L, pH 7.4). For all recordings, the bath contained 50 μM APV and 20 μM CNQX; for mIPSC recordings, 1 μM TTX was also added. Pipettes were pulled from borosilicate glass and filled with a solution containing 130 mM KCl, 10 mM HEPES-NaOH, 1 mM EGTA, 2 mM MgATP, 0.3 mM NaGTP, 6 mM Na-phosphocreatine (~290 mOsm/L, pH 7.3). Recordings were conducted on an inverted microscope using a HEKA EPC 10 combined amplifier and DAQ with digitization at 10 KHz after filtering at 5 kHz. The holding potential was -70 mV and no liquid junction potential correction was applied. For mIPSC analysis, 60 seconds of data were analyzed per cell, and a sliding template was applied in Axograph with the following parameters: $t(\text{rise}) = 1 \text{ ms}$, $t(\text{decay}) = 25 \text{ ms}$, detection threshold set at 3.5-fold the standard deviation of the baseline signal. Plotting and statistical analysis were performed using Prism (GraphPad). All data collection and analyses of raw data were performed by an experimenter blinded to the genotype of the samples.

Biochemical interaction studies

Either GST or GST-gephyrin was co-expressed with His-SUMO-TFG in BL21(DE3) cells and purified onto glutathione agarose resin as described previously (15). The resin was washed extensively and resuspended in an elution buffer containing SDS. Samples were resolved via SDS-PAGE, followed by Coomassie staining or immunoblotting.

For immunoprecipitation from rodent brain extracts, antibodies directed against IgG or TFG were covalently linked to Protein A agarose and incubated with lysates generated by homogenizing brain tissue harvested from adult Sprague Dawley rats. Following extensive washing, bound proteins were eluted under low pH conditions and separated by SDS-PAGE. Coomassie stained proteins identified in TFG immunoprecipitates were excised from gels, digested, and subjected to mass

spectrometry analysis. Equivalent gel regions were taken from IgG immunoprecipitates and similarly subjected to mass spectrometry analysis as controls.

Statistical Methods

All p values were determined by paired t test or ANOVA (followed by a Tukey post hoc test), calculated using Microsoft Excel or GraphPad Prism, and all data are shown as mean +/- SEM, unless otherwise indicated. Significant differences were indicated by a p value less than 0.05.

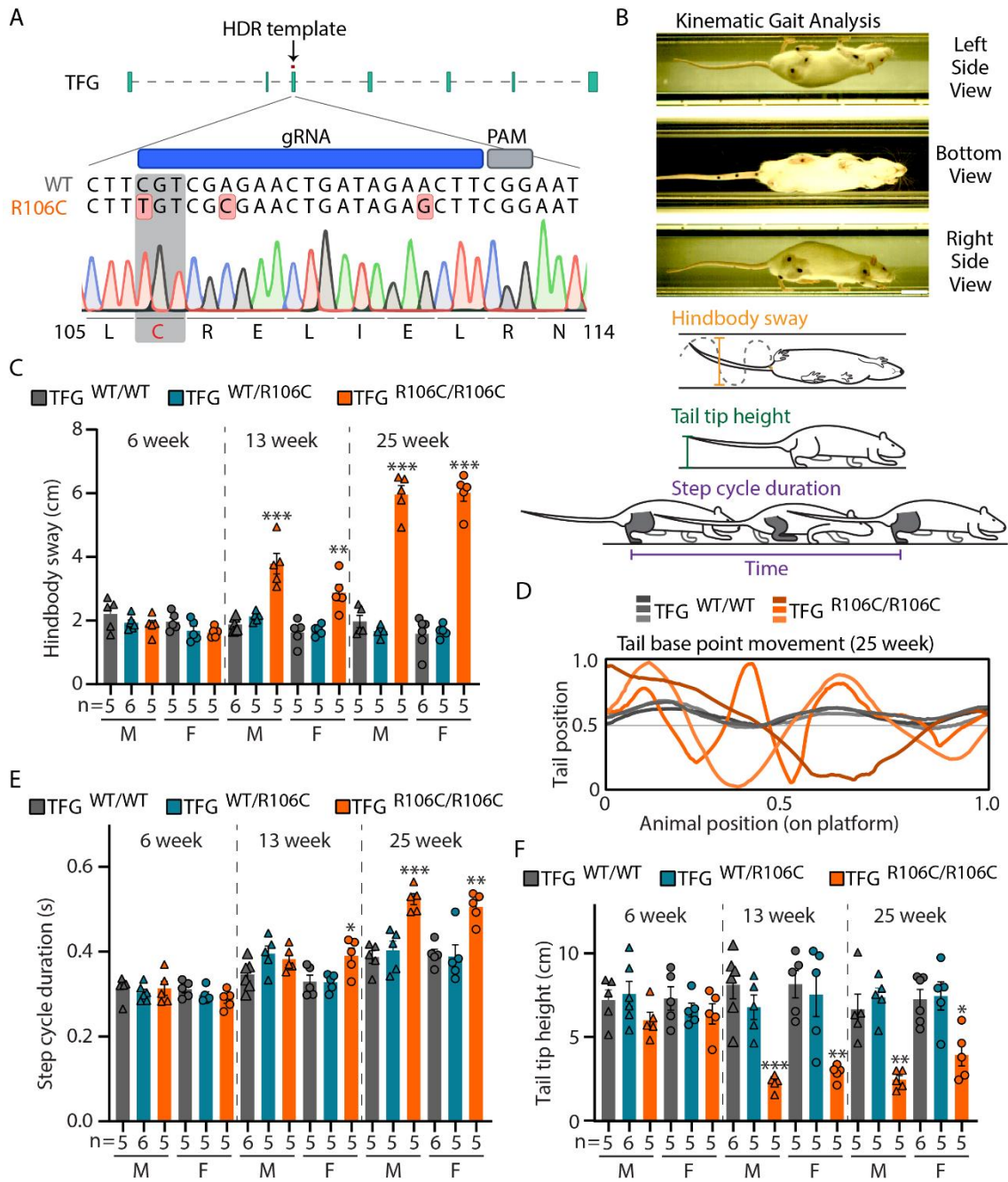


Figure 1. Homozygous TFG p.R106C mutant animals exhibit progressive motor deficits. (A) Schematic illustrating the editing approach used to incorporate the TFG p.R106C mutation into the genome of Sprague Dawley rats is shown (top), as well as a chromatogram obtained following Sanger sequencing of a homozygous mutant animal. (B) Representative image of a marked animal traversing the MotoRater platform (top). Schematics illustrate the manner by which hind body sway, tail tip height, and step cycle duration are quantified (bottom). (C, E, F) Measurements of hind body sway (C), step cycle duration (E), and tail tip height (F) of control, heterozygous TFG p.R106C, and homozygous TFG p.R106C mutant animals at different ages indicated (n, number of animals assayed; M, male; F, female). Error bars represent mean \pm SEM. ** $p < 0.01$ and *** $p < 0.001$, as calculated using an ANOVA test. (D) Representative traces of the tail base point of 25-week old animals (control and homozygous TFG p.R106C) as animals traverse the platform.

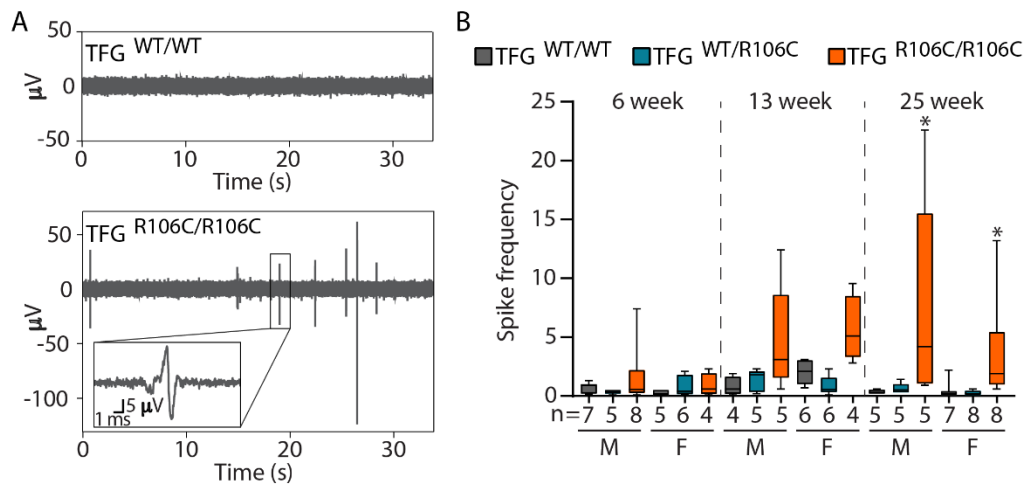


Figure 2. Homozygous TFG p.R106C mutant animals exhibit spontaneous electrical activity in hind limb skeletal muscles. (A) Representative electromyograms recorded from 25-week old male animals (control and homozygous TFG p.R106C). (B) Quantification of the average number of spikes greater than 20 μV over a 40-second recording period in control, heterozygous TFG p.R106C, and homozygous TFG p.R106C mutant animals (n, number of animals assayed; M, male; F, female). Box and whisker plots show data in the 10th-90th percentile. * $p < 0.05$ as calculated by a Dunn's multiple comparison test, following a Kruskal-Wallis test.

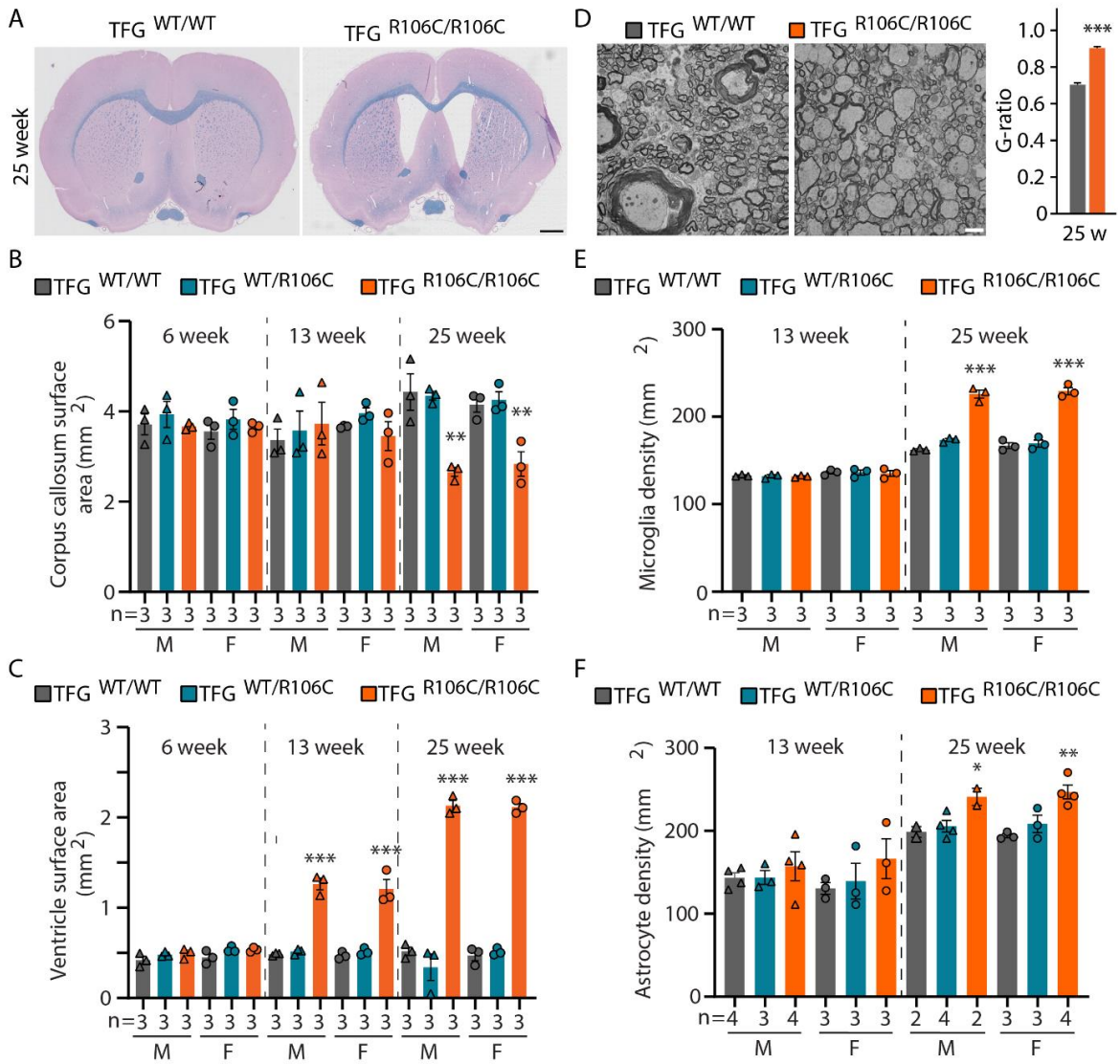


Figure 3. Homozygous TFG p.R106C mutant animals exhibit progressive central nervous system pathology that is consistent with HSP. (A) Representative images of coronal brain sections from 25-week old animals (control and homozygous TFG p.R106C) stained with LFB. Scale bar, 1 mm. (B, C, E, and F) Quantification of the surface area of the corpus callosum (B), the surface area of the ventricles based on H&E staining (C), microglia density based on the presence of Iba1-positive cells in the primary motor cortex (E), and astrocyte density based on the presence of S100beta-positive cells in the primary motor cortex in control, heterozygous TFG p.R106C, and homozygous TFG p.R106C mutant animals (n, number of animals assayed; M, male; F, female). Error bars represent mean +/- SEM. * $p < 0.05$, ** $p < 0.01$, and *** $p < 0.001$, as calculated using an ANOVA test. (D) Representative electron micrographs of the corticospinal tract (lumbar region of the spinal cord) from 25-week old animals (left; control and homozygous TFG p.R106C). Scale bar, 2 μm . Quantification of myelin sheath thickness based on the G-ratio is also shown (right). Error bars represent mean +/- SEM. *** $p < 0.001$, as calculated using an unpaired t test.

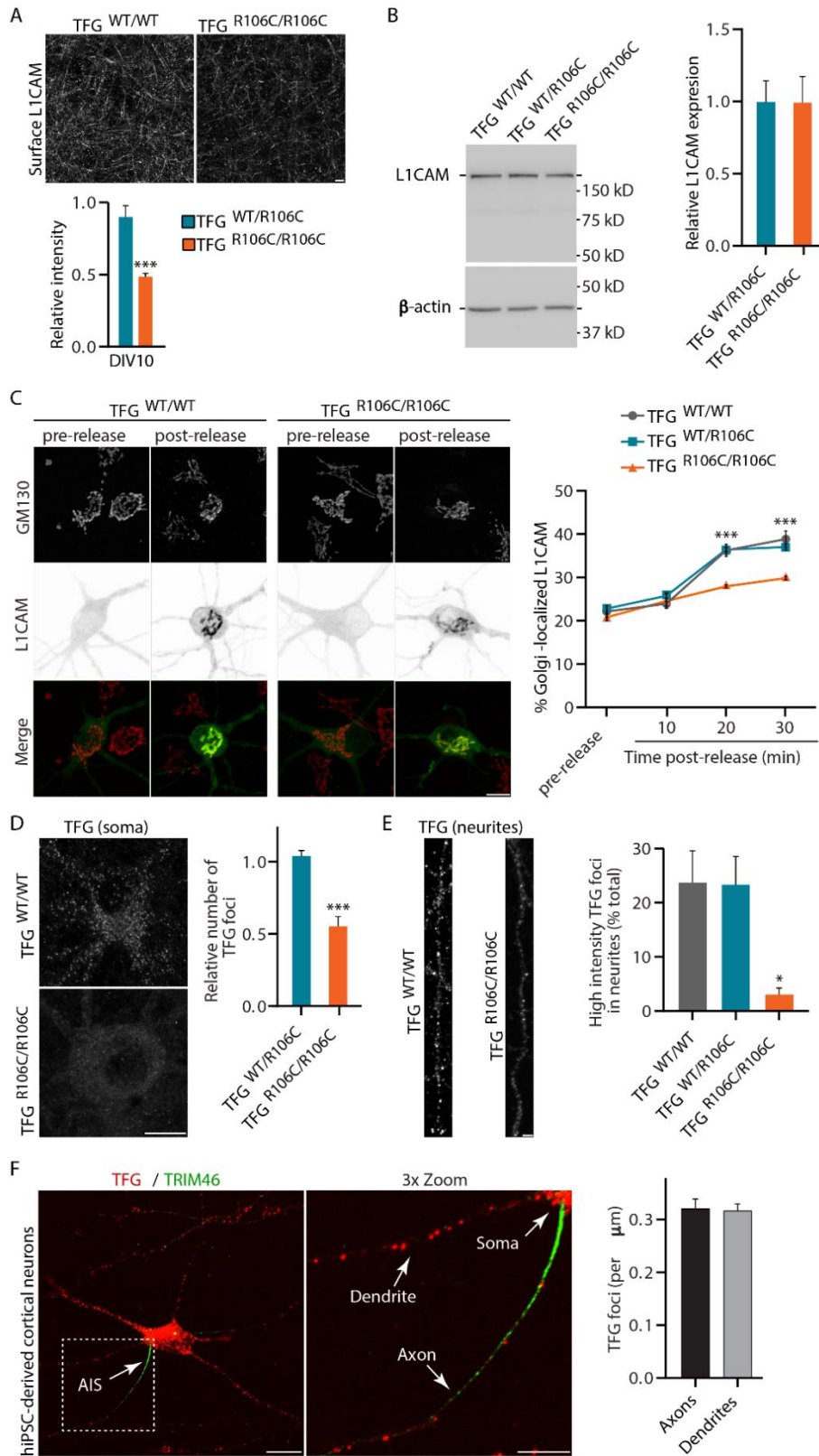


Figure 4. The TFG p.R106C mutation reduces the kinetics of secretory protein transport.

(A) Representative images of primary rat cortical neurons from control and homozygous TFG p.R106C mutant animals grown in vitro for 10 days and stained using antibodies accessible only to cell surface L1CAM (top). Scale bar, 10 μ m. Quantification of the relative levels of surface L1CAM intensity as determined for neurons grown in vitro for 10 days that are heterozygous or homozygous for the TFG p.R106C mutation as compared to control neurons (three biological replicates each). Error bars represent mean \pm SEM. *** $p < 0.001$, as calculated using an ANOVA test. (B) Representative immunoblot analysis of control, heterozygous TFG p.R106C, and homozygous TFG p.R106C mutant neurons grown for 10 days in vitro using antibodies directed against L1CAM (top, left) and beta-actin (bottom, left). Quantification of the relative levels of L1CAM in neurons grown in vitro for 10 days that are heterozygous or homozygous for the TFG p.R106C mutation as compared to control neurons (right; four biological replicates). No statistically significant differences were found. (C) Representative images of control and homozygous TFG p.R106C neurons grown for 14 days in vitro that were transiently transfected with a releasable form of HaloTag-L1CAM following dye-labeling with the JFX650-HaloTag ligand (left). Neurons were fixed and stained using antibodies directed against GM130 before and after the addition of DDS. Scale bar, 10 μ m. Quantification of Golgi-localized HaloTag-L1CAM intensity at various time points after release from the ER in control, heterozygous TFG p.R106C, and homozygous TFG p.R106C mutant neurons (right; three biological replicates each). Error bars represent mean \pm SEM. *** $p < 0.001$, as calculated using an ANOVA test. (D and E) Representative images of control and homozygous TFG p.R106C mutant neurons grown 14 days in vitro and immunostained using antibodies directed against TFG (left). Scale bars, 10 μ m (D) and 2 μ m (E). Quantification showing the relative number of high-intensity TFG structures in heterozygous and homozygous TFG p.R106C mutant neurons grown in vitro for 7 days as compared to control neurons in the soma (D, right) and in neurites (E, right; at least 30 μ m of neurite length examined per sample),

where values are shown as a percentage of the total number of TFG structures analyzed (right; three biological replicates each) is also presented. Error bars represent mean \pm SEM. *** $p < 0.001$ and * $p < 0.05$, as calculated using an ANOVA test. (F) Representative images of control iPSC-derived neurons immunostained using antibodies directed against TFG (red; left) and TRIM46 (green; left). Scale bars, 10 μm and 5 μm (zoomed panel). Quantification of the number of TFG structures present in axons and dendrites is also shown (right; three biological replicates each). Error bars represent mean \pm SEM. No statistically significant differences were identified.

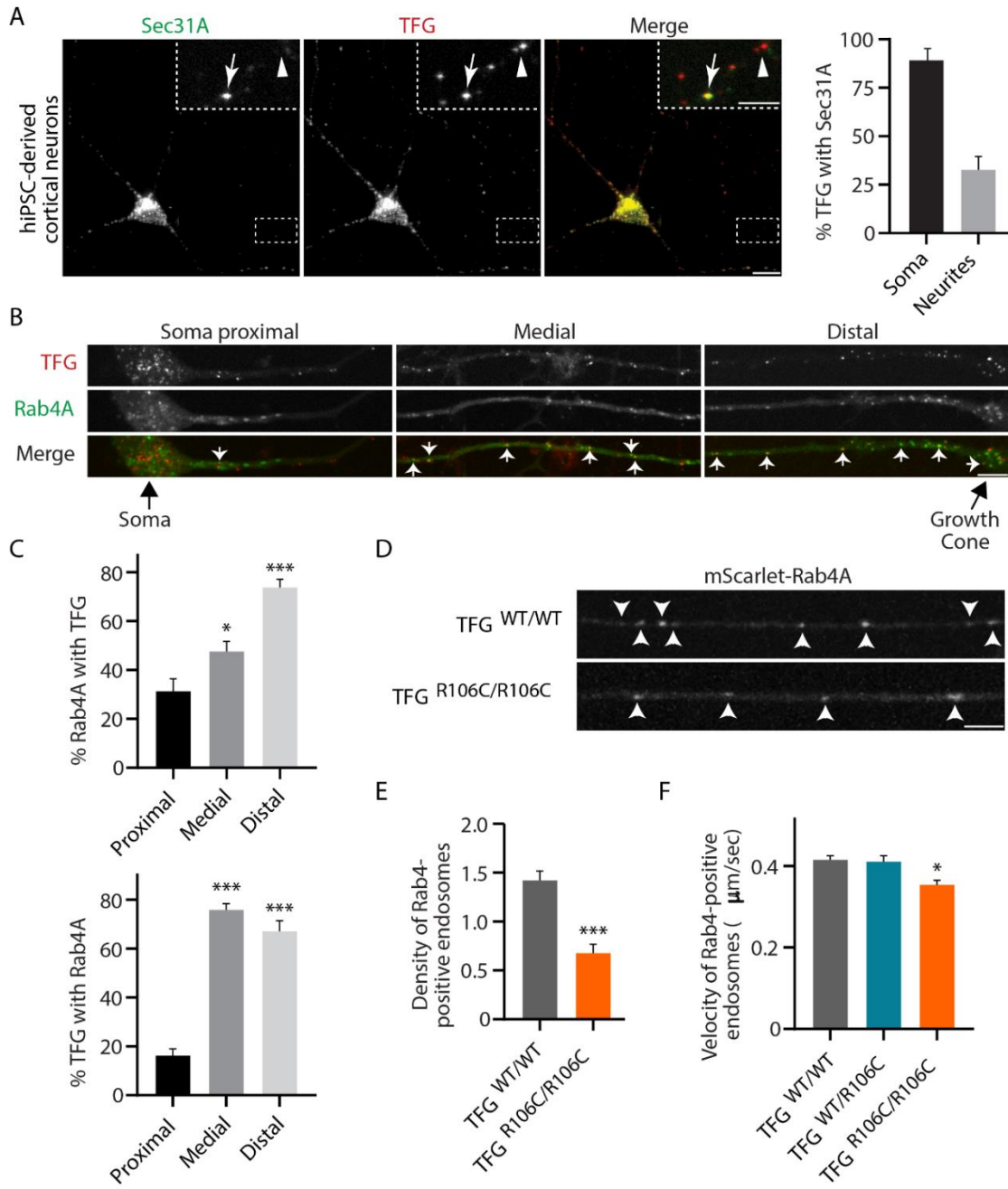


Figure 5. TFG regulates the dynamics of Rab4A-positive endosomes. (A) Representative images of control iPSC-derived neurons immunostained using antibodies directed against Sec31A (green; left) and TFG (red; left). Scale bar, 10 μm . Quantification of the percentage of TFG that co-localizes with Sec31A in the soma and in neuronal processes is also shown (right; three biological replicates with more than 3500 structures analyzed). Error bars represent mean \pm SEM. (B) Representative images of control iPSC-derived neurons expressing a GFP fusion to TFG (red) from its endogenous locus and mScarlet-Rab4A (green) transduced following lentiviral infection in different locations along neurites (soma proximal, within 70 μm of the soma; medial, > 100 μm from the soma and > 150 μm from the growth cone; distal, within 150 μm of the growth cone). Arrows highlight sites of co-localization. Scale bar, 10 μm . (C) Quantification of the percentage of Rab4A that co-localizes with TFG (top) and the percentage of TFG that co-localizes with Rab4A (bottom) in different regions of neuronal processes is shown (three biological replicates). Error bars represent mean \pm SEM. *** $p < 0.001$ and * $p < 0.05$, as calculated using an ANOVA test. (D) Representative images of control and homozygous TFG p.R106C mutant iPSC-derived neurons transduced with lentivirus to express mScarlet-Rab4A. Arrows highlight Rab4A-positive structures. Scale bar, 10 μm . (E and F) Quantification of the density (E) and velocity (F) of Rab4A-positive structures in control and TFG p.R106C mutant neurons (three biological replicates each). Error bars represent mean \pm SEM. *** $p < 0.001$ and * $p < 0.05$, as calculated using an ANOVA test.

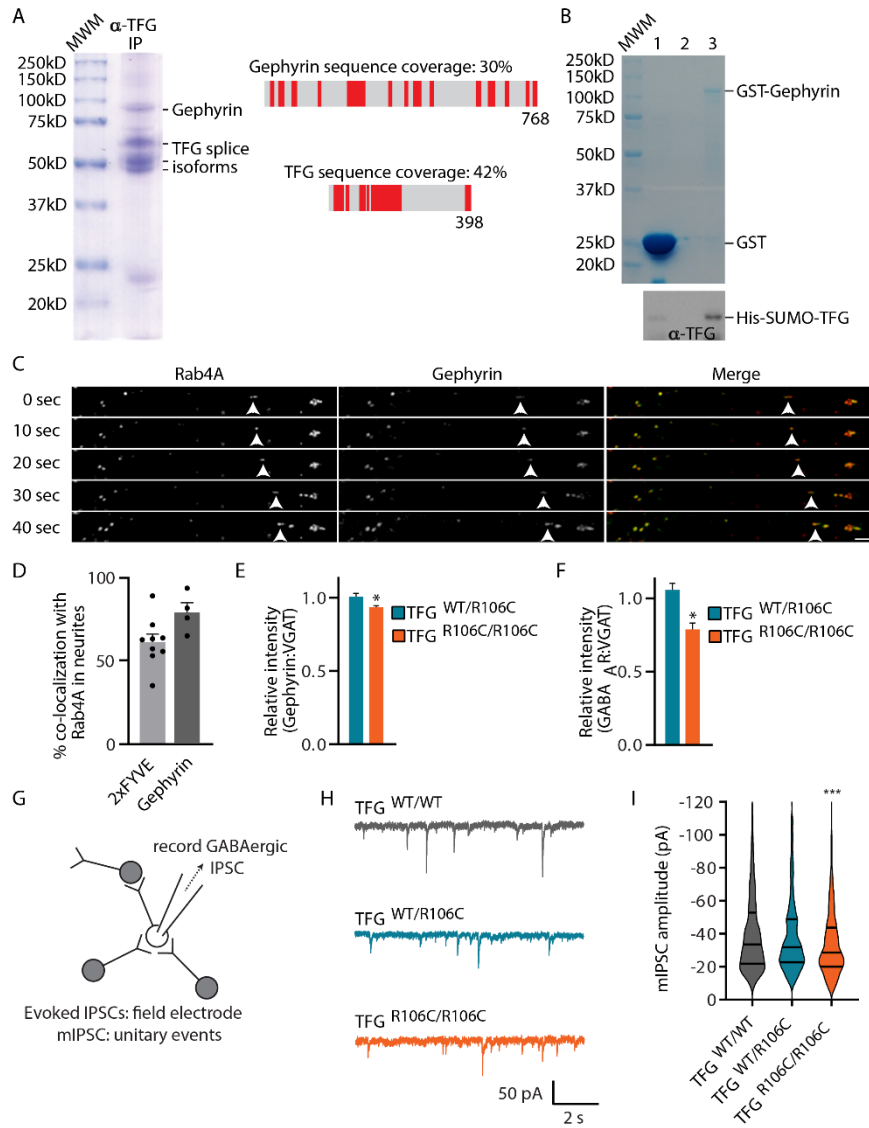


Figure 6. TFG regulates the endosomal trafficking of gephyrin in neurons. (A) Representative Coomassie-stained SDS-PAGE gel showing proteins recovered and identified using mass spectrometry following TFG immunoprecipitation from rat brain extracts is shown (left; three biological replicates performed). The distribution of peptides identified by mass spectrometry, together with the percentage sequence coverage for gephyrin and TFG, is also shown (red; right). (B) Representative images of a Coomassie-stained gel (top) and immunoblot (bottom) are shown following a GST pull-down experiment from extracts co-expressing His-SUMO-TFG and either GST or a GST fusion to gephyrin (three biological replicates performed). (C) Representative images of control primary cortical rat neurons grown in culture for 14 days, co-expressing a mScarlet fusion to Rab4A (red; transduced following lentiviral infection) and probe for gephyrin fused to GFP (green; following transfection). Arrowheads highlight sites where Rab4A and gephyrin are transported together within neurites. Scale bar, 10 μ m. (D) Quantification of the percentage of Rab4A that co-localizes with a probe for PI3P (2xFYVE) and gephyrin in different regions of neuronal processes is shown (three biological replicates; neurons grown 14 days in vitro). Error bars represent mean \pm SEM. (E and F) Quantification of the relative intensities of gephyrin (E) and the GABA_A receptor (F) that were directly juxtaposed to VGAT staining in control and TFG p.R106C mutant primary rat cortical neurons grown in culture for 21 days (three biological replicates each). Error bars represent mean \pm SEM. * $p < 0.05$, as calculated using an ANOVA test. (G) Schematic showing whole-cell patch-clamp measurement of GABAergic currents in culture cortical neurons. (H) Representative traces of mIPSC recordings obtained from control, heterozygous TFG p.R106C, and homozygous TFG p.R106C mutant neurons. (I) Violin plot of mIPSCs recorded from control, heterozygous TFG p.R106C, and homozygous TFG p.R106C mutant neurons (700-1100 events per genotype). Horizontal black bars demarcate quartiles. The plot was truncated at -120 pA for clarity of display. ***, $p < 0.001$, as calculated using a Kruskal-Wallis test.

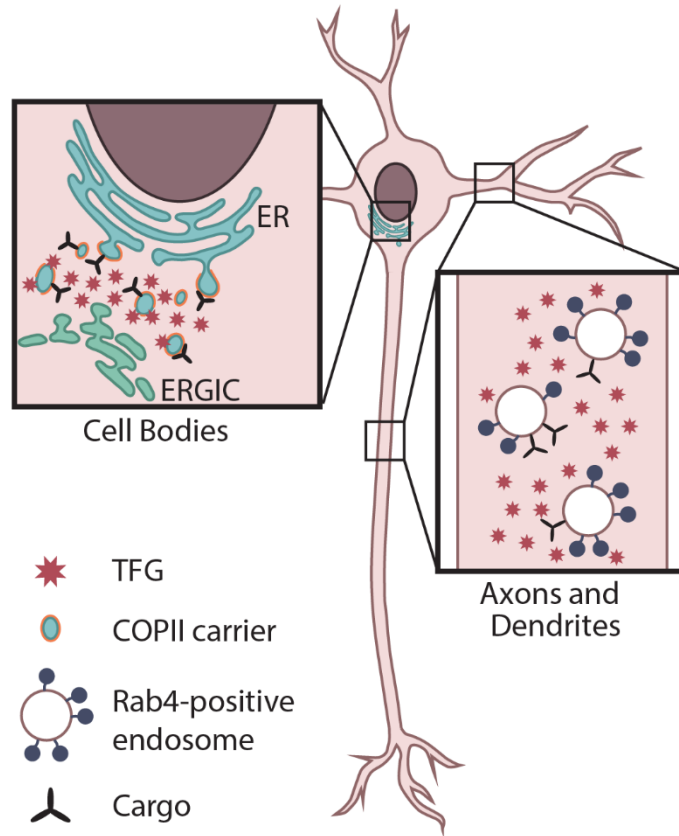


Figure 7. Model for TFG function in neurons. TFG distributed throughout neurons functions distinctly in the soma (regulation of cargo transport from the ER to the ERGIC via COPII-coated transport carriers) as compared to axons and dendrites (regulates transport of Rab4A-positive recycling endosomes).

References

1. R. Olivares-Moreno, P. Rodriguez-Moreno, V. Lopez-Virgen, M. Macías, M. Altamira-Camacho, G. Rojas-Piloni, Corticospinal vs rubrospinal revisited: an evolutionary perspective for sensorimotor integration. *Front Neurosci.* **15**, 686481 (2021).
2. Q. Welniarz, I. Dusart, E. Roze, The corticospinal tract: evolution, development, and human disorders. *Dev. Neurobiol.* **77**, 810-829 (2017).
3. R. Chaudhary, V. Agarwal, M. Rehman, A. S. Kaushik, V. Mishra, Genetic architecture of motor neuron diseases. *J. Neurol. Sci.* **434**, 120099 (2022).
4. S. Sangari, M. A. Perez, Imbalanced Corticospinal and Reticulospinal Contributions to Spasticity in Humans with Spinal Cord Injury. *J. Neurosci.* **39**, 7872-7881 (2019).
5. C. Blackstone, Converging cellular themes for the hereditary spastic paraplegias. *Curr. Opin. Neurobiol.* **51**, 139-146 (2018).
6. L. E. O. Elsayed, I. Z. Eltazi, A. E. Ahmed, G. Stevanin, Insights into clinical, genetic, and pathological aspects of hereditary spastic paraplegias: a comprehensive overview. *Front. Mol. Biosci.* **8**, 690899 (2021).
7. C. Beetz, et al., Inhibition of TFG function causes hereditary axon degeneration by impairing endoplasmic reticulum structure. *Proc. Natl. Acad. Sci. USA* **110**, 5091–5096 (2013).
8. L. E. O. Elsayed, et al., Hereditary spastic paraplegias: identification of a novel SPG57 variant affecting TFG oligomerization and description of HSP subtypes in Sudan. *Eur. J. Hum. Genet.* **25**, 100-110 (2016).
9. M. Khorrami, M. A. Tabatabaiefar, E. Khorram, O. Yaghini, M. Rezaei, A. Hejazifar, M. Riahinezhad, M. Kheirollahi, Homozygous TFG gene variants expanding the mutational and clinical spectrum of hereditary spastic paraplegia 57 and a review of literature. *J. Hum. Genet.* **66**, 973-981 (2021).

10. T. Miyabayashi, et al., A novel homozygous mutation of the TFG gene in a patient with early onset spastic paraplegia and later onset sensorimotor polyneuropathy. *J. Hum. Genet.* **64**, 171-176 (2019).
11. G. V. Harlalka, et al., Novel Genetic, Clinical, and Pathomechanistic Insights into TFG-Associated Hereditary Spastic Paraplegia. *Hum. Mutat.* **37**, 1157-1161 (2016).
12. A. Greco, et al., The DNA rearrangement that generates the TRK-T3 oncogene involves a novel gene on chromosome 3 whose product has a potential coiled-coil domain. *Mol. Cell. Biol.* **15**, 6118-6127 (1995).
13. K. Witte, et al., TFG-1 function in protein secretion and oncogenesis. *Nat. Cell Biol.* **13**, 550-558 (2011).
14. A. Johnson, et al., TFG clusters COPII-coated transport carriers and promotes early secretory pathway organization. *EMBO J.* **12**, 811-827 (2015).
15. M. G. Hanna, et al., TFG facilitates outer coat disassembly on COPII transport carriers to promote tethering and fusion with ER–Golgi intermediate compartments. *Proc. Natl. Acad. Sci. USA* **114**, E7707-E7716 (2017).
16. J. Peotter, W. Kasberg, I. Pustova, A. Audhya, COPII-mediated trafficking at the ER/ERGIC interface. *Traffic* **20**, 491-503 (2019).
17. J. McCaughey, et al., TFG Promotes Organization of Transitional ER and Efficient Collagen Secretion. *Cell Rep.* **15**, 1648-1659 (2016).
18. T. Yamamotoya, et al., Trk-fused gene (TFG) regulates pancreatic β cell mass and insulin secretory activity. *Sci. Rep.* **7**, 13026 (2017).
19. M. Levi-Ferber, Y. Salzberg, M. Safra, A. Haviv-Chesner, H. E. Bülow, S. Henis-Korenblit, It's all in your mind: determining germ cell fate by neuronal IRE-1 in *C. elegans*. *PLoS Genet.* **10**, e1004747 (2014).

20. D. Yoo, W. Lee, S. Lee, J. Sung, G. S. Jeon, A Novel TFG Mutation in a Korean Family with α -Synucleinopathy and Amyotrophic Lateral Sclerosis. *Mov. Disord.* **37**, 384-391 (2022).
21. T. Kawarai, et al., Pathomechanisms of motor neuron death by mutant TFG. *Rinsho Shinkeigaku* **23**, 1199 (2013).
22. H. Ishiura, et al., The TRK-fused gene is mutated in hereditary motor and sensory neuropathy with proximal dominant involvement. *Am. J. Hum. Genet.* **91**, 320-329. (2012).
23. S. S. Lee, et al., Proximal dominant hereditary motor and sensory neuropathy with proximal dominance association with mutation in the TRK-fused gene. *JAMA Neurol.* **70**, 607-615 (2013).
24. P. C. Tsai, et al., A novel TFG mutation causes Charcot-Marie-Tooth disease type 2 and impairs TFG function. *Neurology* **83**, 903-912 (2014).
25. H. Maebayashi, et al., Expression and Localization of TRK-Fused Gene Products in the Rat Brain and Retina. *Acta. Histochem. Cytochem.* **45**, 15-23 (2012).
26. T. Yagi, D. Ito, N. Suzuki, TFG-Related Neurologic Disorders: New Insights Into Relationships Between Endoplasmic Reticulum and Neurodegeneration. *J. Neuropathol. Exp. Neurol.* **75**, 299-305 (2016).
27. K. Maeda, R. Idehara, K. I. Mukaisho, Presence of colocalised phosphorylated TDP-43 and TFG proteins in the frontotemporal lobes of HMSN-P. *J. Neurol. Neurosurg. Psychiatry* **91**, 1231-1232 (2020).
28. G. M. Rosenberg, K. A. Murray, L. Salwinski, M. P. Hughes, R. Abskharon, D. S. Eisenberg, Bioinformatic identification of previously unrecognized amyloidogenic proteins. *J. Biol. Chem.* **298**, 101920 (2022).
29. N. Murakami, et al., Proteasome impairment in neural cells derived from HMSN-P patient iPSCs. *Mol. Brain* **10**, 7 (2017).

30. S. Yamashita, et al., Muscle pathology of hereditary motor and sensory neuropathy with proximal dominant involvement with TFG mutation. *Muscle Nerve* **60**, 739-744 (2019).
31. J. Li, L. Meng, R. Wu, Z. Xie, Q. Gang, W. Zhang, Z. Wang, Y. Yuan, Sural nerve pathology in TFG-associated motor neuron disease with sensory neuropathy. *Neuropathology* **39**, 194-199 (2019).
32. E. L. Slosarek et al., Pathogenic TFG Mutations Underlying Hereditary Spastic Paraplegia Impair Secretory Protein Trafficking and Axon Fasciculation. *Cell Rep.* **24**, 2248-2260 (2018).
33. A. Catania, et al., R106C TFG variant causes infantile neuroaxonal dystrophy "plus" syndrome. *Neurogenetics* **19**, 179-187 (2018).
34. M. Carinci, et al., TFG binds LC3C to regulate ULK1 localization and autophagosome formation. *EMBO J.* **40**, e103563 (2021).
35. T. Yagi, D. Ito, N. Suzuki, Evidence of TRK-Fused Gene (TFG1) function in the ubiquitin-proteasome system. *Neurobiol. Dis.* **66**, 83-91 (2014).
36. B. Ellenbroek, J. Youn, Rodent models in neuroscience research: is it a rat race? *Dis. Model Mech.* **9**, 1079-1087 (2016).
37. A. L. Towe, Relative Numbers of Pyramidal Tract Neurons in Mammals of Different Sizes. *Brain Behav. Evol.* **7**, 1-17 (1973).
38. J. K. Fink, Hereditary spastic paraplegia: clinico-pathologic features and emerging molecular mechanisms. *Acta Neuropathol.* **126**, 307-328 (2013).
39. R. Allison, et al., Defects in ER-endosome contacts impact lysosome function in hereditary spastic paraplegia. *J. Cell Biol.* **216**, 1337-1355 (2017).
40. D. Edmison, L. Wang, S. Gowrishankar, Lysosome Function and Dysfunction in Hereditary Spastic Paraplegias. *Brain Sci.* **11**, 152 (2021).

41. H. Tariq, S. Naz, TFG associated hereditary spastic paraplegia: an addition to the phenotypic spectrum. *Neurogenetics* **18**, 105-109 (2017).
42. A. Alavi, et al., HMSN-P caused by p.Pro285Leu mutation in TFG is not confined to patients with Far East ancestry. *Neurobiol. Aging* **36**, 1606.e1-1606.e7 (2015).
43. T. Fullam, J. Statland, Upper motor neuron disorders: Primary lateral sclerosis, upper motor neuron dominant amyotrophic lateral sclerosis, and hereditary spastic paraplegia. *Brain Sci.* **11**, 611 (2021).
44. A. Mathis, et al., DeepLabCut: markerless pose estimation of user-defined body parts with deep learning. *Nat. Neurosci.* **21**, 1281-1289 (2018).
45. D. F. Preisig, et al., High-speed video gait analysis reveals early and characteristic locomotor phenotypes in mouse models of neurodegenerative movement disorders. *Behav. Brain Res.* **311**, 340-353 (2016).
46. G. Sheean, J. R. McGuire, Spastic Hypertonia and Movement Disorders: Pathophysiology, Clinical Presentation, and Quantification. *PM R.* **1**, 827-833 (2009).
47. K. R. Servelhere, et al., Brain Damage and Gene Expression Across Hereditary Spastic Paraplegia Subtypes. *Mov. Disord.* **36**, 1644-1653 (2021).
48. E. Kara, et al., Genetic and phenotypic characterization of complex hereditary spastic paraplegia. *Brain* **139**, 1904-1918 (2016).
49. F. F. da Graça, T. J. R. de Rezende, L. F. R. Vasconcellos, J. L. Pedroso, O. G. P. Barsottini, M. C. França, Neuroimaging in Hereditary Spastic Paraplegias: Current Use and Future Perspectives. *Front. Neurol.* **9**, 1117 (2019).
50. L. Vits, et al., MASA syndrome is due to mutations in the neural cell adhesion gene L1CAM. *Nat. Genet.* **7**, 498-413 (1994).

51. M. Jouet, et al., X-linked spastic paraplegia (SPG1), MASA syndrome and X-linked hydrocephalus result from mutations in the L1 gene. *Nat. Genet.* **7**, 402-407 (1994).
52. C. K. Glass, K. Saijo, B. Winner, M. C. Marchetto, F. H. Gage, Mechanisms Underlying Inflammation in neurodegeneration. *Cell* **140**, 918-934 (2010).
53. H. S. Kwon, S. H. Koh, Neuroinflammation in neurodegenerative disorders: the roles of microglia and astrocytes. *Transl. Neurodegener.* **9**, 1-12 (2020).
54. V. M. Rivera, et al., Regulation of protein secretion through controlled aggregation in the endoplasmic reticulum. *Science* **287**, 826–830 (2000).
55. A. B. Bowen, A. M. Bourke, B. G. Hiester, C. Hanus, M. J. Kennedy, Golgi-independent secretory trafficking through recycling endosomes in neuronal dendrites and spines. *Elife* **6**, e27362 (2017).
56. V. M. Rivera, et al., Regulation of protein secretion through controlled aggregation in the endoplasmic reticulum. *Science* **287**, 826-830 (2000).
57. T. Kanadome, H. Shibata, K. Kuwata, T. Takahara, M. Maki, The calcium-binding protein ALG-2 promotes endoplasmic reticulum exit site localization and polymerization of Trk-fused gene (TFG) protein. *FEBS J.* **284**, 56-76 (2017).
58. M. G. Hanna, J. L. Peotter, E. B. Frankel, A. Audhya, Membrane Transport at an Organelle Interface in the Early Secretory Pathway: Take Your Coat Off and Stay a While: Evolution of the metazoan early secretory pathway. *Bioessays* **40**, e1800004 (2018).
59. S. L. Palay, G. E. Palade, The fine structure of neurons. *J. Biophys. Biochem. Cytol.* **1**, 69-88 (1955).
60. P. M. Novikoff, A. B. Novikoff, N. Quintana, J. J. Hauw, Golgi apparatus, GERL, and lysosomes of neurons in rat dorsal root ganglia, studied by thick section and thin section cytochemistry. *J. Cell Biol.* **50**, 859-886 (1971).

61. C. E. Holt, E. M. Schuman, The central dogma decentralized: new perspectives on RNA function and local translation in neurons, *Neuron* **80**, 648-57 (2013).
62. A. M. Craig, G. Banker, W. Chang, M. E. McGrath, A. S. Serpinskaya, Clustering of gephyrin at GABAergic but not glutamatergic synapses in cultured rat hippocampal neurons. *J. Neurosci.* **16**, 3166-3177 (1996).
63. S. K. Tyagarajan, J. M. Fritschy, Gephyrin: a master regulator of neuronal function? *Nat. Rev. Neurosci.* **15**, 141-156 (2014).
64. R. Pizzarelli, et al., Tuning GABAergic inhibition: gephyrin molecular organization and functions. *Neuroscience* **439**, 125-136 (2020).
65. D. J. Gillooly, C. Raiborg, H. Stenmark, Phosphatidylinositol 3-phosphate is found in microdomains of early endosomes. *Histochem. Cell Biol.* **120**, 445-53 (2003).
66. T. Papadopoulos, et al., Endosomal phosphatidylinositol 3-phosphate promotes gephyrin clustering and GABAergic neurotransmission at inhibitory postsynapses. *J. Biol. Chem.* **292**, 1160-1177 (2017).
67. G. G. Gross, Recombinant probes for visualizing endogenous synaptic proteins in living neurons. *Neuron* **78**, 971-985 (2013).
68. F. A. Chaudhry, R. J. Reimer, E. E. Bellocchio, N. C. Danbolt, K. K. Osen, R. H. Edwards, J. Storm-Mathisen, The vesicular GABA transporter, VGAT, localizes to synaptic vesicles in sets of glycinergic as well as GABAergic neurons. *J. Neurosci.* **18**, 9733-9750 (1998).
69. C. Blackstone, Cellular pathways of hereditary spastic paraplegia. *Annu. Rev. Neurosci.* **35**, 25-47 (2012).
70. C. Blackstone, C. J. O’Kane, E. Reid, Hereditary spastic paraplegias: membrane traffic and the motor pathway. *Nat. Rev. Neurosci.* **12**, 31-42 (2011).

71. C. Beetz, et al., A spastic paraplegia mouse model reveals REEP1-dependent ER shaping. *J. Clin. Invest.* **123**, 4273-4282 (2013).
72. M. Khundadze, et al., A hereditary spastic paraplegia mouse model supports a role of ZFYVE26/SPASTIZIN for the endolysosomal system. *PLoS Genet.* **9**, e1003988 (2013).
73. B. Genc, O. Gozutok, P. H. Ozdinler, Complexity of generating mouse models to study the upper motor neurons: let us shift focus from mice to neurons. *Int. J. Mol. Sci.* **20**, 3848 (2019).
74. A. Slanzi, G. Iannoto, B. Rossi, E. Zenaro, G. Constantin, *In vitro* Models of Neurodegenerative Diseases. *Front. Cell Dev. Biol.* **8**, 328 (2020).
75. C. Goizet, et al., SPG15 is the second most common cause of hereditary spastic paraplegia with thin corpus callosum. *Neurology* **73**, 1111-1119 (2009).
76. M. Khundadze, et al., A hereditary spastic paraplegia mouse model supports a role of ZFYVE26/SPASTIZIN for the endolysosomal system. *PLoS Genet.* **9**, e1003988 (2013).
77. J. W. Connell, R. Allison, E. Reid, Quantitative gait analysis using a motorized treadmill system sensitively detects motor abnormalities in mice expressing ATPase defective spastin. *PLoS One* **11**, 1-16 (2016).
78. M. S. Brill, et al., Branch-Specific Microtubule Destabilization Mediates Axon Branch Loss during Neuromuscular Synapse Elimination. *Neuron* **92**, 845-856 (2016).
79. A. Tarrade, et al., A mutation of spastin is responsible for swellings and impairment of transport in a region of axon characterized by changes in microtubule composition. *Hum. Mol. Genet.* **15**, 3544-3558 (2006).
80. A. T. Lopes, et al., Spastin depletion increases tubulin polyglutamylation and impairs kinesin-mediated neuronal transport, leading to working and associative memory deficits. *PLoS Biol.* **18**, 1-29 (2020).

81. L. Qiang, E. Piermarini, P. W. Baas, New hypothesis for the etiology of SPAST-based hereditary spastic paraplegia. *Cytoskeleton* **76**, 289-297 (2019).
82. L. Qiang, et al., Hereditary spastic paraplegia: gain-of-function mechanisms revealed by new transgenic mouse. *Hum. Mol. Genet.* **28**, 1136-1152 (2019).
83. S. Weller, J. Gärtner, Genetic and clinical aspects of X-linked hydrocephalus (L1 disease): mutations in the L1CAM gene. *Hum. Mutat.* **18**, 1-12 (2001).
84. Y. Tai, N. B. Gallo, M. Wang, J. R. Yu, L. van Aelst, Axo-axonic Innervation of Neocortical Pyramidal Neurons by GABAergic Chandelier Cells Requires AnkyrinG-Associated L1CAM. *Neuron* **102**, 358-372.e9 (2019).
85. Y. B. Hu, E. B. Dammer, R. J. Ren, G. Wang, The endosomal-lysosomal system: from acidification and cargo sorting to neurodegeneration. *Transl. Neurodegener.* **4**, 18 (2015).
86. G. Colozza, Y. Jami-Alahmadi, A. Dsouza, N. Tejada-Muñoz, L. V. Albrecht, E. A. Sosa, J. A. Wohlschlegel, E. M. De Robertis, Wnt-inducible Lrp6-APEX2 interacting proteins identify ESCRT machinery and Trk-fused gene as components of the Wnt signaling pathway. *Sci. Rep.* **10**, 21555 (2020).
87. M. Perez Verdaguier, T. Zhang, S. Surve, J. A. Paulo, C. Wallace, S. C. Watkins, S. P. Gygi, A. Sorkin, Time-resolved proximity labeling of protein networks associated with ligand-activated EGFR. *Cell Rep.* **39**, 110950 (2022).
88. B. Zörner, et al., Profiling locomotor recovery: comprehensive quantification of impairments after CNS damage in rodents. *Nat. Methods* **7**, 701-708 (2010).
89. G. Chen, et al., Chemically defined conditions for human iPSC derivation and culture. *Nat. Methods* **8**, 424-429 (2011).

Chapter 4. Acetyl-CoA flux from the cytosol to the ER regulates engagement and quality of the secretory pathway

The work presented in this chapter has been published:

Dieterich, I.A., Cui, Y., Braun, M.M., Lawton, A.J., Robinson, N.H., **Peotter, J.L.**, Yu, Q., Casler, J.C., Glick, B.S., Audhya, A., Denu, J.M., Puglielli, L. (2021) Acetyl-CoA flux from the cytosol to the ER regulates engagement and quality of the secretory pathway. *Scientific Reports*.

Abstract

N ϵ -lysine acetylation in the ER is an essential component of the quality control machinery. ER acetylation is ensured by a membrane transporter, AT-1/SLC33A1, which translocates cytosolic acetyl-CoA into the ER lumen, and two acetyltransferases, ATase1 and ATase2, which acetylate nascent polypeptides within the ER lumen. Dysfunctional AT-1, as caused by gene mutation or duplication events, results in severe disease phenotypes. Here, we used two models of AT-1 dysregulation to investigate dynamics of the secretory pathway: AT-1 sTg, a model of systemic AT-1 overexpression, and AT-1S113R/+, a model of AT-1 haploinsufficiency. The animals displayed reorganization of the ER, ERGIC, and Golgi apparatus. In particular, AT-1 sTg animals displayed a marked delay in Golgi-to-plasma membrane protein trafficking, significant alterations in Golgi-based N-glycan modification, and a marked expansion of the lysosomal network. Collectively our results indicate that AT-1 is essential to maintain proper organization and engagement of the secretory pathway.

1. Introduction

N ϵ -lysine acetylation in the Endoplasmic Reticulum (ER) has emerged as an essential component of the quality control (QC) machinery that maintains protein homeostasis (proteostasis) within the ER¹⁻⁶. ER acetylation requires an ER membrane transporter, AT-1/SLC33A1, which translocates acetyl-CoA from the cytosol to the ER lumen, and two ER membrane-bound acetyltransferases, ATase1/NAT8B and ATase2/NAT8, which acetylate ER cargo proteins within the lumen of the organelle^{1,3,7}. The acetylation of ER cargo nascent glycoproteins requires ATase1 and ATase2 to interact with the oligosaccharyl transferase complex (OST) and acetylate correctly folded nascent glycoproteins that are transiting across the ER membrane^{1,2}. Studies performed with type I glycoproteins suggest that successful acetylation of the nascent polypeptide is necessary for successful engagement of the secretory pathway^{2,8}. Supporting evidence comes from mouse models of increased or decreased ER acetylation⁴⁻⁶.

Loss-of-function mutations or gene duplication events in *AT-1/SLC33A1* are associated with severe disease phenotypes spanning from spastic paraplegia (heterozygous mutation) to developmental delay and premature death (homozygous mutations)⁹⁻¹¹ and intellectual disability with autistic-like traits and progeria-like dysmorphic features (gene duplication)^{12,13}. These human disorders have been effectively recapitulated in mouse models. AT-1^{S113R/S113R} mice, which lack AT-1 activity, die during embryogenesis, while AT-1^{S113R/+} mice, a model of AT-1 haploinsufficiency, develop peripheral and central neuropathy as well as propensity to infections and cancer⁴. Mice with neuronal-specific overexpression of AT-1 (AT-1 nTg) develop an autistic-like phenotype⁵ while mice with systemic overexpression (AT-1 sTg) develop a progeria-like phenotype⁶.

In this study, we investigated the outcomes of dysregulated cytosol-to-ER acetyl-CoA flux within AT-1 sTg and AT-1^{S113R/+} mice on the engagement and functional organization of the secretory pathway, as well as the overall quality of secreted glycoproteins (referred to as the secretome).

We found that AT-1 sTg animals display enlarged cisternae within the rough ER, enlarged ER Golgi Intermediate Compartment (ERGIC), and a marked delay in protein trafficking to the cell surface, while AT-1^{S113R/+} mice display contraction of the Golgi apparatus. The AT-1 sTg cellular phenotype was associated with significant alterations in Golgi-based N-glycan modification, highlighting changes in the overall quality of the secretome, together with marked expansion of the lysosomal network. Collectively our results indicate that AT-1 is essential to maintain proper organization and engagement of the secretory pathway. Our results also highlight the possibility that the Golgi apparatus harbors a check point for QC of efficient post-translational N-glycosylation, allowing glycoproteins that fail QC to be diverted to the lysosomal compartment.

2. Results

Aberrant AT-1 activity affects secretory pathway-related processes

To dissect how changes in cytosol-to-ER flux of acetyl-CoA might affect the secretory pathway, we used mass spectrometry-based strategies¹⁴ to examine the proteome and acetyl-proteome (stoichiometry of lysine acetylation) of AT-1 sTg and AT-1^{S113R/+} mice. The effect of these genetic manipulations to the cytosol-to-ER flux of acetyl-CoA is reported elsewhere^{4,6,14,15}. The analysis identified dynamic changes to protein abundance and acetylation across several essential and functional components of the secretory pathway (Fig. 1, Supplementary Table S1). Comparison of all proteomic datasets indicates that the changes imparted by AT-1 affect the secretory pathway more dramatically than other metabolic pathways¹⁴. Protein abundance changes found to be enriched in KEGG pathways at either level of regulation (proteome or acetyl-proteome) and in either model were used as the input for clustering. Therewithin, five clear sub-clusters emerged: transcription (spliceosome), translation initiation factors, ribosome, proteasome, and chaperones. Of the 117 proteins found to be enriched, 30 proteins showed significant changes in acetylation and 109 displayed significant changes in overall

levels. Finally, 22 proteins showed changes at the level of both the proteome and the acetyl-proteome. The majority of changes imparted in acetylation stoichiometry were observed in two sub-clusters: ribosomes, with 12 proteins, and chaperones, with 10 proteins. Overwhelmingly, 106 of the 117 secretory pathway proteins showed changes in the AT-1 sTg proteome, indicating a robust response to increased cytosol-to-ER acetyl-CoA flux. Of note, we found significant changes within the Sec61, Sec62 and Sec63 complex, which allows translocation of newly synthesized proteins into the ER¹⁶; Pdia3, Ero1l, Ero1lb and Calr, which ensure formation of disulfide bonds and folding of nascent glycoproteins within the calreticulin/calnexin cycle¹⁷; and Sec13 and Sec31, which make the outer layer of the coat that captures newly synthesized ER cargo proteins within COPII structures^{18,19}.

When taken together, these results indicate that acetyl-CoA homeostasis differentially impacts sub-clusters within the secretory pathway at the level of the proteome, acetyl-proteome, or both. However, in contrast to mitochondria- and lipid-related metabolic clusters¹⁴, the secretory pathway is largely modulated at the level of the proteome.

Altered AT-1 activity results in morphological reorganization of the ER, ERGIC, and Golgi apparatus

Next, we used mouse embryonic fibroblasts (MEFs) from the above mouse models to determine whether identified proteomic changes impact the functional organization of the secretory pathway. Structure-illumination microscopy (SIM) revealed enlarged cisternae within the rough ER of AT-1 sTg MEFs (Fig. 2a). Successfully folded ER transiting proteins are captured at specialized ER structures referred to as ER exit sites (ERES) and then anterogradely transported by COPII-coated transport carriers, which emerge from transitional ER, to the ERGIC and then the Golgi apparatus²⁰⁻²². To determine whether the expansion of the rough ER coincided with increased formation of ERES/COPII structures, we probed for several members of the COPII coat, including Sec13, Sec31, Sec23, Sec24,

and Sec16. However, we did not detect major differences in the number of individual puncta (Fig. 2b–f, Supplementary Fig. S1a–d), nor in the co-localization of Sec13 and Sec31 (Fig. 2g, Supplementary Fig. S1a), which reflect the formation of the outer COPII coat¹⁹, or the co-localization Sec23 and Sec24 (Fig. 2h, Supplementary Fig. S1b), which reflect the formation of the inner COPII coat²³. Similarly, there were no changes in co-localization of Sec31 and Sec 24 (Fig. 2i, Supplementary Fig. S1c) or Sec13 and Sec16 (Fig. 2j, Supplementary Fig. S1d), which reflect assembly of the inner coat to the outer coat as well as budding events at the transitional ER²⁴. Overall, these results suggest that there are no major changes in number nor assembly of COPII cargo structures in either of the AT-1 models.

Next, we used SIM with anti-ERGIC-53 and anti-GM130 antibodies to determine structural changes at the level of the ERGIC and Golgi apparatus, respectively. The results showed a marked expansion of the ERGIC compartment in AT-1 sTg (Fig. 2k) and a significant reduction in volume and surface area of the Golgi apparatus in AT-1^{S113R/+} (Fig. 2l). The above SIM findings were supported by the presence of numerous vesicles in close proximity of the ER and Golgi apparatus resembling ERGIC-structures in AT-1 sTg mice, and disorganized and somewhat smaller Golgi structures in AT-1^{S113R/+} mice as visualized by electron microscopy (Fig. 2m).

Collectively, the above microscopy-based studies revealed expansion of the ER and ERGIC in AT-1 sTg and reduced Golgi apparatus in AT-1^{S113R/+} mice. Overall, they support the conclusion that changes in cytosol-to- ER flux of acetyl-CoA, as determined by increased or reduced AT-1 activity, regulate the organization of the secretory pathway.

Altered AT-1 activity disrupts normal protein trafficking

To determine whether the above structural reorganization of the secretory pathway highlights changes in protein trafficking within the AT-1 models, we used a previously characterized inducible ER release system that employs tandem repeats of the conditional aggregation domain (CAD), FKBP (F_M),

fused to a protein of interest^{25,26}. The F_M domain dimerizes in the ER and inhibits transport out of the ER. This dimerization must be solubilized with a CAD ligand for the protein of interest to be released from the ER.

To examine the initial budding events at the ER (Fig. 3a, Exp. 1), we used 4×F_M-mCh-NL1²⁶, such that neuroligin bound to mCherry could be visualized as it exited the ER. Using this strategy, we did not observe differences in either cargo velocity (Fig. 3b) nor percent of cargo release (Fig. 3c) between WT and either AT-1 model. Consistent with the microscopy of COPII proteins (Fig. 2b–j, Supplementary Fig. S1a–d), these results indicate that the formation of COPII structures from transitional ER is overall preserved in both AT-1 models. Next, to assess ER-to-Golgi trafficking (Fig. 3a, Exp. 2), we used the DsRedExpress2-FKBP(LV)-GalNAcT2- msGFP2 construct expressing a DsRed cargo protein and a GFP bound GalNAcT, which resides in the *trans*-Golgi. Prior to release, the distribution of DsRed in the ER and the GFP in the Golgi apparatus did not substantially overlap indicating successful sequestration of the two probes. By 2–4 min following CAD availability, all genotypes showed accumulation in the Golgi apparatus. However, at 18 min and beyond, the WT showed cargo dispersion from the Golgi apparatus, whereas the AT-1 sTg and AT-1^{S113R/+} did not (Fig. 3d,e), highlighting a delay in exiting the Golgi apparatus across both AT-1 models.

Finally, to assess protein trafficking to the plasma membrane (Fig. 3a, Exp. 3), we used a 4×F_M-HaloTag-L1CAM construct containing a HaloTag, which is labeled with a cell impermeable dye at the cell surface. DDS was added to initiate cargo release and cells were visualized every 10 min from 20 to 70 min post-release. In WT MEFs, the intensity of cell surface L1CAM expression steadily climbed with time (Fig. 3f,g), with the steepest slope from 20–50 min, and reaching maximum intensity from 50 to 70 min (Fig. 3f,g). By contrast, in AT-1^{S113R/+} MEFs, L1CAM showed a delay in trafficking to the cell surface up to 40 min and then nearly returned to WT levels at 50–70 min (Fig. 3f,g). Most importantly, AT-1 sTg MEFs remained well below WT across the entire experimental settings (Fig. 3f,g)

displaying a significant delay in L1CAM delivery to the cell surface.

The above results indicate that both AT-1 models can efficiently transport nascent glycoproteins from the ER to the Golgi apparatus but experience important alterations when transitioning through the Golgi apparatus. Particularly significant is the delay in Golgi-to-cell surface transport observed in AT-1 sTg mice. These data raise the question of whether defective post-translational processing of N-glycosylated cargo proteins within the Golgi apparatus is responsible for the defective transition and delivery.

Aberrant AT-1 models display defects in Golgi-dependent N-glycan modification and a shift in the quality of the secretome

The initial GlcNAc₂Man₉Glc₃ oligosaccharide structure that is added within the ER by the OST undergoes major modifications as glycoproteins move through the ER and Golgi apparatus. Specifically, the three terminal glucose are removed and the high-mannose structure is trimmed to allow final modification, which includes addition of fucose and galactose in the *cis/medial*-Golgi and sialic acid in the *trans*-Golgi and *trans*-Golgi network²⁷. Importantly, the oligosaccharide chains define much of the functions and activity of glycoproteins²⁸⁻³⁰. Therefore, the complexity of the oligosaccharide chains can serve as a marker of efficient transition through the Golgi apparatus as well as a direct measure of the quality of the secretome (Supplementary Fig. S2).

In order to resolve the quality of the secretome, we developed a new integrated workflow that allows global analysis of the N-glycoproteome in the tissue. The approach uses sequential hydrophilic interaction chromatography (HILIC) for glycopeptide enrichment, coupled to electron-transfer higher-energy collision dissociation (ETHcD)³¹. HILIC allows specific and enhanced enrichment of N-glycopeptides prior to LC-MS/MS analysis while ETHcD allows highly confident site-specific characterization of intact N-glycopeptides by incorporating fragment ions that result from both glycan

and peptide dissociation into one spectrum.

Both human⁹⁻¹³ and mouse^{4,5} data indicate that the nervous system is particularly vulnerable to changes in AT-1 activity. Furthermore, neurons respond to the overexpression of AT-1 by altering the expression of their proteome, and building more dendrites and synaptic terminals that heavily rely on the engagement of the secretory pathway⁵. Therefore, we decided to investigate the quality of the N-glycoproteome in the brain of AT-1 sTg and AT-1^{S113R/+} mice.

We found significant changes in 175 and 255 glycoforms of the female (Fig. 4a) and male (Fig. 4b) AT-1 sTg cortex, and in 126 and 60 glycoforms of the female (Fig. 4c) and male (Fig. 4d) AT-1^{S113R/+} cortex. A similar outcome was observed in the hippocampus with 180 and 112 glycoforms affected in female and male AT-1 sTg mice, and 179 and 214 glycoforms affected in female and male AT-1^{S113R/+} mice (Supplementary Fig. S3a-d).

N-glycans were categorized based on their biological maturity, from least mature to most mature: high man- nose, paucimannose, complex/hybrid, fucose, and sialic acid (Supplementary Fig. S2). Interestingly, most of the changes in glycosylation profile that we observed in both cortex and hippocampus appeared to occur at the Golgi interface (Fig. 4e-g and Supplementary Fig. S3e-h; see also Supplementary Fig. S2). These alterations could not be attributed to immediate changes of the glycosylation machinery within the Golgi apparatus, as reflected by the mRNA levels of the fucose transporter (SLC35C1), fucosyltransferase (FUT8), sialic acid transporter (SLC35A1), sialyltransferases (ST3GAL3, ST6GAL1, ST6GAL2), galactose transporter (SLC35A2), nor the galactosyltransferases (B4GALT2, B4GALT4) (Supplementary Fig. S4).

In order to evaluate the heterogeneity of the glycoproteome, we quantified significantly changed glycans per glycosite (Fig. 4i-l). The AT-1 sTg male and AT-1^{S113R/+} female showed the highest heterogeneity, with 23% and 27% (respectively) of glycosites having more than one glycan structure change significantly on a glycosite. AT-1^{S113R/+} female also showed the highest proportion of

multiple glycosites changing on a single protein (33% of the proteins showed more than one glycosite being affected). However, the heterogeneity of multiple glycosites on one protein being affected was ubiquitous across both models and sexes (Fig. 4m–p). These results were relatively consistent in the hippocampus (Supplementary Fig. S3i–p). Collectively, these findings illustrate the heterogeneous and complex nature of the N-glycan modifications caused by changes in AT-1 activity; multiple glycans on a glycosite are altered, as are the number of glycosites per protein.

To gain insight into glycosite specific changes, we examined glycan type distribution as they pertained to the number of sites affected per protein. AT-1 sTg female cortex displayed an even distribution of sialic acid, whereas fucose, high mannose, and complex/hybrid species showed a higher appearance on multiple sites per protein (Fig. 5a). These findings might highlight changes in specificity of individual glycosylation events imparted upon by defective transition of the glycoproteins within the Golgi apparatus. Comparing the female cortex of AT-1 sTg to AT-1^{S113R/+} mice, again the majority of fucose and complex/hybrid appear on more than one site per protein; however, sialic acid and high mannose show an even distribution between one site and more than one site per protein (Fig. 5c). AT-1 sTg male cortex shows that the majority of fucose and complex/hybrid glycans are on more than one glycosite per protein, whereas high mannose and sialic acid display an even distribution across number of sites (Fig. 5b). The very few glycan types in AT-1^{S113R/+} male cortex show an even distribution of all glycan types except high mannose, which only exists on one site per protein (Fig. 5d). Overall similar results, with only minor differences, were observed in the hippocampus across models (Supplementary Fig. S5).

To understand the biological relevance of the changes observed within the entire secretome, all glycoforms were categorized into subcellular locations based on their GO Cellular Compartment terms. Across both AT-1 models and sexes, the subcellular locations which showed the greatest changes include vesicle, extracellular space, neural, and plasma membrane (Fig. 5e–h). Similar results were observed in

the hippocampus (Supplementary Fig S5e,f,g,h). Albeit with some intrinsic differences, most of the significant changes observed across genetic models, brain regions, and sexes were accounted for by fucose, sialic acid and high mannose (Fig. 5e–h and Supplementary Fig S5e,f,g,h). Furthermore, across many of these analyses, we found a substantial amount of high mannose structures among proteins that are clustered within the plasma membrane and cell surface subgroups. Therefore, Golgi-dependent glycosylation events appear to be more affected and cellular compartments/pathways that depend on successful Golgi-to-plasma membrane transport appear to be more dramatically affected within our genetic models.

The adaptations addressed thus far indicate that similar pathways and subcellular locations are being affected in AT-1 sTg and AT-1^{S113R/+}. To determine whether there was concordance across all groups, we examined overlapping glycoforms according to their subcellular location, considering whether the glycoprotein had an increase or decrease expression when compared with WT. Interestingly, the most divergent (opposite) changes between AT-1 sTg and AT-1^{S113R/+} included vesicle, extracellular, neural, and plasma membrane compartments, which, as highlighted before, depend on successful Golgi-to-plasma membrane transport (Fig. 6a). Conversely, the most convergent changes were found in the lysosome and Golgi subgroups (Fig. 6a). These differences and similarities were conserved across sex and brain region thus highlighting a specific biological response.

When analyzed for glycoprotein and glycosite, we observed 28% (female) and 17% (male) convergent changes in glycoproteins and 14% (female) and 10% (male) convergent changes in glycosites across the cortex of AT-1 sTg and AT-1^{S113R/+} mice (Fig. 6b,c). A similar trend was observed in the hippocampus with a 35% (female) and 20% (male) overlap in altered glycoproteins, but only a 4% (female) and 12% (male) overlap in the glycosites affected (Fig. 6b,c). When we compared overlap between cortex with hippocampus, AT-1 sTg mice showed a 32% (female) and 19% (male) overlap in glycoproteins, and a 15% (female) and 11% (male) overlap in glycosites (Fig. 6b,c). Similarly, AT-

1S113R/+ mice showed a 24% (female) and 19% (male) overlap in glycoproteins, and a 13% (female) and 11% (male) overlap in glycosites.

Aberrant AT-1 models display expansion of the lysosomal network

Under normal conditions, a terminal mannose-6-phosphate (M6P) unit serves as a recognition signal for lysosomal-targeted enzymes. Sorting is mediated by two specific M6P receptors (M6PRs), which bind to M6P in the Golgi apparatus and deliver lysosomal enzymes to the lysosomes^{32,33}. The drastic expansion of high-mannose structures lacking a terminal glucose observed in AT-1 sTg mice can potentially disrupt normal M6PR-mediated functions resulting in mis-targeting of non-lysosomal cargo glycoproteins from the Golgi apparatus to the lysosomes thus overloading the lysosomal network.

To determine whether this was indeed the case, we used EM and studied MEFs from AT-1 sTg and AT-1S113R/+ mice. Consistent with the above hypothesis, we observed a striking expansion of the lysosomal network in the AT-1 sTg model, where the cytosol appeared loaded with electron dense organelles (Fig. 7a). To confirm the identity of these organelles, we used the lysosomal-specific probe, LysoTracker. We observed a marked increase in both number and area of lysosomes in AT-1 sTg MEFs when compared to WT MEFs, thus highlighting the expansion of the lysosomal network (Fig. 7b). Conversely, AT-1S113R/+ MEFs displayed significantly smaller lysosomes than WT (Fig. 7b). No differences across genotypes were observed when we labeled the cells with a peroxisomal probe, used as negative control.

Finally, assessment of M6PR in AT-1 sTg MEFs revealed a significant expansion of both the cation-dependent (CD) and cation-independent (CI) networks suggesting increased cycling of CD-M6PR and CI-M6PR between the Golgi apparatus and the endosomal/lysosomal compartments (Fig. 7d,e).

3. Discussion

Both cell- and mouse-based studies indicate that the ER acetylation machinery is essential to maintain proteostasis within the ER. Essential features include: (1) a QC-like process where acetylation of correctly folded glycoproteins allows them to successfully leave the ER and engage the secretory pathway; and (2) disposal of toxic protein aggregates through the induction of reticulophagy. The former process requires ATase1 and ATase2 to interact with the OST while the nascent polypeptide enters the organelle; the latter requires tight regulation of the acetylation status of ATG9A, which is essential for the engagement of FAM134B and SEC62 and the activation of the LC3 β ^{6,34,35}.

Acetyl-CoA, which serves as the donor for acetylation in the ER, is synthesized in the cytosol and must be transported across the ER membrane by AT-1. In this study, we used AT-1 sTg and AT-1^{S113R/+} mice with increased and reduced AT-1 activity, respectively, to study how the secretory pathway adapts to changes in cytosol-to-ER flux of acetyl-CoA. Through the analysis of the proteome and acetyl-proteome, we determined that many proteins involved with essential ER features, such as protein biosynthesis and insertion within the ER, post-translational modification, folding, QC and ER-to-Golgi trafficking were altered. These changes were paralleled by significant reorganization of the secretory pathway. Specifically, AT-1 sTg mice displayed reorganization of the ER and expansion of the ERGIC network, while AT-1^{S113R/+} mice displayed a contraction of the Golgi apparatus. Furthermore, these morphological changes were paralleled by evident changes in the trafficking of newly-synthesized glycoproteins out of the ER. Particularly significant was the delay in Golgi-to-plasma membrane transport observed in AT-1 sTg mice. Analysis of the N-glycoproteome revealed significant and widespread changes in both AT-1 sTg and AT-1^{S113R/+} mice. Importantly, proteins that showed the most significant and divergent changes across genetic models were assigned to trafficking vesicles, extracellular space, neural, and plasma membrane compartments, all requiring post-translational maturation within the Golgi apparatus and successful post-Golgi transport across the secretory pathway.

Furthermore, the great majority of changes involved Golgi-specific glycan species thus highlighting a possible defect in the ability of the nascent glycoprotein to successfully transition in a progressive fashion through the N-glycan modification machinery of the Golgi apparatus. The apparent defects in Golgi-specific N-glycan modification as well as delayed Golgi-to-plasma membrane transition observed in AT-1 sTg mice was accompanied by a striking expansion of the M6PR and lysosomal networks, which likely involves mistargeting of glycoproteins with high-mannose structures lacking a terminal glucose by the M6PR.

Overexpression of AT-1 in cellular systems is accompanied by increased incorporation of O-propargyl- puromycin and azide-modified mannosamine, highlighting both increased protein biosynthesis and increased terminal sialylation^{5,6}. Furthermore, neuronal overexpression of AT-1 caused a significant expansion of the proteome with 476 proteins found to be upregulated; an effect that was connected to the expansion of the dendritic and synaptic network⁵. The results described here suggest that in AT-1 sTg the expansion of the ER and the ERGIC, together with the increase in ER-to-Golgi transport of cargo material is not paralleled by compensatory changes within the Golgi apparatus to ensure post-translational N-glycosylation. It is also possible that the increased availability of acetyl-CoA within the ER, as caused by overexpression of AT-1 might affect the activity and specificity of the ATases thus resulting in incorrectly folded glycoproteins to be acetylated and forced to transition toward the Golgi apparatus. Indeed, individual acetyltransferases possess different K_m values within the normal physiological range of acetyl-CoA, and changes or fluctuations in the concentrations of acetyl-CoA can reduce or promote the acetylation of specific lysine residues^{1,36}. Furthermore, the analysis of the proteome identified significant changes within the chaperone sub-cluster, perhaps reflecting increased abundance of mis- folded glycoproteins in the ER. If indeed the changes in post-translational maturation of N-glycoproteins reflect the aberrant transition of incorrectly folded glycoproteins to the Golgi apparatus, we could argue that the delay in Golgi-to-plasma membrane transition and increased diversion

of cargo material to the lysosomal compartment is part of a QC-like event within the Golgi apparatus attempting to prevent successful transport of incorrectly folded polypeptides to their final destination. This would explain why we observed minimal changes in the glycosylation status of Golgi resident proteins. Interestingly, down-regulation of the Golgi-based CMP-sialic acid and GDP-fucose transporters impedes successful Golgi-based glycosylation and prevents Golgi-to-cell surface transport of glycoconjugates³⁷. This block in protein trafficking is paralleled by induction of ER stress and inhibition of protein translation, suggesting that active crosstalk between the ER and the Golgi apparatus regulates dynamics of the secretory pathway³⁷.

Overall, these results support the conclusion that the cytosol-to-ER flux of acetyl-CoA can affect organelle dynamics across the secretory pathway with widespread consequences on Golgi-specific post-translational glycosylation and the quality of the secretome. Therefore, acetyl-CoA homeostasis, impinged upon by the ER acetylation machinery, has far reaching consequences in metabolic reprogramming across cellular compartments.

4. Methods

Animals

All animal experiments were carried out in accordance with the NIH Guide for the Care and Use of Laboratory Animals, and received ethical approval by the Institutional Animal Care and Use Committee of the University of Wisconsin-Madison. AT-1^{S113R/+} animals were generated by crossing mice carrying the Slc33a1-S113R mutation to WT animals⁴. AT-1^{S113R/+} animals were studied between 2.5 to 3.5 months of age. Generation of AT-1 sTg mouse was achieved by crossing Rosa26:tTA mice with pTRE AT-1 mice to generate ROSA26:tTA;pTRE- AT-1 (AT-1 sTg mice)⁶. AT-1 sTg mice were studied at 2.5 to 3.5 months of age. Age- matched wild-type (WT) littermates were used as controls. Males were used for the proteome and acetyl-proteome, as described previously¹⁴.

Males and females were used for all other experiments in this study.

Mouse embryonic fibroblast isolation

Isolation of mouse embryonic fibroblasts, MEFs, were described previously⁴. Briefly, embryos were collected from pregnant females at embryonic day 12.5 to 13.5. Embryos (without heads or visceral organs) were minced in sterile EDTA (0.25%; Mediatech), then incubated in a 37 °C CO₂ incubator for 30–45 min. Complete MEF media (DMEM-high glucose, 10% FBS, penicillin/streptomycin/ glutamine mixture, fungizone) was used to quench the trypsin; tissue was further broken by gentle pipetting. Cells were spun at (1000 rpm for 5 min), and the supernatant was discarded. Cells were washed again in MEF media, then plated. Confluent cells were passaged at 1:4 dilutions by using trypsin–EDTA.

Stoichiometry of acetylation

Quantification of acetylation stoichiometry follows methods described previously, with the following modifications^{14,38,39}. Liver protein samples (200 µg) from mitochondrial and cytosolic subcellular fractions were denatured in urea buffer (8 M urea (deionized), 100 mM ammonium bicarbonate (pH = 8.0), 5 mM DTT) and incubated at 60 °C for 20 min⁴⁰. Cysteines were alkylated with 50 mM iodoacetamide, then incubated for 20 min. Two rounds of ~ 20 µmol heavy isotopic D₆-acetic anhydride (Cambridge Isotope Laboratories) chemically acetylated the samples, which were then diluted to 2 M urea using 100 mM ammonium bicarbonate (pH=8.0) before digestion with 1:100 trypsin at 37 °C for 4 h. Before a second digestion with 1:100 gluC, samples were diluted to 1 M urea. Chemically acetylated peptides were fractionated into 6 fractions using a Shimadzu LC-20AT HPLC system with a Phenomenex Gemini NX-C18 column (5 µm, 110Å, 150 × 2.0 mm). Data-independent acquisition (DIA) analysis was conducted by a Thermo Q-Exactive Orbitrap coupled to a Dionex

Ultimate 3000 RSLC nano UPLC with a Waters Atlantic reversed phase column (100 μm \times 150 mm). A spectral library containing all light and heavy acetyl-lysine feature pairs was generated to deconvolute and analyze the DIA spectra using the openly available MaxQuant (v1.6.1) software package. Spectral library samples were treated with C^{12} -acetic anhydride (Sigma), but were otherwise processed identically to the experimental samples and analyzed using data dependent acquisition (DDA) mass spectrometry analysis. A combined library was formed from DDA runs of both the mitochondrial and cytosolic fractions. Heavy acetyl fragment ion pairs were generated in silico, such that the spectral library would contain both the light (endogenous) acetylation peaks and the heavy (chemical) acetylation peaks. Spectronaut (v10) was used to process the experimental samples using the generated spectral library. The subcellular fraction experimental samples were processed separately using an in-house R script, which can be accessed through the GitHub link: [<http://doi.org/10.5281/zenodo.3238525>]; stoichiometry was calculated using the ratio of endogenous (light) fragment ion peak area over the total (endogenous and chemical) fragment ion peak area. All fractions were combined for downstream analysis. Proteins were filtered as significant changes if $P < 0.05$ compared to WT. The raw data, processed data, spectral library, and the analysis logs detailing the Spectronaut analyses settings have been deposited to the ProteomeXchange Consortium via the MassIVE partner repository with the dataset identifier PXD014013 [<http://proteomecentral.proteomexchange.org/cgi/GetDataset?ID=PX014013>].

Quantitative proteomics

Quantification of the proteome was described previously¹⁴. Briefly, liver samples of cytosol, mitochondria, and nucleus were homogenized, then lysed (8 M urea, 50 mM Tris, pH = 8, 5 mM CaCl_2 , 20 mM NaCl, 1 EDTA-free Roche protease inhibitor tablet and 1 Roche PhosSTOP phosphatase inhibitor tablet) with a probe sonicator. Crude lysates were centrifuged (14,000 $\times g$; 5 min), and supernatant protein concentrations were measured by Pierce BCA Protein Assay (Pierce, Rockford, IL).

400 µg of protein lysate was reduced in 5 mM dithiothreitol (DTT), followed by alkylation in 15 mM iodoacetamide (IAA), quenched by adding DTT to 5 mM, and diluted with Tris buffer (pH = 8) to 0.9 M urea. Proteins were digested with trypsin (Promega, Madison, WI), and quenched by adding trifluoroacetic acid (TFA) to a final concentration of 0.3% and desalted with C18 SepPak cartridges (Waters, Milford, MA). Peptides were vacuum dried and reconstituted in 0.5 M TEAB prior to labeling. Samples were assigned to two batches of 4-plex dimethylated leucine (DiLeu) tags each in biological duplicate. 4 mg of each DiLeu tags were suspended in anhydrous DMF, 4-(4,6-dimethoxy-1,3,5-triazin-2-yl)-4-methyl-morpholinium tetrafluoroborate (DMTMM) and N-methylmorpholine (NMM) at 0.6 × molar ratios, then vortexed and centrifuged. The supernatant was mixed with 400 µg tryptic peptides for each condition. Peptides were labeled at a 10:1 label to peptide mass ratio, then vortexed and quenched by adding 5% NH₂OH to the final concentration of 0.25%. 4-plex mixtures were purified by strong cation exchange liquid chromatography (SCX LC) with a PolySULFOETHYL A column (200 mm × 2.1 mm, 5 µm, 300 Å, PolyLC, Columbia, MD). Labeled peptides were collected cleaned, and fractionated with a Kinetex C18 column (5 µm, 100 Å, Phenomenex, Torrance, CA), and a binary mobile phase at pH = 10. Peptides were reconstituted in 0.1% formic acid (FA) and subjected to reversed phase LC–MS/MS analysis with an Orbitrap Fusion Lumos Tribrid mass spectrometer (Thermo Fisher Scientific, San Jose, CA) interfaced with a Dionex Ultimate 3000 UPLC system (Thermo Fisher Scientific, San Jose, CA). Peptides were loaded onto a microcapillary column custom-packed with Bridged Ethylene Hybrid C18 particles (1.7 µm, 130 Å, Waters). Labeled peptide were separated with a 90 min gradient. Survey scans of peptide precursors from *m/z* 350 to 1500 were performed and an AGC target of 2×10^5 with a maximum injection time of 100 ms. The top 20 intense precursor ions were selected for HCD fragmentation. Raw files were processed with Proteome Discoverer 2.1 engine (Thermo Fisher Scientific, San Jose, CA) with Byonic search engine (Protein Metrics Inc, San Carlos, CA). Spectra were searched using the Uniprot *Mus musculus* database. DiLeu labels on peptide N-

termini and lysine residues (+ 145.12801 Da) and carbamidomethylation on cysteine residues (+ 57.02146 Da) were considered fixed modifications. Identifications were filtered to 1% peptide and protein FDR. Proteome Discoverer was used for quantitation; only the PSMs that contained all reporter ion channels were considered. Reporter ion ratio values for protein groups were exported to Microsoft Excel and all fractions were combined for downstream analysis (see statistics section for processing). Significant proteins were determined using Fisher's method ($P < 0.05$). The mass spectrometry proteomics data have been deposited to the ProteomeXchange Consortium via the PRIDE partner repository with the dataset identifier PXD013736 [<http://proteomecentral.proteomexchange.org/cgi/GetDataset?ID=PX013736>].

DiLeu labeling and glycoproteomics

12-plex DiLeu⁴¹ labeling was conducted as previously reported¹⁴. Briefly, dissected brain region samples of AT-1 sTg, AT-1^{S113R/+} and WT mouse models were homogenized, then lysed in 8 M urea buffer with a probe sonicator. Lysate containing proteins was reduced in 5 mM dithiothreitol (DTT) at room temperature for 1 h, followed by alkylation in 15 mM iodoacetamide (IAA) for 30 min in the dark. Alkylation was quenched by adding DTT to 5 mM. The alkylated protein was diluted and then digested with trypsin (Promega, Madison, WI) at 1:50 enzyme to protein ratio at 37 °C for 18 h. Tryptic peptides were desalted with C18 SepPak cartridges (Waters, Milford, MA), dried under vacuum, and reconstituted in 0.5 M TEAB before labeling.

DiLeu tags were suspended in anhydrous DMF and combined with 4-(4,6-dimethoxy-1,3,5-triazin-2-yl)-4-methyl-morpholinium tetrafluoroborate (DMTMM) and N-methylmorpholine (NMM) at 0.6 × molar ratios to tags. The mixture was vortexed at room temperature for 1 h. Following centrifugation, the supernatant was immediately mixed with tryptic peptides from one condition (10:1 tag to peptide w/w), and vortexed at room temperature for 2 h. The reaction was quenched by NH₂OH.

Each batch of labeled peptides was combined respectively as 12-plex mixtures.

Glycopeptide enrichment

DiLeu labeled glycopeptides were enriched using in-house packed SAX- HILIC SPE tips following previously reported procedure with minor modification^{42,43}. 3 mg of cotton wool was inserted into a 200 μ L TopTip. SAX LP bulk material was dispersed in 1% TFA as a 10 mg/200 μ L slurry and activated for 15 min under vigorous vortexing. After activation, 60 μ L slurry was added to the spin-tip. Solvent was removed by centrifugation at 1200 rpm for 2 min, after which the SAX material was packed at the top of the tip. The stationary phase was then conditioned by 300 μ L 1% TFA and 300 μ L loading buffer (80% ACN, 1% TFA), each repeated 3 times. 2 mg of DiLeu labeled peptides were aliquoted to 200 μ g. Each aliquot was dissolved in 300 μ L loading buffer and loaded onto the tips by centrifugation at 1200 rpm for 2 min; the flow through was collected and loaded again to ensure complete retention. The tips were then washed with 300 μ L loading buffer for a total of 6 times, after which the four eluted fractions of 300 μ L 70% ACN with 0.2% FA, 53% ACN with 0.2% FA, 30% ACN with 0.2% FA and 5% ACN with 0.2% FA were collected in four separate PE tubes. Corresponding fractions from the ten aliquots were pooled and dried under vacuum before MS analysis.

LC-MS/MS analysis of intact glycopeptides

Enriched glycopeptides in each fraction were reconstituted in 0.1% FA and subjected to reversed phase LC-MS/MS analysis with an Orbitrap Fusion Lumos mass spectrometer (Thermo Fisher Scientific, San Jose, CA) interfaced with a Dionex Ultimate 3000 UPLC system (Thermo Fisher Scientific, San Jose, CA). Peptides were separated on a 15 cm length, 75 μ m i.d. custom-packed BEH C18 (1.7 μ m, 130 Å, Waters) capillary column with an 80 min gradient from 0 to 30% ACN (0.1% FA). Mass spectrometer was operated in a top 20 data-dependent acquisition mode with HCD-product

dependent- EThcD fragmentation⁴⁴. Survey scans of peptide precursors from m/z 400 to 2000 were performed at resolving power of 120 K and AGC target of 4×10^5 with a maximum injection time of 150 ms. Tandem MS acquisition was at resolving power of 60 K, AGC target of 5×10^4 and dynamic exclusion of 12 s of 10 ppm mass tolerance. The top 20 intense precursor ions were selected and subjected to HCD fragmentation at a normalized collision energy of 33%. If signature oxonium ions (HexNAc 204.087 m/z , HexNAcHex 366.140 m/z , HexNAc fragments 138.055 m/z and 168.065 m/z) of intact glycopeptides were detected by HCD survey scan, an EThcD hybrid fragmentation was triggered. ETD reaction time was set to 30, 20 or 10 ms when precursor charge states were $z=2, 3-5$ or $6-7$. HCD supplemental activation energy was 33%. Maximum ion injection times for HCD survey scan and EThcD scan are 125 and 250 ms.

Glycoproteome data processing

Raw files were processed with Byonic search engine (Protein Metrics Inc, San Carlos, CA) embedded within Proteome Discoverer 2.1 (Thermo Fisher Scientific, San Jose, CA). Spectra were searched against the SwissProt *Mus musculus* proteome database (August 13, 2016; 24,903 entries). Trypsin digestion missed cleavage was set < 3 . The parent mass error tolerance was 10 ppm, and fragment mass tolerance was 0.01 Da. Fixed modifications were specified as carbamidomethylation (+ 57.02146 Da) on C residues and 12-plex DiLeu (+ 145.12801 Da) on peptide N-terminus and K. Dynamic modifications included oxidation of M (+ 15.99492 Da, rare1), deamidation (+ 0.984016 Da, rare1) of N or Q, and N-glycosylation (common1). Glycan modifications were specified as Byonic embedded mammalian N-glycan database (309 entries). Identifications were filtered to 1% protein FDR. Gene ontology annotation of glycoprotein and Student's t-test of glycopeptide quantitation results were performed using Perseus software⁴⁵. Riley et al. reported useful tools to analyze large-scale site-specific glycoproteomics data⁴⁶. Results were further processed by in-house written R scripts. Glycopeptides were

exclusively categorized into five glycan type categories based on glycan composition: (1) sialic acid (containing NeuAc/NeuGc), (2) fucose (containing Fucose), (3) complex/hybrid (> 2 NeuAc), (4) high-mannose (2 NeuAc and > 5 Hex), and (5) paucimannose (2 NeuAc and < 5 Hex). The N-glycoproteomics data have been deposited to the Proteome Xchange Consortium via the PRIDE partner repository with the data set identifier PXD019770 [<http://proteomecentral.proteomexchange.org/cgi/GetDataset?ID=PXD019770>].

Quantitative post-acquisition data set analysis

The proteome and the acetyl-proteome were analyzed as described previously¹⁴. Cluster analysis was determined using KEGG pathways which arose during pathway analysis^{47,48}. For the secretory pathway-related cluster, all proteins that were found in the following KEGG pathways in either of the AT-1 models and in either of the proteome or acetyl stoichiometry were included: protein processing in the ER, ribosome, proteasome, spliceosome, and RNA transport. These proteins were the input for a STRING analysis. Proteins with no interactions were hidden, with the minimum required interaction score set at high confidence (0.7). Active interaction sources included all sources except textmining. To determine subcellular localization for glycoproteome data, proteins were categorized according to their Uniprot GO Cellular Component annotation. Proteins were placed inclusively, into the following categories as done previously¹⁴: “plasma membrane”; “other membrane” (includes GO terms with the word ‘membrane’ exclusive of plasma membrane); “neural” (includes GO terms that contain ‘axon’, ‘neuro’, or ‘myelin’); “ER” (includes any term that contains ‘endoplasmic’); “Golgi” (includes terms that contain ‘Golgi’ and do not contain ‘endoplasmic’); “cell surface” (includes any GO term that includes ‘surface’); “synapse”, “extracellular”, “vesicle”, “lysosome”, and “secreted” (include terms with their respective names); and “none listed” (includes any GO term that did not contain any of the other 11 subcellular groups used). The protein-glycan networks of significantly altered glycopeptides ($p < 0.05$)

were created in R 3.6.0 using the igraph and ggnetwork library. Subcellular locations of glycopeptides were grouped from GO cellular component terms according to the same rules as in (Riley)⁴⁶. Pairwise Euclidean distances between subcellular groups of significant glycopeptides from different quantitative experiments was calculated. Each GO group was considered as a 1707-dimension vector with each glycopeptide as a direction. The dimension vector was constructed by the union set of significantly altered glycopeptides across samples. The magnitude of the dimension is + 1 or - 1 for corresponding up- or down- regulated glycopeptides. Upset plots detailing the overlap between significantly altered glycoproteins and glycosites between datasets were created using the UpSetR package in R Studio. KEGG pathway enrichment and visualization of significant glycoproteins against *Mus Musculus* gene were performed with clusterProfiler library, Benjamini–Hochberg adjustment was performed to an FDR of 0.05⁴⁶.

Immunocytochemistry

Cultured primary MEF cells were transfected with a plasmid carrying ER3- mCherry fusion protein, KDEL, and ER signal peptide (Gift from Michael Davidson; Addgene Plasmid #55,041) or transfected with CellLight Golgi-GFP BacMam 2.0 (C10592, ThermoFisher Scientific) overnight. The coverslips were then fixed with paraformaldehyde for 10 min, (4%, 15,710, Electron Microscopy Sciences), and permeabilized with 0.1% Triton TM-X100 (Roche Applied Science) for 5 min, followed by an incubation in blocking buffer (10% BSA, 5% goat serum in PBS) for one hour. All antibodies were diluted in antibody dilution buffer (1% BSA, 5% goat serum in PBS) and stained with ERGIC-53 (E1031, Sigma Aldrich, 1:80), Sec13 (A303- 980A, Bethyl Laboratories or H00006396-B02P, Novus Biologicals, 1:50), Sec16 (A300-648A, Bethyl Laboratories. 1:50), Sec31A (sc-136233, SantaCruz Biotechnology, 1:50), Sec24C (A304-760A, Bethyl Laboratories, 1:50), Sec23 (ab99552, Abcam, 1:50), GM130 (610,823, BD Bioscience, 1:100), CI-M6PR (ab124767, Abcam, 1:200), or CD-M6PR

(ab134153, Abcam, 1:50) for overnight incubation. Cells were washed three times in PBS and incubated with secondary antibodies AlexaFluor488 (A-11034, 1:1000) and AlexaFluor647 (A-21463 or A-21447, 1:1000) for one hour. Cells were washed three times in PBS; Fluoro-Gel II with DAPI (17985-50, Electron Microscopy Sciences) was used to mount the cover slips. Images were acquired using Structured Illumination Microscopy (Nikon SIM), and analyzed in Imaris imaging software (Bitplane, Oxford Instruments) using the Surfaces and Spots modules. Images of cells stained for CI-M6PR and CD-M6PR were acquired using both SIM and confocal microscopy (Nikon A1), and were analyzed using the surfaces module in Imaris imaging software. To stain for peroxisomes, CellLight Peroxisome-GFP, BacMam 2.0 (C10604, ThermoFisher) was used, and to stain for lysosomes, LysoTracker Green DND-26 (L7526, ThermoFisher) was used. Images were acquired using A1R-HD confocal microscope (Nikon) using a 20 \times and 60 \times water objective.

Electron microscopy

MEFs were grown on coverslips and fixed in 2.5% glutaraldehyde, 2.0% paraformaldehyde buffered in 0.1 M sodium phosphate buffer (PB) for 1 h at room temperature (RT). The samples were then rinsed 5 \times 5 min in PB, and post-fixed in 1% osmium tetroxide and 1% potassium ferrocyanide in 0.1 M PB for 1 h at room temperature (RT), then rinsed in PB as before. Dehydration was performed in a graded ethanol series (35, 50, 70, 80, 90% for 5 min each step, 95% for 7 min, 100% for 3 \times 7 min) at RT, and then transitioned in dry acetone 2 \times 7 min at RT. Fully dehydrated samples were infiltrated in increasing concentrations of Durcupan ACM (Sigma-Aldrich) and acetone mixtures in the following order: 20 min incubation in 25% PolyBed 812, 75% acetone, 20 min incubation in 50% PolyBed812, 50% acetone, 1 h incubation in 75% PolyBed 812, 25% acetone, and finally a 45 min incubation at 60 $^{\circ}$ C in 100% PolyBed 812. Embedding and polymerization took place in fresh Durcupan ACM for 24 h at 60 $^{\circ}$ C. The coverslips were removed with hydrofluoric acid and the samples were sectioned on a Leica EM

UC6 ultramicrotome at 100 nm. The sections were collected on 300 mesh thin-bar Cu grids (EMS Hatfield, PA), and post-stained with uranyl acetate and lead citrate. The sectioned samples were viewed at 80 kV on a Philips CM120 transmission electron microscope and documented with an AMT BioSprint12 digital camera (Advanced Microscopy Techniques, Woburn, MA).

Live cell imaging

For all live cell imaging experiments, an ER inducible release system was used such that transfected MEFs expressed a fluorescently labeled protein to an aggregation domain that trapped the protein in the ER. Following a 48 h incubation period post transfection, cells were treated with a solubilizer to induce ER release. Solubilizing agents used were dependent on construct identity and are detailed in subsequent sections. To visualize early protein trafficking events from the ER, MEFs were transfected with the 4×F_M-mCh-NL1 plasmid (Gift from Matthew Kennedy). Before imaging, cells were treated with DDS (635,054, Takara) at a final concentration of 1 μM to induce release from the ER. Images were collected every 3 s for a duration of 3 min within 10 min of DDS induced solubilization with an AIR-HD confocal microscope (Nikon) using a 60× water objective. Imaris imaging software with the Spots module was used to track vesicle movement. The maximum velocity of each cargo was tracked, and the mean of maximum velocity was recorded for each cell. If cargo trafficked more than 2 μm in 3 min, the cargo was categorized as “released”. The number of released cargo over total cargo in each cell was used to calculate percent release. To visualize trafficking from the ER to the Golgi, MEFs were transfected with the DsRedExpress2-FKBP(LV)-GalNAcT2-msGFP2 plasmid. As this aggregation domain is slightly different from the one used to measure ER budding, a different solubilizer, SLF (10007974, Cayman Chemical Co.), was added at a final concentration of 100 μM. Images were acquired with an ImageXpress Micro 4 (Molecular Devices) using a 40× air objective every 2 min for a total of 30 min following solubilizer addition. Imaris imaging software was used to measure the colocalization

of the green and red channels. Accumulation in the Golgi was quantified by measuring the sum of DsRed intensity as it overlapped with the GFP channel. To overcome cell-to-cell intensity variability, each cell was normalized to its maximum intensity over the 30 min. To visualize trafficking to the cell surface, MEFs were transfected with a plasmid containing 4×F_M-Halo-L1CAM. DDS was added to cells at 1 μM. Ten minutes prior to imaging, a cell impermeant halo dye was added to the cells at a final concentration of 100 nM. Cells were then washed three times with DMEM before imaging. DDS was added to cells at 1 μM. Full cell z-stack images were taken with a TI2 Spinning Disk Confocal Microscope (Nikon) using a 60× oil objective every 10 min from 20 to 70 min post solubilizer addition. Fluorescence intensity was measured from max intensity projections using FIJI.

Real-time PCR

Real-time PCR (qPCR) was performed using the Roche 480 lightcycler and Sybr Green Real Time PCR Master Mix (04707416001, Roche). Expression levels were normalized against GAPDH levels, and are expressed as percent of control. PCR primers specific to each gene are summarized in Supplementary Table S2 (Bio-Rad Laboratories; Prime PCR assay). The cycling parameters were as follows: 95 °C, 10 s; 60 °C, 20 s; and 72 °C, 30 s, for a total of 45 cycles. Primers are listed in Supplementary Table S2.

Statistics

Data analysis was performed in Graphpad Prism v 8.3.1 (GraphPad Software, Inc) and R v3.5.1. Data are expressed as mean ± standard deviation or SEM, as noted in each instance. For the proteomics, fold changes were computed within each DiLeu batch experiment. An F-test was used to test for equivalent variance among groups, and a Student's t test was performed assuming equal or unequal variance according to the results of the F-test. A final fold change was calculated by averaging the two

experiments together, and the p-values of the two separate DiLeu experiments were combined using Fisher's method as implemented in the R package metap (R version 3.5.1). For the glycoproteomics, a Student's t-test was performed. For trafficking experiments, a two-way ANOVA was used with multiple comparisons reported at each time point. For all other analyses, comparison of the means was performed using a Student's t-test, or a one-way ANOVA. The following statistical significance was used: * $P < 0.05$; ** $P < 0.005$; # $P < 0.0005$.

Data availability

The proteomics data have been deposited in the ProteomeXchange Consortium via the PRIDE partner repository with the accession code PXD013736. The acetyl-proteomics data have been deposited to the ProteomeXchange Consortium via the MassIVE partner repository with the accession code PXD014013. The R script that was used to process the acetyl-proteomics data has been deposited on Github with the identifier (search terms: AT1 Acetylation Stoich) (<https://doi.org/10.5281/zenodo.3238525>). The N-glycoproteomics data have been deposited to the Proteome Xchange Consortium via the PRIDE partner repository with the data set identifier PXD019770. The authors declare that all other data supporting the findings of this study are available within the paper and its supplementary tables.

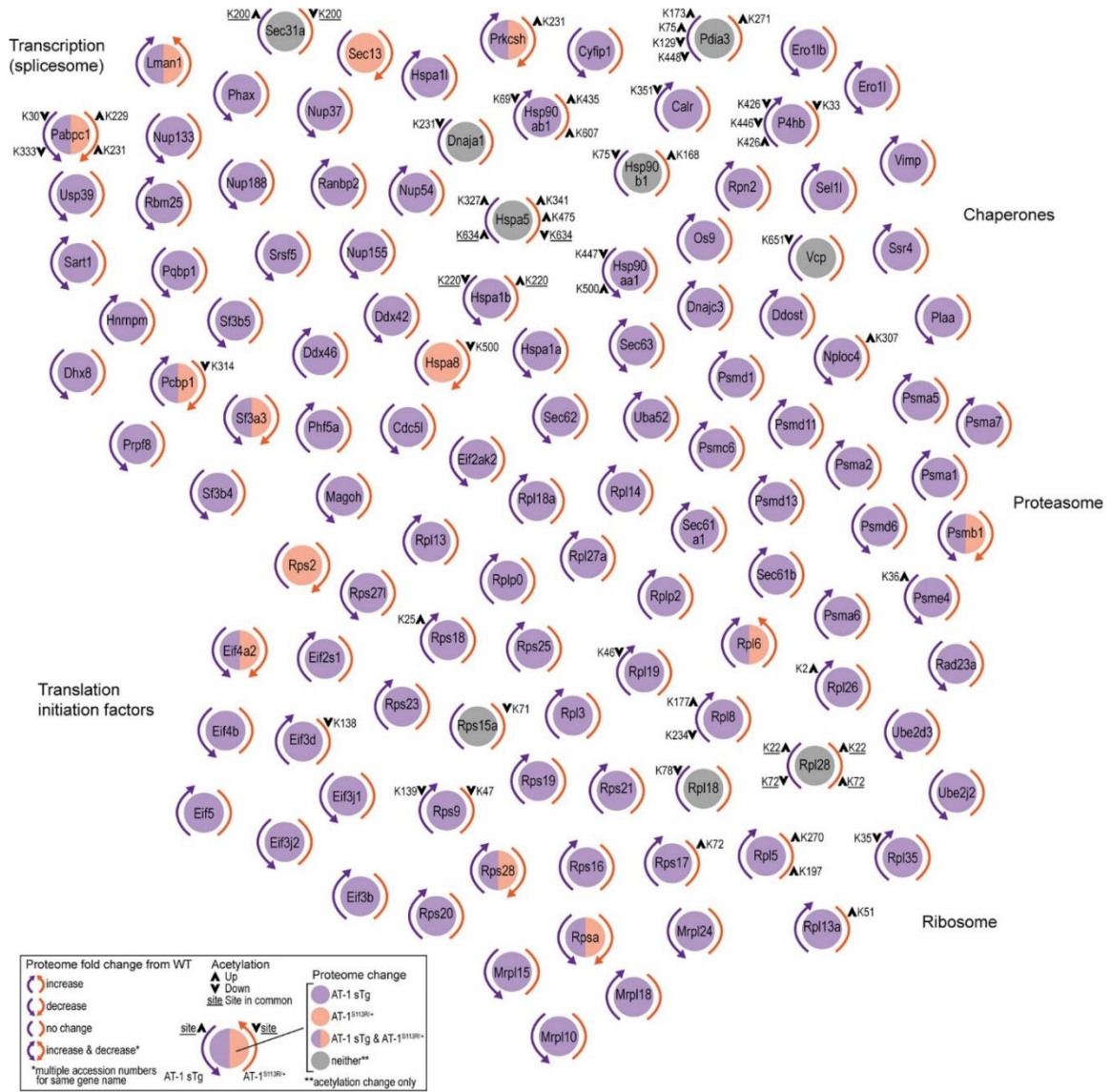


Figure 1. AT-1 sTg and AT-1^{S113R/+} display proteomic changes across secretory pathway-related processes. Proteins with significantly changing abundance and acetylation stoichiometry identified across secretory pathway-related KEGG pathways from liver fractions are shown in clusters (n = 4 WT; n = 4 AT-1 sTg; n = 4 AT-1^{S113R/+}). Changes in proteome are indicated by a purple (AT-1 sTg), orange (AT-1^{S113R/+}), or grey (neither proteome changed) circle; corresponding colored arrows indicate increase, decrease, or no change in proteome compared with WT. Acetylation stoichiometry changes are designated with a black arrow on the corresponding AT-1 model in which it changed significantly. If a site changes significantly in both models, the site is underlined.

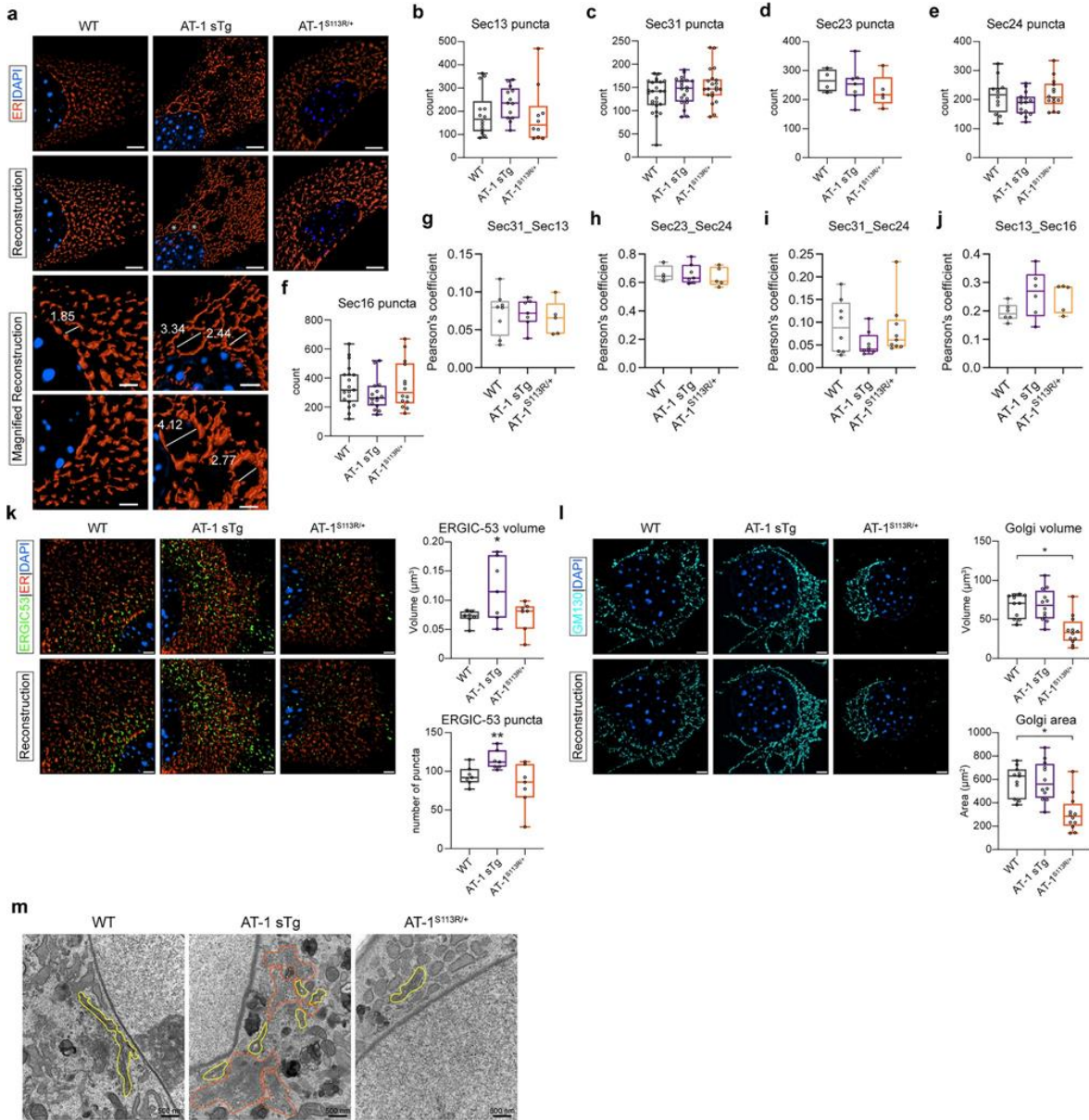


Figure 2. Morphological reorganization of ER, ERGIC and Golgi apparatus in aberrant AT-1 models.

(a) Representative ER morphology in primary-cultured MEFs using ER3-mCherry (scale bar, 3 μ m). White asterisk (*) indicates an enlarged cisternae within the perinuclear rough ER. High-magnification areas for WT and AT-1 sTg are shown (scale bar, 2 μ m). (b–f) Quantification of puncta revealed using SIM microscopy in primary-cultured MEFs in (b) Sec13 puncta (n = 14 WT; n = 13 AT-1 sTg; n = 10 AT-1S113R/+), (c) Sec31 puncta (n = 25 WT; n = 20 AT-1 sTg; n = 21 AT-1S113R/+), (d) Sec23 puncta (n = 4 WT; n = 7 AT-1 sTg; n = 5 AT-1S113R/+), (e) Sec24 puncta (n = 12 WT; n = 15 AT-1 sTg; n = 14 AT-1S113R/+), (f) Sec16 puncta (n = 19 WT; n = 15 AT-1 sTg; n = 14 AT-1S113R/+). (g–j) Pearson's coefficient of puncta revealed using SIM microscopy in primary-cultured MEFs in (g) Sec31 and Sec13 puncta (n = 8 WT; n = 7 AT-1 sTg; n = 5 AT-1S113R/+), (h) Sec23 and Sec24 puncta (n = 4 WT; n = 7 AT-1 sTg; n = 5 AT-1S113R/+), (i) Sec31 and Sec24 puncta (n = 8 WT; n = 8 AT-1 sTg; n = 9 AT-1S113R/+), (j) Sec13 and Sec16 puncta (n = 6 WT; n = 6 AT-1 sTg; n = 5 AT-1S113R/+). (k) ERGIC morphology in primary-cultured MEFs using ERGIC-53 antibody (scale bar, 3 μ m) and quantified using Imaris reconstruction of volume and number of puncta (n = 7 WT; n = 7 AT-1 sTg; n = 7 AT-1S113R/+). (l) Golgi apparatus morphology in primary-cultured MEFs using GM130 antibody (scale bar, 3 μ m) and quantified using Imaris reconstruction of volume and area (n = 11 WT; n = 12 AT-1 sTg; n = 12 AT-1S113R/+). (m) Representative electron microscopy of MEFs from WT, AT-1 sTg, and AT-1S113R/+. Yellow outlines Golgi structures and orange outlines disorganized secretory structures and vesicles. (scale bar, 500 nm). MEFs from multiple cells from 3 biologically independent animals for each genotype for (b–l). One-way ANOVA. *P < 0.05; **P < 0.005.

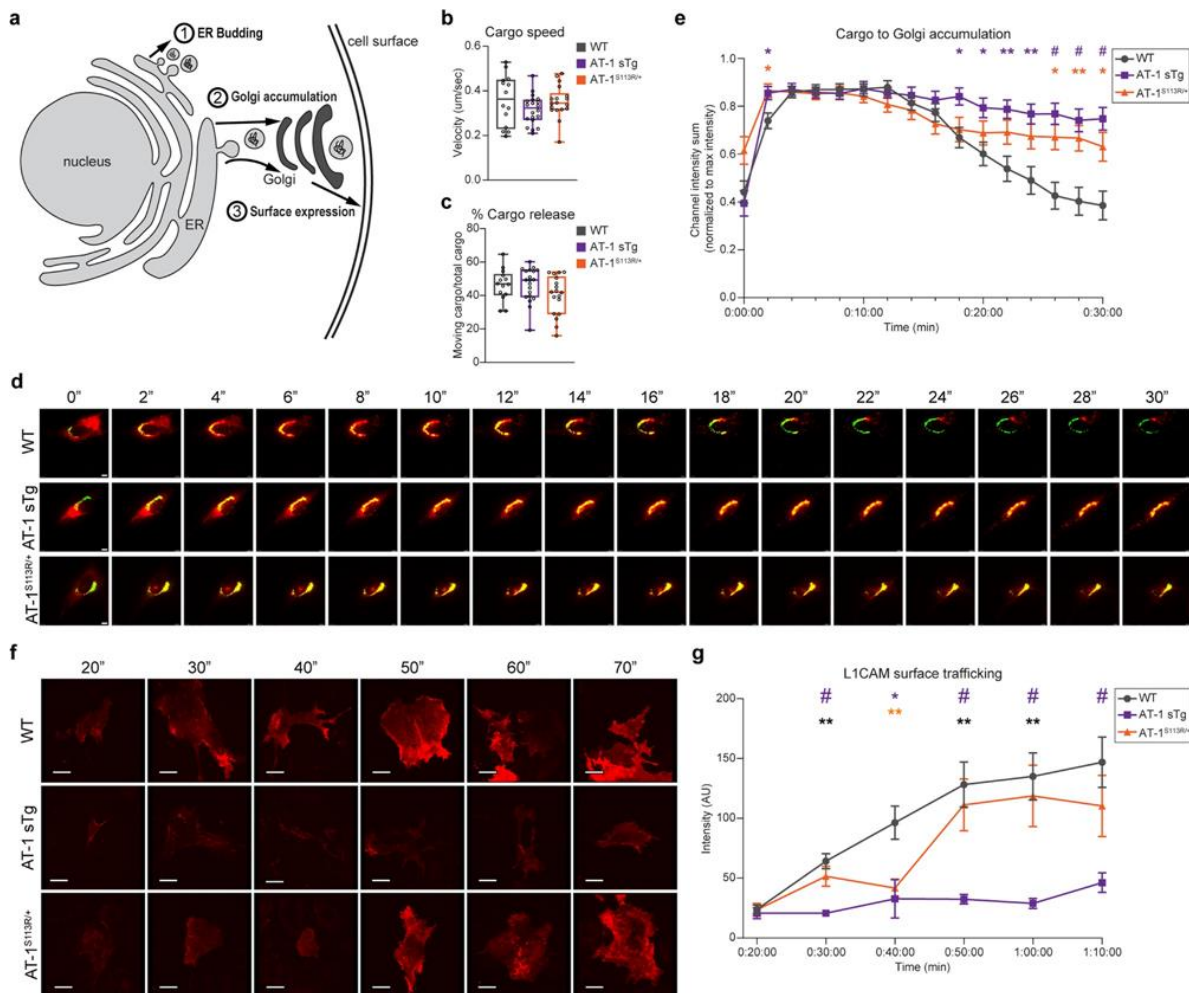


Figure 3. Aberrant AT-1 models demonstrate altered protein trafficking through the secretory pathway.

(a) Schematic of three experiments used to assess protein trafficking in the secretory pathway. Experiment 1 assesses protein-laden carriers following release from the ER; solubilizer-dependent cargo fluoresces for visualization. Experiment 2 quantifies the time for ER cargo to accumulate in the Golgi apparatus and then egress; solubilizer-dependent DsRed cargo traffics to GFP-labeled Golgi. Experiment 3 quantifies the time for ER cargo to reach the cell surface; solubilizer-dependent cargo with a HaloTag ligand is tracked for 70 min with HaloTag cell impermeable dye added prior to imaging. (b,c) Maximum speed of cargo release (b), and the percentage of cargo release (c), are tracked for 3 min after solubilizer induced cargo release in MEFs (MEFs from multiple cells from 3 biologically independent animals for each genotype n = 14 WT; n = 20 AT-1 sTg; n = 18 AT-1^{S113R/+}; MEF cells from 3 biologically independent animals for each group for (b,c). Student's T-test. (d) Representative cargo (red) accumulation in the Golgi (green) every 2 min, for 30 min in MEFs from WT, AT-1 sTg, and AT-1^{S113R/+} (scale bar, 40 μ m). (e) Cargo accumulation in the Golgi over 30 min in primary- cultured MEFs (MEFs from multiple cells from 3 biologically independent animals for each genotype at each time point, n = 27 WT; n = 22 AT-1 sTg; n = 23 AT-1^{S113R/+}). Mean with SEM are represented at each time point. (f) Representative surface trafficking of L1CAM in MEFs from WT, AT-1 sTg, and AT-1^{S113R/+} (scale bar, 40 μ m). (g) L1CAM intensity at the cell surface in MEFs (MEFs from multiple cells from 3 biologically independent animals for each genotype at each time point, n = 42–76 WT; n = 10–27 AT-1 sTg; n = 19–34 AT-1^{S113R/+}). Mean with SEM are represented at each time point. Two-way ANOVA with multiple comparisons at each time point for (e,g). Purple and orange statistics indicate differences between AT-1 sTg and WT, and between AT-1^{S113R/+} and WT, respectively. Grey statistics indicate difference between AT-1 sTg and AT-1^{S113R/+}. *P < 0.05; **P < 0.005; #P < 0.0001.

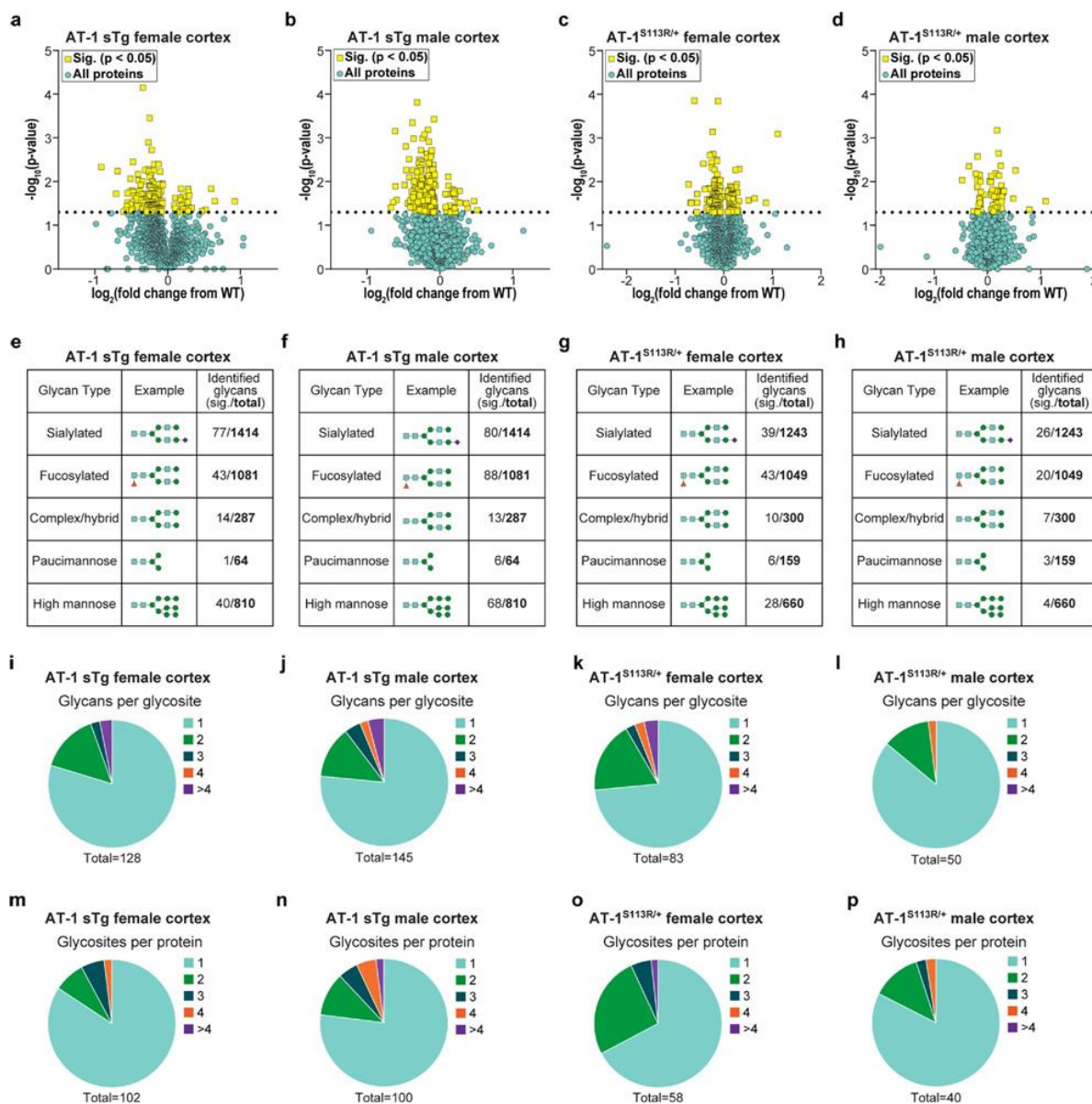


Figure 4. AT-1 sTg and AT-1^{S113R/+} display N-glycoproteomic changes across many cortical glycoforms. (a,b) Volcano plot displaying all quantified glycoproteins in the cortex of AT-1 sTg (a) female (n=3) and (b) male (n = 3), compared with age-matched WT littermates. Statistically significant proteins (175 in female; 255 in male) are highlighted in yellow, and all other proteins are designated in blue. Student's T-test, P<0.05. (c,d) Volcano plot displaying all quantified glycoproteins in the cortex of AT-1^{S113R/+} (c) female (n = 3) and (d) male (n = 3), compared with age-matched WT littermates. Statistically significant proteins (126 in female; 60 in male) are highlighted in yellow, and all other proteins are designated in blue. Student's T-test, P<0.05. (e–h) Identified glycans are categorized into five glycan types, and are divided by significant over total identified in cortical (e) AT-1 sTg female, (f) AT-1 sTg male, (g) AT-1^{S113R/+} female, and (h) AT-1^{S113R/+} male. (i–l) Significant glycans per glycosite are identified in cortical (i) AT-1 sTg female, (j) AT-1 sTg male, (k) AT-1^{S113R/+} female, and (l) AT-1^{S113R/+} male. (m–p) Significant glycosites per protein are identified in cortical (m) AT-1 sTg female, (n) AT-1 sTg male, (o) AT-1^{S113R/+} female, and (p) AT-1^{S113R/+} male.

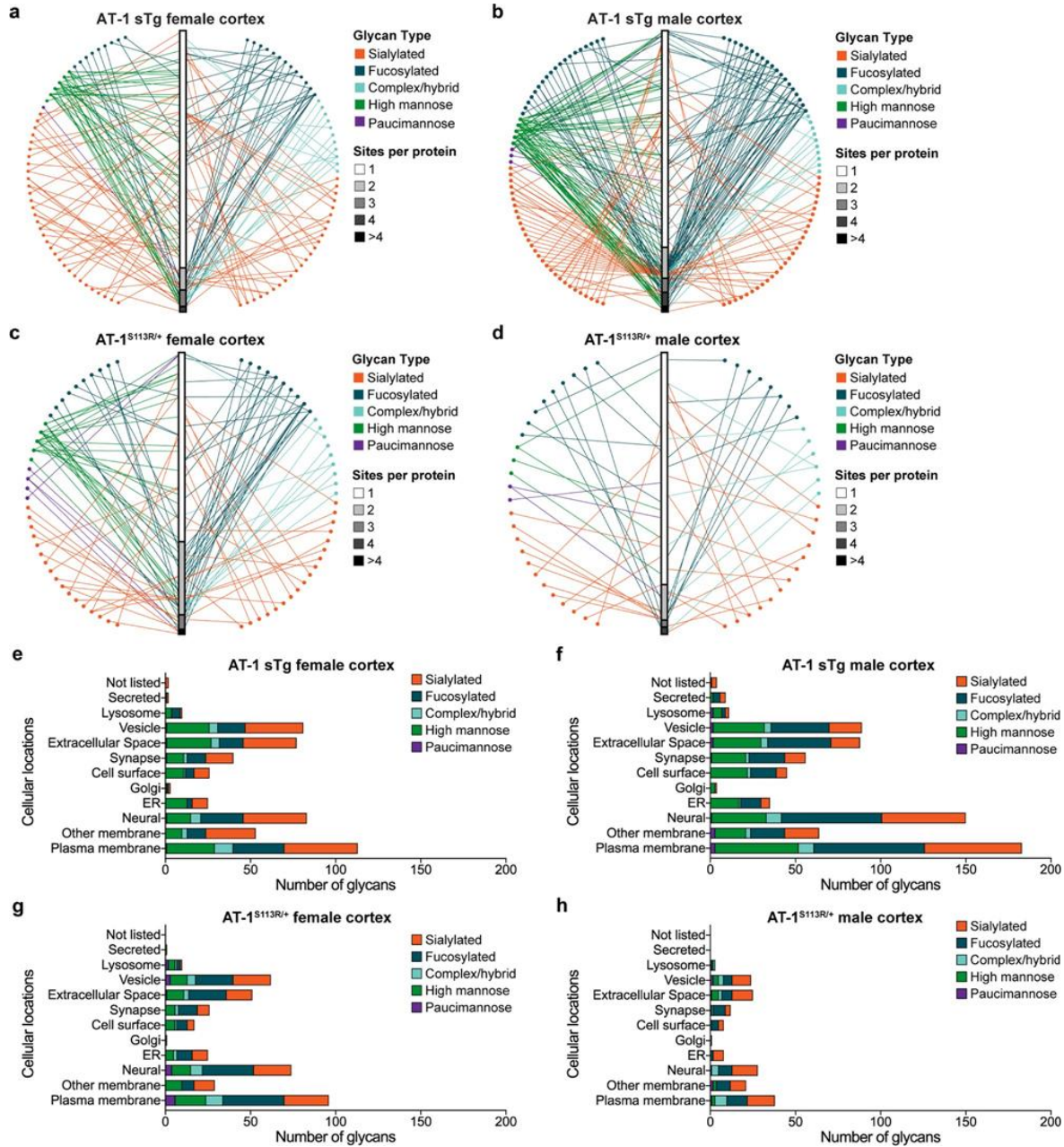


Figure 5. AT-1 sTg and AT-1^{S113R/+} display a highly heterogeneous cortical secretome. (a–d) Network of significant glycan types plotted to glycoprotein for cortical (a) AT-1 sTg female, (b) AT-1 sTg male, (c) AT-1^{S113R/+} female, and (d) AT-1^{S113R/+} male. Circle represents glycan type, with each node representing a specific glycan tree. Glycans intersect with their protein, organized by the number of glycosites identified on that glycoprotein. (e–h) Glycosylation distribution according to subcellular localizations as defined by GO cellular component terms in cortical (e) AT-1 sTg female, (f) AT-1 sTg male, (g) AT-1^{S113R/+} female, and (h) AT-1^{S113R/+} male.

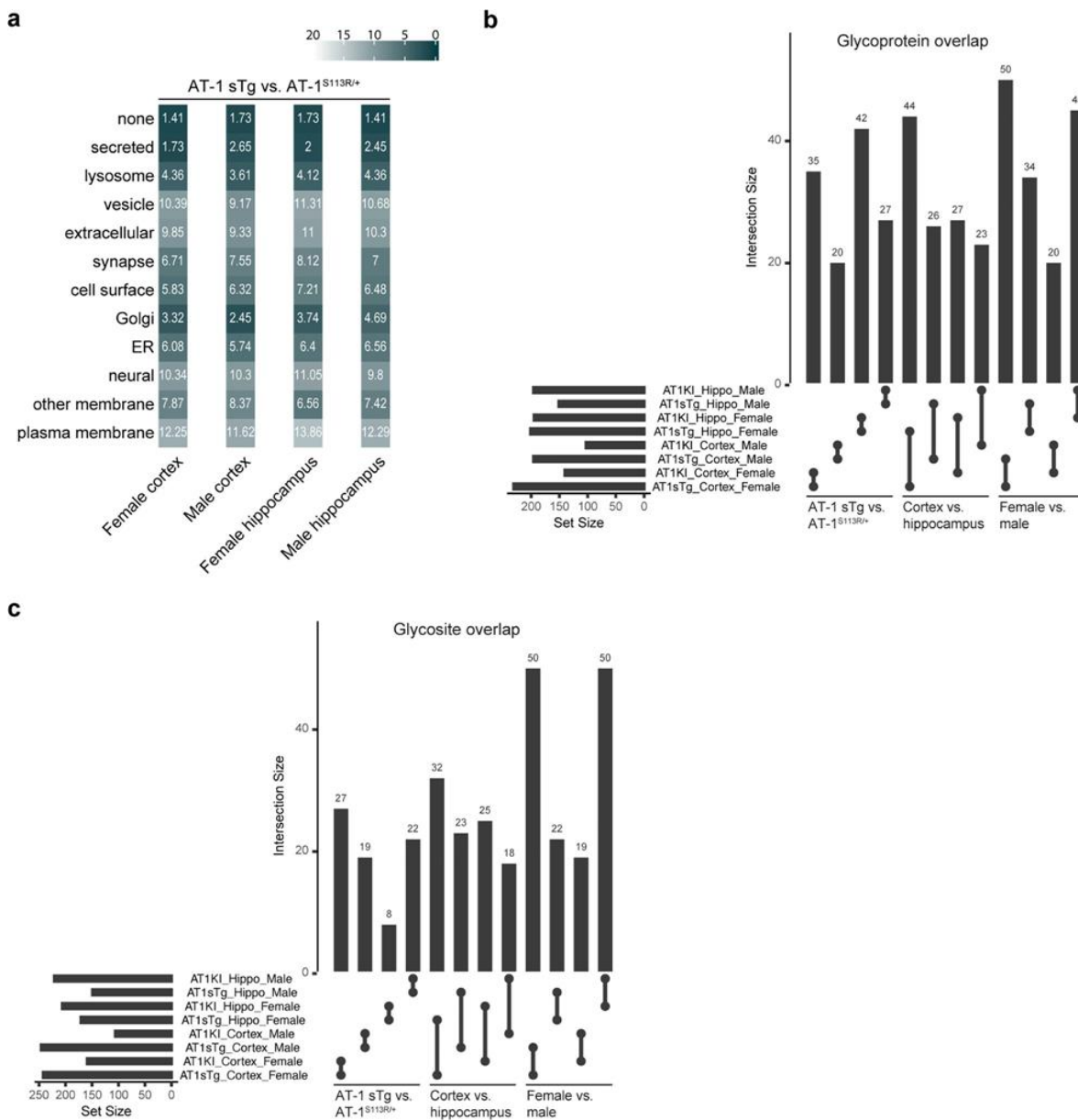


Figure 6. AT-1 sTg and AT-1S113R/+ display both divergent and convergent N-glycoproteomic changes across subcellular locations. (a) Euclidean distances comparing the distance between significant glycoforms found in AT-1 sTg and AT-1S113R/+ , broken down by sex and brain region. Distances were calculated according to their subcellular locations, with higher similarity indicated with dark colors. (b,c) Significant glycoprotein (b) and glycosite (c) overlap is examined at the level of model (AT-1 sTg v. AT-1S113R/+), brain region (cortex vs. hippocampus) and sex (female vs. male). The upper bar graph indicates the size of intersection and the left bar graphs shows total number of significant glycoproteins (b) or glycosites (c) in each dataset.

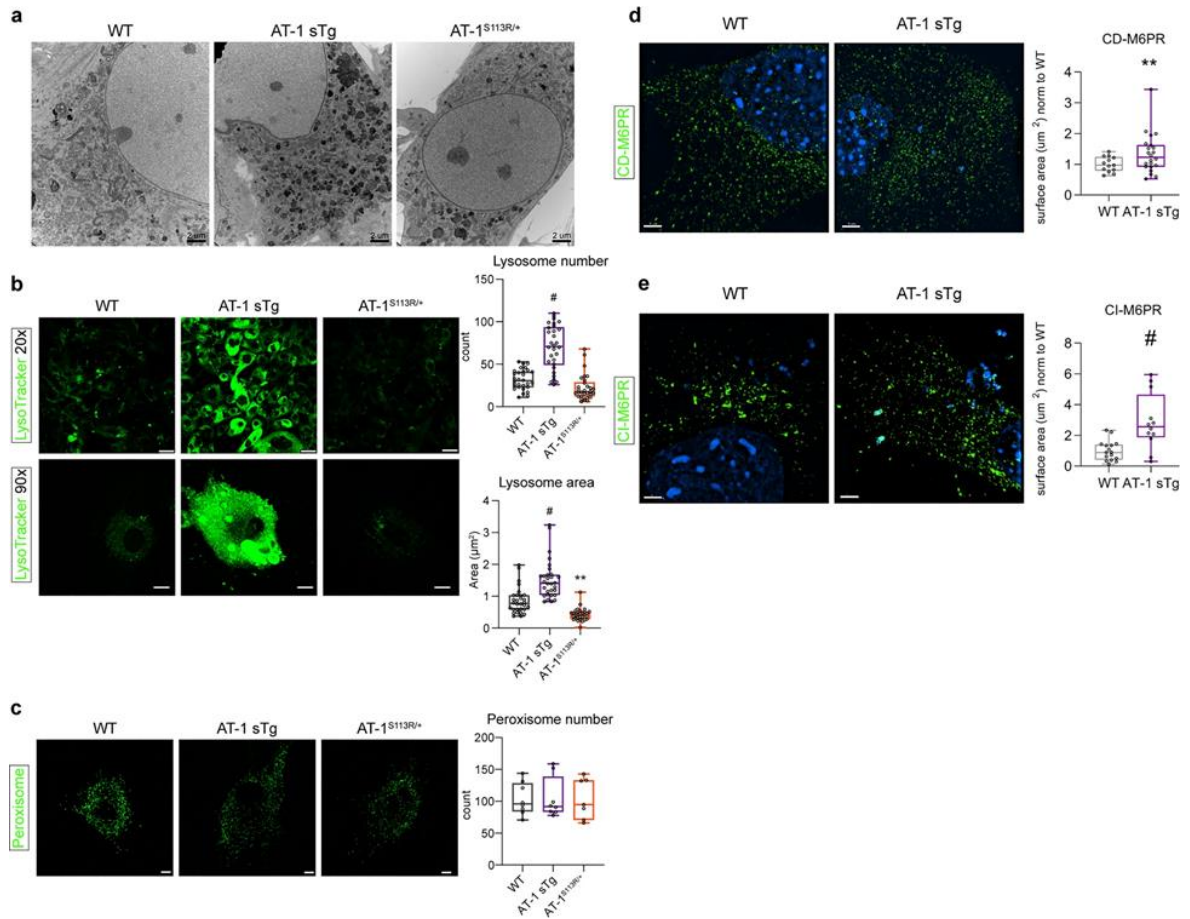
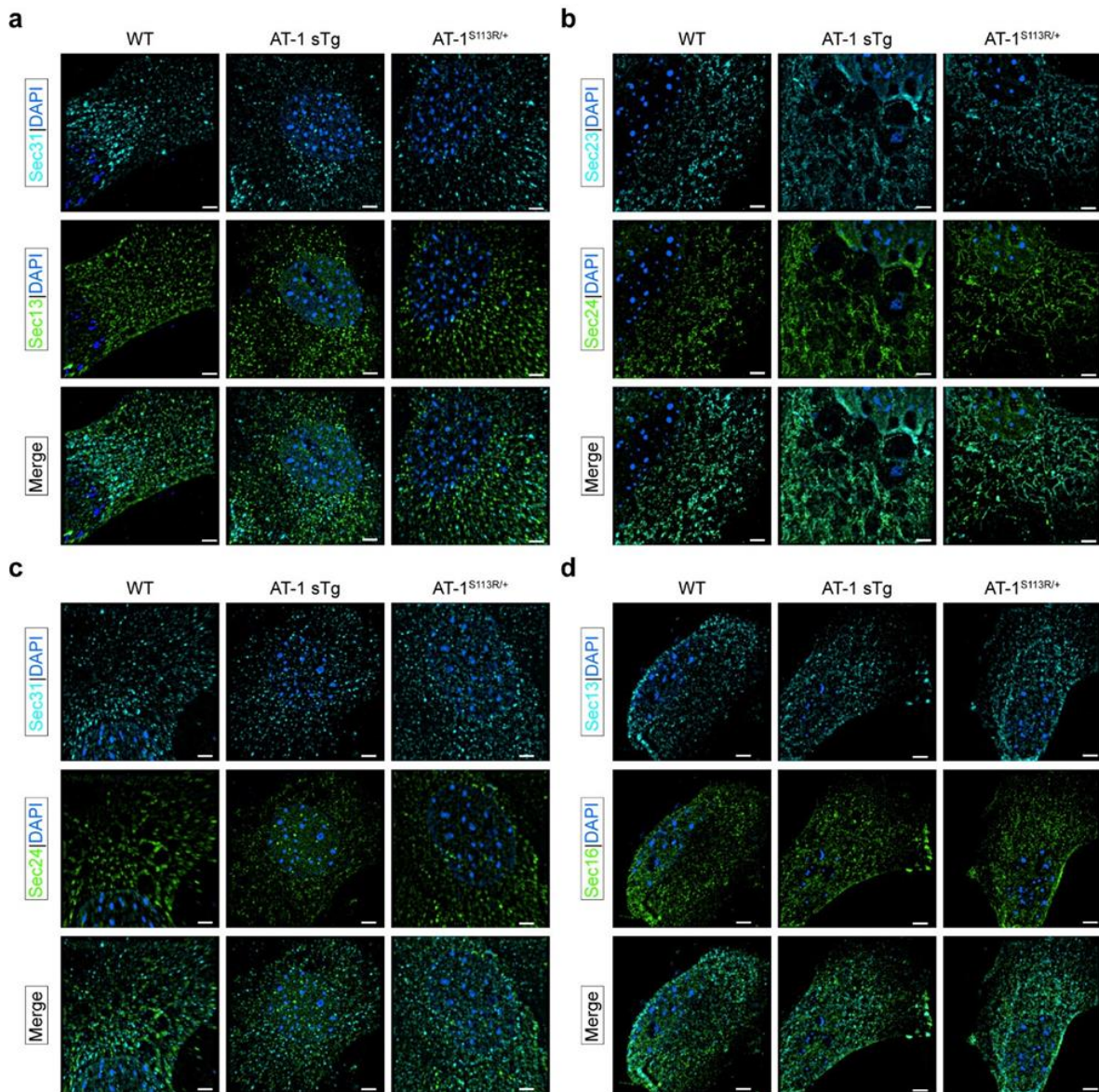
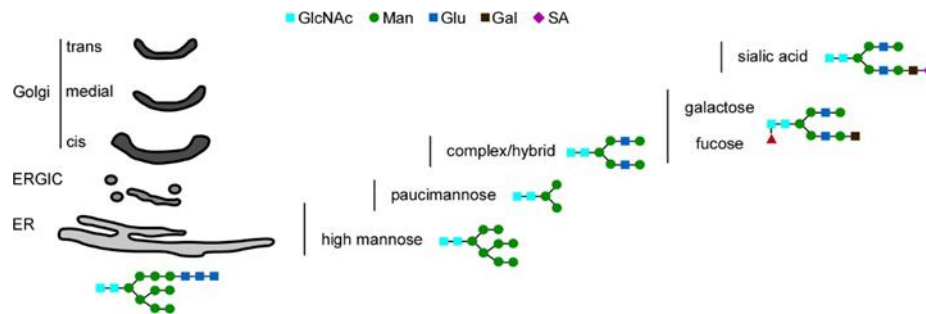


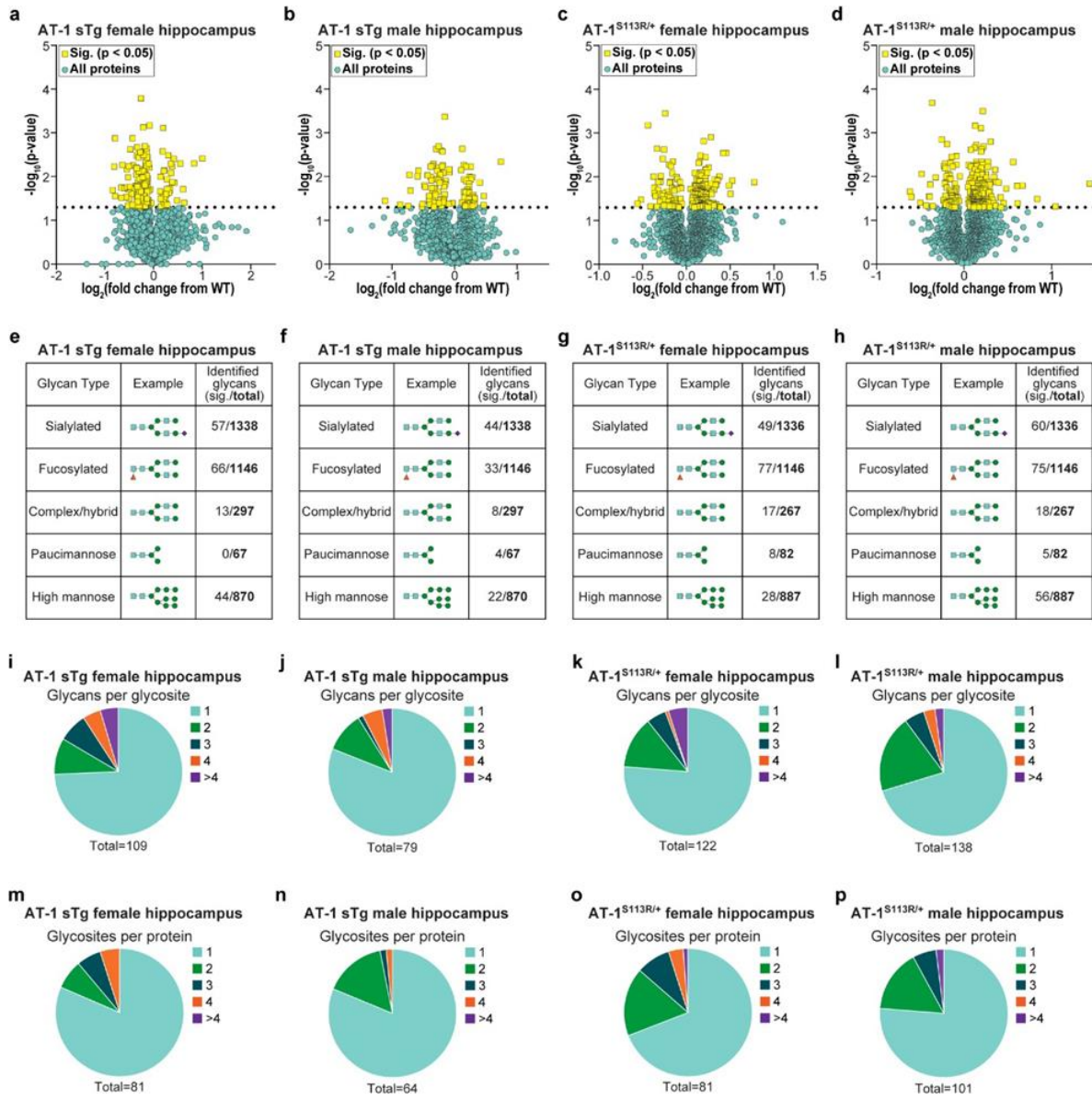
Figure 7. AT-1 sTg and AT-1^{S113R/+} display alterations in the CD-M6PR, CI-M6PR, and lysosomal networks. (a) Representative electron microscopy of MEFs from WT, AT-1 sTg, and AT-1^{S113R/+} (scale bar, 2 μ m). (b) Lysosomal morphology in primary-cultured MEFs using LysoTracker stain (20 \times scale bar, 30 μ m; 90 \times scale bar, 15 μ m) and quantified using Imaris reconstruction of surface area and number of puncta (n = 30 WT; n = 30 AT-1 sTg; n = 30 AT-1^{S113R/+}). (c) Peroxisome morphology in primary-cultured MEFs using Peroxisome CellLight stain (scale bar, 10 μ m) and quantified using Imaris reconstruction of number of puncta (n = 8 WT; n = 8 AT-1 sTg; n = 7 AT-1^{S113R/+}). (d) Representative CD-M6PR in primary cultured MEFs using CD-M6PR antibody (scale bar, 3 μ m). Surface area was quantified using Imaris reconstruction (n = 13 WT; n = 22 AT-1 sTg). (e) Representative CI-M6PR in primary cultured MEFs using CI-M6PR antibody (scale bar, 3 μ m). Surface area was quantified using Imaris reconstruction (n = 16 WT; n = 12 AT-1 sTg). Two-way ANOVA (b,c). Welch's t test (d,e). **P < 0.005; #P < 0.0001.



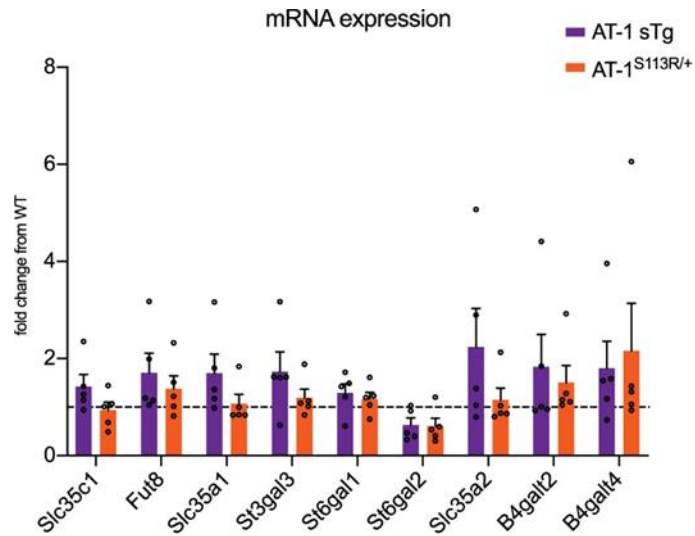
Supplementary Figure S1. Aberrant AT-1 models show no major changes in number nor assembly of COPII cargo structures. Representative SIM images of COPII proteins in primary-cultured MEFs: (a) Sec31 and Sec13; (b) Sec23 and Sec24; (c) Sec 31 and Sec24; (d) Sec13 and Sec16. Scale bar, 3 μ m.



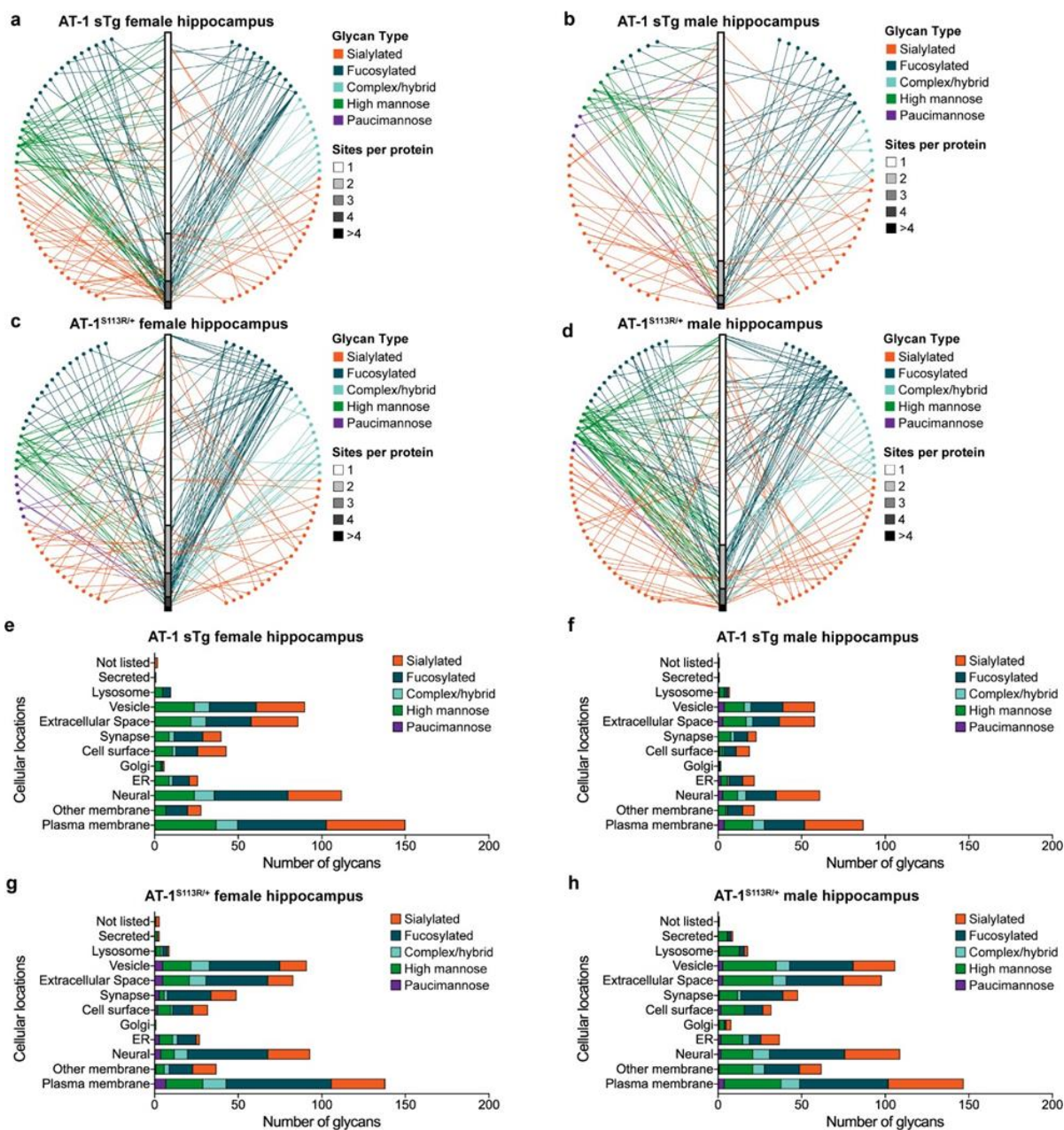
Supplementary Figure S2. Schematic view of N-glycan modification across the secretory pathway. The preformed ER-based GlcNAc₂Man₉Glu₃ is processed as the nascent glycoprotein transits through the Golgi apparatus. Only general oligosaccharide structures are shown here. Simple and complex variations of the structure presented here are possible.



Supplementary Figure S3. AT-1 sTg and AT-1^{S113R/+} display N-glycoproteomic changes across many hippocampal glycoforms. (a, b) Volcano plot displaying all quantified glycoproteins in the hippocampus of AT-1 sTg (a) female (n = 3) and (b) male (n = 3), compared with age-matched WT littermates. Statistically significant proteins (180 in female; 112 in male) are highlighted in yellow, and all other proteins are designated in blue. Student's T-test, $P < 0.05$. (c, d) Volcano plot displaying all quantified glycoproteins in the hippocampus of AT-1^{S113R/+} (c) female (n = 3) and (d) male (n = 3), compared with age-matched WT littermates. Statistically significant proteins (179 in female; 214 in male) are highlighted in yellow, and all other proteins are designated in blue. Student's T-test, $P < 0.05$. (e, f, g, h) Identified glycans are categorized into five glycan types, and are divided by significant over total identified in hippocampal (e) AT-1 sTg female, (f) AT-1 sTg male, (g) AT-1^{S113R/+} female, and (h) AT-1^{S113R/+} male. (i, j, k, l) Significant glycans per glycosite are identified in hippocampal (i) AT-1 sTg female, (j) AT-1 sTg male, (k) AT-1^{S113R/+} female, and (l) AT-1^{S113R/+} male. (m, n, o, p) Significant glycosites per protein are identified in hippocampal (m) AT-1 sTg female, (n) AT-1 sTg male, (o) AT-1^{S113R/+} female, and (p) AT-1^{S113R/+} male.



Supplementary Figure S4. AT-1 sTg and AT-1^{S113R/+} show no difference in mRNA of Golgi- specific glycosylation proteins. (a) mRNA levels of *Slc35c1*, *Fut8*, *Slc35a1*, *St3gal3*, *St6gal1*, *St6gal2*, *Slc35a2*, *B4galt2*, and *B4galt4* in MEF samples (MEFs from biologically independent animals; WT, n = 5; AT-1 sTg, n = 5; AT-1S113R/+, n = 5). Two-tailed Student's t test.



Supplementary Figure S5. AT-1 sTg and AT-1^{S113R/+} display a highly heterogeneous hippocampal secretome. (a, b, c, d) Network of glycan type plotted to glycoprotein for hippocampal (a) AT-1 sTg female, (b) AT-1 sTg male, (c) AT-1^{S113R/+} female, and (d) AT-1^{S113R/+} male. Circle represents glycan type, with each node representing a specific glycan tree. Glycans intersect with their protein, organized by the number of glycosites identified on that glycoprotein. (e, f, g, h) Glycosylation distribution according to subcellular localizations as defined by GO cellular component terms in hippocampal (e) AT-1 sTg female, (f) AT-1 sTg male, (g) AT-1^{S113R/+} female, and (h) AT-1^{S113R/+} male.

Supplementary Table S1. Cluster analysis of secretory pathway-related proteins (from Fig. 1)

Gene symbol	AT-1 sTg		AT-1 S113R/+	
	proteome	acetyl-proteome site (change)	proteome	acetyl-proteome site (change)
Lman1	0.313	ns	0.081; 0.026	ns
Sec31a	ns	K200 (0.470)	ns	K200 (-0.293)
Sec13	ns	ns	-0.367	ns
Hspa11	0.239	ns	ns	ns
Prkcsh	0.500	ns	-0.529	K206 (0.214)
Cyfip1	-0.976	ns	ns	ns
Pdia3	ns	K129 (-0.799); K173 (0.002); K448 (-0.093); K75 (0.063)	ns	K271 (0.113)
Ero11b	-1.126	ns	ns	ns
Ero11	0.346; -0.494	ns	ns	ns
Pabpc1	-0.526	K30 (-0.037); K333 (- 0.089)	-0.560	K229 (0.028); K231 (0.002)
Nup133	-0.219	ns	ns	ns
Phax	-0.753; -1.042	ns	ns	ns
Nup37	-0.496	ns	ns	ns
Dnaja1	ns	K14 (-0.009)	ns	ns
Hsp90ab1	0.276	K69 (-0.355)	ns	K435 (0.606); K607 (0.018)
Calr	0.597	K351 (-0.197)	ns	ns
P4hb	0.599; 0.596; 0.502	K426 (-0.207; 0.047); K446 (-0.011)	ns	K33 (-0.146)
Usp39	-0.035	ns	ns	ns
Rbm25	0.566; -0.642	ns	ns	ns
Nup188	-0.413	ns	ns	ns
Ranbp2	0.826	ns	ns	ns
Nup54	0.423	ns	ns	ns
Hsp90b1	ns	K75 (-0.237)	ns	K168 (0.081)
Rpn2	0.801	ns	ns	ns
Sel1l	0.530	ns	ns	ns

Vimp	0.725; 0.770	ns	ns	ns
Sart1	0.743; -1.008	ns	ns	ns
Pqbp1	-0.637	ns	ns	ns
Srsf5	-0.560	ns	ns	ns
Nup155	-0.276	ns	ns	ns
Hspa5	ns	K327 (0.116); K634 (0.102)	ns	K634 (-0.148); K341 (0.589); K475 (0.271)
Hsp90aa1	-0.561	K447 (-0.620); K500 (0.082)	ns	ns
Os9	0.382	ns	ns	ns
Vcp	ns	K651 (-0.012)	ns	ns
Ssr4	0.790	ns	ns	ns
Hnrnpm	0.348; 0.350	ns	ns	ns
Sf3b5	-0.008	ns	ns	ns
Ddx42	-0.816	ns	ns	ns
Hspa1b	-0.672	K220 (-0.201)	ns	K220 (0.336)
Dnajc3	0.533; 0.042	ns	ns	ns
Ddost	0.479	ns	ns	ns
Plaa	-0.285	ns	ns	ns
Dhx8	-0.629	ns	ns	ns
Pcbp1	0.555	ns	-0.335	K314 (-0.153)
Ddx46	0.517	ns	ns	ns
Hspa8	ns	ns	-0.189	K500 (-0.102)
Hspa1a	-0.672	ns	ns	ns
Sec63	0.288; -0.356	ns	ns	ns
Psm1	0.370	ns	ns	ns
Nploc4	-0.487	ns	ns	K307 (0.126)
Prpf8	-0.361	ns	ns	ns
Sf3a3	-0.768	ns	-0.343	ns
Phf5a	0.910	ns	ns	ns
Cdc5l	-1.098	ns	ns	ns
Sec62	-0.596	ns	ns	ns
Uba52	0.857	ns	ns	ns
Psm11	0.681	ns	ns	ns

Psma5	0.426; 0.501	ns	ns	ns
Psma7	0.736; 0.718; 0.723	ns	ns	ns
Sf3b4	-0.498	ns	ns	ns
Magoh	-1.519	ns	ns	ns
Eif2ak2	-0.467	ns	ns	ns
Magoh	-1.519	ns	ns	ns
Eif2ak2	-0.467	ns	ns	ns
Rpl18a	0.744	ns	ns	ns
Rpl14	1.143	ns	ns	ns
Psmc6	0.438	ns	ns	ns
Psmc13	0.320	ns	ns	ns
Psma2	0.672	ns	ns	ns
Psma1	0.466; 0.690; 0.692	ns	ns	ns
Rps2	ns	ns	-0.175; -0.176	ns
Rpl13	0.500; 0.462	ns	ns	ns
Rpl27a	1.769	ns	ns	ns
Sec61a1	0.576; 0.574	ns	ns	ns
Psmc6	-0.287	ns	ns	ns
Psmc1	-0.396	ns	-0.082	ns
Rps271	-0.786	ns	ns	ns
Rplp0	0.387; 0.476; 0.491	ns	ns	ns
Rplp2	0.552	ns	ns	ns
Sec61b	0.828	ns	ns	ns
Psma6	0.631	ns	ns	ns
Psmc4	-1.092	K36 (0.051)	ns	ns
Eif4a2	-0.785	ns	-0.291	ns
Eif2s1	0.268	ns	ns	ns
Rps18	0.045	K25 (0.107)	ns	ns
Rps25	0.202	ns	ns	ns
Rpl19	0.003	K46 (-0.034)	ns	ns
Rpl6	0.344	ns	0.289	ns

Rpl26	0.658	K2 (0.061)	ns	ns
Rad23a	-0.320	ns	ns	ns
Eif4b	-0.694	ns	ns	ns
Eif3d	0.198	ns	ns	K138 (-0.002)
Rps23	0.907	ns	ns	ns
Rps15a	ns	ns	ns	K71 (-0.192)
Rpl3	0.321; 0.483	ns	ns	ns
Rpl8	0.868	K177 (0.004); K234 (-0.321)	ns	ns
Ube2d3	-0.343	ns	ns	ns
Eif5	0.471	ns	ns	ns
Eif3j1	-0.403	ns	ns	ns
Rps9	0.538	K139 (-0.056)	ns	K47 (-0.057)
Rps19	0.414	ns	ns	ns
Rps21	0.923	ns	ns	ns
Rpl18	ns	K78 (-0.246)	ns	ns
Rpl28	ns	K22 (0.119); K72 (-0.366)	ns	K72 (0.296); K22 (0.113)
Ube2j2	-0.553	ns	ns	ns
Eif3j2	-0.403	ns	ns	ns
Rps28	0.398	ns	-0.296	ns
Rps16	0.496	ns	ns	ns
Rps17	0.922; 0.658	ns	ns	K72 (0.055)
Rpl5	0.598; 0.683	ns	ns	K270 (0.025); K197 (0.112)
Rpl35	1.028	K35 (-0.070)	ns	ns
Eif3b	0.426	ns	ns	ns
Rps20	1.727; 0.505	ns	ns	ns
Mrpl15	-0.355	ns	ns	ns
Rpsa	-0.270	ns	-0.260; -0.415	ns
Mrpl24	-0.035	ns	ns	ns
Rpl13a	0.395; 0.817	ns	ns	K51 (0.243)
Mrpl10	-0.253	ns	ns	ns
Mrpl18	0.181	ns	ns	ns

Supplementary Table S2. Primers used for Real Time PCR

Primer Pair	Forward Sequence	Reverse Sequence
<i>SLC35C1</i>	5'-GCGCTGACTGGAGTCTCTG-3'	5'-AGGTGACAAAAATGGGGGTATC-3'
<i>FUT8</i>	5'-CTTGCAGACCGACTCCTAAGA-3'	5'-CAAGGTTGTGGACGAATCAAGT-3'
<i>SLC35A2</i>	5'-GTTGGAACCTGGGTCCACTAC-3'	5'-GGTGAGACCTTTGAGCACTTC -3'
<i>B4GALT2</i>	5'-GGAGCACCACCTACGCTATTG-3'	5'-GATTCGGGTCATCCATAGGGA-3'
<i>B4GALT4</i>	5'-GCCATCCTCATTCCACAC-3'	5'-GTCCCAGTTCTCCTCCTT-3'
<i>B4GALT5</i>	5'-CCAACCACGACCTTTCTTCCT-3'	5'-ATCGTCCATTGCGATCTCACT-3'
<i>SLC35A1</i>	5'-GCTCCGGCGAGAGAAAATGT-3'	5'-TCTTAAAGCTACGGTGTAAGCG-3'
<i>ST3GAL1</i>	5'-AAGCTGGACTCTAAACTGCCT-3'	5'-TGCTGGCTTGGAGAACCTG-3'
<i>ST6GAL1</i>	5'-CTCCTGTTTGCCATCATCTGC-3'	5'-GGGTCTTGTTTGCTGTTTGAGA-3'
<i>ST6GAL2</i>	5'-CCAGGTGTACCTCTGAGCCA-3'	5'-AGCACTGTCAATGAAGTGATGG-3'
<i>GAPDH</i>	5'-AGGTTCGGTGTGAACGGATTTG-3'	5'-TGTAGACCATGTAGTTGAGGTCA-3'

References

1. Farrugia, M. A. & Puglielli, L. Nepsilon-lysine acetylation in the endoplasmic reticulum—a novel cellular mechanism that regulates proteostasis and autophagy. *J. Cell Sci.* <https://doi.org/10.1242/jcs.221747> (2018).
2. Ding, Y., Dellisanti, C. D., Ko, M. H., Czajkowski, C. & Puglielli, L. The endoplasmic reticulum-based acetyltransferases, ATase1 and ATase2, associate with the oligosaccharyl-transferase to acetylate correctly folded polypeptides. *J. Biol. Chem.* 289, 32044–32055 (2014).
3. Jonas, M. C., Pehar, M. & Puglielli, L. AT-1 is the ER membrane acetyl-CoA transporter and is essential for cell viability. *J. Cell. Sci.* 123, 3378–3388 (2010).
4. Peng, Y. *et al.* Deficient import of acetyl-CoA into the ER Lumen causes neurodegeneration and propensity to infections, inflammation, and cancer. *J. Neurosci.* 34, 6772–6789 (2014).
5. Hullinger, R. *et al.* Increased expression of AT-1/SLC33A1 causes an autistic-like phenotype in mice by affecting dendritic branching and spine formation. *J. Exp. Med.* 213, 1267–1284 (2016).
6. Peng, Y. *et al.* Increased transport of acetyl-CoA into the endoplasmic reticulum causes a progeria-like phenotype. *Aging Cell* <https://doi.org/10.1111/accel.12820> (2018).
7. Ko, M. H. & Puglielli, L. Two endoplasmic reticulum (ER)/ER golgi intermediate compartment-based lysine acetyltransferases post-translationally regulate BACE1 levels. *J. Biol. Chem.* 284, 2482–2492 (2009).
8. Mak, A. B. *et al.* Post-translational regulation of CD133 by ATase1/ATase2-mediated lysine acetylation. *J. Mol. Biol.* 426, 2175–2182 (2014).
9. Huppke, P. *et al.* Mutations in SLC33A1 cause a lethal autosomal-recessive disorder with congenital cataracts, hearing loss, and low serum copper and ceruloplasmin. *Am. J. Hum. Genet.* 90, 61–68 (2012).
10. Chiplunkar, S. *et al.* Huppke-Brendel syndrome in a seven months old boy with a novel 2-bp

- deletion in SLC33A1. *Metab Brain Dis.* 31, 1195–1198 (2016).
11. Lin, P. *et al.* A missense mutation in SLC33A1, which encodes the acetyl-CoA transporter, causes autosomal-dominant spastic paraplegia (SPG42). *Am. J. Hum. Genet.* 83, 752–759 (2008).
 12. Sanders, S. J. *et al.* Multiple recurrent de novo CNVs, including duplications of the 7q11.23 Williams syndrome region, are strongly associated with autism. *Neuron* 70, 863–885 (2011).
 13. Prasad, A. *et al.* A discovery resource of rare copy number variations in individuals with autism spectrum disorder. *G3* 2, 1665–1685 (2012).
 14. Dieterich, I. A. *et al.* Acetyl-CoA flux regulates the proteome and acetyl-proteome to maintain intracellular metabolic crosstalk. *Nat. Commun.* 10, 3929. <https://doi.org/10.1038/s41467-019-11945-9> (2019).
 15. Hullinger, R. & Puglielli, L. Molecular and cellular aspects of age-related cognitive decline and Alzheimer's disease. *Behav. Brain Res.* 322, 191–205. <https://doi.org/10.1016/j.bbr.2016.05.008> (2017).
 16. Rapoport, T. A., Li, L. & Park, E. Structural and mechanistic insights into protein translocation. *Annu. Rev. Cell. Dev. Biol.* 33, 369–390 (2017).
 17. Feige, M. J. & Hendershot, L. M. Disulfide bonds in ER protein folding and homeostasis. *Curr. Opin. Cell Biol.* 23, 167–175 (2011).
 18. Lederkremer, G. Z. *et al.* Structure of the Sec23p/24p and Sec13p/31p complexes of COPII. *Proc. Natl. Acad. Sci. U.S.A.* 98, 10704–10709 (2001).
 19. Stagg, S. M. *et al.* Structure of the Sec13/31 COPII coat cage. *Nature* 439, 234–238 (2006).
 20. Zanetti, G., Pahuja, K. B., Studer, S., Shim, S. & Schekman, R. COPII and the regulation of protein sorting in mammals. *Nat. Cell. Biol.* 14, 20–28 (2012).
 21. Budnik, A. & Stephens, D. J. ER exit sites—localization and control of COPII vesicle formation.

- FEBS Lett.* 583, 3796–3803 (2009).
22. Peotter, J., Kasberg, W., Pustova, I. & Audhya, A. COPII-mediated trafficking at the ER/ERGIC interface. *Traffic* 20, 491–503 (2019).
 23. Bi, X., Corpina, R. A. & Goldberg, J. Structure of the Sec23/24-Sar1 pre-budding complex of the COPII vesicle coat. *Nature* 419, 271–277 (2002).
 24. Watson, P., Townley, A. K., Koka, P., Palmer, K. J. & Stephens, D. J. Sec16 defines endoplasmic reticulum exit sites and is required for secretory cargo export in mammalian cells. *Traffic* 7, 1678–1687 (2006).
 25. Rivera, V. M. *et al.* Regulation of protein secretion through controlled aggregation in the endoplasmic reticulum. *Science* 287, 826–830 (2000).
 26. Bowen, A. B., Bourke, A. M., Hiester, B. G., Hanus, C. & Kennedy, M. J. Golgi-independent secretory trafficking through recycling endosomes in neuronal dendrites and spines. *eLife* <https://doi.org/10.7554/eLife.27362> (2017).
 27. Hirschberg, C. B., Robbins, P. W. & Abeijon, C. Transporters of nucleotide sugars, ATP, and nucleotide sulfate in the endoplasmic reticulum and Golgi apparatus. *Annu. Rev. Biochem.* 67, 49–69 (1998).
 28. Millar, A. H. *et al.* The scope, functions, and dynamics of posttranslational protein modifications. *Annu. Rev. Plant Biol.* <https://doi.org/10.1146/annurev-arplant-050718-100211> (2019).
 29. Chang, I. J., He, M. & Lam, C. T. Congenital disorders of glycosylation. *Ann. Transl. Med.* 6, 477. <https://doi.org/10.21037/atm.2018.10.45> (2018).
 30. Narimatsu, H. *et al.* Current technologies for complex glycoproteomics and their applications to biology/disease-driven glycoproteomics. *J. Proteome Res.* <https://doi.org/10.1021/acs.jproteome.8b00515> (2018).

31. Yu, Q. *et al.* Electron-transfer/higher-energy collision dissociation (EThcD)-enabled intact glycopeptide/glycoproteome characterization. *J. Am. Soc. Mass Spectrom.* 28, 1751–1764 (2017).
32. Hirst, J., Futter, C. E. & Hopkins, C. R. The kinetics of mannose 6-phosphate receptor trafficking in the endocytic pathway in HEp-2 cells: the receptor enters and rapidly leaves multivesicular endosomes without accumulating in a prelysosomal compartment. *Mol. Biol. Cell.* 9, 809–816 (1998).
33. Wang, S. *et al.* A role of Rab29 in the integrity of the trans-Golgi network and retrograde trafficking of mannose-6-phosphate receptor. *PLoS ONE* 9, e96242. <https://doi.org/10.1371/journal.pone.0096242> (2014).
34. Pehar, M., Jonas, M. C., Hare, T. M. & Puglielli, L. SLC33A1/AT-1 protein regulates the induction of autophagy downstream of IRE1/XBP1 pathway. *J. Biol. Chem.* 287, 29921–29930 (2012).
35. Peng, Y. *et al.* Improved proteostasis in the secretory pathway rescues Alzheimer’s disease in the mouse. *Brain* 139, 937–952 (2016).
36. Freiman, R. N. & Tjian, R. Regulating the regulators: Lysine modifications make their mark. *Cell* 112, 11–17 (2003).
37. Xu, Y. X., Liu, L., Caffaro, C. E. & Hirschberg, C. B. Inhibition of Golgi apparatus glycosylation causes endoplasmic reticulum stress and decreased protein synthesis. *J. Biol. Chem.* 285, 24600–24608 (2010).
38. Lindahl, A. J., Lawton, A. J., Baeza, J., Dowell, J. A. & Denu, J. M. Site-specific lysine acetylation stoichiometry across subcellular compartments. *Methods Mol. Biol.* 1983, 79–106 (2019).
39. Baeza, J. *et al.* Revealing dynamic protein acetylation across subcellular compartments. *J.*

- Proteome Res.* 19, 2404–2418 (2020).
40. Baeza, J. *et al.* Stoichiometry of site-specific lysine acetylation in an entire proteome. *J. Biol. Chem.* 289, 21326–21338 (2014).
 41. Frost, D. C., Greer, T. & Li, L. High-resolution enabled 12-plex DiLeu isobaric tags for quantitative proteomics. *Anal. Chem.* 87, 1646–1654 (2015).
 42. Cui, Y. *et al.* Finding the sweet spot in ERLIC mobile phase for simultaneous enrichment of N-glyco and phosphopeptides. *J. Am. Soc. Mass Spectrom.* 30, 2491–2501 (2019).
 43. Selman, M. H., Hemayatkar, M., Deelder, A. M. & Wührer, M. Cotton HILIC SPE microtips for microscale purification and enrichment of glycans and glycopeptides. *Anal. Chem.* 83, 2492–2499 (2011).
 44. Yu, Q., Shi, X., Feng, Y., Kent, K. C. & Li, L. Improving data quality and preserving HCD-generated reporter ions with EThcD for isobaric tag-based quantitative proteomics and proteome-wide PTM studies. *Anal. Chim. Acta* 968, 40–49 (2017).
 45. Tyanova, S. *et al.* The Perseus computational platform for comprehensive analysis of (prote)omics data. *Nat. Methods* 13, 731–740 (2016).
 46. Riley, N. M., Hebert, A. S., Westphall, M. S. & Coon, J. J. Capturing site-specific heterogeneity with large-scale N-glycoproteome analysis. *Nat. Commun.* 10, 1311. <https://doi.org/10.1038/s41467-019-09222-w> (2019).
 47. Kanehisa, M. Toward understanding the origin and evolution of cellular organisms. *Protein Sci.* 28, 1947–1951 (2019).
 48. Kanehisa, M., Furumichi, M., Sato, Y., Ishiguro-Watanabe, M. & Tanabe, M. KEGG: Integrating viruses and cellular organisms. *Nucleic Acids Res.* <https://doi.org/10.1093/nar/gkaa970> (2020).

Chapter 5. Discussion and future directions

Cellular function and health require proper transport of a diversity of proteins through the early secretory pathway, and disruptions in this pathway have been linked to a number of diseases including neurological disorders.^{1,2} Previous research has established that the initial step in protein transport out of the ER largely relies on coat protein complex II (COPII) to properly package and facilitate cargo transport from the ER to the ER Golgi intermediate compartment (ERGIC). This process is orchestrated through a number of proteins and their specific functions in mediating COPII transport. Integral to COPII function is the clustering of the COPII machinery, which has largely been linked to TFG.^{3,4} Interestingly, mutations in TFG have been identified in several neurological disorders and current research has begun to answer the question of how such mutations in the early secretory pathway specifically affect neuronal health and function and eventually lead to disease.^{5,6,7,8,9,10}

Utilizing one of these mutations in TFG, this work has identified a defect in the rate at which proteins are transported from the ER to the Golgi as well as a previously undescribed role for TFG in facilitating recycling endosome transport in neurites.¹¹ Taken together, this has highlighted how a mutation in a ubiquitously expressed protein specifically affects the central nervous system. The p.R106C TFG mutation, identified in patients with Hereditary Spastic Paraplegia (HSP), showed a distinct lack of TFG clustering at ERES which resulted in a delay in the trafficking of L1 cell adhesion molecule (L1CAM) transport from the ER to the Golgi.¹¹ Interestingly, this work also revealed that TFG clusters are present in axons and dendrites, predominantly colocalizing with Rab4-positive endosomes, and that the p.R106C TFG mutation decreases both the number and velocity of these recycling endosomes. Such defects in endosomal transport in neurites was linked to a decrease in clustering of important inhibitory post-synaptic proteins, gephyrin and GABA_AR.¹¹ Although this research found changes to a few select proteins, it is likely that the p.R106C TFG mutation has an impact on the overall transport of proteins, both through its canonical role in the early secretory pathway as well as the newly described role via recycling endosomes.

The mechanism by which TFG functions in facilitating recycling endosome transport in neurites still remains unknown. Based on the function of TFG in COPII transport, it may function to sequester or cluster cargo and/or endosomes to specific sites to enable transport.⁴ Further research is needed to answer these and other questions related to how this function is specifically regulated to neurites. Although this work did not identify lysosomal swelling, such as have been identified in other HSP models, a closer examination of lysosome function and the ubiquitin-proteasome system is necessary given the close relationship between the endosome and lysosomal systems. Given the long lifespan of neurons, even slight perturbations in this pathway may lead to cellular toxicity and eventual death over time.

To further understand the relationship between mutations in TFG and neurological disorders, other cell types found in the CNS should be evaluated. Aside from the cortical neurons, used in the work to understand the p.R106C mutation in TFG, glial cells, such as astrocytes, should be investigated to understand the impacts of this mutation outside of neurons. Astrocytes have many important roles in the CNS and are known to promote neuronal health and recovery after injury. However, defects in astrocyte function have also been linked to neurological disorders such as Alzheimer and Huntington disease.¹² To understand if and how astrocytes are affected in the R106C HSP model, primary astrocytes can be collected and used to determine if TFG localization is distributed, such as found in neurons homozygous for the p.R106C TFG mutation, and if there is any impact on trafficking through the early secretory pathway. Further studies can also be used to determine if there are any downstream effects on overall astrocyte function that may contribute to a decline in neuronal health. Additionally, rodent models may be used for gene therapy experiments to determine if early-stage overexpression of WT TFG leads to marked rescue of the observed gait defects. Such experiments can directly target neurons, glial cells such as astrocytes, or both, to determine the impact each cell type has on the progression of disease.

Although a considerable amount of research has been dedicated to unfolding the mechanism by which TFG functions in its canonical role in the early secretory pathway there are still many nuances yet to be understood. One important question is how this and other downstream pathways are altered in the presence of disease-causing mutations, such as TFG p.R106C. By utilizing a rodent model that strongly recapitulates patient phenotypes and provides a physiologically relevant *in vivo* model, this work illustrated a neuronal specific impact on protein transport that resulted in a decrease in synaptic protein clustering. Highlighting why neurons may be specifically susceptible to deviations in proper protein transport. Integral to this work and findings was the development and use of physiologically relevant models that avoided overexpression artifacts. Continued work in this p.R106F TFG mutation, as well as other neurological disorders, will benefit immensely from the use of such relevant models.

References

1. Harlalka, G. V *et al.* Novel Genetic , Clinical , and Pathomechanistic Insights into TFG-Associated Hereditary Spastic Paraplegia. *Hum. Mutat.* 37, 1157–1161 (2016).
2. Blackstone, C. Converging cellular themes for the hereditary spastic paraplegias. *Curr. Opin. Neurobiol.* 51, 139–146 (2018).
3. Peotter, J., Kasberg, W., Pustova, I. & Audhya, A. COPII-mediated trafficking at the ER/ERGIC interface. *Traffic* 1–13 (2019). doi:10.1111/tra.12654
4. Johnson, A. *et al.* TFG clusters COPII-coated transport carriers and promotes early secretory pathway organization. *EMBO* 34, 811–827 (2015).
5. Slosarek, E. L. *et al.* Pathogenic TFG Mutations Underlying Hereditary Spastic Paraplegia Impair Secretory Protein Trafficking and Axon Fasciculation. *Cell Rep.* 24, 2248–2260 (2018).
6. Alavi, A. *et al.* HMSN-P caused by p.Pro285Leu mutation in TFG is not confined to patients with Far East ancestry. *Neurobiol. Aging* 36, 1606.e1-1606.e7 (2015).
7. Maeda, K., Idehara, R. & Mukaisho, K. I. Presence of colocalised phosphorylated TDP-43 and TFG proteins in the frontotemporal lobes of HMSN-P. *J. Neurol. Neurosurg. Psychiatry* 91, 1231–1232 (2020).
8. Tsai, P. C. *et al.* A novel TFG mutation causes Charcot-Marie-Tooth disease type 2 and impairs TFG function. *Neurology* 83, 903–912 (2014).
9. Yoo, D., Lee, W., Lee, S., Sung, J. & Jeon, G. S. A Novel TFG Mutation in a Korean Family with α -Synucleinopathy and Amyotrophic Lateral Sclerosis. *Mov. Disord.* 37, 384–391 (2022).
10. Elsayed, L. E. O. *et al.* Hereditary spastic paraplegias: identification of a novel SPG57 variant affecting TFG oligomerization and description of HSP subtypes in Sudan. *Eur. J. Hum. Genet.* 25, 100–110 (2016).
11. Peotter, J. L. *et al.* TFG regulates multiple trafficking pathways in cortical neurons to promote

their long-term maintenance. *Manuscript in Preparation*.

12. Siracusa, R., Fusco, R. & Cuzzocrea, S. Astrocytes: Role and functions in brain pathologies. *Front. Pharmacol.* 10, 1–10 (2019).

Appendix A. Pathogenic TFG mutations underlying Hereditary Spastic Paraplegia impair secretory protein trafficking and axon fasciculation

The work presented in this appendix has been published:

Slosarek, E.L., Schuh, A.L., Pustova, I., Johnson, A., Bird, J., Johnson, M., Frankel, E.B., Bhattacharya, N., Hanna, M.G., Burke, J.E., Ruhl, D.A., Quinney, K., Block, S., **Peotter, J.L.**, Chapman, E.R., Sheets, M.D., Butcher, S.E., Stagg, S.M., Audhya, A. (2018) Pathogenic TFG mutations underlying Hereditary Spastic Paraplegia impair secretory protein trafficking and axon fasciculation. *Cell Reports*.

Abstract

Length-dependent axonopathy of the corticospinal tract causes lower limb spasticity and is characteristic of several neurological disorders, including hereditary spastic paraplegia (HSP) and amyotrophic lateral sclerosis. Mutations in Trk-fused gene (TFG) have been implicated in both diseases, but the pathomechanisms by which these alterations cause neuropathy remain unclear. Here, we biochemically and genetically define the impact of a mutation within the TFG coiled-coil domain, which underlies early-onset forms of HSP. We find that the TFG (p.R106C) mutation alters compaction of TFG ring complexes, which play a critical role in the export of cargoes from the endoplasmic reticulum (ER). Using CRISPR-mediated genome editing, we engineered human stem cells that express the mutant form of TFG at endogenous levels and identified specific defects in secretion from the ER and axon fasciculation following neuronal differentiation. Together, our data highlight a key role for TFG-mediated protein transport in the pathogenesis of HSP.

1. Introduction

The pyramidal motor system in humans directs voluntary movement. In particular, long cortical neurons that extend from layer V of the cerebral cortex into the spinal cord enable skilled limb mobility.⁴ The maintenance of these corticospinal neurons depends heavily on axonal transport of proteins, lipids, organelles, and other vesicular carriers. Thus, it is perhaps unsurprising that numerous regulators of membrane trafficking and organelle dynamics have been implicated in neurodegenerative disease.^{42, 33} Among inherited neuropathies, hereditary spastic paraplegias (HSPs) and hereditary motor and sensory neuropathies (HMSNs) are the most common, collectively affecting hundreds of thousands of individuals worldwide.^{7, 43} Despite their prevalence and severity, specific pathomechanisms underlying most of these disorders remain unknown. Nevertheless, the genetic diversity of HSPs provides an opportunity to delineate biochemical pathways that contribute to lifelong axon function.

With recent advances in whole-genome and exome sequencing technologies, there has been a surge in the identification of mutations that contribute to the development of peripheral neuropathies. Using this approach, we and others have demonstrated that point mutations in tropomyosin receptor kinase fused gene (TFG) (also known as SPG57) contribute to the pathology of HSPs, HMSNs, and amyotrophic lateral sclerosis (ALS).^{14, 3, 18, 48} However, in none of these cases is it clear how the mutations lead to axonopathy. Based on functional and localization studies, TFG plays an important role in maintaining the integrity of the early secretory pathway.^{45, 16, 11, 22} In the absence of TFG, subdomains on the endoplasmic reticulum (ER) that produce COPII-coated transport carriers separate away from ER-Golgi intermediate compartments (ERGICs), slowing the export of secretory cargoes from the ER and triggering an ER stress response.¹⁶ Additionally, the organization of the ER is impaired following TFG depletion, as is the normal distribution of mitochondria in fibroblasts.^{45, 16} Recently, the effect of overexpressing a mutant form of TFG implicated in HSP (p.R106C) was assessed in cultured murine neurons, which revealed a reduction in the size of mitochondria in neurites.¹² Together, these

data suggest that the pathogenicity of the TFG (p.R106C) mutation may relate to an unidentified role in regulating mitochondrial function, although the artificial nature of overexpressing TFG or depleting it using small interfering RNAs (siRNAs) poorly simulates the disease condition.

A more physiologically relevant alternative to defining the impact of mutations in neurons has evolved with the development of stem cell technologies. Tissue samples acquired from patients are now routinely cultured and reprogrammed *in vitro* to generate induced pluripotent stem cells (iPSCs), which can be differentiated toward a number of distinct fates, including the telencephalic glutamatergic cortical neurons that are affected in HSP.^{41, 8} Previous studies showed that patient-derived fibroblasts harboring the pathogenic SPG3A (p.P342S) mutation could be reprogrammed and differentiated into forebrain neurons, enabling the identification of neurite outgrowth defects and reduced mitochondrial transport in mutant cells.⁸ Although this approach is promising, it remains to be determined whether the observed phenotypes are a direct result of the SPG3A (p.P342S) mutation alone or a combination of the hypomorphic SPG3A allele with other genetic variants in the background used. More recently, clustered regularly interspaced short palindromic repeats (CRISPR)-mediated genome editing has been used to correct mutations implicated in disease and determine their relevance to phenotypes observed.^{47, 19} Nevertheless, the use of patient-derived iPSCs introduces genetic variability, which can complicate the interpretation of data collected.

More than 70 genetic loci have been linked to the various forms of HSP, with most gene products identified possessing putative roles in axon pathfinding, axon myelination, organelle dynamics, motor-dependent transport, and/or lipid metabolism.²⁰ In the majority of cases, there is minimal information regarding the functional consequences of the specific mutations identified. Here, we use a combination of structural biology, stem cell technology, and high-resolution imaging to define the impact of the TFG (p.R106C) mutation. Our findings demonstrate that the mutation impairs TFG complex assembly, which interferes with its function in the early secretory pathway, promotes ER stress,

and disrupts the ability of axons to self-associate. These data suggest that the long axons of the cortico-spinal tract are particularly susceptible to relatively modest deficits in protein secretion and highlight this pathway as a potential therapeutic target for axonopathies that affect peripheral motor function.

2. Results

A clinically relevant mutation in TFG disrupts its ability to form compact ring complexes

Mutations within the TFG coiled-coil domain (amino acids 97–124) have been suggested to impair its function and underlie early-onset forms of HSP.^{3, 12} To gain an understanding of the mechanism by which such mutations affect TFG, we conducted a series of biochemical and structural studies comparing the recombinant wild-type protein with the TFG (p.R106C) mutant, which has been identified in numerous HSP patients. Since the C terminus of TFG is intrinsically disordered¹⁶, we focused our attention on the TFG N terminus (amino acids 1–193), which includes a PB1 domain (amino acids 10–91), as well as the coiled-coil domain, followed by a serine/threonine-rich region (Figure 1A). We showed previously that the TFG (p.R106C) mutation modestly alters the hydrodynamic properties of TFG³, but its specific impact on the helical character of the coiled-coil domain remains unclear. To address this issue, we first conducted circular dichroism (CD) spectroscopy on various TFG isoforms. These studies revealed no significant differences in the helicity of the TFG (p.R106C) mutant as compared to wild-type TFG (Figure 1B). In contrast, mutation of six key leucine residues to valine (L97V, L105V, L109V, L112V, L120V, and L123V), which is predicted to completely disorder the heptad repeat pattern of the coiled-coil domain, resulted in a dramatic change in the circular dichroism spectrum, consistent with a loss in over-all helicity (Figure 1B). We next examined the hydrodynamic properties of the isolated coiled-coil domain of wild-type TFG and the TFG (p.R106C) mutant. Based on a combination of size exclusion chromatography and multiangle light scattering, both proteins exhibited a similar ability to homo-oligomerize *in vitro* (Figures 1C and 1D). In contrast, mutation of the six leucine

residues within the coiled-coil domain to valine blocked self-association, resulting in the presence of monodisperse monomers of approximately 26 ± 3 kDa in mass (predicted molecular weight of 20.1 kDa) (Figures 1C and 1D). Together, these data indicate that the TFG (p.R106C) mutation does not fully disrupt or unfold the coiled-coil domain.

To gain further insight into the impact of the TFG (p.R106C) mutation, we next used small-angle X-ray scattering (SAXS), a solution-based technique that can report on the conformation of biological macromolecules.²⁷ We used a smaller fragment of TFG for these studies (amino acids 1–138) to facilitate *ab initio* modeling. SAXS analysis of wild-type TFG produced consistent scattering profiles over several protein concentrations (150–750 mM) (Figure 1E), and the excluded particle (Porod) volume was used to estimate its mass to be ~130 kDa, consistent with the predicted mass of 126.1 kDa for a TFG octamer, based on amino acid composition. From these data, we also determined the radius of gyration (R_g) to range from 35.1 ± 0.1 Å (750 mM) to 38.0 ± 0.3 Å (150 mM), depending on protein concentration (Figures S1A–S1C). Similarly, the maximal inter-atomic distance (D_{max}) was concentration dependent, ranging from 94 to 120 Å, with higher compaction of the octamer observed at elevated protein concentrations (Figure S1C). SAXS envelopes were defined *ab initio* based on the scattering profiles. Seventeen independent models were aligned and averaged (based on two different protein concentrations), with a mean normalized spatial discrepancy (NSD) of 0.83, to reveal an octameric ring-like structure comparable in organization to that defined previously by three-dimensional single-particle electron microscopy (Figure 1F). The extensive similarity of the envelope with our prior electron microscopy-based analysis of TFG validates the use of SAXS for studying the impact of the TFG (p.R106C) mutation on the conformation of the octameric complex (Figure S1D).

SAXS analysis of TFG (p.R106C) produced consistent scattering profiles over the same protein concentrations examined for the wild-type protein (150–750 mM) (Figure 1G). However, in contrast to the wild-type protein, TFG (p.R106C) exhibited significantly higher R_g values (41.5 ± 0.9 Å, 150 mM;

41.3 ± 1.2 Å, 375 mM; 41.6 ± 1.0 Å, 750 mM) that did not vary based on protein concentration (Figures S1E and S1F). The D_{\max} of TFG (p.R106C) was similarly concentration independent (on average, 141 ± 4 Å), suggesting a less compact organization relative to the wild-type protein (Figure S1C). Based on the scattering profiles collected at two protein concentrations, SAXS envelopes were defined *ab initio*. Twenty independent models were aligned and averaged, with a mean NSD of 0.90, to reveal a larger, more asymmetric assembly, as compared to the wild-type protein complex (Figure 1H). Collectively, these data suggest that the TFG (p.R106C) mutation impairs the function of the coiled-coil domain to generate compact octameric ring-like complexes. To investigate this idea further, we examined the conformation of the TFG N terminus lacking the entire coiled-coil domain (amino acids 1–96) using SAXS. Based on hydrodynamic studies and multiangle light scattering, this region of TFG formed oligomers in solution (Figure S1G), consistent with the presence of a type I/II PB1 domain.³⁹ SAXS analysis of this TFG fragment produced consistent scattering profiles irrespective of protein concentration (450–900 mM), and we determined the radius of gyration (R_g) to be 36.1 ± 0.2 Å, with a D_{\max} of 105 Å (Figures S1H and S1I). Twenty independent models were aligned and averaged (based on two different protein concentrations), with a mean NSD of 0.90, to reveal an oligomer in the shape of a curved tube (Figure S1J). This conformation closely resembles that of the intact TFG N terminus harboring its coiled-coil domain, except that key contacts necessary to bring together the ring-like structure appear to be absent. These data support the idea that the coiled-coil domain plays an important role in regulating TFG complex assembly to generate compact ring structures.

To directly visualize differences in the wild-type and mutant TFG complexes, we used single-particle electron microscopy. As described previously¹⁶, wild-type TFG typically forms ring-like structures that are approximately 10–11 nm in diameter, as visualized under negative stain (Figure 2A). In contrast, under identical buffer conditions (50 mM HEPES, pH 7.6; 100 mM NaCl), TFG (p.R106C)

complexes exhibited a more heterogeneous arrangement of protomers and largely failed to form compact ring structures (Figure 2B). Notably, the predicted isoelectric point for TFG is ~5.5. We therefore dialyzed the wild-type TFG complexes into a buffer with this pH and observed that they exhibited reduced aggregation and improved staining homogeneity. Under these conditions, the propensity of TFG (p.R106C) complexes to form ring structures was increased (Figure 2C), consistent with the idea that the mutant protein is deficient for normal assembly but that the equilibrium can be shifted by lowering the pH. Nevertheless, although the TFG (p.R106C) mutant appeared capable of forming ring-like structures under these buffer conditions, we found that individual particles appeared more disorganized and distorted as compared to the wild-type protein (Figure 2D). In contrast, mutation of six leucine residues to valine within the coiled-coil domain blocked TFG ring assembly (Figure S2A). Collectively, our findings strongly suggest that the TFG (p.R106C) mutation specifically perturbs the normal conformation of TFG ring structures without having a dramatic effect on the ability of TFG protomers to self-associate.

To determine whether the specific presence of a positively charged residue at amino acid 106 in TFG is important for normal ring assembly, we additionally examined a TFG (p.R106K) mutant. We found that this mutation neither impaired the ability of the coiled-coil domain to self-associate, nor did it perturb the overall architecture of TFG ring complexes, even at neutral pH (Figures S2B and S2C). However, the clinically relevant TFG (p.R22W) mutation, which is located within the PB1 domain and also underlies an early-onset form of complicated HSP⁹, caused a similar perturbation in ring assembly as compared to the TFG (p.R106C) mutation (Figure S2D), suggesting that proper folding and self-association of the PB1 domain is also critical for TFG complex formation. Consistent with this idea, examination a TFG (p.K14A) mutant, which impairs the ability of type I/II PB1 domains to self-associate³⁹, strongly inhibited TFG ring assembly under all conditions tested (Figure S2E). Together, these data underscore the importance of both the PB1 and coiled-coil domains in assembling TFG

complexes with a functional conformation.

To determine whether the altered conformation of TFG (p.R106C) affects its distribution in cells, we initially used a replacement strategy in which endogenous TFG is depleted using an siRNA targeting its 3[′]-UTR and an exogenous, doxycycline inducible isoform is expressed after directed transgene insertion into the “safe harbor” AAVS1 locus.^{16, 28} Using this system, we found that wild-type TFG accumulates with markers of COPII transport at the ER/ERGIC interface in human hTERT-immortalized RPE-1 cells (Figures S2F and S2G). Similarly, a mutation in the coiled-coil domain that maintains positive charge at residue 106, TFG (p.R106K), failed to perturb its distribution in cells (Figures S2F and S2G). In contrast, at similar levels of expression (Figure S2H), TFG (p.R106C) exhibited reduced accumulation at the ER/ERGIC interface, as did another mutant that neutralizes positive charge at residue 106, TFG (p.R106A) (Figures S2G and S2I). Additionally, the TFG (p.R106C and p.R106A) mutations led to the appearance of more TFG-positive structures that failed to exhibit staining for COPII components, including several enlarged foci that exhibited high levels of the mutant TFG proteins (Figures S2I and S2J). Mutation of six leucine residues to valine within the coiled-coil domain resulted in a dramatic redistribution of TFG away from the ER/ERGIC interface, further highlighting the importance of this domain to proper TFG localization (Figure S2K).

The TFG (p.R106C) mutation impairs secretory protein trafficking and elevates ER stress

To establish a more physiologically relevant system to define the impacts of the TFG (p.R106C) mutation, we leveraged CRISPR technology to incorporate two nucleotide changes into well-characterized IMR90-4 human iPSCs. The first edit (c.316C>T) corresponds to the mutation found in HSP patients, while the second (c.321A>C) is silent, but introduces a novel restriction site to facilitate the identification of genome-edited cells. We screened a total of 300 edited clonal cell lines by PCR and restriction digest after single-cell sorting and identified 25 candidates for direct sequencing. Of

these, we selected three homozygous clones (clones A–C), three heterozygous clones (clones D–F), and a control clone that was homozygous for the c.321A>C silent mutation, but failed to incorporate a change at nucleotide 316 (clone G) for further analysis (Figure 3A). Upon passaging, each clone exhibited a similar morphology as compared to IMR90-4, growing as individual colonies, and all stained positively for pluripotency markers, including Nanog, SSEA4, and Oct4 (Figures 3B and S3A). Additionally, karyotype analysis revealed no discernable defects in any of the clones following CRISPR-mediated genome editing (Figures 3C and S3B).

We and others have shown previously that TFG is expressed ubiquitously in mammals.^{3,21} To determine the impact of the TFG (p.R106C) mutation, we differentiated each human iPSC clone toward a variety of cell fates. Given the importance of TFG at the ER/ERGIC interface, we initially generated tyrosinase-positive melanocytes (ectodermal lineage) and vimentin-positive fibroblasts (mesodermal lineage), both of which are amenable to assays for secretory pathway function (Figure S4A). Based on immunoblot analysis, TFG expression levels were not affected by presence of the p.R106C mutation in either cell type (Figures S4B and S4C). Immunofluorescence staining revealed that TFG (p.R106C) expressed at endogenous levels accumulated normally at the ER/ERGIC interface in homozygous, genome-edited fibroblast clones (Figures 4A, 4B, and S4D). However, in differentiated melanocytes, TFG (p.R106C) exhibited diminished co-localization with COPII transport carriers, relative to wild-type TFG (Figures 4C and 4D). Instead, we consistently observed numerous structures, which labeled positively for TFG, but lacked other components of the early secretory pathway. Moreover, we found that the levels of TFG (p.R106C) at the ER/ERGIC interface were modestly, but significantly reduced as compared to wild-type TFG in control melanocytes (Figure S4D). Based on two-hybrid analysis, this was not due to a defect in the ability of TFG to associate with the COPII component Sec23 (Figure S4E), which we showed previously to be critical for TFG accumulation at the ER/ERGIC interface.¹¹ Together, these data indicate that the TFG (p.R106C) mutation affects its distribution, but only in a cell-

type-specific manner.

To define potential impacts on early secretory pathway function, we transduced iPSC-derived melanocytes with a retrovirus encoding a GFP-tagged, temperature-sensitive form of vesicular stomatitis virus G protein (VSVG) (ts045), which misfolds and accumulates in the ER at 40°C, but folds properly and is capable of ER exit upon shift to 32°C.²⁵ Cells expressing low levels of VSVG were imaged live following temperature shift. In control melanocytes, VSVG moved rapidly from the ER and began to accumulate in the perinuclear Golgi within 5–7 min (Figure 5A). Although the average timing of VSVG appearance at the Golgi did not differ significantly in melanocytes expressing TFG (p.R106C), we observed prolonged accumulation of the cargo at punctate structures throughout the peripheral ER in mutant cells relative to controls, suggesting a delay during transport through the early secretory pathway (Figures 5A and 5B). Specifically, in contrast to control melanocytes, which exhibited only transient elevations in VSVG intensity at punctate structures prior to Golgi accumulation, VSVG levels accumulated to higher levels at such sites and persisted for a longer period of time in melanocytes expressing TFG (p.R106C) (Figures 5A and 5B).

Defects in the kinetics of protein secretion are often associated with an elevated unfolded protein response (UPR).⁴⁶ To determine whether the TFG (p.R106C) mutation leads to an activation of ER stress sensors, we stably transduced iPSC-derived fibroblasts and melanocytes to express a luciferase-based reporter of XBP1 mRNA splicing.¹⁵ Control iPSC-derived cells exhibited negligible levels of luciferase luminescence, but treatment with a low concentration of tunicamycin, which leads to protein misfolding in the ER, resulted in an increase in XBP1 mRNA splicing (Figure S4F). Melanocytes exhibited a particularly strong ER stress response, as compared to fibroblasts. Strikingly, even in the absence of tunicamycin, cells expressing the homozygous TFG (p.R106C) mutation also exhibited elevated XBP1 mRNA splicing (Figure S4F), consistent with our finding that these cells show a kinetic delay in protein secretion from the ER. Since XBP1 mRNA splicing is largely regulated by the

IRE1 ER stress sensor, we directly examined its activity in control and TFG (p.R106C) melanocytes by assessing the phosphorylation state of its kinase activation loop.²⁶ Immunoblot analysis confirmed that cells expressing the homozygous TFG (p.R106C) mutation exhibit constitutive activation of the IRE1 branch of the UPR (Figure 5C).

To determine whether heightened IRE1 activity sensitizes TFG (p.R106C)-expressing cells to additional forms of ER stress, we examined cargo transport to the Golgi following treatment and washout of brefeldin A (BFA), a fungal metabolite that inhibits guanine nucleotide exchange activity on several Arf-type GTPases, leads to the redistribution of integral membrane Golgi proteins to the ER, and dramatically increases ER stress signaling.^{13, 5} For this assay, we transfected iPSC-derived fibroblasts and melanocytes with a GFP fusion to the transmembrane Golgi enzyme mannosidase II (ManII). In the absence of BFA, ManII accumulated at the Golgi in all clones, irrespective of the TFG isoform expressed, and addition of BFA resulted in the expected redistribution of ManII to the ER (Figure 5D). Within 120 min after BFA removal, more than 80% of control fibroblasts exhibited complete re-accumulation of ManII at the Golgi (Figures 5D and 5E). In contrast, fibroblasts that were homozygous for the TFG (p.R106C) mutation largely retained ManII in the ER at this time point (Figures 5D and 5E). After an extended period of washout, ManII was ultimately able to reach the Golgi in the mutant fibroblasts, again indicating that the TFG (p.R106C) mutation impairs the kinetics of protein secretion but does not block it (Figure 5D). Similarly, melanocytes harboring the homozygous TFG (p.R106C) mutation also exhibited a delay in ManII trafficking to the Golgi following BFA washout (Figure 5F). Together, our findings suggest that hypomorphic mutations in TFG, which disrupt its ring-like conformation, impact protein trafficking and the ER stress response in multiple cell lineages.

The distribution of TFG in cortical neurons is disrupted by the p.R106C mutation

Patients with the TFG (p.R106C) mutation exhibit progressive loss of gait and motor control, suggesting a particularly important function for TFG in neurons of the corticospinal tract.³ We therefore used control and genome-edited iPSCs to generate Tbr1- and Tau-positive glutamatergic cortical neurons using established protocols (Figures S5A and S5B). The timing of differentiation was indistinguishable between control and TFG (p.R106C) mutant cells (Figure S5C), and similar to iPSC-derived fibroblasts and melanocytes, the overall levels of TFG in differentiated cortical neurons were not affected by the presence of the p.R106C mutation (Figure S5D). qPCR analysis further indicated that expression of TFG was also unaffected by presence of the mutation (Figure S5E). Additionally, whole-cell patch-clamp recordings revealed no significant differences in synaptic activity or the membrane properties of homozygous TFG (p.R106C) neurons as compared to control (Figures S6A–S6C). These studies suggest that the TFG (p.R106C) mutation does not inhibit the differentiation of cortical neurons nor their spontaneous electrical activity *in vitro*.

We next examined early secretory pathway organization in iPSC-derived neurons, focusing on the distribution of markers associated with the Golgi apparatus and formation of COPII-coated transport carriers. Using antibodies directed against GM130, a *cis*-Golgi matrix tethering protein, we found that the Golgi was largely limited to cell bodies in control neurons, juxtaposed to the nucleus, and homozygous expression of TFG (p.R106C) failed to dramatically impact its distribution or morphology (Figure S6D). In contrast, the localization of TFG in the mutant neurons was perturbed, similar to what we observed in iPSC-derived melanocytes. Specifically, we found that TFG (p.R106C) was more poorly retained at the ER/ERGIC interface in cell bodies and exhibited a more diffuse distribution throughout neurons (Figures 6A and S6D). These data are consistent with the idea that the p.R106C mutation alters TFG localization, most prominently in cells of the ectodermal lineage. Based on a previous study, overexpression of TFG (p.R106C) in primary murine hippocampal neurons results

in the fragmentation of mitochondria.¹² The mechanistic basis of this effect is unknown. However, our findings in RPE-1 cells indicate that overexpressed TFG (p.R106C) exhibits an enhanced propensity to form enlarged aggregates (see Figure S2I), which contrasts the distribution of the mutant protein when expressed at endogenous levels, and may indirectly affect mitochondrial morphology. We therefore conducted measurements of mitochondrial volume in Tau-positive neurites following differentiation of genome-edited human iPSCs. Our analysis revealed no significant discrepancies between the control and TFG (p.R106C) mutant neurons (Figure S6E). We additionally analyzed mitochondrial motility and found no significant differences in the percentage of motile mitochondria, nor their average rate of movement in neurites (Figure S6F). Together, these data suggest that the presence of the TFG (p.R106C) mutation is unlikely to have a direct effect on mitochondrial dynamics, including fission/fusion events.

Recent studies have also suggested that lysosomal defects are commonly associated with several mutations underlying HSPs.¹ We therefore immunostained control and TFG (p.R106C) mutant neurons with the late endosome/lysosome marker LAMP-1 and measured the volumes of structures identified in cell bodies. Our analysis failed to demonstrate any differences in lysosome size or morphology between control and TFG (p.R106C) mutant neurons (Figure S6G), and we also failed to observe lysosome-enriched axonal swellings, as previously observed in mutant SPG4 patient-derived neurons.^{8, 1} Similarly, changes in autophagic flux, which have been frequently associated with neurodegenerative diseases²³, were not detected in TFG (p.R106C) mutant neurons, as indicated by the relative levels of lipidated (LC3-II) versus non-lipidated (LC3-I) LC3 (Figure S6H).

TFG functions to promote axon bundling

Previous work suggested that defects in ER structure/function caused by mutations in SPG3A (atlastin-1) contribute to neurodegenerative disease by impairing axon growth.⁸ To determine whether

the TFG (p.R106C) mutation causes a similar effect, we generated iPSC-derived neurospheres and measured axon outgrowth following their transfer to coverslips. We found that homozygous neurons expressing TFG (p.R106C) extended axons to a similar length as observed in control neurons (Figures 6B and 6C). However, during these studies, we also noted that control axons rapidly form bundles after emerging from neurospheres (Figure 6B). In contrast, neurons expressing TFG (p.R106C) failed to exhibit normal axon fasciculation (Figures 6B and 6D). We also examined iPSC-derived neurons expressing the dominant-acting SPG3A (p.P342S) mutation and found that axon bundling occurred normally (Figure 6D). Together, these data suggest that TFG plays a distinct role from other regulators of ER function in axon maintenance.

Since our earlier studies suggested that the TFG (p.R106C) mutation causes an elevation in ER stress, we investigated the possibility that increased UPR signaling may affect the ability of axons to bundle. In an attempt to test this idea, we treated neurospheres with a low concentration of tunicamycin that was sufficient to activate IRE1, and examined neurite morphology over several days. Within 2 days of treatment, neurite outgrowth was found to be significantly impaired, and by day 5, neurites had largely undergone retraction and degeneration (Figure S7), preventing us from determining whether axon bundling was directly impacted. We therefore decided to explore alternative mechanisms by which the TFG (p.R106C) mutation might affect establishment or maintenance of axon contact.

Homotypic axon fasciculation is largely mediated by adhesion molecules that must be secreted to the surface of axons to engage one another via extracellular domains.⁴⁴ Based on our findings that cells only expressing TFG (p.R106C) exhibit defects in cargo transport from the ER, we speculated that the defect in axon bundling may result from impaired trafficking of adhesion molecules. To address this possibility, we stained genome-edited iPSC-derived neurons using antibodies directed against a subset of calcium-dependent and calcium-independent cell adhesion molecules.³⁸ As compared to controls, we found that the levels of cell surface L1CAM in particular were reduced in the axons of neurons

expressing TFG (p.R106C), consistent with the idea that its transport to the cell surface was impaired (Figures 7A and 7B). Importantly, this change was not a result of diminished LICAM expression (Figure 7C). Instead, these data suggest that efficient membranetrafficking in the early secretory pathway plays a critical role in maintaining neuronal homeostasis, especially in the long cortico-spinal motor neurons that undergo degeneration in HSPs.

3. Discussion

Over the past several years, it has become evident that ER homeostasis plays a critical role in maintaining neuronal health. Mutations in numerous factors that regulate ER structure and function have been linked to a variety of neurodegenerative diseases, potentially by affecting calcium signaling, lipid biosynthesis, membrane trafficking, and/or interorganellar communication.^{4, 10} Based on our previous work demonstrating that TFG regulates protein transport at the ER/ERGIC interface^{45, 16, 11}, we hypothesized that TFG variants implicated in neurological disorders impair the secretion of biosynthetic cargoes. Here, we find that iPSC-derived cortical neurons homozygous for TFG (p.R106C) exhibit reduced levels of an important adhesion molecule at the surface of axons, which impedes their ability to self-associate. Based on post-mortem studies, loss of axon fasciculation within the corticospinal tract is commonly associated with motor neuropathies.³¹ This defect may contribute to reduced nerve conduction speed, which has been documented in several HSP patients harboring mutations in the TFG N terminus.³ Together, our findings highlight the importance of efficient secretory egress from the ER in maintaining proper neuronal function, especially in the long cortical neurons that extend into the spinal cord.

Our structural and biochemical studies indicate that pathological mutations in the TFG N terminus lead to conformational abnormalities in TFG complexes, which significantly affect their distribution, but only in certain cell types. Nonetheless, kinetic delays in protein secretion appear to be

more widespread in cells expressing homozygous TFG (p.R106C). These findings suggest that the mutation in the TFG coiled-coil domain has at least two distinct effects, one of which is dependent on cell lineage, while the other is not. The distribution of a protein is often regulated by interacting partners, which may be differentially expressed in various tissues. For example, the membrane-associated protein CIP4 functions in the endocytic pathway in fibroblasts but regulates membrane protrusion in neurons and cancer cells, largely due to unique interactions in these different cell types.³² Similarly, cortical neurons may express specific factors that facilitate TFG localization but are only able to function appropriately when TFG complexes adopt their compact ring-like architecture. Based on this idea, it follows that homozygous TFG (p.R106C) individuals exhibit pronounced CNS phenotypes, but more limited perturbations in other tissues.

Independent of cell type, homozygous expression of TFG (p.R106C) slows protein export from the ER, which likely underlies the constitutive elevation in ER stress we observe in both iPSC-derived fibroblasts and melanocytes. At a mechanistic level, it remains unknown how the TFG (p.R106C) mutation causes this defect. One possibility is that the conformational change in TFG ring complexes impairs their ability to concentrate at the ER/ERGIC interface to promote outer COPII coat dissociation, which is a prerequisite for ER-derived transport carriers to tether and fuse with ERGIC membranes.¹¹ Alternatively, the loosely assembled TFG (p.R106C) oligomers may not function optimally to organize COPII budding sites, which could preferentially affect the transport of bulky, high-molecular-weight cargoes.²² The retention of such cargoes could subsequently lead to additional consequences, including an elevation of ER stress.³⁰ Importantly, elevated ER stress resulting from a deficit in protein secretion may also contribute to neurodegeneration.³⁵ Several studies have shown that neuronal ER stress is a hallmark of Alzheimer's disease, Huntington's disease, synucleinopathies, ALS, and prion disease, although many of the models used are based on the overexpression of mutated genes identified in patient studies.^{40, 24, 6} Our findings here emphasize the danger of this approach, as ectopically overexpressed TFG

(p.R106C) behaves differently in cells when compared to the mutant expressed at endogenous levels. Nevertheless, therapeutic strategies to reduce ER stress and the UPR have been used on several models of neurodegenerative disease with varying levels of success.²⁹ Our data suggest that some HSPs may also respond to this approach, although improved animal models will be necessary to formally test this possibility.

Although we identified L1CAM as one particular cargo in neurons that seems to rely heavily on TFG function for efficient secretion, it is likely that other secretory proteins are similarly affected. Notably, L1CAM was one of the first genes implicated in the pathogenesis of HSP and mutations affecting it result in the most common form of X-linked HSP, often associated with the absence of L1CAM cell surface expression and impaired axonal adhesion.^{20, 2, 34} Patients expressing mutant isoforms of L1CAM typically exhibit thinning of the corpus callosum with early-onset leg spasticity, consistent with phenotypes observed in patients with mutations in TFG.^{3, 36, 17} Our data demonstrating a defect in axon fasciculation in iPSC-derived neurons expressing TFG (p.R106C) further support an intimate connection between TFG function and L1CAM cell surface expression. Considering the length of neurons in the corticospinal tract, even minor perturbations to L1CAM trafficking may affect bundling of distal axon segments, especially during neurite outgrowth. In contrast, a similarly modest reduction in ER export in a fibroblast or melanocyte would have a more limited impact on cell growth. Confirmation of this idea will require further studies in patients with TFG mutations or the development of an appropriate animal model.

4. Experimental procedures

Recombinant protein expression and purification

All recombinant proteins were expressed using BL21(DE3)-T1^R bacteria (Sigma-Aldrich) and purified initially using glutathione agarose beads (for GST-fusion proteins) or nickel affinity resin

(polyhistidine-tagged proteins). Eluted or cleaved proteins were subsequently applied onto ion exchange and/or gel filtration columns for further purification.¹⁶ For circular dichroism spectroscopy, purified proteins were analyzed using a 0.1-cm path length quartz cell in 25 mM sodium phosphate (pH 7.2). Spectra were collected using a model 202SF circular dichroism spectrophotometer at 25°C. For mass determination, proteins were examined by dynamic light scattering using a Wyatt mini-DAWN TREOS three-angle light-scattering detector coupled to a high-resolution size exclusion chromatography system. ASTRA software was used to calculate molecular mass.³⁷

SAXS data collection

Data were collected at sector 12-ID-B of the Advanced Photon Source (APS) at Argonne National Laboratory and obtained at a wavelength of 1.54 Å and a sample-detector distance of 4 m (small-angle) and 30 cm (wide-angle) resulting in a total momentum transfer range of $0.01 < q < 2.31 \text{ \AA}^{-1}$. Data were collected for buffer and protein at 25°C for 2 min (APS), and buffer subtraction was adjusted for the excluded volume of the protein. The predicted scattering intensity at $q = 0 \text{ \AA}^{-1}$ and the radius of gyration (R_g) were determined by Guinier analysis²⁷ and compared between two to three concentrations to detect interparticle interference and concentration-dependent changes in conformation.

Single-particle electron microscopy

Purified proteins (4 mL) at a concentration of 0.01 mg/mL were placed on plasma-cleaned carbon-coated grids, washed with water, and stained with 2% uranyl formate as described previously.¹⁶ Imaging was conducted using an FEI Titan Krios transmission electron microscope operated at 120 keV and equipped with a Gatan Ultrascan 4,000 3 4,000 charge-coupled device (CCD) camera. Class averages were generated by reference-free alignment.¹⁶

CRISPR-mediated genome editing

For CRISPR-mediated editing, iPSCs were electroporated with a plasmid encoding Cas9-GFP, a guide RNA targeting TFG (5⁰-GAAGTTCTATCAGTT CTCGA-3⁰), and a single-stranded oligonucleotide to incorporate the desired point mutations via homology directed repair. Cells were sorted using a BD FACSAria III cell sorter based on GFP fluorescence, and individual colonies were harvested after 1 week and moved to individual Matrigel-coated dishes. The incorporation of point mutations was confirmed following genomic DNA preparation, PCR amplification, and Sanger sequencing. For karyotype analysis, Giemsa banding was outsourced to WiCell Cytogenetics Laboratory. Stem cell maintenance and differentiation procedures are detailed in Supplemental Experimental Procedures.

Immunofluorescence and confocal microscopy

For immunofluorescence analysis, cells were fixed using paraformaldehyde (4%) and stained using primary antibodies at a final concentration of 1 mg/mL, as described previously.¹⁶ Imaging was conducted on a swept-field confocal microscope using a Roper CoolSnap HQ2 CCD camera and a Nikon 603, 1.4 numerical aperture (NA) Plan Apo oil objective lens. Acquisition parameters were controlled by Nikon Elements, and image analysis was conducted using ImageJ or Imaris (Bitplane) software. BFA treatments (10 mg/mL) were each conducted for 1 hr at 37°C, followed by washout using pre-warmed media. Cells expressing GFP-tagged VSVG were incubated overnight at 40°C and subsequently placed into a Tokai Hit stage top incubator set to 32°C for live-cell imaging. Particle tracking, volume measurements, and linescan analysis for intensity measurements were conducted in an unbiased manner using Imaris software.

Statistical methods

All p values were determined by paired t test or ANOVA, calculated using Microsoft Excel or GraphPad Prism, and data are shown as mean \pm SEM. Significant differences were indicated by a p value less than 0.05.

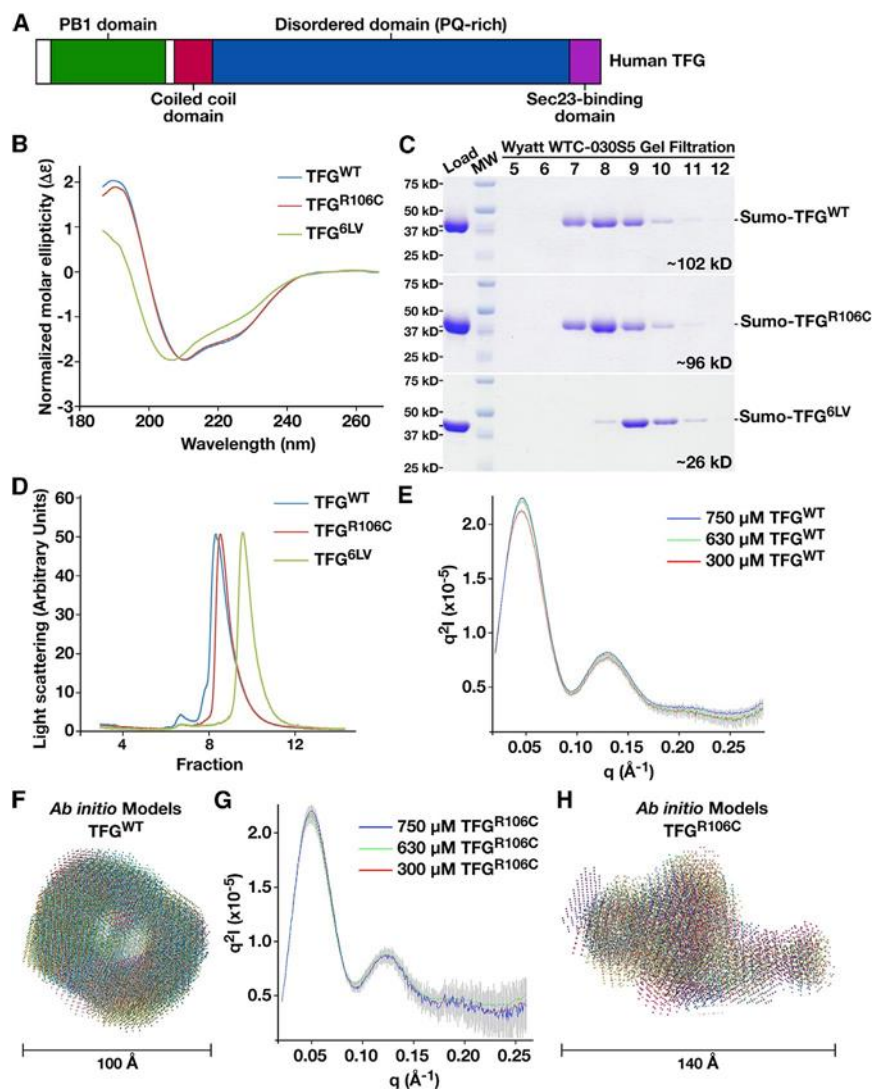


Figure 1. The TFG (p.R106C) Mutation Alters the Conformation of TFG Ring Complexes

(A) Cartoon highlighting the various domains of human TFG, including its PB1 domain (green), coiled-coil domain (red), disordered domain (blue), and Sec23-binding domain (purple). (B) Circular dichroism (CD) spectroscopy was used to characterize the N terminus of various TFG isoforms (amino acids 1–193; wild-type TFG, TFG [p.R106C], and TFG harboring six leucine- to-valine mutations throughout its coiled-coil domain; n = 3 for each). (C and D) Purified recombinant isoforms of TFG (amino acids 92–138; wild-type TFG, TFG [p.R106C], and TFG harboring six leucine-to- valine mutations throughout its coiled-coil domain) fused to a monomeric SUMO tag were separated over a gel filtration column (Wyatt WTC-030S5) that was coupled to a multiangle light-scattering device. Eluted fractions were separated by SDS/ PAGE and stained using Coomassie Blue to highlight their elution profiles (C) (n = 3 each). Average molecular masses were calculated using ASTRA software (n = 3 each), and light-scattering profiles for each protein are shown (D). (E and G) Representative Kratky scattering profiles generated from the analysis of three concentrations of wild-type TFG (E) or TFG (p.R106C) (G) following SAXS (n = 3 each). All experiments were conducted in 50 mM Tris-HCl, pH 7.6, 10 mM DTT, and 100 mM NaCl. (F and H) Ab initio models of the N terminus (amino acids 1–138) of wild-type TFG (F) and TFG (p.R106C) (H). At least 17 structures of each protein were generated using the program DAMMIF, and dummy atom models were overlaid. The normalized spatial discrepancy (NSD) of the wild TFG SAXS envelope was 0.83, and the NSD of the TFG (p.R106C) mutant was 0.90. See also Figure S1.

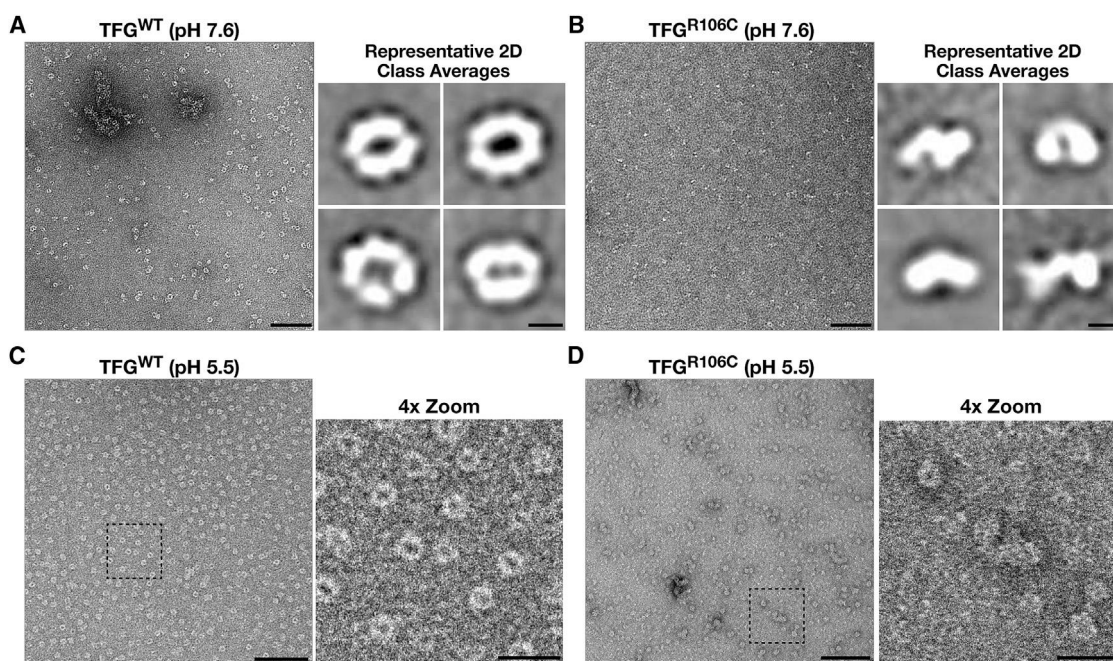


Figure 2. The TFG (p.R106C) Mutation Perturbs the Assembly of Compact Ring Structures (A and B) Recombinant wild-type TFG (A) and TFG (p.R106C) (B) were imaged by negative-staining electron microscopy following purification in 50 mM HEPES, pH 7.6, and 100 mM NaCl ($n = 3$ each). Montage of representative class averages (amino acids 1–193 in both cases) generated by reference-free alignment and classification are shown (right panels). Scale bars, 100 nm (left) and 5 nm (right, class averages). (C and D) Recombinant wild-type TFG (C) and TFG (p.R106C) (D) were imaged by negative-staining electron microscopy following purification in 50 mM MES, pH 5.5, and 100 mM NaCl ($n = 3$ each). Representative higher-magnification views of individual complexes are shown (right panels). Scale bars, 100 nm (left) and 25 nm (right). See also Figure S2.

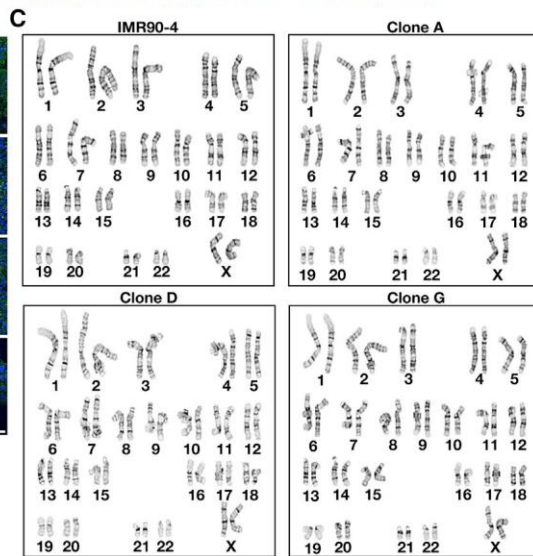
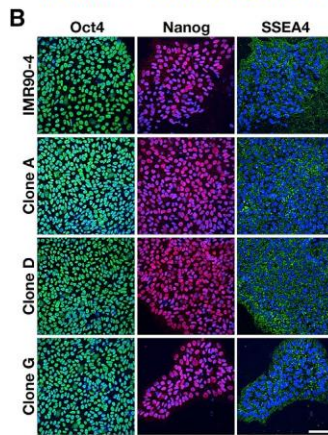
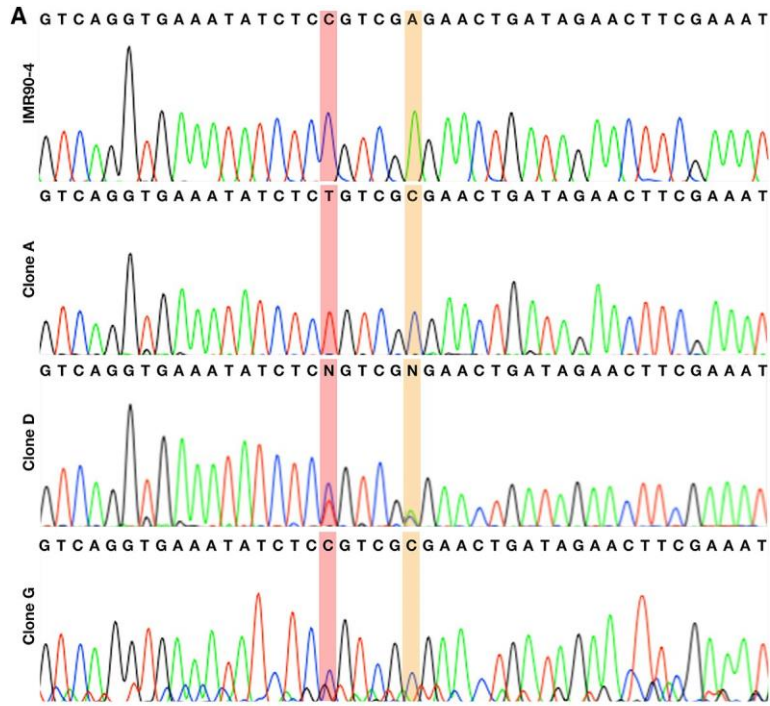


Figure 3. Generation of Human iPSCs Harboring the TFG (p.R106C) Mutation (A) Representative Sanger sequencing traces of TFG exon 4 from control (IMR90-4) and genome-edited (clones A, D, and G) iPSCs. The single-nucleotide change found in HSP patients is highlighted in red, while the silent mutation incorporated to enable facile identification of edited clones is highlighted in yellow. (B) Control iPSCs (IMR90-4 and clone G) and iPSCs harboring a mutation in TFG (clones A and D) were fixed and stained using anti-bodies directed against Oct4, Nanog, and SSEA4 together with Hoechst 33342 (n = 3 each). Maximum intensity projections are shown. Scale bar, 100 μ m. (C) Giemsa banding analysis was performed on control iPSCs (IMR90-4 and clone G) and iPSCs harboring a mutation in TFG (clones A and D), revealing no changes in karyotype that resulted from CRISPR-mediated genome editing. See also Figure S3.

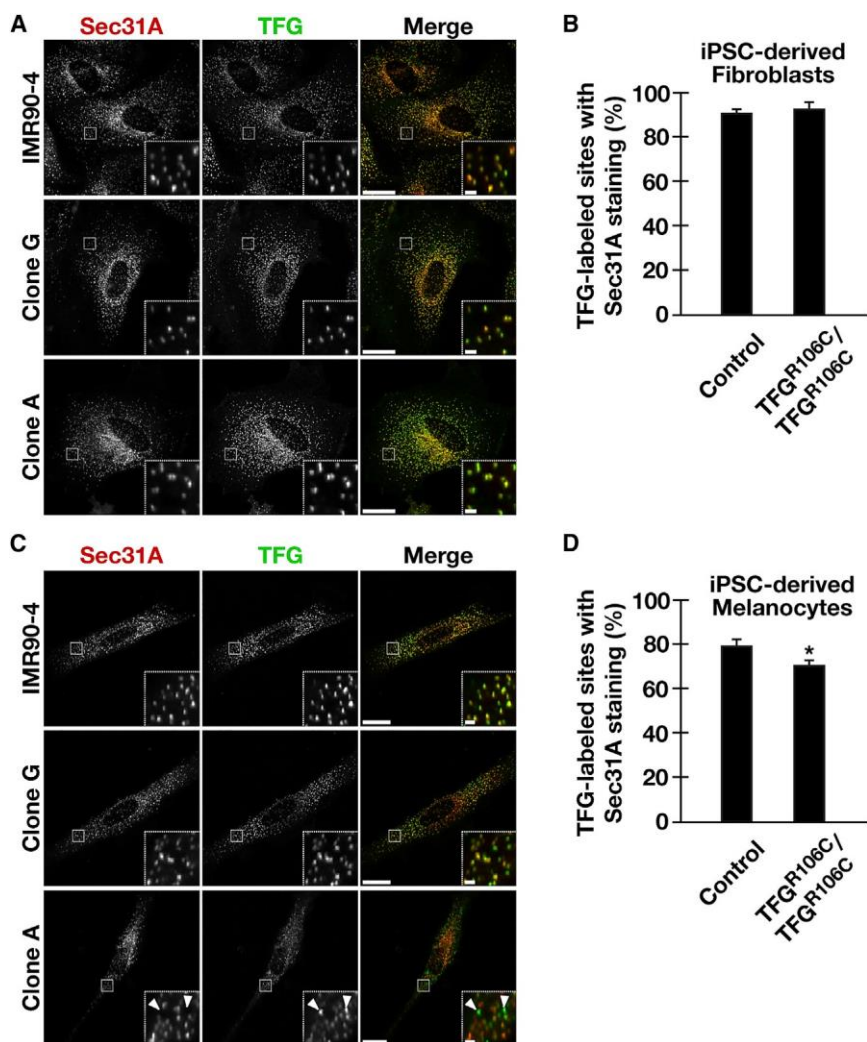


Figure 4. The TFG (p.R106C) Mutation Alters Its Distribution in a Cell-Type-Specific Manner

(A) Representative control (IMR90-4 and clone G) and homozygous TFG (p.R106C) expressing (clone A) iPSC-derived fibroblasts were fixed and stained using antibodies directed against Sec31A (red) and TFG (green) and imaged using swept-field confocal optics. Maximum intensity projections are shown. Scale bars, 10 μ m and 1 μ m (insets). (B) Quantification of the percentage of TFG- labeled structures that exhibit Sec31A staining in control (IMR90-4 and clone G) and homozygous TFG (p.R106C)-expressing fibroblasts (clones A, B, and C). Error bars represent mean \pm SEM; $n > 10$ different cells per condition; three biological replicates each. No statistically significant difference was found, as calculated using a paired t test. (C) Representative control (IMR90-4 and clone G) and homozygous TFG (p.R106C)-expressing (clone A) iPSC-derived melanocytes were fixed and stained using antibodies directed against Sec31A (red) and TFG (green) and imaged using swept-field confocal optics. Maximum intensity projections are shown. Scale bars, 10 μ m and 1 μ m (insets). (D) Quantification of the percentage of TFG- labeled structures that exhibit Sec31A staining in control (IMR90-4 and clone G) and homozygous TFG (p.R106C)-expressing melanocytes (clones A, B, and C). Error bars represent mean \pm SEM; $n > 10$ different cells per condition; three biological replicates each. * $p < 0.05$, as calculated using a paired t test. See also Figure S4.

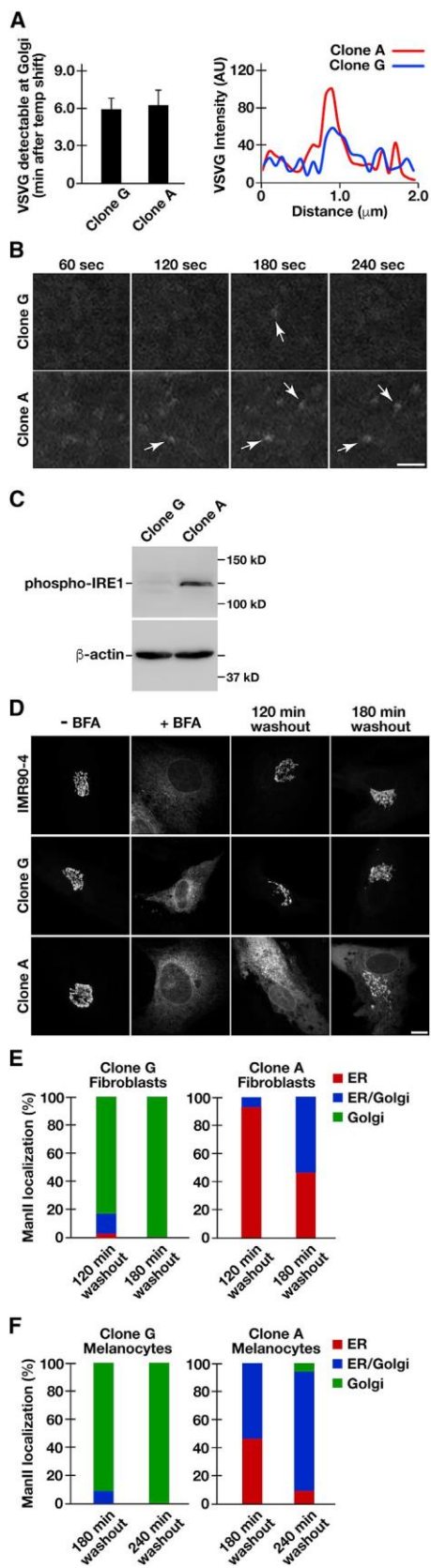


Figure 5. The TFG (p.R106C) Mutation Impairs Its Function in Differentiated Cells

(A) Representative control (clone G) and homozygous TFG (p.R106C)-expressing (clone A) iPSC-derived melanocytes were transduced to express ts045 VSVG-GFP and imaged live using swept-field confocal optics following shift to 32°C. The period of time required for VSVG-GFP to reach the perinuclear Golgi, as determined by an elevation in fluorescence intensity relative to the surrounding ER, was measured in both cases (left). Error bars represent mean \pm SEM; $n > 5$ different cells per condition. No statistically significant difference was found, as calculated using a paired t test. Representative linescan analyses highlight the difference in the fluorescence intensity of VSVG-GFP that accumulates in punctate structures throughout the peripheral ER, prior to its appearance in the Golgi (right; $n > 50$ punctate structures per condition; five biological replicates each). (B) Representative images of the peripheral ER obtained using swept-field confocal optics in the iPSC-derived cell lines described in (A) at various time points after shift to 32°C. Scale bar, 2 μ m. (C) Representative immunoblot analysis of extracts generated from control (clone G) and TFG (p.R106C) (clone A) iPSC-derived melanocytes using antibodies directed against phospho-IRE1 and b-actin ($n = 3$). (D) Representative control (IMR90-4 and clone G) and homozygous TFG (p.R106C)-expressing (clone A) iPSC-derived fibroblasts transfected with ManII-GFP were incubated in the presence and absence of BFA or following BFA washout. Cells were fixed under the conditions indicated and imaged using swept-field confocal optics. Maximum intensity projections are shown. Scale bar, 10 μ m. (E and F) The distribution of ManII-GFP was quantified in control and TFG (p.R106C) iPSC-derived fibroblasts (E) and melanocytes (F) at two different time points following BFA washout. More than 100 cells were analyzed for each condition; three biological replicates each. See also Figure S4.

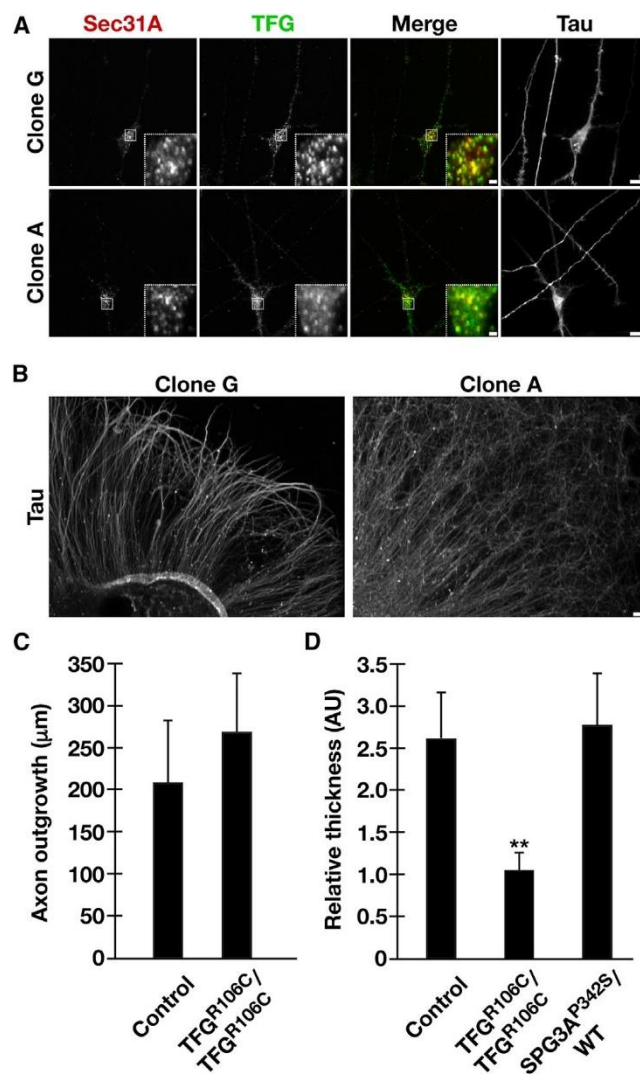


Figure 6. The TFG (p.R106C) Mutation Leads to a Defect in Axon Fasciculation in iPSC-Derived

Neurons (A) Representative control (clone G) and homozygous TFG (p.R106C)-expressing (clone A) iPSC-derived cortical neurons were fixed and stained using antibodies directed against Sec31A (red), TFG (green), and Tau (white), and imaged using swept-field confocal optics. Maximum intensity projections are shown. Scale bars, 10 μ m and 1 μ m (insets). (B) Representative control (clone G) and homozygous TFG (p.R106C)-expressing (clone A) neurospheres were plated onto glass coverslips, and axon outgrowth was examined following fixation and staining using antibodies directed against Tau after 1 week. Maximum intensity projections are shown. Scale bar, 20 μ m. (C) Quantification of axon outgrowth observed in control (IMR90-4 and clone G) and homozygous TFG (p.R106C)-expressing neurospheres (clones A, B, and C) 1 week after plating. Error bars represent mean \pm SEM; $n > 10$ neurospheres per condition; three biological replicates each. No statistically significant difference was found, as calculated using a paired t test. (D) Quantification of axon bundling in control (IMR90-4 and clone G), homozygous TFG (p.R106C)-expressing neurospheres (clones A, B, and C), and heterozygous SPG3A (p.P342S)-expressing neurospheres (16) 1 week after plating was calculated based on the ratio of axon thickness measured using linescan analysis at 150 μ m from the edge of the neurosphere to the thickness measured 10 μ m from the neurosphere. Error bars represent mean \pm SEM; $n > 10$ neurospheres per condition; three biological replicates each. ****** $p < 0.01$, as calculated using an ANOVA test. See also Figures S5 and S6.

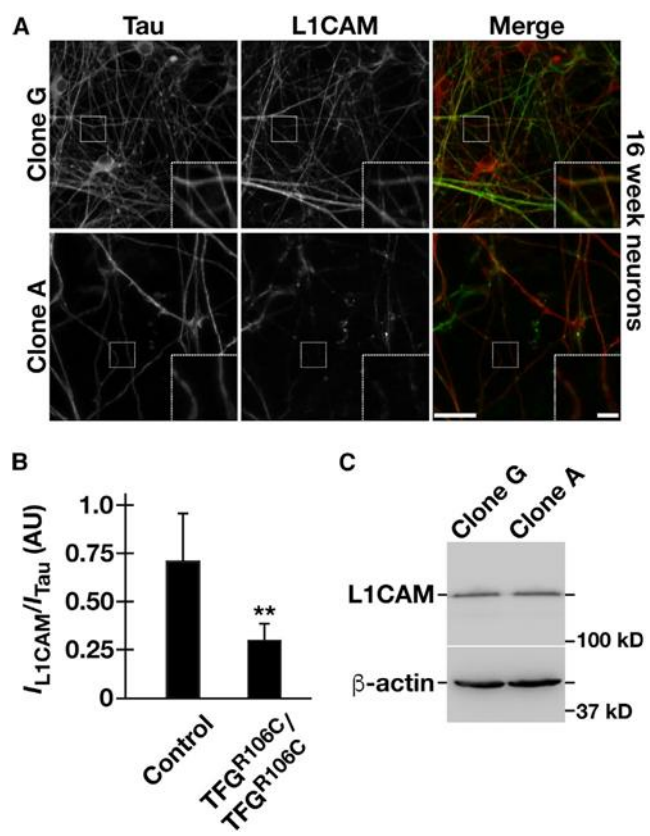


Figure 7. The TFG (p.R106C) Mutation Leads to a Defect in L1CAM Accumulation at the Surface of Axons in iPSC-Derived Neurons (A) Representative control (clone G) and homozygous TFG (p.R106C)-expressing (clone A) cortical neurons were grown for 16 weeks in culture and subsequently incubated live with antibodies directed against L1CAM (green). Neurons were then fixed and stained using antibodies directed against Tau (red). Maximum intensity projections are shown. Scale bars, 20 μ m and 5 μ m (insets). (B) Fluorescence intensity (I) of L1CAM relative to Tau in axons from control (clone G) and homozygous TFG (p.R106C) mutant iPSC-derived neurons. Error bars represent mean \pm SEM; $n > 50$ axons per condition; three biological replicates each. $^{***}p < 0.01$ (compared with control), calculated using a paired t test. (C) Representative immunoblot analysis of control iPSC-derived neurons (clone G) and neurons harboring the homozygous TFG (p.R106C) mutation (clone A) using antibodies directed against L1CAM and b-actin. Densitometry analysis was performed to quantify changes in L1CAM levels relative to b-actin in both control and homozygous TFG (p.R106C)-expressing iPSC-derived neurons ($n = 3$). No statistically significant difference was found, as calculated using a paired t test. See also Figure S7.

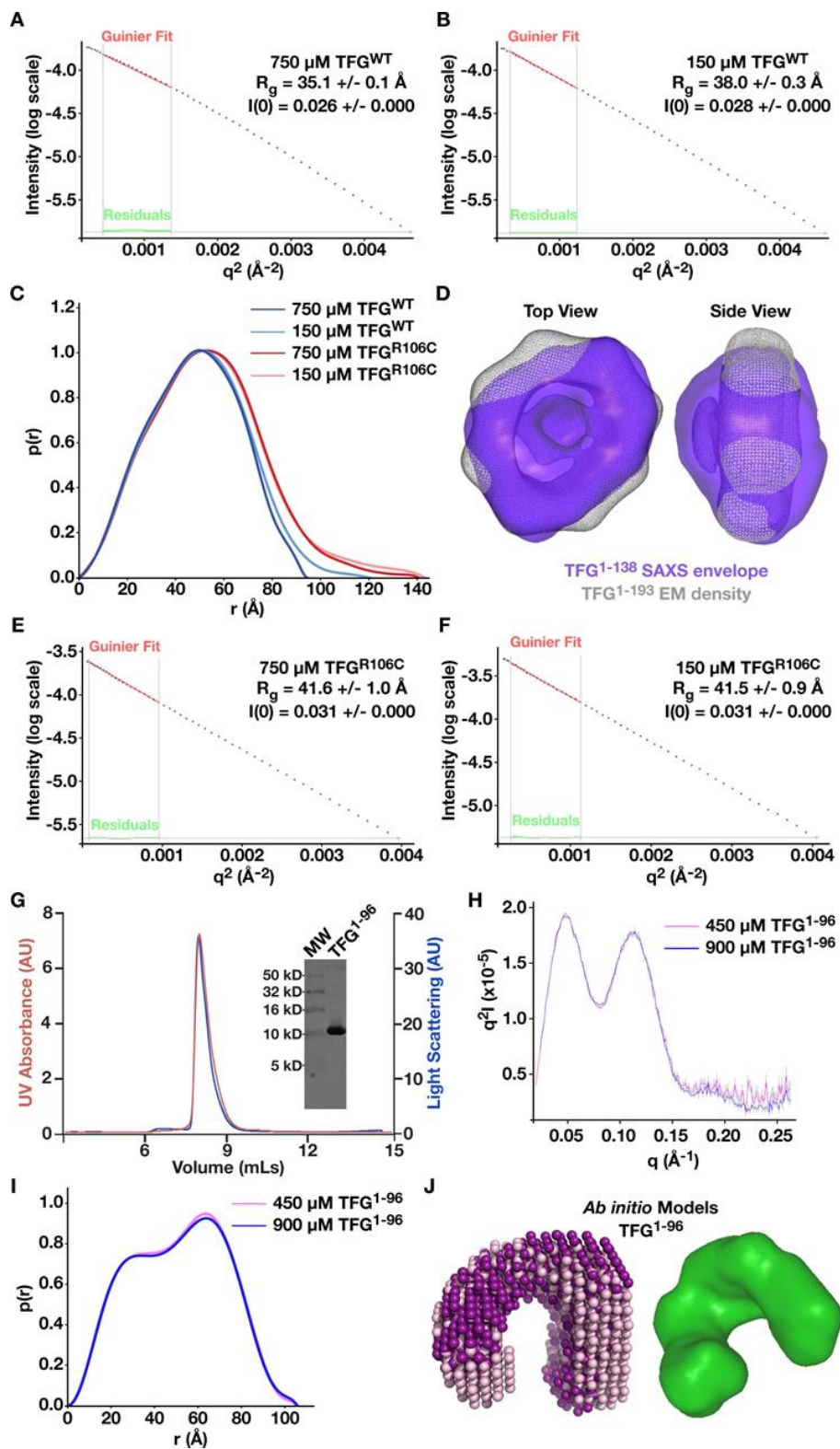


Figure S1. The TFG coiled coil domain plays a key role in the assembly of TFG octameric ring structures, Related to Figure 1. (A, B, E, and F) Direct estimation of the radius of gyration, R_g , and the extrapolated intensity at zero scattering angle, $I(0)$ for wild type TFG (amino acids 1-138) (A and B) and TFG (p.R106C) (E and F) was based on Guinier analysis conducted at two protein concentrations ($n=3$ each). Aggregation is not observed, and the residuals exhibit a linear behavior in all cases. (C) Pair distance distribution function plots of wild type TFG and TFG (p.R106C) at two protein concentrations. (D) An averaged *ab initio* model of the TFG amino-terminus (amino acid 1-138) (blue) is overlaid with the electron microscopy density of TFG (amino acids 1-193) defined previously (EMDataBank accession code EMD-6076). (G) Purified recombinant TFG (amino acids 1-96) was separated over an gel filtration column that was coupled to a multi-angle light scattering device ($n=3$). Both the UV absorbance (red) and the light scattering (blue) profiles are shown and a sample of the purified protein separated by SDS/PAGE and stained using Coomassie Blue is included. (H) Representative Kratky scattering profiles generated from the analysis of two concentrations of wild type TFG (amino acids 1-96) following SAXS. Experiments were conducted in 50 mM Tris-HCl, pH 7.6, 10 mM DTT, and 100 mM NaCl ($n=3$). (I) Pair distance distribution function plots of wild type TFG (amino acids 1-96) at two protein concentrations. (J) *Ab initio* models of the TFG amino-terminus (amino acid 1-96). Twenty structures were generated using the program DAMMIF, and two overlaid dummy atom models are shown (left). The twenty structures were then averaged with DAMAVER, yielding a normalized spatial discrepancy (NSD) of 0.90. The averaged SAXS envelope for wild type TFG (amino acids 1-96) is depicted (right).

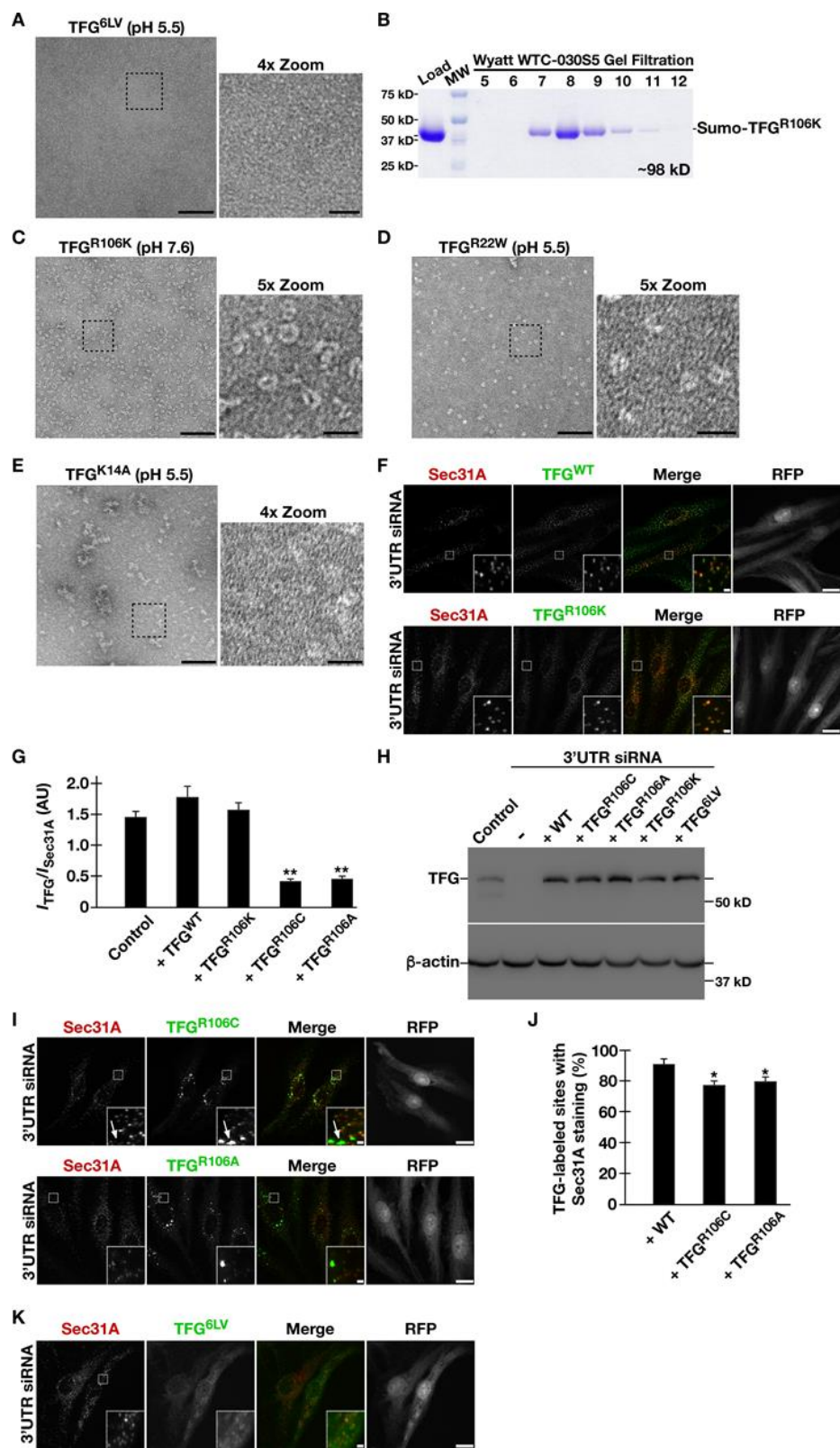


Figure S2. The TFG coiled coil domain plays a key role in the assembly of TFG octameric ring structures, Related to Figure 2.

(A) Recombinant TFG (amino acids 1-193) harboring 6 leucine to valine mutations within its coiled coil domain were imaged by negative stain electron microscopy following purification in 50 mM MES, pH 5.5, and 100 mM NaCl. A higher magnification view of individual particles is shown (right). Scale bars, 100 nm (left) and 25 nm (right). (B) A purified recombinant form of TFG (p.R106K; amino acids 92-138) fused to a monomeric SUMO tag was separated over a gel filtration column coupled to a multi-angle light scattering device. Eluted fractions were separated by SDS/PAGE and stained using Coomassie Blue (n=3). Molecular mass was calculated using ASTRA software. (C-E) Recombinant TFG (amino acids 1-193) harboring various mutations (p.R106K (C), p.R22W (D), or p.K14A (E)) were imaged by negative stain electron microscopy following purification in either 50 mM MES, pH 5.5, or 50 mM HEPES, pH 7.6. Higher magnification views of individual particles are shown (right). Scale bars, 100 nm (left) and 25 nm (right). (F, I, and K) Representative RPE-1 cells treated with siRNAs targeting the 3'UTR of endogenous TFG were induced to ectopically express wild type TFG or a mutant TFG isoform, followed by fixation and staining using antibodies directed against Sec31A and TFG. Maximum intensity projections are shown. RFP expression, also induced by doxycycline, was used to identify cells with similarly low levels of TFG expression. Arrows in panel I highlight the presence of large TFG (p.R106C)- positive structures that have little associated Sec31 staining. Scale bars, 10 μ m and 1 μ m (inset). (G) Fluorescence intensity (I) of TFG relative to Sec31A was quantified in RPE-1 cells ectopically expressing various TFG isoforms following depletion of endogenous TFG. Error bars represent mean \pm SEM; n > 30 cells per condition; 3 biological replicates each. **p < 0.01 (compared with control), calculated using an ANOVA test. (H) Representative immunoblot analysis of control cells and TFG depleted cells ectopically expressing various TFG isoforms (n=3). (I) Quantification of the percentage of TFG-labeled structures that exhibit Sec31A staining in TFG depleted cells induced to express various forms of TFG following

treatment with doxycycline (3 ng/mL). Error bars represent mean \pm SEM; $n > 30$ cells per condition; 3 biological replicates each. * $p < 0.05$, calculated using an ANOVA test.

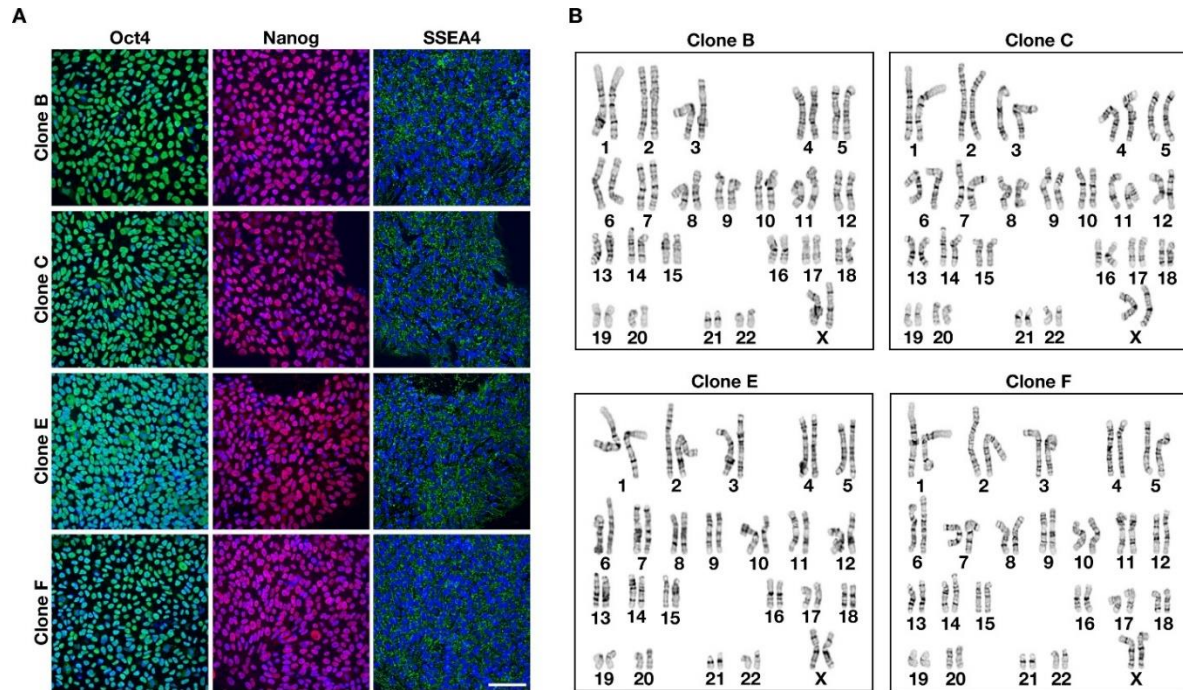


Figure S3. Incorporation of the TFG (p.R106C) mutation into human iPSCs, Related to Figure 3.

(A) Human iPSCs harboring heterozygous or homozygous TFG p.R106C mutations (Clones B, C, E, and F) were fixed and stained using antibodies directed against Oct4, Nanog, and SSEA4 together with Hoechst 33342 (n=3 each). Maximum intensity projections are shown. Scale bar, 100 μ m. (B) Giemsa banding analysis was performed on iPSCs harboring a mutation in TFG (Clones B, C, E, and F), revealing no changes in karyotype that resulted from CRISPR-mediated genome editing.

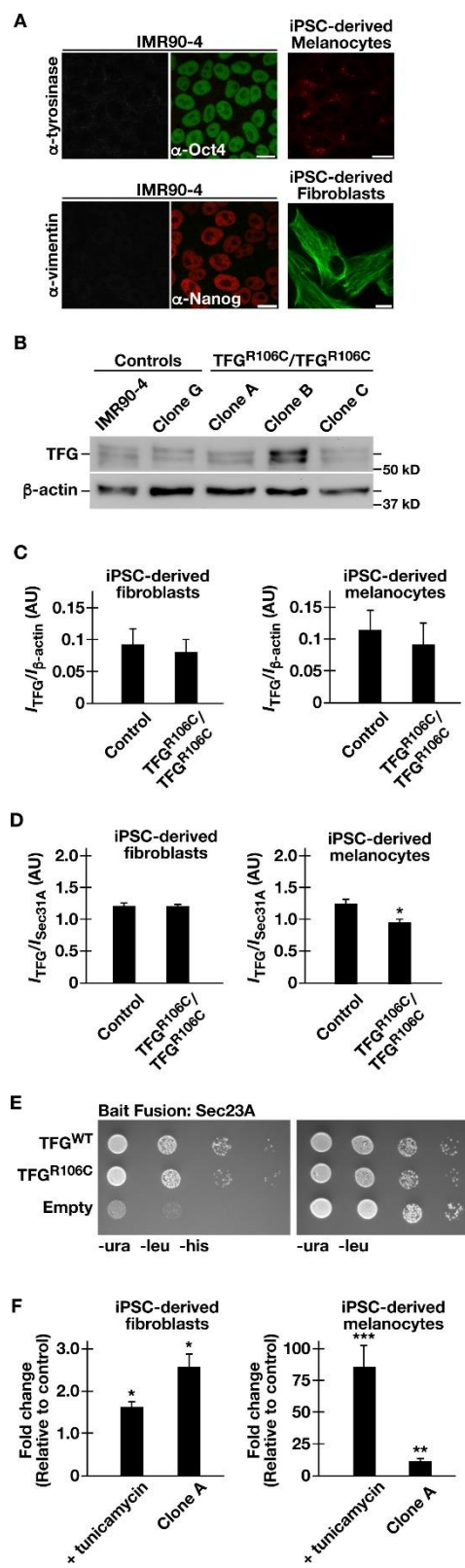


Figure S4. Characterization of human iPSCs harboring the TFG (p.R106C) mutation following differentiation to fibroblast and melanocyte fates, Related to Figures 4 and 5.

(A) Representative control iPSCs and iPSC-derived cell types (fibroblasts and melanocytes) were fixed and stained using antibodies directed against Oct4, Nanog, tyrosinase, and/or vimentin (n=3 each). Maximum intensity projections are shown. Scale bars, 10 μ m. (B) Representative immunoblot analysis of control iPSC-derived fibroblasts (IMR90-4 and Clone G) and fibroblasts harboring the homozygous TFG (p.R106C) mutation (Clones A-C) using antibodies directed against TFG and β -actin. (C) Densitometry analysis was performed to quantify changes in TFG levels relative to β -actin in both control and homozygous TFG (p.R106C) expressing iPSC-derived fibroblasts and melanocytes (n=3). No statistically significant difference was found, as calculated using a paired t test. (D) Fluorescence intensity (I) of TFG relative to Sec31A in iPSC-derived fibroblasts and melanocytes from control (IMR90-4 and Clone G) and homozygous TFG (p.R106C) expressing mutants (Clones A-C). Error bars represent mean \pm SEM; n > 30 cells per condition; 3 biological replicates each. *p < 0.05 (compared with control), calculated using a paired t test. (E) Yeast co-expressing plasmids encoding Sec23A (bait fusion) and several unique prey constructs were plated (10-fold dilutions, left to right) on- either selective (-Ura, -Leu, -His) or histidine supplemented medium for 48 hours (n=3). (F) Quantification of changes in luciferase-dependent luminescence relative to control (stably transduced IMR90-4 and Clone G) upon addition of tunicamycin (up to 5 μ g/mL overnight) or in cells harboring the homozygous TFG (p.R106C) mutation (Clone A). Error bars represent mean \pm SEM; 3 biological replicates each. ***p < 0.005, **p < 0.01, or *p < 0.05 (compared with control), calculated using a paired t test.

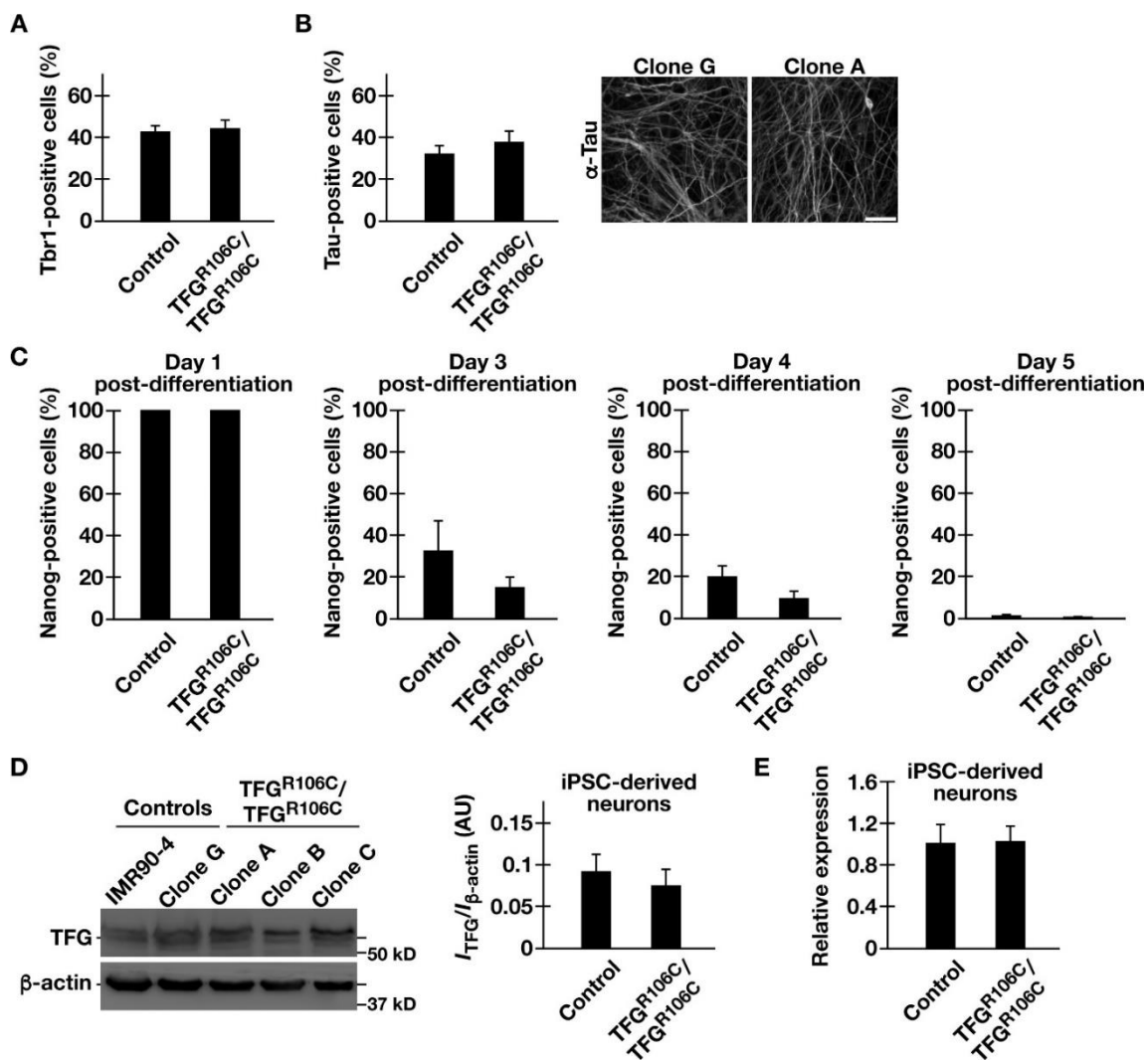


Figure S5. The TFG (p.R106C) mutation does not impair neuronal differentiation, Related to

Figure 6. (A-C) Flow cytometry was used to determine the percentage of cells expressing Tbr1 (A), Tau (B), and Nanog (C) in control (IMR90-4 and Clone G) or homozygous TFG (p.R106C) mutants (Clones A-C) after initiation of neuronal differentiation (C) or 12 weeks after neuronal differentiation (A and B). Error bars represent mean \pm SEM; 3 biological replicates each. No statistically significant difference was observed between conditions, based on a t test. Representative images of control (Clone G) or homozygous TFG (p.R106C) iPSC-derived neurons (Clone A) after 16 weeks of neuronal differentiation subsequent to fixing and staining with antibodies directed against Tau (B, right). Maximum intensity projections are shown. Scale bar, 50 μ m. (D) Representative immunoblot analysis of control iPSC-derived cortical neurons (IMR90-4 and Clone G) and neurons harboring the homozygous TFG (p.R106C) mutation (Clones A-C) using antibodies directed against TFG and β -actin (left). Densitometry analysis was performed to quantify changes in TFG levels relative to β -actin in both control and homozygous TFG (p.R106C) expressing iPSC-derived neurons (right, n=3). Error bars represent mean \pm SEM. No statistically significant difference was found, as calculated using a paired t test. (E) Quantitative PCR was used to measure the relative expression of TFG in wild-type iPSC-derived neurons (IMR90-4) as compared to control (Clone G) and homozygous TFG (p.R106C) mutant neurons (Clones A-C) (n=3 each). Error bars represent mean \pm SEM. No statistically significant difference was found, as calculated using an ANOVA test.

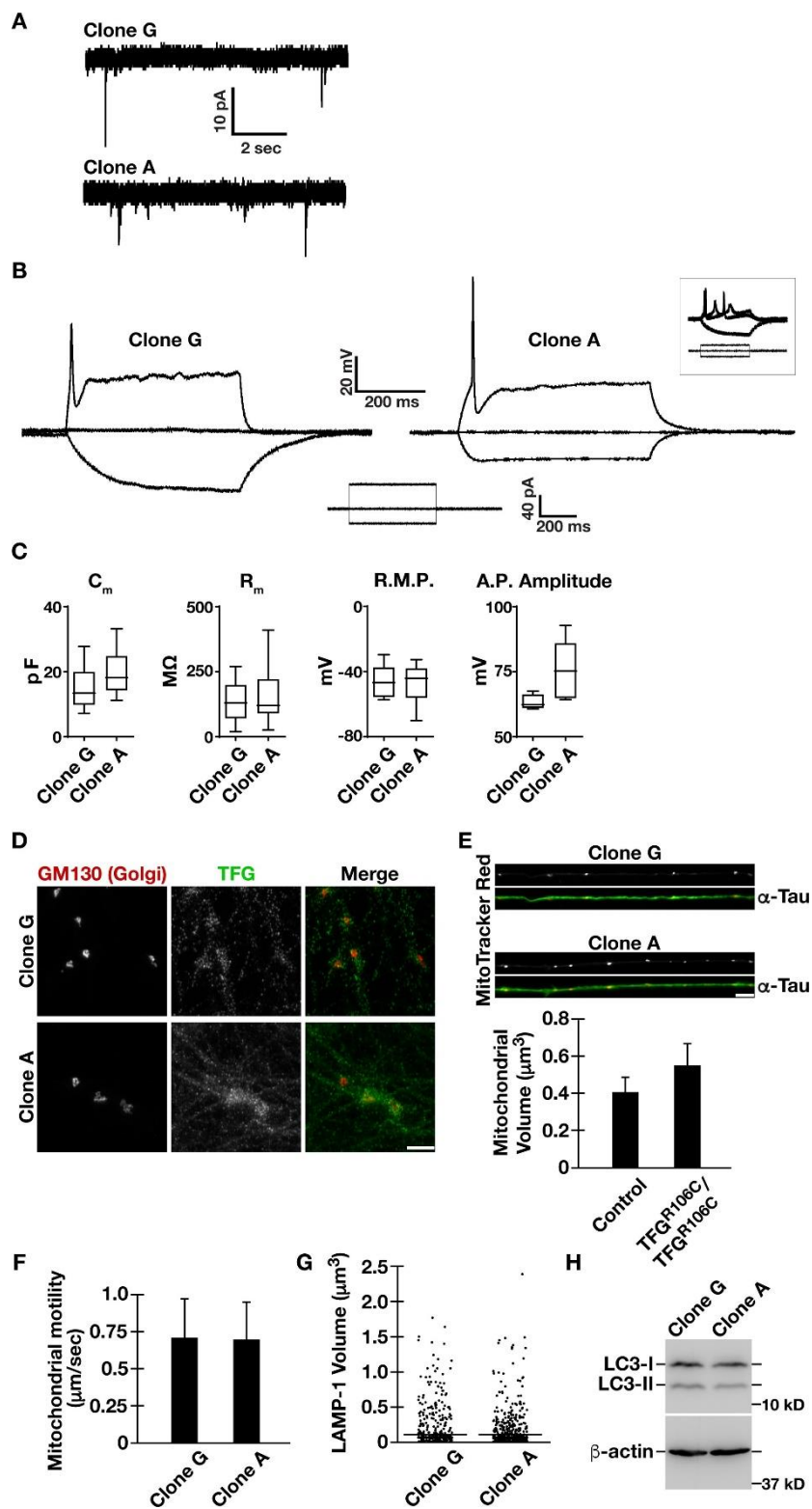


Figure S6. The TFG (p.R106C) mutation does not affect the electrophysiology of iPSC-derived neurons, Related to Figure 6. (A) Example voltage clamp traces showing spontaneous synaptic activity from control (Clone G; top) and homozygous TFG (p.R106C) mutant (Clone A; bottom) neurons. (B) Example membrane potential traces from control (Clone G; left) and homozygous TFG (p.R106C) mutant (Clone A; right) neurons. Smaller trace (center) shows applied current steps. Action potentials were observed in 40% of control neurons and 45% of homozygous TFG (p.R106C) mutant neurons. Occasional repetitive spiking (inset, far right) was also observed. (C) Quantification of membrane properties across cells (C_m , specific capacitance; R_m , resistance; R.M.P., resting membrane potential; A.P., action potential). No significant differences were observed between conditions, based on t tests ($n = 17$ cells, Clone G, and 11 cells, Clone A, from > 3 preparations). (D) Representative images of control (Clone G) and homozygous TFG (p.R106C) mutant (Clone A) neurons that were fixed and stained using antibodies directed against GM130 (red) and TFG (green). Maximum intensity projections are shown. Scale bar, 20 μm . (E) Representative images of control (Clone G) and homozygous TFG (p.R106C) mutant (Clone A) iPSC-derived neurons that were labeled with MitoTracker Red live and subsequently fixed and stained using antibodies directed against Tau (green). Maximum intensity projections are shown. Scale bar, 20 μm . The volumes of mitochondria imaged under these conditions were calculated using Imaris software. No statistically significant difference was found between control (IMR90-4 and Clone G) and homozygous TFG (p.R106C) mutant (Clones A-C) neurons, as calculated using a paired t test ($n > 30$ neurons per condition; 3 biological replicates each). (F) Particle tracking was used to measure the velocity of motile mitochondria in control (Clone G) and homozygous TFG (p.R106C) mutant (Clone A) iPSC-derived neurons that had been labeled with Rhodamine 123. No statistically significant difference was found, as calculated using a paired t test ($n > 30$ neurons per condition; 3 biological replicates each). (G) The volumes of LAMP-1 positive structures in control (Clone G) and homozygous TFG (p.R106C) mutant (Clone A) iPSC-derived

neuronal cell bodies were calculated using Imaris software. A scatter plot of all data is shown. No statistically significant difference was found, as calculated using a paired t test ($n > 30$ neurons per condition; 3 biological replicates each). (H) Representative immunoblot analysis of control iPSC-derived cortical neurons (Clone G) and neurons harboring the homozygous TFG (p.R106C) mutation (Clone A) using antibodies directed against LC3 and β -actin. Densitometry analysis was performed to quantify changes in LC3-I vs. LC3-II levels relative to β -actin in both control and homozygous TFG (p.R106C) expressing iPSC-derived neurons ($n=3$). No statistically significant difference was found, as calculated using a paired t test.

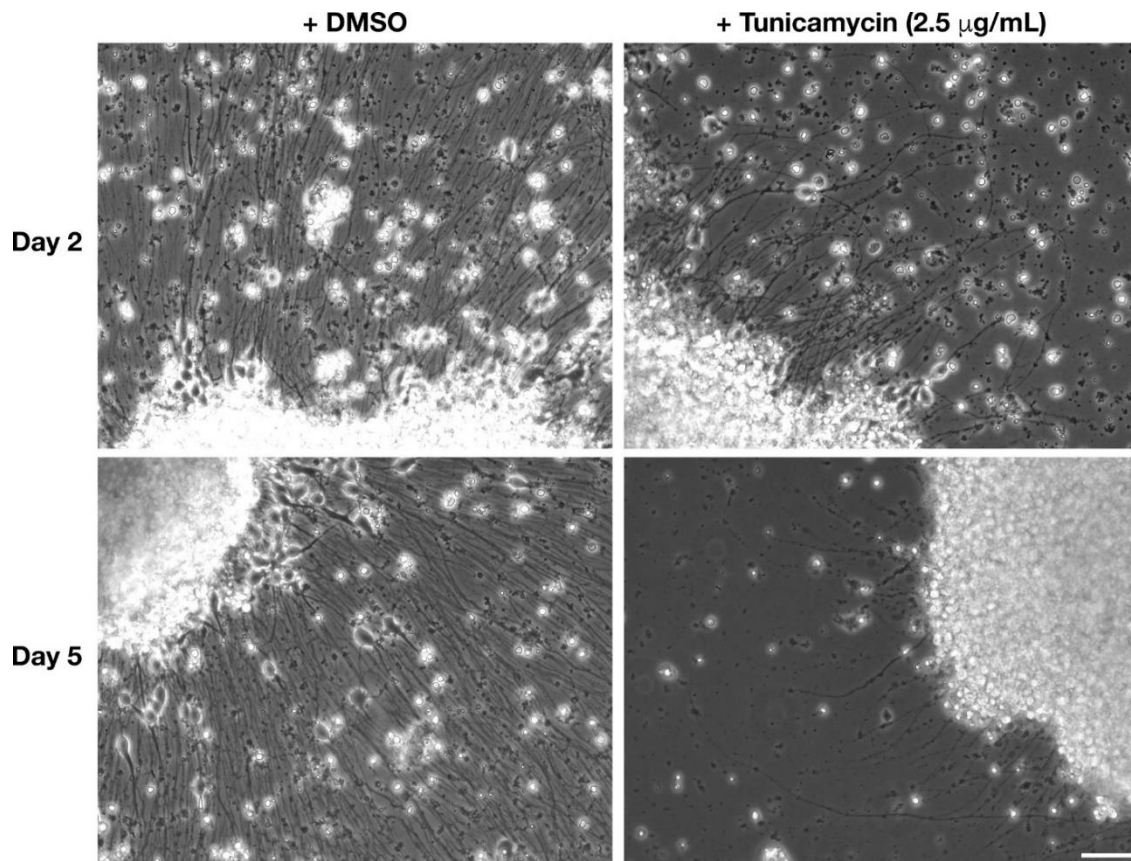


Figure S7. ER stress induced by tunicamycin impairs axon outgrowth and maintenance, Related to Figures 6 and 7. Control iPSC-derived neurospheres were plated onto glass coverslips and grown in the presence or absence of tunicamycin (2.5 µg/mL). Axon outgrowth was examined using brightfield imaging at various timepoints, as tunicamycin-treated neurons could not withstand fixation and immunostaining. Scale bar, 50 µm.

References

1. Allison, R., Edgar, J.R., Pearson, G., Rizo, T., Newton, T., Günther, S., Berner, F., Hague, J., Connell, J.W., Winkler, J., et al. (2017). Defects in ER-endosome contacts impact lysosome function in hereditary spastic paraplegia. *J. Cell Biol.* 216, 1337–1355.
2. Barry, J., Gu, Y., and Gu, C. (2010). Polarized targeting of L1-CAM regulates axonal and dendritic bundling in vitro. *Eur. J. Neurosci.* 32, 1618–1631.
3. Beetz, C., Johnson, A., Schuh, A.L., Thakur, S., Varga, R.E., Fothergill, T., Hertel, N., Bomba-Warczak, E., Thiele, H., Nürnberg, G., et al. (2013). Inhibition of TFG function causes hereditary axon degeneration by impairing endoplasmic reticulum structure. *Proc. Natl. Acad. Sci. USA* 110, 5091–5096.
4. Blackstone, C. (2012). Cellular pathways of hereditary spastic paraplegia. *Annu. Rev. Neurosci.* 35, 25–47.
5. Citterio, C., Vichi, A., Pacheco-Rodriguez, G., Aponte, A.M., Moss, J., and Vaughan, M. (2008). Unfolded protein response and cell death after depletion of brefeldin A-inhibited guanine nucleotide-exchange protein GBF1. *Proc. Natl. Acad. Sci. USA* 105, 2877–2882.
6. Colla, E., Coune, P., Liu, Y., Pletnikova, O., Troncoso, J.C., Iwatsubo, T., Schneider, B.L., and Lee, M.K. (2012). Endoplasmic reticulum stress is important for the manifestations of α -synucleinopathy in vivo. *J. Neurosci.* 32, 3306–3320.
7. de Souza, P.V.S., de Rezende Pinto, W.B.V., de Rezende Batistella, G.N., Bortholin, T., and Oliveira, A.S.B. (2017). Hereditary spastic paraplegia: clinical and genetic hallmarks. *Cerebellum* 16, 525–551.
8. Denton, K.R., Lei, L., Grenier, J., Rodionov, V., Blackstone, C., and Li, X.J. (2014). Loss of spastin function results in disease-specific axonal defects in human pluripotent stem cell-based models of hereditary spastic paraplegia. *Stem Cells* 32, 414–423.

9. Elsayed, L.E., Mohammed, I.N., Hamed, A.A., Elseed, M.A., Johnson, A., Mairey, M., Mohamed, H.E., Idris, M.N., Salih, M.A., El-Sadig, S.M., et al. (2016). Hereditary spastic paraplegias: identification of a novel SPG57 variant affecting TFG oligomerization and description of HSP subtypes in Sudan. *Eur. J. Hum. Genet.* 25, 100–110.
10. Fowler, P.C., Byrne, D.J., and O’Sullivan, N.C. (2016). Rare disease models provide insight into inherited forms of neurodegeneration. *J. Rare Dis. Res. Treat.* 1, 17–21.
11. Hanna, M.G., 4th, Block, S., Frankel, E.B., Hou, F., Johnson, A., Yuan, L., Knight, G., Moresco, J.J., Yates, J.R., 3rd, Ashton, R., et al. (2017). TFG facilitates outer coat disassembly on COPII transport carriers to promote tethering and fusion with ER-Golgi intermediate compartments. *Proc. Natl. Acad. Sci. USA* 114, E7707–E7716.
12. Harlalka, G.V., McEntagart, M.E., Gupta, N., Skrzypiec, A.E., Mucha, M.W., Chioza, B.A., Simpson, M.A., Sreekantan-Nair, A., Pereira, A., Günther, S., et al. (2016). Novel genetic, clinical, and pathomechanistic insights into TFG- associated hereditary spastic paraplegia. *Hum. Mutat.* 37, 1157–1161.
13. Helms, J.B., and Rothman, J.E. (1992). Inhibition by brefeldin A of a Golgi membrane enzyme that catalyses exchange of guanine nucleotide bound to ARF. *Nature* 360, 352–354.
14. Ishiura, H., Sako, W., Yoshida, M., Kawarai, T., Tanabe, O., Goto, J., Takahashi, Y., Date, H., Mitsui, J., Ahsan, B., et al. (2012). The TRK-fused gene is mutated in hereditary motor and sensory neuropathy with proximal dominant involvement. *Am. J. Hum. Genet.* 91, 320–329.
15. Jheng, J.R., Lau, K.S., Tang, W.F., Wu, M.S., and Horng, J.T. (2010). Endoplasmic reticulum stress is induced and modulated by enterovirus 71. *Cell. Microbiol.* 12, 796–813.
16. Johnson, A., Bhattacharya, N., Hanna, M., Pennington, J.G., Schuh, A.L., Wang, L., Otegui, M.S., Stagg, S.M., and Audhya, A. (2015). TFG clusters COPII-coated transport carriers and promotes early secretory pathway organization. *EMBO J.* 34, 811–827.

17. Jouet, M., Rosenthal, A., Armstrong, G., MacFarlane, J., Stevenson, R., Paterson, J., Metzberg, A., Ionasescu, V., Temple, K., and Kenrick, S. (1994). X-linked spastic paraplegia (SPG1), MASA syndrome and X-linked hydrocephalus result from mutations in the L1 gene. *Nat. Genet.* 7, 402–407.
18. Kawarai, T., Morita, M., Morigaki, R., Fujita, K., Nodera, H., Izumi, Y., Goto, S., Nakano, I., and Kaji, R. (2013). [Pathomechanisms of motor neuron death by mutant TFG]. *Rinsho Shinkeigaku* 23, 1199.
19. Li, H.L., Fujimoto, N., Sasakawa, N., Shirai, S., Ohkame, T., Sakuma, T., Tanaka, M., Amano, N., Watanabe, A., Sakurai, H., et al. (2015). Precise correction of the dystrophin gene in Duchenne muscular dystrophy patient induced pluripotent stem cells by TALEN and CRISPR-Cas9. *Stem Cell Reports* 4, 143–154.
20. Lo Giudice, T., Lombardi, F., Santorelli, F.M., Kawarai, T., and Orlandi, A. (2014). Hereditary spastic paraplegia: clinical-genetic characteristics and evolving molecular mechanisms. *Exp. Neurol.* 261, 518–539.
21. Maebayashi, H., Takeuchi, S., Masuda, C., Makino, S., Fukui, K., Kimura, H., and Tooyama, I. (2012). Expression and localization of TRK-fused gene products in the rat brain and retina. *Acta Histochem. Cytochem.* 45, 15–23.
22. McCaughey, J., Miller, V.J., Stevenson, N.L., Brown, A.K., Budnik, A., Heesom, K.J., Alibhai, D., and Stephens, D.J. (2016). TFG promotes organization of transitional ER and efficient collagen secretion. *Cell Rep.* 15, 1648–1659.
23. Menzies, F.M., Fleming, A., Caricasole, A., Bento, C.F., Andrews, S.P., Ashkenazi, A., Füllgrabe, J., Jackson, A., Jimenez Sanchez, M., Karabiyik, C., et al. (2017). Autophagy and neurodegeneration: pathogenic mechanisms and therapeutic opportunities. *Neuron* 93, 1015–1034.

24. Ogen-Shtern, N., Ben David, T., and Lederkremer, G.Z. (2016). Protein aggregation and ER stress. *Brain Res.* 1648 (Pt B), 658–666.
25. Presley, J.F., Cole, N.B., Schroer, T.A., Hirschberg, K., Zaal, K.J., and Lippincott-Schwartz, J. (1997). ER-to-Golgi transport visualized in living cells. *Nature* 389, 81–85.
26. Prischi, F., Nowak, P.R., Carrara, M., and Ali, M.M. (2014). Phosphoregulation of Ire1 RNase splicing activity. *Nat. Commun.* 5, 3554.
27. Putnam, C.D., Hammel, M., Hura, G.L., and Tainer, J.A. (2007). X-ray solution scattering (SAXS) combined with crystallography and computation: defining accurate macromolecular structures, conformations and assemblies in solution. *Q. Rev. Biophys.* 40, 191–285.
28. Qian, K., Huang, C.T., Chen, H., Blackburn, L.W., 4th, Chen, Y., Cao, J., Yao, L., Sauvey, C., Du, Z., and Zhang, S.C. (2014). A simple and efficient system for regulating gene expression in human pluripotent stem cells and derivatives. *Stem Cells* 32, 1230–1238.
29. Remondelli, P., and Renna, M. (2017). The endoplasmic reticulum unfolded protein response in neurodegenerative disorders and its potential therapeutic significance. *Front. Mol. Neurosci.* 10, 187.
30. Ríos-Barrera, L.D., Sigurbjörnsdóttir, S., Baer, M., and Leptin, M. (2017). Dual function for Tango1 in secretion of bulky cargo and in ER-Golgi morphology. *Proc. Natl. Acad. Sci. USA* 114, E10389–E10398.
31. Robberecht, W., and Philips, T. (2013). The changing scene of amyotrophic lateral sclerosis. *Nat. Rev. Neurosci.* 14, 248–264.
32. Saengsawang, W., Mitok, K., Viesselmann, C., Pietila, L., Lombard, D.C., Corey, S.J., and Dent, E.W. (2012). The F-BAR protein CIP4 inhibits neurite formation by producing lamellipodial protrusions. *Curr. Biol.* 22, 494–501.
33. Saheki, Y., and De Camilli, P. (2017). Endoplasmic reticulum-plasma membrane contact sites.

- Annu. Rev. Biochem. 86, 659–684.
34. Schäfer, M.K., and Frotscher, M. (2012). Role of L1CAM for axon sprouting and branching. *Cell Tissue Res.* 349, 39–48.
 35. Scheper, W., and Hoozemans, J.J. (2015). The unfolded protein response in neurodegenerative diseases: a neuropathological perspective. *Acta Neuropathol.* 130, 315–331.
 36. Schrandt-Stumpel, C., Höweler, C., Jones, M., Sommer, A., Stevens, C., Tinschert, S., Israel, J., and Fryns, J.P. (1995). Spectrum of X-linked hydrocephalus (HSAS), MASA syndrome, and complicated spastic paraplegia (SPG1): clinical review with six additional families. *Am. J. Med. Genet.* 57, 107–116.
 37. Schuh, A.L., Hanna, M., Quinney, K., Wang, L., Sarkeshik, A., Yates, J.R., and Audhya, A. (2015). The VPS-20 Subunit of the Endosomal Sorting Complex ESCRT-III Exhibits an Open Conformation in the Absence of Upstream Activation. *Biochem. J.* 466, 625–637.
 38. Sheng, L., Leshchyns'ka, I., and Sytnyk, V. (2013). Cell adhesion and intracellular calcium signaling in neurons. *Cell Commun. Signal.* 11, 94.
 39. Sumimoto, H., Kamakura, S., and Ito, T. (2007). Structure and function of the PB1 domain, a protein interaction module conserved in animals, fungi, amoebas, and plants. *Sci. STKE* 2007, re6.
 40. Valenzuela, V., Martínez, G., Duran-Aniotz, C., and Hetz, C. (2016). Gene therapy to target ER stress in brain diseases. *Brain Res.* 1648 (Pt B), 561–570.
 41. Vazin, T., Ball, K.A., Lu, H., Park, H., Ataeijannati, Y., Head-Gordon, T., Poo, M.M., and Schaffer, D.V. (2014). Efficient derivation of cortical glutamatergic neurons from human pluripotent stem cells: a model system to study neurotoxicity in Alzheimer's disease. *Neurobiol. Dis.* 62, 62–72.
 42. Wang, X., Huang, T., Bu, G., and Xu, H. (2014). Dysregulation of protein trafficking in

- neurodegeneration. *Mol. Neurodegener.* 9, 31.
43. Weis, J., Claeys, K.G., Roos, A., Azzedine, H., Katona, I., Schröder, J.M., and Senderek, J. (2017). Towards a functional pathology of hereditary neuropathies. *Acta Neuropathol.* 133, 493–515.
 44. Winther, M., and Walmod, P.S. (2014). Neural cell adhesion molecules belonging to the family of leucine-rich repeat proteins. *Adv. Neurobiol.* 8, 315–395.
 45. Witte, K., Schuh, A.L., Hegermann, J., Sarkeshik, A., Mayers, J.R., Schwarze, K., Yates, J.R., 3rd, Eimer, S., and Audhya, A. (2011). TFG-1 function in protein secretion and oncogenesis. *Nat. Cell Biol.* 13, 550–558.
 46. Wu, J., and Kaufman, R.J. (2006). From acute ER stress to physiological roles of the unfolded protein response. *Cell Death Differ.* 13, 374–384.
 47. Xie, F., Ye, L., Chang, J.C., Beyer, A.I., Wang, J., Muench, M.O., and Kan, Y.W. (2014). Seamless gene correction of b-thalassemia mutations in patient-specific iPSCs using CRISPR/Cas9 and piggyBac. *Genome Res.* 24, 1526–1533.
 48. Yagi, T., Ito, D., and Suzuki, N. (2016). TFG-related neurologic disorders: new insights into relationships between endoplasmic reticulum and neurodegeneration. *J. Neuropathol. Exp. Neurol.* 75, 299–305.